UNIVERSITY OF CALIFORNIA, SAN DIEGO

Numerical and analytical studies of two-dimensional vortex pair dynamics in unstratified and stratified environments

A dissertation submitted in partial satisfaction of the
requirements for the degree Doctor of Philosophy

in

Engineering Sciences (Aerospace Engineering)

by

Laura Katherine Brandt

Committee in charge:

Professor Keiko Nomura, Chair
Professor George Carnevale
Professor Fred Driscoll
Professor Stefan Llewellyn Smith
Professor James Rottman

2009

The dissertation of Laura Katherine Brandt is approved, and is acceptable in quality and form for publication on microfilm and electronically:

_____

_____

_____

_____

_____
Chair

University of California, San Diego

2009

DEDICATION

To my husband Steve,
for your love, devotion, support
and putting up with all the late nights.

TABLE OF CONTENTS

LIST OF FIGURES

ACKNOWLEDGEMENTS

There are numerous people who have positively affected me and aided in my success in graduate school. I would like to thank my advisor, Professor Keiko Nomura, for helping me pursue my research interests and broadening my understanding of fluid mechanics. I would also like to thank Professor James Rottman and Professor Stefan Llewellyn Smith for taking time away from their busy schedules to expand my research topic and education. Furthermore, I would like to acknowledge my fellow graduate students, past and present, in the CFD lab for their academic insight and computer troubleshooting.

I would also like to thank the MAE department for being so accommodating and recognizing that each graduate student is a unique individual. Thanks to Gerri Johnson, Linda McKamey and Michelle Vavra in Student Affairs for your administrative support and time spent dealing with graduate student dilemmas. I would also like to recognize Andre Burgos for his attentiveness to computer problems and technical assistance.

I am deeply indebted to ARCS (Achievement Rewards for College Scientists) for their unconditional financial support, allowing me the unique opportunity of selecting a research project that might otherwise not receive funding.

I would like to acknowledge the use of published and submitted material to *Physics of Fluids* and *Journal of Fluid Mechanics*.

Chapter 3, in part, is a reprint of the material as it appears in *Physics of Fluids* Volume 18, pages 1-4. Brandt, L.; Nomura, K., American Institute of Physics, 2006 and *Journal of Fluid Mechanics* Volume 592, pages 413-446. Brandt, L.; Nomura, K., Cambridge University Press, 2007. The dissertation author was the primary investigator and author of these papers.

Chapter 4, in part, is a reprint of the material as it appears in *Journal of Fluid Mechanics* submitted. Brandt, L.; Nomura, K., Cambridge University Press, 2008. The dissertation author was the primary investigator and author of this

paper.

Chapter 5, in part, is a reprint of the material as it appears in *Journal of Fluid Mechanics* Volume 592, pages 413-446. Brandt, L.; Nomura, K., Cambridge University Press, 2007. The dissertation author was the primary investigator and author of this paper.

VITA

Ph.D., Engineering Science (Aerospace Engineering)

University of California, San Diego (2008)

Advisor: Keiko K. Nomura

M.S., Engineering Science (Aerospace Engineering)

University of California, San Diego (2007)

B.S., Aerospace Engineering

University of California, San Diego (2004)

TEACHING EXPERIENCE

Teaching Assistant, University of California, San Diego

Dept of Mechanical and Aerospace Engineering (2004-2007)

Served as T.A. for undergraduate courses: Introduction to Aerospace Engineering, Introduction to Mechanical Engineering, Introduction to Fluid Mechanics, Advanced Fluid Mechanics, Thermodynamics, Experimental Techniques, Aerospace Senior Design Course. Prepared and presented discussion sections, held office hours, responded to student emails, and prepared and presented review sessions. Typically held position of head TA overseeing 100-200 students, multiple TA's and graders.

Departmental Senior Teaching Assistant, University of California, San Diego

Dept of Mechanical and Aerospace Engineering (2005-2008)

Prepared and presented workshops and training sessions for incoming and continuing TA's within the *Dept of Mechanical and Aerospace Engineering.* Held the role of liaison between faculty and TA's and students and TA's when problems arose.

INDUSTRY EXPERIENCE

Hydrodynamicist

Science Applications International Corporation (SAIC) (2008- Present)

Analytically and numerically developing a depth-integrated model for long internal waves propagating over variable bathymetry in two horizontal dimensions. Computationally validating model with known analytical solutions and experimental results.

Systems Engineer Intern

The Boeing Company (Summer 2004)

Conducted trade studies to assist in the formulation of software architecture. Incorporated deferred software systems into requirement schedule to allot for the army's advancement in Future Combat Systems (FCS).

Composites Engineer Intern

NAVAIR (Summer 2003)

Utilized NASTRAN/PATRAN to designate repair zones. Documented repair steps for the F/A-18 horizontal stabilizer structural repair manuals. Performed Hazardous Material Reports (HMR) and initiated Engineering Investigations (EI).

PROFESSIONAL AFFILIATIONS

American institute of Aeronautics and Astronautics (AIAA)

American Physical Society (APS)

AWARDS AND FELLOWSHIPS

2005-2008 Academic Fellowship, Achievement Award for College Scientists (ARCS)

2005-2006 Teaching Assistant of the year, University of California, San Diego, Dept of Mechanical and Aerospace Engineering

JOURNAL PUBLICATIONS

BRANDT, L., NOMURA, K. (2008) A generalized merging criterion for co-rotating vortices. *J. Fluid Mech.*, submitted.

BRANDT, L., NOMURA, K. (2007) The physics of vortex merger and the effects of ambient stable stratification. *J. Fluid Mech.* 592, 413-446.

BRANDT, L., NOMURA, K. (2006) The physics of vortex merger: further insight. *Phys. Fluids* 18, 1-4.

SELECTED CONFERENCE PRESENTATIONS

BRANDT, L., NOMURA, K. Elementary vortex systems and the generation of internal waves. APS Meeting of the Division of Fluid Dynamics, San Antonio, Texas. 2008.

BRANDT, L., NOMURA, K. Viscous interactions of asymmetric co-rotating vortex pairs. APS Meeting of the Division of Fluid Dynamics, Salt Lake City, Utah. 2007.

BRANDT, L., NOMURA, K. Vortex merger in stably stratified fluid. Sixth International Symposium on Stratified Flows, Perth, Australia, 2006.

BRANDT, L., NOMURA, K. Vortex merging in stably stratified fluid. APS Meeting of the Division of Fluid Dynamics, Tampa Bay, Florida. 2006.

BRANDT, L., NOMURA, K. Vortex merging in stably stratified fluid. APS Meeting of the Division of Fluid Dynamics, Chicago, Illinois. 2005.

ABSTRACT OF THE DISSERTATION

Numerical and analytical studies of two-dimensional vortex pair dynamics in unstratified and stratified environments

by

Laura Katherine Brandt

Doctor of Philosophy in Engineering Sciences (Aerospace Engineering)

University of California, San Diego, 2009

Professor Keiko Nomura, Chair

This work investigates fundamental two-dimensional vortex pair dynamics in unstratified and stably stratified environments through numerical and analytical techniques. The study focuses on two main topics: (i) vortex interaction and merging of co-rotating vortex pairs and (ii) internal wave generation by co-rotating and counter-rotating vortex pairs.

Two-dimensional vortex merging in a viscous fluid is studied using numerical simulations. Analysis of the ideal case of two equal co-rotating vortices (symmetric pair) identifies the basic underlying physics of vortex merger. Through the interaction of the vorticity gradient and the mutually induced strain rate near the central hyperbolic point, a tilt in vorticity contours is established. This leads to core detrainment and the entrainment of core fluid into the exchange band, which transforms the flow into a single vortex.

In the case of the asymmetric (unequal strength) vortex pair, the disparity

in the deformation rates between the vortices alters the interaction. A critical value for a strain rate parameter characterizing the establishment of core detrainment is determined. The onset of merging is associated with the achievement of the critical strain by both vortices and a generalized merging criterion is formulated. A classification scheme of the various viscous vortex interactions is developed.

Results for the symmetric, horizontally oriented vortex pair in a weakly stratified fluid provide further insight on vortex merging. The effects of weak stratification depend on the ratio of the diffusive time scale to the turnover time, i.e., the Reynolds number. A crossover Reynolds number is found, above which convective merging is accelerated with respect to unstratified flow and below which it is delayed.

The generation of internal waves by *horizontally* orientated co-rotating and counter-rotating vortex pairs is studied. Linearized inviscid equations are derived that describe the internal wave, vorticity and energy fields. These solutions are compared with nonlinear numerical viscous simulations in moderately and strongly stratified environments. Through evaluation of the energy field, the time at which the flow reaches a steady state for strongly stratified flows is found, along with a characterization of the regimes of strongly and moderately stratified environments.

Chapter 1

Introduction

1.1 Introduction

Vortex pairs are elementary flows that have both fundamental and practical significance. They consist of two *co-rotating* vortices with same sign vorticity or two *counter-rotating* vortices with opposite sign vorticity. Vortices are the fundamental building blocks of more complex flows, such as turbulence, transitional flows and wakes. A pair of vortices is the simplest configuration with which to study vortex interactions. These interactions play a significant role in the transfer of energy and enstrophy across scales. With ambient stable stratification, these interactions and associated energy transfer are complicated by production of baroclinic torque and internal wave generation.

The ideal case of a two-dimensional *symmetric* vortex pair consists of two equal size and equal strength vortices. For counter-rotating vortex pairs in a viscous fluid, it is known that they propagate together in a fixed direction due to their mutually induced velocity and remain a fixed distance apart. The physical mechanisms underlying the behavior of this flow are understood and well studied. In contrast, for co-rotating vortex pairs, the physical mechanisms governing the interactions are not fully understood. Initially these vortices rotate about one

another at a constant distance apart. The vortex cores grow due to diffusion until their size is a certain fraction of the separation distance. At this time, the separation distance rapidly decreases and the vortices merge into a single vortex. Despite the apparent simplicity of this flow, the physics underlying the merging process is unclear.

In engineering and environmental applications, what is more commonly observed are *asymmetric* vortex pairs, with vortices of unequal size and strength. The behavior of such pairs is quite different from *symmetric* vortex pairs. For the counter-rotating vortex pairs, the unequal induced velocities cause the vortices to rotate about one another and the unequal induced strain field causes an asymmetric deformation of the vortices. The final states of these vortices are Reynolds number independent and only dependent on the initial core size and separation distance. For co-rotating vortex pairs, the final states are dependent not only on the initial geometry, but there is also a distinct Reynolds number dependence. Such pairs may result in the destruction of the smaller/weaker vortex (Dritschel and Waugh, 1992). Additional issues arise concerning the definition of merger.

Also of interest is the effect of stable density stratification on these flows, such as is found in the atmosphere and oceans. Wakes, turbulence, transitional flows, etc... can all be subject to stable density stratification. The stirring of the density field by *horizontally* oriented vortex pairs results in the baroclinic generation of vorticity and the production of internal waves. For weak stratification, a counter-rotating vortex pair's separation distance decreases. However, in a strongly stratified fluid, the vortices are found to move apart. This variation is caused by the generated vorticity (Garten et al., 2001). In addition to generated vorticity, the internal wave field produced by these vortices greatly affects the energy transfer in the flow. This energy transfer is shown to be dependent on the level of stratification, which has not been well studied for moderate stratification, when the buoyancy and convective effects are of comparable importance. The presence of stratification may also significantly influence the co-rotating vortex pair. However,

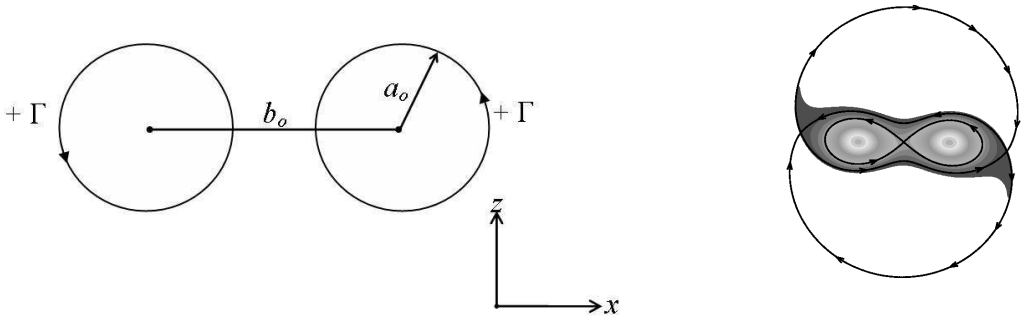

(a) Initial flow field (b) Co-rotating frame

Figure 1.1: (a) Initial symmetric vortices with equal circulation strength, Γ_o, and centers separated by a distance, b_o, with equal core diameters, $2a_o$, (b) Co-rotating frame streamlines superimposed on contours of vorticity for a symmetric unstratified vortex pair. Streamlines indicate the boundary between the inner-core region and the exchange band and the boundary between the exchange band and the outer-recirculation region (location of filamentation).

the behavior of a *horizontally* oriented co-rotating vortex pair in a stably stratified fluid, and in particular the merging process and properties of the generated internal wave field, has not been previously studied.

The motivation of this study is the need for a better understanding of fundamental dynamics of vortex pairs, which are the foundation for a broad scope of flows. The current study will focus on two specific topics:

- co-rotating vortex interactions and merging in unstratified and stratified environments; and
- internal wave generation by co-rotating and counter-rotating vortex pairs.

We will conduct these studies by means of analytical techniques and numerical simulations.

1.2 Literature Review

1.2.1 Unstratified, Symmetric, Co-rotating Vortex Pairs

There have been several proposals for a criterion that predicts the onset of vortex merger. In an unstratified fluid, a pair of *symmetric* vortices of equal circulation, Γ, and equal core radius, a, separated by a distance, b, will rotate about each other due to the mutually induced velocity (figure 1.1a). Much of the previous work on symmetric vortex merger has focused on the determination of $(a/b)_{cr}$ (Rossow, 1977; Saffman and Szeto, 1980; Overman and Zabusky, 1982; Griffiths and Hopfinger, 1987; Meunier et al., 2002), where if the aspect ratio a/b exceeds some critical value, $(a/b)_{cr}$, vortex merger results. Using contour dynamics of uniform vortices, Saffman and Szeto (1980) and Overman and Zabusky (1982) find a critical separation distance, $(a_o/b)_{cr}$, above which equilibrium configurations of non-circular vortices can exist, and below which the vortices are unstable and merge. A linear stability analysis of such equilibrium configurations is performed by Dritschel (1985) which associates the instability with the vortex core boundary deformation. However, in general, experimental measurements (viscous, non-uniform vortices) of $(a/b)_{cr}$ and the onset of instability predicted by analytical stability analysis have varied due to difficulties of measurement and inconsistent definitions of a_{cr} and b_{cr}. Meunier et al. (2002) develop a general merging criterion for equal nonuniform vortices using both a stability analysis and experimental data (viscous flow) in an attempt to generalize all the previous work. The criterion is expressed by $(a/b_o)_{cr}$, with a evaluated from the second moment of vorticity (or angular impulse). In their experiments, the onset of merging is considered to be the transition from a diffusive- to a convective-dominated process, the former characterized by the diffusive growth of the core. The critical values from their stability analysis are comparable, although somewhat lower.

There have been several hypotheses to explain the physical mechanism of

vortex merger. An important study was conducted by Melander et al. (1988). They were the first to examine the flow in a co-rotating reference frame which reveals the differential motion and associated flow structure. This is illustrated here in figure 1.1b which shows the principle streamlines (separatrices) defining three distinct regions in the flow. The *inner core regions* consist of closed streamlines encircling each individual vorticity maximum and correspond to the primary vortices. The *exchange band* consists of closed streamlines encompassing both inner core regions and corresponds to fluid circulating (exchanged) between the two vortices. The two *outer recirculation regions* consist of fluid which circulates in the opposite sense (in the co-rotating frame) to that of the cores and exchange band. Melander et al. (1988) explain the occurrence of merger in terms of the vorticity distribution relative to the separatrices. In particular, when vorticity enters the outer recirculation regions, differential rotation causes the formation of filaments which breaks the symmetry of the flow. This modifies the orientation of the vorticity contours with respect to the streamlines and leads to merger through an inviscid axisymmetrization process. The process of axisymmetrization was studied in detail for an isolated elliptical vortex by Melander et al. (1987b). They indicate both filaments and gradient intensification in the core contribute to asymmetric vorticity. Although the importance of the exchange band was noted, Melander et al. (1988) indicate that merger is driven by filament formation. A subsequent study by Dritschel (1998) shows that non-axisymmetry may persist indefinitely in an inviscid flow suggesting that it is the presence of diffusion that promotes axisymmetrization.

Cerretelli and Williamson (2003) further consider these ideas and demonstrate experimentally that merger is due to the antisymmetric part of the vorticity field which is also considered to be primarily associated with the filaments. They suggest that vorticity enters the outer recirculation region through viscous or turbulent diffusion thereby initiating filament formation. Meunier et al. (2005) explain the role of the filaments and accompanying reduction in b in terms of

conservation of angular momentum. They develop a simple model depicting the role of filamentation. Although the model accurately predicts the initial reduction in b, it does not predict the dominant motion of the vortices, suggesting that some other mechanism is present. Velasco Fuentes (2005) finds that filamentation does not always lead to merger. In the case of vorticity profiles with steeper gradients, merger begins before filamentation takes place. The stability analysis by Dritschel (1985) also precludes the requirement of filamentation for convective merger. Huang (2005) shows that "sheetlike structures" emanating from the vortices, which includes both filament and exchange band fluid, are responsible for the induced merging velocity. The formation of these structures is attributed to a tilt of the major axes of the vortices and the connecting line between the vortex centroids. How the tilt is established is not explained.

1.2.2 Unstratified, Asymmetric, Co-rotating Vortex Pairs

While many studies have focused on the physics behind symmetric co-rotating vortex merger, what is more commonly observed are asymmetric (unequal size and strength) vortex pairs. In this case, there is a greater range of flow behavior and the interaction of the vortices may result in the destruction of the smaller and/or weaker vortex. In the case of asymmetric co-rotating vortex pairs, there are limited studies (Melander et al., 1987a; Dritschel and Waugh, 1992; Mitchell and Driscoll, 1996; Trieling et al., 2005).

Dritschel and Waugh (1992), using detailed contour dynamics simulations, study the inviscid interactions between two unequal sized vortex patches of uniform vorticity and equal strength. They develop a classification of the flow into five distinct regimes based on the changes in the initial and final circulations for the vortices: *elastic interaction* occurs when there are small deformations and essentially no change in circulation of the vortices; *partial straining-out* and *complete straining-out* regimes are associated with a reduction or destruction, respectively,

of the smaller vortex, with no increase in the larger vortex; *complete merger* and *partial merger* correspond to increased circulation of the initially larger vortex, i.e., a compound vortex is ultimately formed which contains ω from both vortices. They develop a flow regime map, in terms of the initial vortex radii ratio and initial separation distance.

Trieling et al. (2005) study the inviscid interactions of unequal vortices with nonuniform vorticity distributions. They consider both unequal-size/equal-vorticity and equal-size/unequal-vorticity cases. They find the same flow regimes of Dritschel and Waugh (1992) to exist for these more general vortex distributions, but the regime boundaries are highly sensitive to the vorticity profile. They show, through contour surgery, the removal of the low level ω contours, that it is this "halo" of low level ω, and not the internal vorticity distribution of the vortex, that causes an increase in the critical distance with decreasing profile steepness. The influence of vorticity distribution was qualitatively similar for both the equal-vorticity and equal-size cases. The resulting mapping of flow regimes is a very complex function of vorticity distribution, initial vortex radii ratio (or initial vortex strength ratio) and initial separation distance.

Ehrenstein and Rossi (1999) and Meunier et al. (2002) consider equilibrium states for nonuniform vortices. In these studies, the critical distance is associated with an exchange of stability, which is considered as the onset of merger. The corresponding vortex configuration is characterized by nearly elliptical streamlines within the inner core region and the formation of a cusp at the outer core boundaries, where ω is low, in the vicinity of the center of the pair. In the case of an asymmetric vortex pair (Ehrenstein and Rossi, 1999), the cusp forms at the outer boundary of the weaker vortex.

Trieling et al. (2005) attempted to calculate the point at which asymmetric pairs would merge in a similar way as Meunier et al. (2002) did for the symmetric pairs, by normalizing the separation distance by the second moment of vorticity. However, this did not produce a universal critical value to characterize the flow

regimes. With significant asymmetry between vortices, merger may not occur and the weaker vortex may be strained-out and either partially or completely destroyed. Dritschel and Waugh (1992) estimate a critical separation distance for complete destruction of the smaller vortex by considering the critical strain rate for an initially circular vortex to undergo irreversible tearing by an imposed adverse shear (Kida, 1981; Legras and Dritschel, 1993; Mariotti et al., 1994). This provides a good estimate for the boundary between partial and complete straining out regimes in the more asymmetric cases (ratio of initial radii $\lesssim 0.4$). The question still remains as to whether or not a critical aspect ratio can be defined for asymmetric merger.

1.2.3 Stratified, Symmetric, Vortex Pairs

The effects of density stratification on *horizontally* oriented vortex pairs greatly affects the flow dynamics with the generation of vorticity and production of internal waves. For co-rotating vortices, there have been numerous studies conducted that look at complex flows containing these pairs. However, the fundamental case of a *horizontally* oriented co-rotating vortex pair in a stably stratified fluid has not been examined.

Contrary to the co-rotating vortex pair, there have been numerous studies conducted that look into the effects of stratification on *horizontal* counter-rotating vortex pairs. One of the first studies to consider a *horizontal* counter-rotating vortex pair in a stratified fluid was Scorer and Davenport (1970). Their study considered an inviscid fluid which neglected baroclinically generated vorticity. Buoyancy effects were considered by equating the vortex pair impulse rate of change to the total buoyancy force, with the conclusion that the vortex pair accelerated downward and that the separation distance increased. This study was succeeded by Saffman (1972), who formulated an approximate solution by considering a constant separation distance. Through the determination of the velocity potential,

he found that the vortex pair decelerated and in time reversed directions, which in turn caused the pair to oscillate. Crow (1974) showed how generated vorticity causes the vortices to move away from one another, thereby validating Scorer and Davenport (1970) theory. This study was succeeded by Hill (1975), who shows that initially the vortex pair decelerates, but eventually detrained vorticity causes a downward acceleration.

In more recent studies, there has been a distinction in levels of stratification. For weak stratification (convective affects dominate over buoyancy affects), a number of numerical studies (Schilling et al., 1996; Spalart, 1996; Garten et al., 1998) have found that the vortex pair's separation distance decreases while the acceleration of the pair increases. However these findings are in direct contrast to those found by experimental results (Sarpkaya, 1983; Delisi et al., 1991), which show there is a deceleration in the flow while the separation distance decreases. In a two-dimensional numerical study, Holzapfel and Gerz (1999) show that early in the flow development the vortex pair decelerates, but that later on the pair begins to accelerate. They attributed these flow characteristics to the generation of opposite signed vorticity through baroclinic torque, which is the same conclusion that Hill (1975) found 24 years earlier.

For very strong stratification (buoyancy affects dominate over convective affects), the flow behaves according to the linearized Navier Stokes equations. Meng and Rottman (1988) analytically derive the linearized inviscid solution for various vortex configurations, including the counter-rotating vortex pair. For strong enough stratification, this solution accurately predicts the flows behavior.

For moderate stratification (buoyancy affects are comparable to convective affects), Garten et al. (1998) found that there is an early adjustment phase of the flow, where the separation of the pair does not change and the flow develops according to Saffman's theory (Saffman, 1972). The duration of this period was found to be dependent on the level of stratification. After this phase, the flow transitions into an advection phase where the separation distance begins to increase

following Crow's theory (Crow, 1974), while the trajectory of the pair may be predicted by Saffman (1972). This work focuses its discussion on the effects of generated vorticity and its affect on the flow. However, little attention is focused on the generation of gravity waves.

In stably stratified fluids disturbances in the density field will generate internal waves. The presence of such waves generated by co-rotating and counter-rotating vortex pairs leads to complex wave-vortex and wave-wave interactions. These interactions are primary attributes of complex turbulent flows found in the oceans and atmosphere. There have been a number of studies, both observational and numerical, that have considered the coherent structures within turbulent motions in unstratified and stratified environments with attention placed on vortex structures (Rogers and Moin, 1987; She et al., 1990; Vincent and Meneguzzi, 1991, 1994; Sandham and Kleiser, 1992; Cadot et al., 1995; Carnevale et al., 1991; Metais et al., 1995; Diamessis and Nomura, 2004). Such structures influence the energy transfer and enstrophy of the flow through the pairing and destruction of the vortices. In stably stratified flows, internal gravity waves also affect the energy and enstrophy of the flow.

There has been numerous observational, experimental and numerical work that demonstrates a strong interaction between internal waves and turbulence. Early studies, such as Lin and Pao (1979) review article on wakes in stratified fluids, find that stratification inhibits fluctuations in the vertical velocity and that turbulence decays more rapidly than internal waves. Lin and Veenhuizen (1974) investigated the decay of grid-generated turbulence in stratified fluid both visually and quantitatively, finding that as the vertical displacements of the fluid increased, the stronger the internal-wave field became. Pao et al. (1968) studied a vortex street in a stratified fluid, observing that the vertical spacing between the vortices decreases downstream and rapidly collapses into internal waves. In a later study (Pao and Lin, 1973), Pao developed a method for distinguishing turbulence from internal waves through their phase characteristics. These early papers focused

primarily on the effect that stratification had on the turbulent source, but placed little attention on the generation of the internal waves.

Staquet and Sommeria (2002) review both numerical and experimental studies that analyze internal gravity waves produced by instabilities and turbulence. Through comparative studies of oceanic and atmospheric observations, experiments and numerical simulations, various properties of wave turbulence were illustrated. They present various statistical models of turbulence generated internal waves for weakly and strongly stratified fields. However, there is a lack of universality among the models, where each model is only valid for a particular range of temporal and spatial scales.

In a recent study conducted by Sutherland et al. (2004), the generation of internal waves by the collapse of a mixed fluid mass immersed in a vertically stratified fluid was studied through laboratory and numerical experiments. Through this study it was found that the long horizontally scaled internal gravity waves cause the mixed region to be significantly distorted, which greatly varied from the collapse of a standard interfacial gravity current. Dohan and Sutherland (2005) studied the generation of internal waves in a uniformly stratified mixed region by use of oscillating grid experiments in the laboratory and two-dimensional numerical simulations. This study focused on the vertically propagating wave field within the quiescent region rather than study the turbulence or interfacial waves as done in numerous other studies (Fernando and Hunt, 1997; McGrath et al., 1997; Briggs et al., 1996). They found that their two-dimensional numerical simulations and their three-dimensional experimental results were consistent. This demonstrates that much insight into turbulence generated internal waves may be found through two-dimensional studies. Their study also suggests that there is a coupling between the turbulence and internal wave field, where most of the horizontal momentum is carried away from the turbulent source by the dominant wave frequencies.

Buhler and McIntyre (1999) formulate an idealized linear model for low-frequency inertia-gravity waves generated by Kelvin-Helmhotltz shear instability

in three-dimensional clear-air turbulence. This model is formulated in terms of an initial value problem, treating the turbulence as instantaneous. They compare this model with nonlinear numerical simulations and find that the linear and nonlinear estimated quantities are of the same order of magnitude. This indicates that linear theory captures relevant features of the emission stage of the Kelvin-Helmhotltz instability. However, they state that nonlinear effects caused by shear on the scale of the mixed region were not considered when comparing nonlinear and linear estimates.

Lighthill (1996) conducts a comprehensive linear analysis of waves emanating from an arbitrary initial disturbance and the residual motions remaining after the waves have propagated away. While this linear method could be used to analyze a strongly stratified turbulent source, nonlinear interactions, which are inherent in moderately to weakly stratified fluids, are neglected. Griffiths (1999) conducted a nonlinear analytical study of the mechanism by which internal gravity waves were generated by a single vortex and the back reaction caused by the waves on the vortex. However while Griffiths's analytical work proved insightful, its result was inconclusive due to the inability of mathematical matching the asymptotic solutions for the different flow regimes.

Therefore, a clear model describing the generation of internal waves from a source valid for all temporal and spatial scales is still missing. From these studies it is seen that some attributes of internal waves from a turbulent source may be studied in two-dimensions and that for strong stratification the flow behavior is predominantly linear. However, nonlinear affects may greatly affect the flows overall behavior depending on the level of stratification. Therefore, it is of interest to study how vortical structures (such as vortex pairs) found in turbulence generate internal waves and the effect that these waves have on the coherent structures.

1.3 Summary and Outstanding Issues

As discussed, there has been a substantial amount of work focused on vortex pairs and their behavior in more complicated flows.

Much of the previous work on symmetric co-rotating vortex pairs has focused on the determination of a critical aspect ratio, $(a/b)_{cr}$, which marks when merger will occur. In general, experimental and numerical measurements of $(a/b)_{cr}$ have varied due to difficulties of measurement and inconsistent definitions of a_{cr} and b_{cr} leading to a discrepancy when predicting merger. The physical mechanism associated with merger is still unclear. Recent studies suggest that merger is not caused by the filaments in the flow, as previously thought, but rather by some other mechanism. This mechanism causes a misalignment of the major axes of the vortices and the connecting line between the vortex centroids, which results in merger. How the misalignment is established has not been explained and requires further attention.

In the case of asymmetric co-rotating vortex pairs, there are limited studies and primarily consider inviscid flow. Existing results indicate there is a greater range of flow behavior and the interaction of the vortices may even result in smaller vortices than that of the original vortex pair or in the destruction of the smaller/weaker vortex. A complex flow regime map is developed based on the flows circulation that indicates when/if merger will occur. However, there is little physical understanding of the flow characteristics and no general predictive methods in place. In general, a clearer description of the vortex interactions and merging criteria is needed.

Turning our attention to stratified flow, we see that the effects of stable density stratification on vortex pair dynamics have been considered in a number of studies. In the case of *horizontal* counter-rotating vortex pair, past research has been able to clearly define and predict the behavior of this flow in strongly and weakly stratified fluids. However, the behavior of the generated internal wave

field in a moderately stratified fluid requires further research. In regards to the *horizontal* co-rotating vortex pair, there have been no previous studies that have looked at this fundamental interaction. While the behavior of counter-rotating and co-rotating vortex pairs have been considered in turbulence, an improved understanding of these flows and associated processes is still needed.

1.4 Objectives

The primary objective of this study is to use numerical and analytical techniques to investigate the fundamental two-dimensional vortex pair dynamics, in particular:

- co-rotating vortex pair interactions and merging; and
- internal wave generation by co-rotating and counter-rotating vortex pairs.

The study was carried out in the five parts, which are listed below along with the specific goals.

- Symmetric co-rotating vortex pairs (unstratified): The merging process of an unstratified symmetric vortex pair in a viscous fluid is first studied through numerical simulations. The primary goals are to:
  - identify the physical mechanism(s) that cause two equal co-rotating vortices to merge.
- Asymmetric co-rotating vortex pairs (unstratified): Once the basic mechanisms of symmetric merger were clear, the merging process of an asymmetric (unequal strength) vortex pair is similarly studied. The primary goals are to:
  - develop a more general understanding of vortex interactions and merger, which includes possibility of the domination/destruction of one vortex; and

  - establish a more generalized merging criterion for unequal vortices.

- Symmetric co-rotating vortex pairs (weakly stratified): The study is continued by considering a symmetric co-rotating vortex pair in a weakly stratified viscous fluid. The primary goals are to:

  - determine the effect of baroclinially generated vorticity on the merging process; and
  - generalize merging criterion for symmetric pairs to include weakly stratified flow.

- Symmetric vortex pairs and the generation of linear internal waves: The production of linear internal waves by various configurations of symmetric vortex pairs is considered analytically. The primary goals are to:

  - using linear theory, show how internal waves are generated, the effect they have on the initial vorticity field and how they transport energy; and
  - validate the analytical approach through numerical simulations of strongly stratified flow.

- Symmetric vortex pairs and the generation of nonlinear internal waves: With an understanding of linear internal wave behavior, the production of nonlinear internal waves by various configurations of symmetric vortex pairs is considered numerically. The primary goals are to:

  - using nonlinear numerical simulations, investigate the effect that different levels of stratification have on the internal wave field, vorticity field and energy transport; and
  - investigate to what extent nonlinear interactions influence the flow for different levels of stratification.

Results of these two-dimensional studies clarify and improve our understanding of the fundamental physics of co-rotating and counter-rotating vortex pairs and vortex interactions. This knowledge will be valuable for accurate prediction and interpretation of more complex flows.

1.5 Dissertation Outline

The remainder of the dissertation is organized into seven chapters:

- Chapter 2 presents the framework in which the investigation took place. The general flow geometry/parameters are outlined and a description of the numerical simulations is given.

- Chapter 3 presents the investigation of the merging of a pair of symmetric vortices in an unstratified viscous fluid. The merging process is resolved into four phases of development and the key underlying physics are identified.

- Chapter 4 presents the interaction of two co-rotating vortices of equal size and varying relative strengths in a viscous fluid. With unequal strengths, the disparity of the vortices alters the interaction and merger may not occur. The flow behavior is distinguished based on the relative onset of the core erosion process. Through scaling analysis and simulation results, a critical nondimensional strain rate characterizing the onset of erosion is determined. If the disparity of strengths is sufficiently large, the critical strain rate is not attained by the stronger vortex and the vortices do not merge.

- Chapter 5 presents the study of symmetric, *horizontally* oriented vortices in a weakly stably stratified viscous fluid. It is found that for weakly stratified flows, the vortices still merge and that the flow develops according to the same four phases of development as in the unstratified flow. The key underlying physics also remains the same, but the addition of baroclinically

generated vorticity (BV) modifies the time scale of the flow development. In general, the effects of stratification depend on the ratio of the diffusive time scale (growth of cores) to the turnover time (establishment of BV), i.e., the Reynolds number. A crossover Reynolds number is found, above which convective merging is accelerated with respect to unstratified flow and below which it is delayed. A critical aspect ratio is found to be the same for both the unstratified and stratified flows.

- Chapter 6 presents an analytical study of the production of linear internal gravity waves by different configurations of two-dimensional *horizontally* oriented vortices in a stably stratified fluid. The vortex systems considered, which consist of initially Lamb-Oseen vortices, include a co-rotating vortex pair, counter-rotating vortex pair and two sets of co-rotating vortex pairs in a quadrupole configuration (VQ). The effect that different source configurations have on the density, vorticity and energy fields is investigated.

- Chapter 7 presents a numerical study of the production of nonlinear internal gravity waves by counter-rotating vortex pairs and VQ in a stably stratified fluid. This investigation looks into the effect of different stratification levels on the density, vorticity and energy fields. In order to understand the effect of the nonlinear and viscous interactions, results from these simulations were compared with the linearized analytical solutions from Chapter 6.

- Chapter 8 concludes the dissertation and summarizes key findings and future research.

Chapter 2

Mathematical Formulation and Numerical Methods

The purpose of this chapter is to set up the initial flow systems, present the governing equations and discuss the numerical procedures for each part of the study. In section 2.1, the initial flow configurations for the study are addressed. This is followed by section 2.2, which will address the primary flow parameters. In section 2.3, the initial vorticity and velocity profiles for each vortex system is addressed and normalized. In section 2.4, the governing equations of the flow are presented and normalized. This chapter will then conclude in section 2.5 with a brief discussion of the numerical schemes used to simulate these flows.

2.1 Initial Flow Systems

Each portion of this study concerns a slightly different flow. However, the common thread connecting all the flow systems is that the initial flow fields consist of the superposition of Lamb-Oseen vortex pairs with Gaussian vorticity distribution, the definition of which will be addressed later in section 2.4.

In chapter 3, we investigate a *symmetric* co-rotating vortex pair in an un-

stratified environment, in which each vortex has the same circulation, Γ_o, and core size, a_o, and the two vortices are separated by a distance, b_o. The geometry of this flow may be seen in figure 2.1a. Here, the spatial coordinates, x, z, correspond to the transverse and vertical directions, respectively. Figure 2.1a may also be used to address the asymmetric co-rotating vortex pair configuration studied in chapter 4. The primary difference between the flows is that in the asymmetric study, the circulations of the two vortices are of different magnitudes.

In chapter 5, the initial flow again considers a *symmetric* co-rotating vortex pair (figure 2.1a). However, in this analysis there is an initially ambient stable density stratification in place, $\bar{\rho}$ (figure 2.2a). Chapters 6 & 7 also considers a stably stratified environment, as in figure 2.2. However in these chapters, different flow configurations are considered: a co-rotating vortex pair (figure 2.1a); a counter-rotating vortex pair (figure 2.1b); and two sets of co-rotating vortices in a quadrupole configuration, *VQ* (figure 2.1c). In *VQ*, the flow is set up such that the direction of the initial outward advection velocity is aligned perpendicular to the horizontal axis.

2.1.1 Stable Density Stratification

In the current study, the flow systems are stratified by means of a linear temperature differential, where the cooler, denser fluid lies beneath the warmer, lighter fluid (figure 2.2). The changes in the density profile may be directly related to the temperature field using a first order Taylor series expansion:

$$\rho(\theta) \approx \rho_o \left[1 + \frac{1}{\rho_o} \frac{\partial \rho(\theta_o)}{\partial \theta} (\theta - \theta_o) \right] \approx \rho_o [1 - \alpha(\theta - \theta_o)], \tag{2.1}$$

where ρ and θ represent the density and temperature, respectfully. The terms θ_o and ρ_o are constant reference values, where $\rho(\theta_o) = \rho_o$. The volumetric expansion coefficient, α, is defined as

$$\alpha \equiv \frac{1}{\rho_o} \frac{\partial \rho(\theta_o)}{\partial \theta}. \tag{2.2}$$

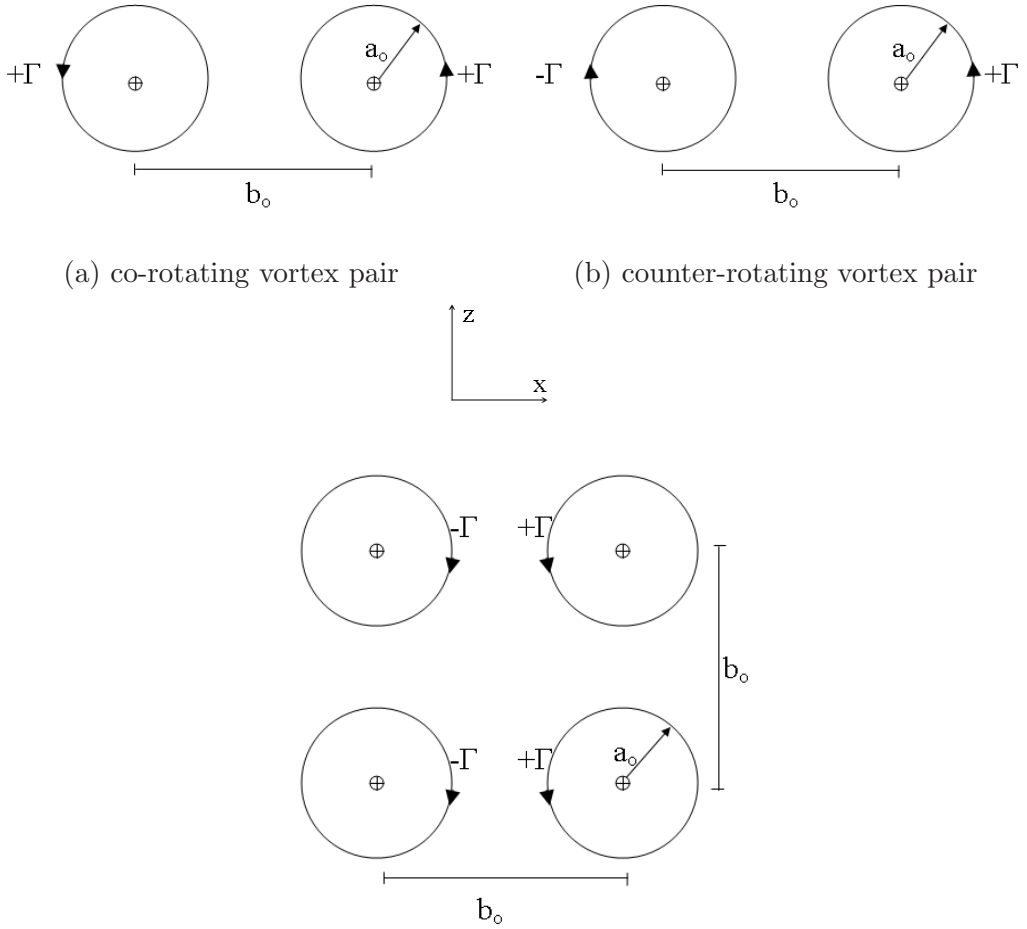

(a) co-rotating vortex pair

(b) counter-rotating vortex pair

(c) *VQ*

Figure 2.1: Coordinate system and initial conditions for flow systems under consideration with vortex circulation strength Γ, vortex centers initially separated by a distance b_o and vortex initial core radius of a_o.

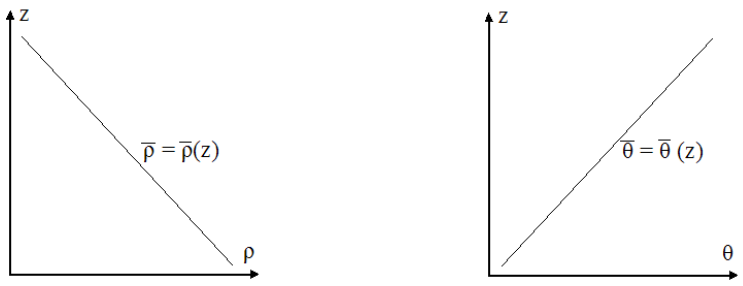

(a) (b)

Figure 2.2: Background linear (a) density profile, $\bar{\rho}$, and (b) temperature profile, $\bar{\theta}$.

In the current study, we are interested in the density perturbations to the mean profile. Therefore, for any point in the flow, we may write the instantaneous density field as $\rho(x,z,t) = \bar{\rho}(z) + \rho'(x,z,t)$. Here $\bar{\rho}(z)$ represents the initial horizontally homogeneous background density that depends only on vertical position and $\rho'(x,z,t)$ represents the deviation (or rather perturbation) away from this value. Similarly, the temperature field may be represented as $\theta(x,z,t) = \bar{\theta}(z) + \theta'(x,z,t)$, where $\bar{\theta}(z)$ is the initial horizontally homogeneous background temperature dependent purely on vertical position and $\theta'(x,z,t)$ is a perturbation away from the this mean value. The background temperature, $\bar{\theta}(z)$, and density, $\bar{\rho}(z)$, fields are shown in figure 2.2. The level of stratification is characterized by the buoyancy frequency, N (also known as the Brunt-Väisälä frequency). This is defined as the frequency at which a fluid particle which is vertically displaced will oscillate within a stably stratified environment:

$$N^2 \equiv -\frac{g}{\rho_o}\frac{d\bar{\rho}(z)}{dz} = \alpha\frac{g}{\rho_o}\frac{d\bar{\theta}(z)}{dz}, \tag{2.3}$$

where g represents gravity. Since we are dealing with a mean density gradient (figure 2.2), $d\bar{\rho}(z)/dz$ = constant, N is constant. Here we define another characteristic density scale, $\Delta\bar{\rho}$, as the change in $\bar{\rho}(z)$ over the length scale of the flow, b_o. The same may be done for the temperature scale, where $\Delta\bar{\theta}$ is defined as the

change in $\bar{\theta}(z)$ over b_o. This leads to:

$$N^2 = -\frac{g}{\rho_o}\frac{\Delta\bar{\rho}}{b_o} = \alpha\frac{g}{\rho_o}\frac{\Delta\bar{\theta}}{b_o}. \tag{2.4}$$

2.2 Flow Parameters

The characteristic length scales of these flows are a_o and b_o. Here, a_o is based on the vorticity second moment, $\int r^2\omega\, dA/\int \omega\, dA$, where r is the radial distance from a vortex centroid, ω is vorticity, and the integral is performed over a single vortex. The initial vortex separation distance may be defined as $b_o = |x_2 - x_1|$, where (x_1, z_1) and (x_2, z_2) are the initial coordinates of the two vortex centroids.

The characteristic velocity is defined based on the initial advection velocity of a symmetric vortex pair,

$$W_o = \Gamma_o/2\pi b_o. \tag{2.5}$$

It should be noted that in the asymmetric vortex pair study, W_o is based on the stronger vortex advection velocity.

The characteristic velocity, W_o, and the buoyancy frequency, N, are used in defining stratification levels. We define the level of stratification based on the Froude number, Fr, which represents the square root of the ratio of inertial to buoyancy forces:

$$Fr = \frac{W_o}{b_o N}. \tag{2.6}$$

If we substitute in (2.4),

$$Fr^2 = -\frac{W_o^2}{b_o g}\frac{\rho_o}{\Delta\bar{\rho}} = \frac{W_o^2}{b_o g}\frac{\rho_o}{\alpha\Delta\bar{\theta}}. \tag{2.7}$$

When dealing with stratified flows, the Prandtl number must be considered. It is defined as the ratio of the viscous diffusion rate to thermal diffusion rate:

$$Pr = \frac{\nu}{\kappa}, \tag{2.8}$$

where κ is the thermal diffusivity. In all cases considered, $Pr = 1$.

Another major parameter in any viscous flow is that of the circulation Reynolds number,

$$Re_\Gamma = \frac{\Gamma_o}{\nu} = 2\pi \frac{b_o W_o}{\nu}, \tag{2.9}$$

where ν represents the kinematic viscosity. This parameter measures the relative magnitude of the inertial to viscous forces.

2.2.1 Flow Parameters and Time Scales

In this study, there are four different levels of stratification considered: unstratified, weakly stratified, moderately stratified, and strongly stratified. These levels of stratification are dependent on the relationship between the inertial and buoyancy forces, which may be expressed in terms of time scales.

The flow behavior is significantly modified based on the level of stratification. Therefore, the expressions for the time scales will be dependent on the level of stratification. For a co-rotating pair in an unstratified or weakly stratified fluid, inertial effects dominate the flow where the vortices are able to rotate about one another. Therefore, when dealing with these flows (chapters 3, 4 & 5), a convective time scale based on the rotational period of the flow is appropriate,

$$t_c = \pi b_o / W_o = 2\pi^2 {b_o}^2 / \Gamma_o. \tag{2.10}$$

For the weakly stratified cases, the fluid is overturned every half revolution. Therefore, the buoyancy time scale may be defined as half the buoyancy period (2.4),

$$t_s = \pi / N. \tag{2.11}$$

For moderately to strongly stratified flows, the buoyancy forces become more prevalent and the vortices are unable to rotate about each other. Therefore, when considering this level of stratification (chapters 6 & 7), it is appropriate to base the

inertial time scale on the time scale of the initial advection velocity of the vortices,

$$t_c = b_o/W_o = 2\pi b_o^2/\Gamma_o. \tag{2.12}$$

Since the vortices do not overturn, the buoyancy time scale may be defined as the inverse of the buoyancy frequency,

$$t_s = 1/N. \tag{2.13}$$

Based on the definitions of the time scales above, it is found that for all levels of stratification considered that $Fr = t_s/t_c$:

$$Fr = \frac{t_s}{t_c} = \frac{W_o}{b_o N} = \frac{\Gamma_o}{2\pi b_o^2 N}. \tag{2.14}$$

For $Fr \ll 1$, the buoyancy effects dominate, $N \gg \Gamma_o/(2\pi b_o^2)$, and the flow is considered strongly stratified and develops on t_s. For $Fr \gg 1$, the inertial effects dominate, $N \ll \Gamma_o/(2\pi b_o^2)$, and the flow is considered weakly stratified and is appropriately studied on t_c. For flows found around $Fr \approx 1$ the flow may be considered moderately stratified, $N \approx \Gamma_o/(2\pi b_o^2)$, and both buoyancy and inertial effects will play a major role in the flow development.

The circulation Reynolds number, $Re_\Gamma = \frac{\Gamma_o}{\nu}$, may also be shown using time scales. A viscous time scale for all flows considered is defined as,

$$t_v = a_o^2/4\nu. \tag{2.15}$$

Therefore, for unstratified or weakly stratified fluids, the circulation Reynolds number is given by,

$$Re_\Gamma = \frac{8\pi^2}{(a_o/b_o)^2}\frac{t_v}{t_c} \tag{2.16}$$

and for moderately to strongly stratified fluids, it is given by,

$$Re_\Gamma = \frac{8\pi}{(a_o/b_o)^2}\frac{t_v}{t_c}. \tag{2.17}$$

2.3 Initial Vorticity and Velocity Profiles

The initial flow field consists of the superposition of Lamb-Oseen (Gaussian) vortices, which are representative of the initial vortices used in Meunier and Leweke (2001) and Garten et al. (1998).

2.3.1 Initial Vorticity Field

The corresponding vorticity distribution for a Lamb-Oseen single vortex with a Gaussian shape profile (rotating in a clockwise direction) is given by,

$$\omega(x,z,t_o) = \Omega_o\, e^{\frac{-((x-x_c)^2+(z-z_c)^2)}{a_o^2}},$$

where $\Omega_o = \Gamma_o/\pi a_o^2$ is the peak magnitude of vorticity and $x_c = z_c = 0$. In the cases of multiple vortices, the flow fields may be added together. The vorticity distribution for a co-rotating vortex pair (rotating in a counter-clockwise direction), with the same a_o, is given by,

$$\omega(x,z,t_o) = \Omega_{o,1}\, e^{\frac{-((x-x_1)^2+(z-z_1)^2)}{a_o^2}} + \Omega_{o,2}\, e^{\frac{-((x-x_2)^2+(z-z_2)^2)}{a_o^2}},$$

where $\Omega_{o,i} = \Gamma_{o,i}/\pi a_o^2$ is the peak magnitude of vorticity for a particular vortex $(i = 1, 2)$ and $x_1 = -x_2 = b_o/2$ and $z_1 = z_2 = 0$. In a similar fashion, the remaining vortex systems vorticity distributions may be equated (Appendix A.1).

2.3.2 Initial Velocity Field

The flow fields under consideration are two dimensional and incompressible. Therefore, the velocity and vorticity equations may be written in terms of the stream function, Ψ, where $u = \frac{\partial \Psi}{\partial z}$, $w = -\frac{\partial \Psi}{\partial x}$ and $\omega_y = -\nabla^2\Psi$ (Laplace's equation). This leads to the following equations for the velocity components u and w for a single vortex (rotating in a counter-clockwise direction):

$$u(x,z,t_o) = \frac{1}{2}\frac{a_o^2\Omega_o(z-z_c)}{(x-x_c)^2+(z-z_c)^2}(1-e^{-((x-x_c)^2-(z-z_c)^2)/a_o^2}) \tag{2.18}$$

$$w(x,z,t_o) = -\frac{1}{2}\frac{a_o^2\Omega_o(x-x_c)}{(x-x_c)^2+(z-z_c)^2}(1-e^{-((x-x_c)^2-(z-z_c)^2)/a_o^2}), \tag{2.19}$$

where $x_c = z_c = 0$. In the case of the co-rotating vortex pair, the velocity components u and w are

$$\begin{aligned} u(x,z,t_o) = &\frac{1}{2}\frac{a_o^2\Omega_{o,1}(z-z_1)}{(x-x_1)^2+(z-z_1)^2}(1-e^{-((x-x_1)^2-(z-z_1)^2)/a_o^2}) \\ &+\frac{1}{2}\frac{a_o^2\Omega_{o,2}(z-z_2)}{(x-x_2)^2+(z-z_2)^2}(1-e^{-((x-x_2)^2-(z-z_2)^2)/a_o^2}) \end{aligned} \tag{2.20}$$

and

$$\begin{aligned} w(x,z,t_o) = &-\frac{1}{2}\frac{a_o^2\Omega_{o,1}(x-x_1)}{(x-x_1)^2+(z-z_1)^2}(1-e^{-((x-x_1)^2-(z-z_1)^2)/a_o^2}) \\ &-\frac{1}{2}\frac{a_o^2\Omega_{o,2}(x-x_2)}{(x-x_2)^2+(z-z_2)^2}(1-e^{-((x-x_2)^2-(z-z_2)^2)/a_o^2}), \end{aligned} \tag{2.21}$$

where $x_1 = -x_2 = b_o/2$ and $z_1 = z_2 = 0$. The velocity distributions for the remaining vortex systems may be found in Appendix A.2.

The characteristic velocity, W_o, is used to non-dimensionalize the velocity distributions. As stated in §2.2, in the flow systems with multiple vortices, W_o is defined as the initial advection velocity of a symmetric vortex pair and may be calculated by substituting in $x = x_1$ and $z = z_1$ into (2.21). The resulting equation for W_o is:

$$W_o = \frac{1}{2}\frac{a_o^2\Omega_{o,1}}{b_o}(1-e^{-b_o^2/a_o^2}). \tag{2.22}$$

We will note that since $z_1 = z_2 = 0$, if the same substitution is made into (2.20) that all terms vanish indicating that their is no initial horizontal advection velocity. The velocity equations are subsequently normalized by W_o providing non-dimensional equations for u and w. For a single vortex:

$$u^*(x,z,t_o) = \frac{a_o(z-z_c)}{(x-x_c)^2+(z-z_c)^2}\left(\frac{1-e^{-((x-x_c)^2-(z-z_c)^2)/a_o^2}}{1-e^{-1}}\right) \tag{2.23}$$

$$w^*(x,z,t_o) = -\frac{a_o(x-x_c)}{(x-x_c)^2+(z-z_c)^2}\left(\frac{1-e^{-((x-x_c)^2-(z-z_c)^2)/a_o^2}}{1-e^{-1}}\right). \tag{2.24}$$

In the case of a co-rotating vortex pair:

$$u^*(x,z,t_o) = \frac{b_o(z-z_1)}{(x-x_1)^2+(z-z_1)^2}\left(\frac{1-e^{-((x-x_1)^2-(z-z_1)^2)/a_o^2}}{1-e^{-b_o^2/a_o^2}}\right) + \frac{\Omega_{o,2}}{\Omega_{o,1}}\frac{b_o(z-z_2)}{(x-x_2)^2+(z-z_2)^2}\left(\frac{1-e^{-((x-x_2)^2-(z-z_2)^2)/a_o^2}}{1-e^{-b_o^2/a_o^2}}\right) \tag{2.25}$$

and

$$w^*(x,z,t_o) = -\frac{b_o(x-x_1)}{(x-x_1)^2+(z-z_1)^2}\left(\frac{1-e^{-((x-x_1)^2-(z-z_1)^2)/a_o^2}}{1-e^{-b_o^2/a_o^2}}\right) - \frac{\Omega_{o,2}}{\Omega_{o,1}}\frac{b_o(x-x_2)}{(x-x_2)^2+(z-z_2)^2}\left(\frac{1-e^{-((x-x_2)^2-(z-z_2)^2)/a_o^2}}{1-e^{-b_o^2/a_o^2}}\right). \tag{2.26}$$

The normalized velocity distributions for all other flow systems are found in Appendix A.3. Note that these normalized equations are dependent on the initial vortex placement, a_o, b_o and $\Omega_{o,2}/\Omega_{o,1}$ (which is equivalent to $Re_{\Gamma,2}/Re_{\Gamma,1}$).

2.4 Governing Equations

This study considers two-dimensional flow in an incompressible fluid. Therefore, the primitive governing equations used in this analysis are the continuity equation, the two-dimensional Navier-Stokes equations and the two-dimensional energy equation. In the above equations, the Boussinesq approximation is utilized. This approximation is made because there are only small perturbations to the flow. Therefore, unless multiplied by gravity, which will cause the specific weight of a fluid particle to appreciably differ from its surround fluid, the density perturbation may be neglected.

Throughout the remainder of this thesis, quantities represented with an (*) are non-dimensional quantities unless otherwise noted. The scaling utilized to normalize these quantities is found in Table 2.1.

Pressure:	$p^* = \frac{p}{\rho_o W_o^2}$	Time:	$t^* = \frac{tW_o}{b_o}$
Temperature:	$\theta^* = \frac{\theta'}{\Delta\theta}$	Density:	$\rho'^* = \frac{\rho'}{\Delta\bar{\rho}}$
Velocity:	$u_i^* = \frac{u_i}{W_o}$	Length:	$x_i^* = \frac{x_i}{b_o}$

Table 2.1: Non-dimensional flow parameters

2.4.1 Continuity Equation

The general form of the continuity equation is defined as:

$$\frac{D\rho}{Dt} + \rho(\nabla \cdot \boldsymbol{v}) = \frac{\partial \rho}{\partial t} + \nabla \cdot (\rho \boldsymbol{v}) = 0, \tag{2.27}$$

where $\boldsymbol{v} = (u, w)$ is the instantaneous velocity. With the assumption of incompressibility, this equation may be rewritten as:

$$\nabla \cdot \boldsymbol{v} = 0, \tag{2.28}$$

which in non-dimensional form (using Table 2.1) becomes:

$$\nabla \cdot \boldsymbol{v}^* = 0. \tag{2.29}$$

2.4.2 Momentum Equation

The general form of the incompressible Navier Stokes equations, with constant viscosity, μ, are:

$$\frac{D\boldsymbol{v}}{Dt} = \frac{\partial \boldsymbol{v}}{\partial t} + \boldsymbol{v} \cdot \nabla \boldsymbol{v} = -\frac{1}{\rho}\nabla p + \frac{\mu}{\rho}\nabla^2 \boldsymbol{v} + \mathbf{g}, \tag{2.30}$$

where $\mathbf{g} = (0, -g)$ is the gravitational acceleration and p is the pressure. By making the substitution $\rho = \bar{\rho}(z) + \rho'(x, z, t)$ into (2.30), we obtain:

$$[\bar{\rho}(z) + \rho'(x, z, t)]\frac{D\boldsymbol{v}}{Dt} = -\nabla p + \mu\nabla^2 \boldsymbol{v} + [\bar{\rho}(z) + \rho'(x, z, t)]\mathbf{g} \tag{2.31}$$

The pressure field may be decomposed into dynamic, $p'(x,z,t)$, and hydrostatic, $\bar{p}(z)$, components: $p = \bar{p}(z) + p'(x,z,t)$. The hydrostatic pressure field may be related to the density by $d\bar{p}/dz = -\bar{\rho}(z)g$. Therefore, the pressure equation may now be re-written as: $p = \int \bar{\rho}(z)\mathbf{g}dz + p'(x,z,t)$. If we substitute this equation into the above Navier Stokes (2.31) and apply the Boussinesq approximation, we obtain:

$$\frac{D\boldsymbol{v}}{Dt} = -\frac{1}{\rho_o}\nabla p' + \nu\nabla^2\boldsymbol{v} + \frac{\rho'}{\rho_o}\mathbf{g}, \tag{2.32}$$

where $\nu = \mu/\rho_o$. In non-dimensional form (using Table 2.1), this equation becomes:

$$\frac{D\boldsymbol{v}^*}{Dt^*} = -\nabla^* p'^* + \left[\frac{\nu}{b_o W_o}\right]\nabla^{2*}\boldsymbol{v}^* + \left[\frac{b_o\mathbf{g}}{W_o^2}\frac{\Delta\bar{\rho}}{\rho_o}\right]\rho'^*. \tag{2.33}$$

It is easy to see that the first term in brackets on the right hand side is 2π times the inverse of the Re_Γ (2.9) and that the second term in brackets is the inverse of $-Fr^2$ (2.7). Therefore, the normalized Navier Stokes equations with the non-dimensional flow parameters are:

$$\frac{D\boldsymbol{v}^*}{Dt^*} = \frac{\partial\boldsymbol{v}^*}{\partial t^*} + \boldsymbol{v}^*\cdot\nabla^*\boldsymbol{v}^* = -\nabla^* p'^* + \frac{2\pi}{Re_\Gamma}\nabla^{2*}\boldsymbol{v}^* - \frac{1}{Fr^2}\rho'^*\hat{e}_z, \tag{2.34}$$

where $\hat{e}$ is a unit vector. It may also be expressed in terms of the perturbed temperature as:

$$\frac{D\boldsymbol{v}^*}{Dt^*} = \frac{\partial\boldsymbol{v}^*}{\partial t^*} + \boldsymbol{v}^*\cdot\nabla^*\boldsymbol{v}^* = -\nabla^* p'^* + \frac{2\pi}{Re_\Gamma}\nabla^{2*}\boldsymbol{v}^* + \frac{1}{Fr^2}\theta'^*\hat{e}_z. \tag{2.35}$$

2.4.3 Energy Equation

The energy equation for an incompressible fluid may be reduced to a convection-diffusion equation. Written in terms of density, the energy equation is:

$$\frac{\partial\rho}{\partial t} + \boldsymbol{v}\cdot\nabla\rho = \kappa\nabla^2\rho, \tag{2.36}$$

where κ is the thermal diffusivity. Substituting $\rho = \bar{\rho}(z) + \rho'(x,y,z,t)$ into (2.36) returns:

$$\frac{\partial\rho'}{\partial t} + \boldsymbol{v}\cdot\nabla\rho' + w\frac{d\bar{\rho}}{dz} = \kappa\nabla^2\rho'. \tag{2.37}$$

The corresponding normalized equation using Table 2.1 is:

$$\frac{\partial \rho'^*}{\partial t^*} + \boldsymbol{v}^* \cdot \nabla \rho'^* + w^* = \left[\frac{\kappa}{b_o W_o}\right] \nabla^{*2} \rho'^* = \frac{2\pi}{PrRe_\Gamma} \nabla^{*2} \rho'^*. \tag{2.38}$$

Written in terms of the temperature perturbation, the normalized energy equation is:

$$\frac{\partial \theta'^*}{\partial t^*} + \boldsymbol{v}^* \cdot \nabla \theta'^* + w^* = \left[\frac{\kappa}{b_o W_o}\right] \nabla^{*2} \theta'^* = \frac{2\pi}{PrRe_\Gamma} \nabla^{*2} \theta'^*. \tag{2.39}$$

2.5 Overview of Numerical Simulations

To conduct these studies, the governing equations (2.29), (2.35) and (2.39) were solved using direct numerical simulations. Two codes were used: **DISTUF** and **DIABLO**. Both numerical schemes are based on a uniform discretized computational domain and have periodic boundary conditions.

2.5.1 DISTUF

For the symmetric cases in unstratified and weakly stratified environments, a CFD code known as **DISTUF** was utilized. It was written by Gerz et al. (1989). **DISTUF** makes use of a numerical solution procedure based on two computational phases. The first phase contains a second order finite difference scheme on a *staggered* discretized grid that solves for diffusion and advection with second order explicit Adams-Bashforth time integration. The second phase uses a Poisson solver to implicitly update the pressure field.

The non-dimensional Navier Stokes equations (2.35) may be broken down into terms:

Unsteady Acceleration Term:	$\partial \boldsymbol{v}^*/\partial t^*$
Convective Acceleration Term:	$\boldsymbol{v}^* \cdot \nabla^* \boldsymbol{v}^*$
Pressure Gradient Term:	$-\nabla^* p'^*$
Viscous Term:	$\frac{2\pi}{Re_\Gamma} \nabla^{2*} \boldsymbol{v}^*$
Buoyancy Term:	$\frac{1}{Fr^2} \theta'^* \hat{e}_z$

In **DISTUF**'s first computational phase, the viscous, buoyancy, and convective terms are explicitly solved using a second-order accurate finite-difference approximation. Since the code is written on a *staggered* grid, the algebraic average of two grid points separated by one grid interval is used when taking derivatives. The unsteady acceleration term is then integrated using the second order Adams-Bashforth scheme. Note that the pressure field is neglected in this first phase. The temperature field is calculated in the same fashion as the velocity field using the energy equation (2.39).

In the second computational phase, the pressure field is implicity solved using a Poisson solver. This method is used in order to ensure that the flow is divergence free, i.e. that it satisfies the continuity equation (2.29). Fast Fourier Transforms in the horizontal directions and Gaussian elimination are used in solving the Poisson equations. Once calculated, the pressure term is used to update the velocity equations found in the first phase.

2.5.2 DIABLO

While the velocity and temperature fields calculated by **DISTUF** were accurate for the symmetric flows found in unstratified and weakly stratified environments, a need for an increase in accuracy was found when dealing with different strength vortices and strong stratification. Therefore, a different CFD code, known as **DIABLO**, was used for these flow systems. This easy-to-follow code was developed by graduate students at the University of California San Diego under

the supervision of Thomas Bewely. The code is capable of solving the governing equations in rectangular two- or three-dimensional domains. There are currently two options for boundary conditions: triply periodic or doubly periodic (stress-free and/or wall condition imposed in one direction). In the simulations conducted, the domain is two-dimensional with periodic boundary conditions imposed in both directions. In the fully periodic version of the code, **DIABLO** uses spectral methods for spatial differentiation and a mixed Crank-Nicolson and Runga-Kutta fractional step algorithm for temporal integration.

As in **DISTUF**, the computational routine is broken down into two phases: velocity/ temperature solver and pressure corrector. In **DIABLO**'s first phase, the convective and buoyancy terms are handled explicitly where exact derivatives are taken in Fourier space. Since **DIABLO** utilizes Fourier transforms, the unsteady acceleration and viscous terms are handled implicitly. The terms found in the energy equation (2.39) are handled in a similar manner for the temperature field. We note that as in **DISTUF**, the first computational phase neglects the pressure term.

In the second phase, a Poisson solver is used to calculate the divergence. This is done in Fourier space for speed and accuracy. The velocity fields calculated in the first phase are then updated with the corrective term.

2.5.3 Resolution of Numerical Simulations

In the unstratified two-dimensional calculations, the computational domain has dimensions of $L_x = L_z = 12b_o$, and employs 1024^2 grid points. In order to allow adequate room for the mixing of the density field, the computational domain in the stratified two-dimensional calculations has dimensions of $L_x = L_z = 24b_o$, and employs 2048^2 grid points. This allows, for an initial aspect ratio of $a_o/b_o = 0.157$, approximately 27 grid points across the core of each vortex (i.e., $2a_o$). Resolution tests using 54 grid points across the core showed minimal differences in computed

quantities (e.g., the integrated quantity a differed by a maximum of 0.4%) thereby indicating a resolution independent solution. Domain size independence was also examined. In the these simulations, the periodic boundary conditions used are, in general, inconsistent with the nonzero circulation of these flows. Rather than attempting to negate the circulation by introducing an unphysical background flow such as done in Melander et al. (1987b), we consider a sufficiently large domain to minimize the effect of neighboring vortices and far-field flow interaction. Domain size tests were conducted for the unstratified flows and compared both integrated (e.g. a) and local (e.g., strain rate, vorticity) quantities for a range of $L_x = L_z = L$ domain sizes and showed maximum differences of 0.01% between $L = 12b_o$ and $L = 24b_o$ results. In addition, the induced flow from neighboring vortices was computed and found to be negligible.

2.5.4 Summary of Simulations Conducted

The geometry of the vortex pair is specified by the dipole aspect ratio, a_o/b_o. In all the simulations presented, we consider a fixed initial aspect ratio of $a_o/b_o = 0.157$.

In chapter 3, an unstratified symmetric vortex pair is studied for $Re_\Gamma = 5000$. This study is expanded upon in chapter 4, where an asymmetric co-rotating vortex pair is studied in an unstratified fluid. These vortex pairs have the same initial aspect ratio, but their circulation strengths vary with respect to one another. The stronger vortex circulation strength, for all simulations, is $Re_\Gamma = 5000$ and the weaker vortex strength varies with respect to the stronger vortex by $Re_{\Gamma,2}/Re_{\Gamma,1} = 1, 0.9, 0.8, 0.7$, 0.6, 0.5 and 0.4.

In chapter 5, the study conducted in chapter 3 is further modified to include the effects of Re_Γ and stratification, Fr. The range of Reynolds number considered are $2000 \leq Re_\Gamma \leq 5000$. The Froude numbers considered are $Fr = 2, 3, 5$ and ∞.

In chapter 6, an analytical study into the effect of strong density stratifi-

cation for different configurations of vortex pairs is conducted. In strong stratification, viscosity is deemed negligible so that Re_Γ is not considered. In the results presented, this model was validated with linearized inviscid numerical simulations for $Fr = 0.01$

In chapter 7, a numerical investigation into the effects of moderate stratification was investigated. In all simulations $Re_\Gamma = 5000$. A range of stratification levels were investigated, $Fr = 0.01, 0.05, 0.1, 0.3, 0.5, 1$.

Chapter 3

Symmetric co-rotating vortex pairs (unstratified)

In this chapter, we will discuss the merging of an unstratified co-rotating vortex pair of equal size and strength. Only one Reynolds number is considered in this chapter, $Re_\Gamma = 5000$, in order to set up the framework with which to study the flow.

The discussion of results will proceed as follows. First the flow development is discussed in detail and the flow's general behavior, phases and structure is laid out (§3.1). This is followed by a discussion of the merging processes in relation to the mechanism of merger (§3.2) and the coupled interaction of strain and vorticity (§3.3). The chapter concludes with the redefining of the flow phases of merger based on the interaction of strain and vorticity (§3.4).

3.1 Flow behavior and development

The flow development may easily be seen when viewing time sequences of vorticity contours (figure 3.1), where the vortices are seen to rotate about one another due to the mutually induced velocity. In the cases considered in this

study, the vortex pair rotates in a counter-clockwise direction. Before merging is initiated, the rate of rotation is nearly equal to that of a two point vortex system, $\Gamma/\pi b^2$ (figure 3.2). At early times (figures 3.1a-e, ${t_c}^* \leq 1.31$), the vortices grow due to viscous diffusion. They also adjust to the induced strain field, which results in an elliptic deformation of the cores. Later in time (figures 3.1f-h, ${t_c}^* \geq 1.45$), more significant deformation is observed, particularly at the lowest vorticity contour levels. At the outer locations of the vortex pair, filamentation occurs, and in the vicinity of the center of rotation, a tilt in the vorticity contours develops. The major axes of the vortices are tilted with respect to the connecting line of the vortices; subsequently, the vortex centers are rapidly drawn towards and around each other (figures 3.1i-k, ${t_c}^* \geq 1.97$). The rate of rotation of the vortex pair increases due to conservation of angular momentum (figure 3.2). The inward spiral motion leaves the filaments wrapped around the vortex centers (figure 3.1l). At late times (not shown), the overall flow consists of essentially a single structure within which the two vorticity maxima revolve. In time, the two maxima eventually disappear by viscous diffusion. A single vortex is established.

In previous studies (Cerretelli and Williamson, 2003; Melander et al., 1988; Meunier, 2001), vortex merging in a viscous unstratified fluid is considered to occur in three phases: the first diffusive phase, the convective phase, and the second diffusive phase; the phases designated by the behavior of the separation distance, $b(t)$, and the core size, $a(t)$. Time histories of $b^* = b/b_o$ and ${a^*}^2 = a^2/{b_o}^2$ are given in figure 3.3. Note that the core size in figure 3.3b, a_ω, is defined in terms of the second moment of vorticity, and that in figure 3.3c, a_θ, in terms of the radial location of maximum azimuthal velocity (averaged over azimuthal coordinate). At ${t_c}^* = 0$, $a_\theta = 1.12\, a_\omega$, as expected for a Lamb-Oseen vortex. We note that a_θ will assist in the analysis of asymmetric and stratified flows found in chapters 4 & 5, respectively.

During the first diffusive phase, $b(t)$ remains relatively constant (figure 3.3a) while $a(t)$ grows by viscous diffusion (figure 3.3b,c). The development of both $a_\omega^2(t)$

(a) $t_c{}^* = 0.26$

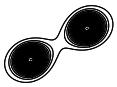

(b) $t_c{}^* = 0.55$

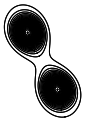

(c) $t_c{}^* = 0.78$

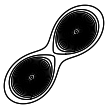

(d) $t_c{}^* = 1.07$

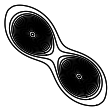

(e) $t_c{}^* = 1.31$

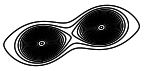

(f) $t_c{}^* = 1.45$

(g) $t_c{}^* = 1.69$

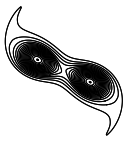

(h) $t_c{}^* = 1.78$

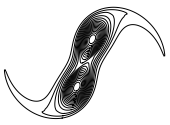

(i) $t_c{}^* = 1.97$

(j) $t_c{}^* = 2.05$

(k) $t_c{}^* = 2.12$

(l) $t_c{}^* = 2.16$

Figure 3.1: Line plots of vorticity contours for $Re_{\Gamma} = 5000$.

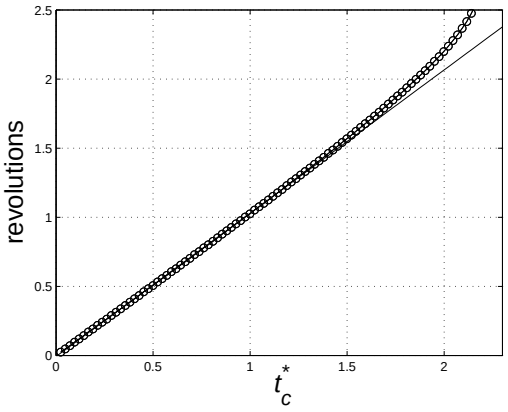

Figure 3.2: Revolutions versus time for $Re = 5000$.

and $a_\theta^2(t)$ is linear and essentially follows the behavior of a single vortex,

$$a^2 \;=\; c^2 \nu t \;+\; {a_o}^2 \tag{3.1}$$

or in nondimensional form

$$a^{*2} \;=\; c^2 \frac{2\pi^2}{Re_\Gamma} t_c^* \;+\; {a_o}^{*2}\,. \tag{3.2}$$

The growth rate constants for $a_\omega^2(t)$ and $a_\theta^2(t)$ are determined to be $c_\omega = 2.11$ and $c_\theta = 2.17$, respectively. We note that for a Lamb-Oseen vortex, $c_\omega = 2.0$ and $c_\theta = 2.24$ (Saffman, 1992). The end of the diffusive phase is typically marked by the deviation of $a^2(t)$ from its linear growth (transition from a diffusive to convective dominated process). This occurs for both $a_\omega^2(t)$ and $a_\theta^2(t)$ at ${t_c}^* \sim 1.7$ (figure 3.3b,c) which corresponds to a critical core size of $(a_\omega/b_o)_{cr} \approx 0.23$, which is comparable to reported values by Meunier et al. (2002). The convective phase corresponds to the predominant reduction in $b^*(t)$. Note that in the latter part of this phase, $b^*(t)$ exhibits a rapid and nearly linear decrease. The convective phase terminates when b reaches approximately $0.20b_o - 0.25b_o$ at which point the inward velocities at the centroids are nearly zero. The second diffusive phase is characterized by a slow reduction in $b^*(t)$ (not shown) as the two ω maxima diffuse into one. Beyond this time, development of $a^2(t)$ (for single merged vortex) eventually returns to linear growth by diffusion (Cerretelli and Williamson, 2003).

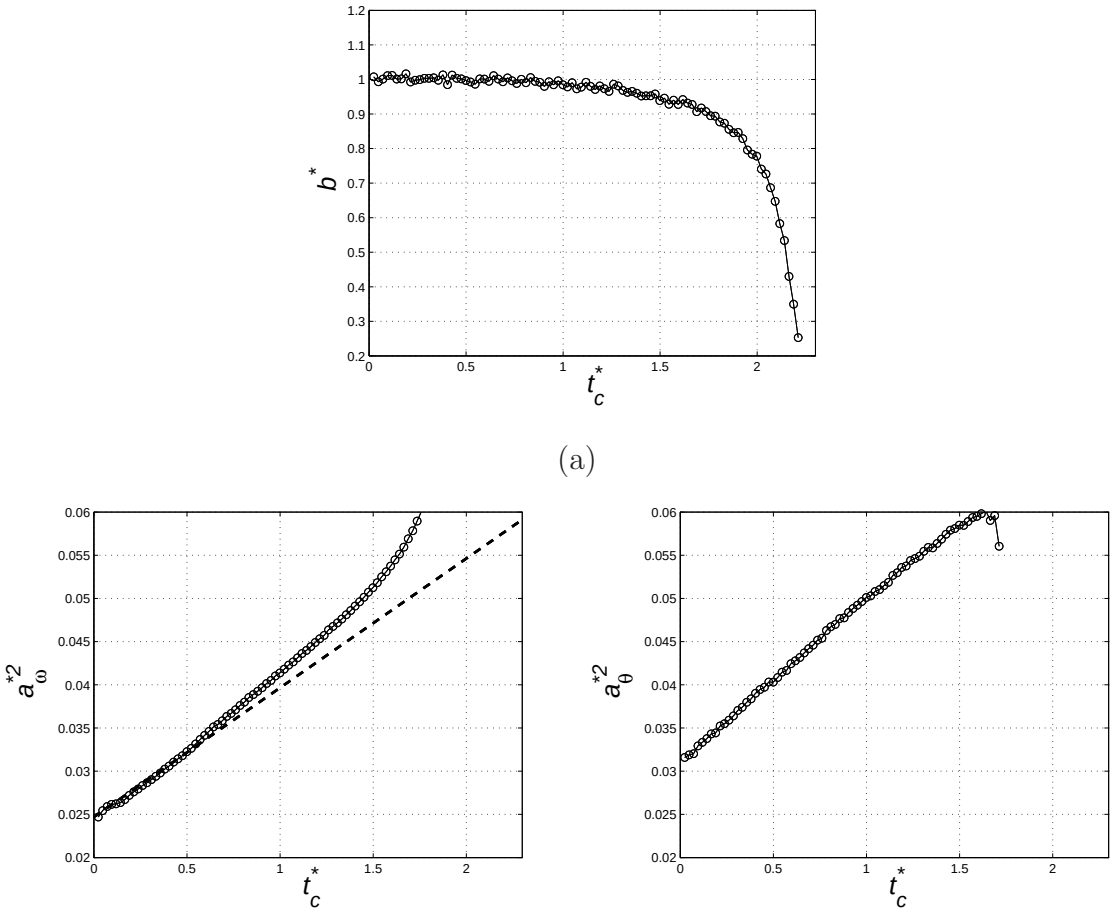

Figure 3.3: Time development of (a) separation distance, $b^*(t) = b(t)/b_o$, (b) core size evaluated by second moment, $a_\omega^2(t)/b_o^2$, (c) core size evaluated by maximum azimuthal velocity, $a_\theta^2(t)/b_o^2$. The dashed line in (b) corresponds to (3.2) where $c = c_\theta/1.12 = 1.94$.

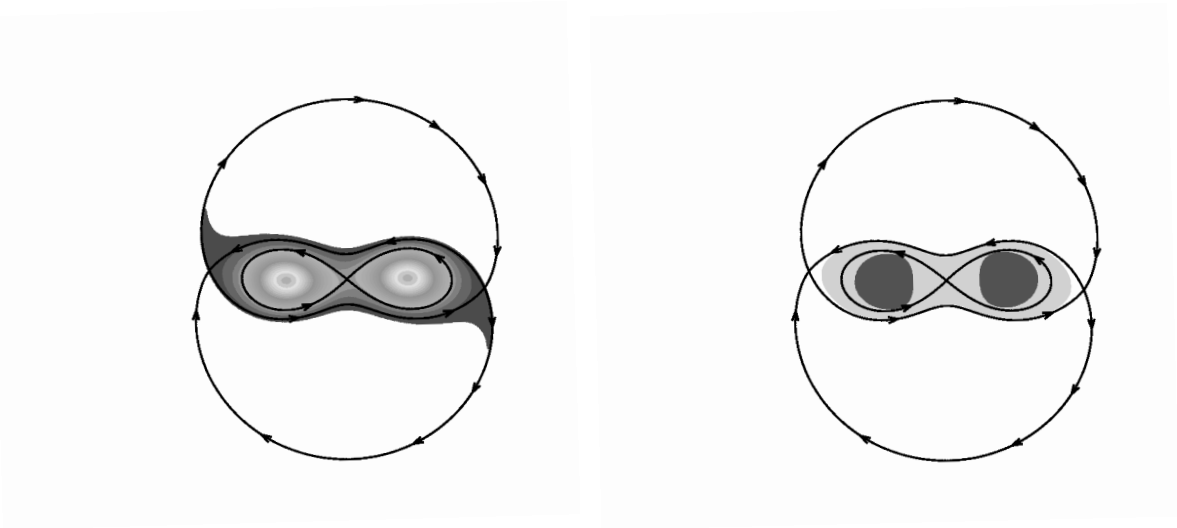

(a) (b)

Figure 3.4: Streamlines in co-rotating frame with (a) vorticity contours superimposed and (b) shading indicating flow region analysis based on velocity gradient tensor (Dark gray: cores, light gray: exchange band, white: outer-recirculation region, i.e. filaments), for $Re_\Gamma = 5000$ at $t_c^* = 1.88$.

3.2 Physical Mechanisms

The basic physical mechanisms of the merging process are now considered. As discussed in §1.2.1, there is some uncertainty about the specific source of the merging velocity, and thus $b(t)$. We address this directly by considering the contribution of each of the distinct flow regions, i.e., the inner cores, the exchange band, and the filaments (figure 3.4a). The flow regions are identified in our analysis as follows. First, the inner recirculation (cores and exchange band) and outer recirculation (filaments) regions are distinguished by the sign of ω in the co-rotating frame, since the outer recirculation is associated with differential rotation. Next, the cores and exchange band are distinguished by considering the second invariant of the velocity gradient tensor (co-rotating frame), $II = (\boldsymbol{\omega}^2/2 - \mathsf{S}^2)/2$, where S is the strain rate tensor (Nomura and Post, 1998). Thus, $II > 0$ corresponds to

rotation dominated regions which effectively characterizes the cores, and $II < 0$ corresponds to strain dominated regions which characterizes the exchange band. We note that in two-dimensional flow, $II > 0$ is equivalent to the λ_2 criterion for vortex identification of Jeong and Hussain (1995). Figure 3.4b illustrates the three defined regions used in the analysis sampling. Although our identification scheme is not based on a strict definition, a sensitivity analysis indicates that it appears to capture the main portion and behavior of these regions. The sampling method is effective through most of the convective phase of the flow. Beyond this, a fundamental transformation of the flow structure occurs and the identification procedure is terminated since the rotation rate can no longer be accurately evaluated.

With the flow regions identified, the velocity field induced by each region is computed using the Biot-Savart law. These velocities are then integrated in time. Figure 3.5 shows the contribution of the flow regions to the *change* in $b^*(t)$, $\Delta b^*_{region}(t)$. This is determined by evaluating the inward velocity induced at the vortex centroids by each region and integrating it in time. The contribution of the filaments, which begins at ${t_c}^* \approx 1$, corresponds to the initial, slow decrease in $b^*(t)$. The contribution of the exchange band, which begins at ${t_c}^* \approx 1.7$, is associated with the predominant and rapid decrease in $b^*(t)$ during the latter part of the convective phase. We note that the contribution of the inner cores oscillates about zero through the diffusive phase (not shown). In the flow considered here, just after ${t_c}^* \approx 1.7$, the cores contribute to an increase in $b^*(t)$.

Figure 3.6 shows the induced flow fields of each of the regions in the vicinity of the center of rotation (a hyperbolic point) at two times (${t_c}^* = 1.69$, 1.97). At ${t_c}^* = 1.69$ (figures 3.6a-c), the velocities induced by the cores are still dominant; those of the filaments are at least an order of magnitude less due to the relatively low ω in this region. However, an inward component of the velocities between the cores is detected in the filament induced flow field (figure 3.6b), consistent with the results in figure 3.5. From figure 3.6a, we observe a tilt in the lowest level ω contours and the associated misalignment of ω with the streamlines (the actual

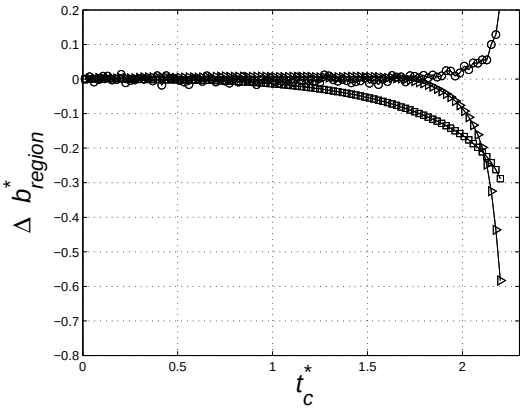

Figure 3.5: Contribution of flow regions to separation distance development, $\Delta b^*_{region}(t)$, for $Re_\Gamma = 5000$ (Symbols: ○: cores, □: filaments, ▷: exchange band).

streamlines are close to those of the core induced velocities at this time). The exchange band induced velocity field (figure 3.6c) corresponds to weak circulatory motion between the two cores. At $t_c{}^* = 1.97$ (figures 3.6d-f), the ω contours show vorticity from the core regions entrained into the exchange band. The velocities induced by the exchange band (figure 3.6f) thereby become significant with magnitudes comparable to those induced by the cores and correspond to predominantly rotational motion about the center of the vortex pair. In time, as more of the core vorticity is entrained into the exchange band, this induced flow strengthens and eventually dominates the flow.

The overall merging process is now considered. Meunier et al. (2005) produced a model of vortex merging that considers the effect of the filaments. Although it predicts quite well the initial gradual reduction of $b^*(t)$, it fails to predict the final rapid reduction. However, as shown in figure 3.5, the dominant reduction in $b^*(t)$ is due to the exchange band. This is the missing mechanism in the model. The process is initiated when core vorticity enters the exchange band through a tilt in ω contours near the center hyperbolic point (figure 3.6a). Vorticity is ad-

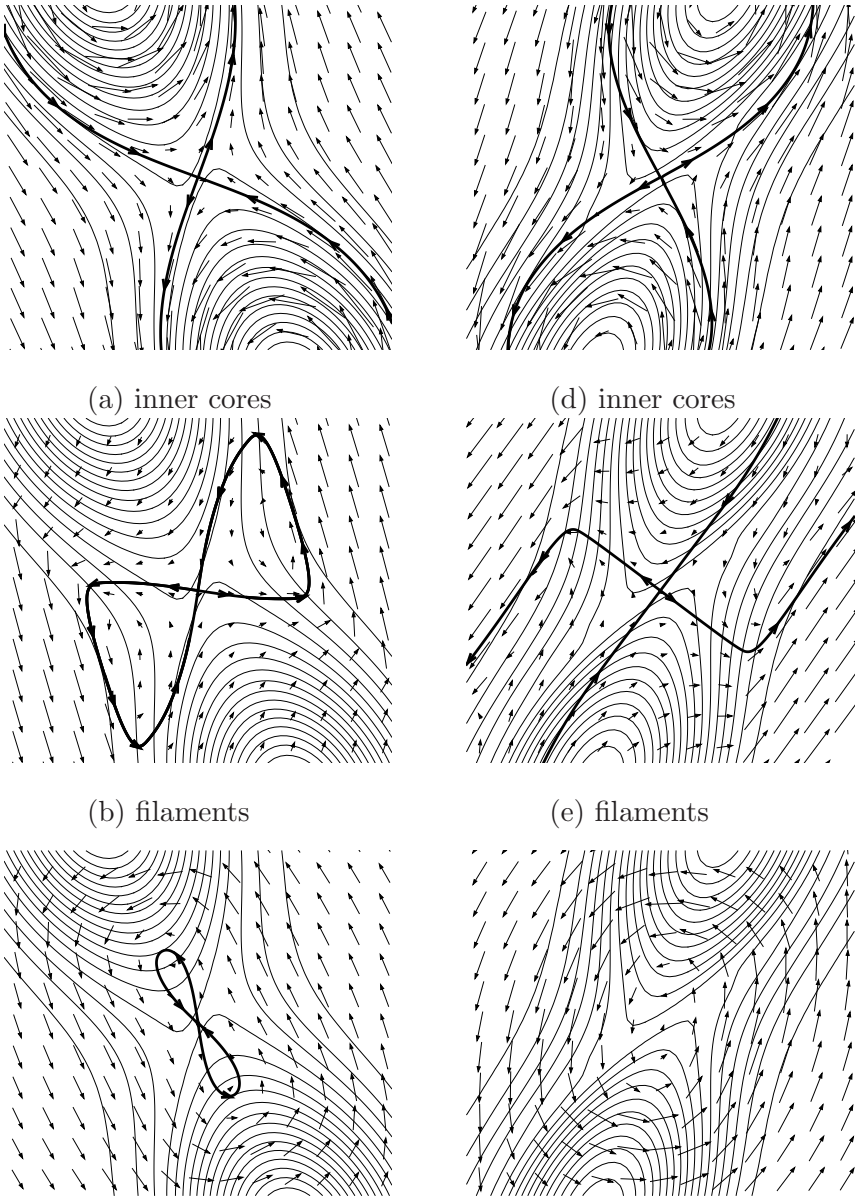

(a) inner cores (d) inner cores

(b) filaments (e) filaments

(c) exchange band (f) exchange band

Figure 3.6: Vorticity contours (thin solid lines) superimposed with vectors showing the induced velocity field of the indicated flow regions for $Re_\Gamma = 5000$ at (a)-(c) $t_c{}^* = 1.69$, (d)-(f) $t_c{}^* = 1.97$. The dark solid line represents the induced flow streamline which passes through the center hyperbolic point.

vected away from its source core and into the exchange band; the inner cores are thereby stripped and eroded (figure 3.6d). At some point, the cores themselves are entrained. This corresponds to the rapid linear decrease in $b^*(t)$ associated with the induced flow by the exchange band (figure 3.5). We therefore consider the *convective phase* to consist of two components: i) induced motion of filaments advects the two vortices towards each other and ii) core erosion and entrainment by the exchange band, the latter transforming the structure of the flow to essentially a single vortex.

3.3 Influence of strain and vorticity on vortex merger

In order to understand the deformation of the vortices, and, in particular, how the tilt in ω contours develops, we first consider the structure and behavior of the rate of strain, S. Since this is a two-dimensional incompressible flow, the two principal eigenvalues of S are equal in magnitude and opposite in sign, and the corresponding eigenvectors are easily computed. Early in the first diffusive phase, the strain rate field is characteristic of two separate vortices, i.e., a band of high strain surrounds each of the cores, and the associated eigenvectors are oriented 45° from the radial direction. During this phase, as viscous diffusion increases the core size, the strain bands correspondingly spread outward. The strain bands interact and result in a locally enhanced region of strain in the vicinity of the center of rotation (see figure 3.7a-c).

Figure 3.8a,b shows the time development of the non-dimensionalized local (principal) strain rate evaluated at the center of rotation. As a reference value, we consider the *external* strain at a given location, defined as the strain rate induced by one vortex if the other vortex was not present. The strain field for a Lamb-Oseen

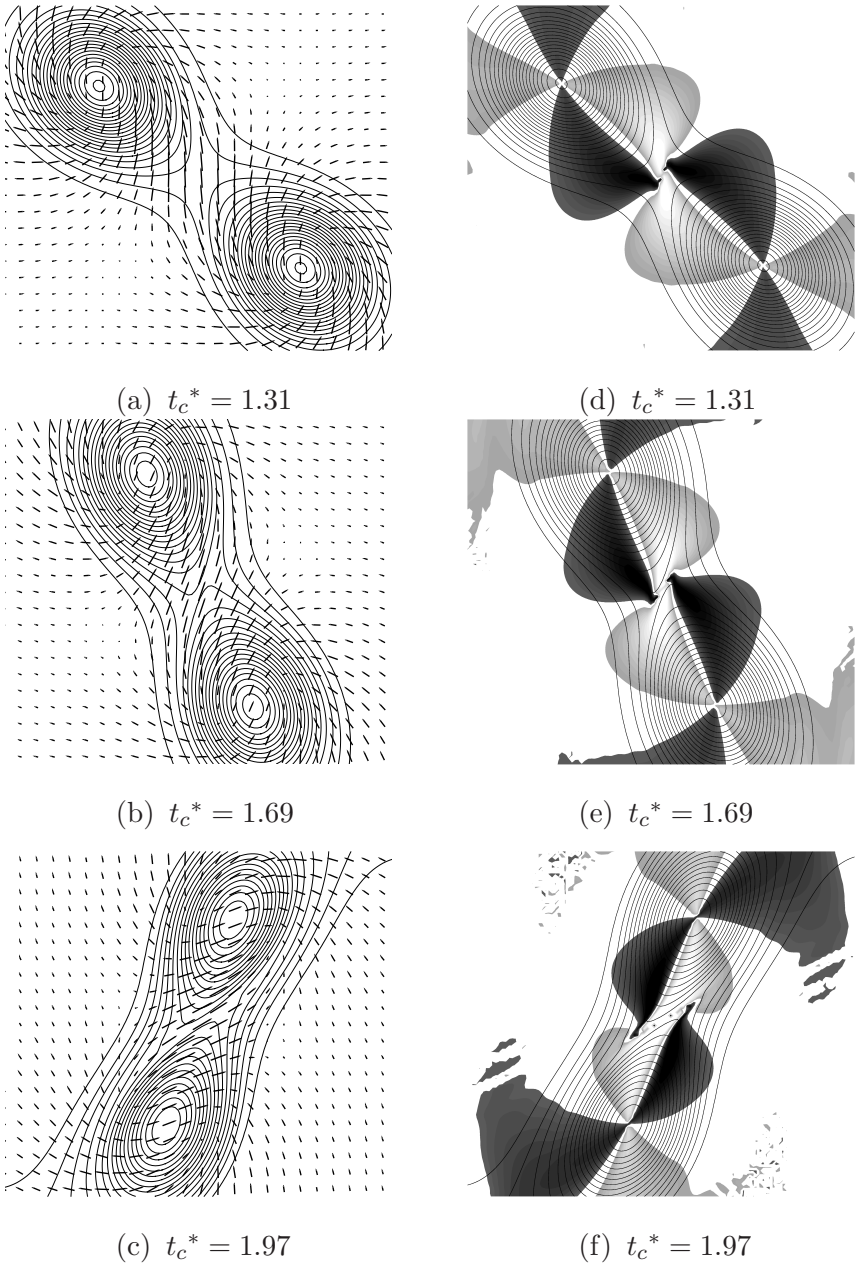

(a) $t_c^* = 1.31$ (d) $t_c^* = 1.31$

(b) $t_c^* = 1.69$ (e) $t_c^* = 1.69$

(c) $t_c^* = 1.97$ (f) $t_c^* = 1.97$

Figure 3.7: Close-up of vorticity contours with (a)-(c) superimposed principal extensional strain (vectors indicating magnitude of eigenvalue and direction of eigenvector), (d)-(f) gray shading corresponding to $|\nabla\omega|^2$ production term, $P_s = -(\nabla\omega^T \mathsf{S} \nabla\omega)/|\nabla\omega|^2$ (light gray scale: $P_s > 0$, dark gray scale: $P_s < 0$), for $Re_\Gamma = 5000$.

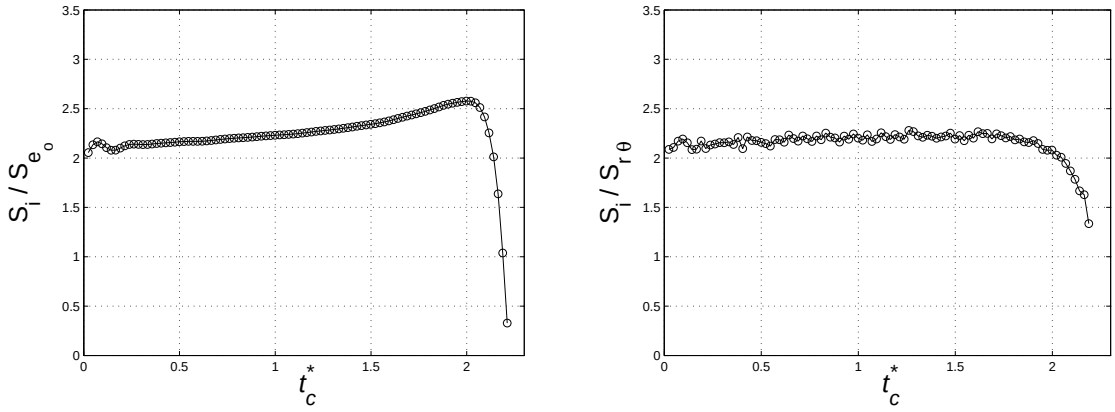

(a) (b)

Figure 3.8: Time development of the local strain rate, S_i, at the center of rotation normalized by the external strain rates (3.3) (a) $S_{eo} = S_{r\theta}(b/2, 0)$, (b) $S_{r\theta}(b/2, t)$ for $Re_\Gamma = 5000$.

vortex (Saffman, 1992) is given by,

$$S_{r\theta}(r,t) \;=\; \frac{\Gamma_o}{2\pi}\left[-\frac{1}{r^2} \;+\; \left(\frac{1}{a^2} \;+\; \frac{1}{r^2}\right)\exp\left(-\frac{r^2}{a^2}\right)\right]. \tag{3.3}$$

At $t = 0$ (large b/a and $b = b_o$), the external strain value at the center of rotation ($r = b/2$) is $S_{r\theta}(r, 0) = 4\,\Gamma_o/(2\pi {b_o}^2)$. The strain values plotted in figure 3.8a are non-dimensionalized by the constant value, $S_{r\theta}(r, 0) = S_{eo}$, and in figure 3.8b by the time varying external strain, $S_{r\theta}(r, t)$, which accounts for both $b(t)$ and $a(t)$. Results indicate that the local strain rate increases linearly during the diffusive phase. Initially the value is approximately twice the external strain indicating that the contributions from each of the vortices are nearly additive. The main increase during the convective phase is due to the reduction in $b(t)$. We note that although $S_{r\theta}(r, t)$ describes the overall behavior quite well for some time, the scaled strain in figure 3.8b does exhibit a slow increase until $t_c{}^* \approx 1.7$, at which time it decreases and deviates from $S_{r\theta}(r, t)$ significantly. This corresponds to the start of the exchange band process.

The interaction of the vortices will also influence the directionality of S,

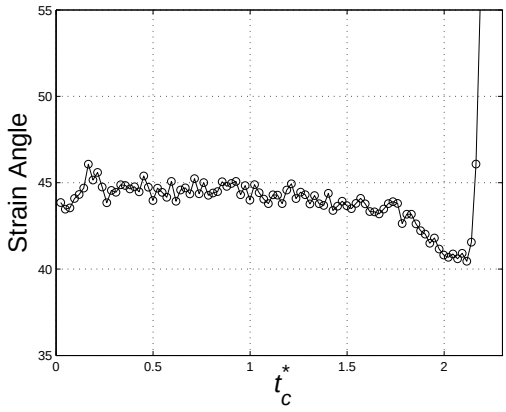

Figure 3.9: Time development of the angle between extensional strain eigenvector and vortex connecting line at the center of rotation for $Re_\Gamma = 5000$.

which will in turn affect subsequent vortex deformation (3.4). Figure 3.9 shows the angle between the extensional strain eigenvector and the vortex connecting line at the center of rotation, i.e., the *relative orientation* of the extensional strain with respect to the vortex pair. At early times, the angle remains approximately 45° due to the relatively weak interaction between the vortices. At approximately ${t_c}^* \approx 1.0$, the angle begins to decrease. At ${t_c}^* \approx 1.7$, the angle is reduced to approximately 43°. At this time, the exchange band process is initiated (figure 3.5). Close inspection of the induced flow fields (figure 3.6a-c), and in particular the streamlines passing through the center hyperbolic point indicating local extensional straining, demonstrates that the exchange band is responsible for the reduction in this angle. Note that the induced flow by the filaments tends to increase this angle (figure 3.6b). At ${t_c}^* \approx 2.1$, the angle reaches approximately 40°, beyond which it then rapidly increases. This indicates a substantial change in the flow, i.e., core entrainment, which corresponds to the time $b^*(t)$ begins its rapid and nearly linear descent (figure 3.3a). The reduction in strain orientation is associated with the development of the tilt in ω contours (see figure 3.7a-c). We will consider this angle as an indicator of the tilt, which results from a dynamic interaction between

vorticity and strain.

In a two-dimensional flow, the interaction of ω and S is understood in terms of the vorticity gradient, $\nabla\omega$, which may undergo reorientation and amplification by S. It is directly related to the behavior of vorticity contours since $-\nabla\omega/|\nabla\omega|$ is the local normal vector of an isovorticity contour line. The equation for $|\nabla\omega|^2$ is,

$$\frac{D\frac{1}{2}|\nabla\omega|^2}{Dt} \;=\; |\nabla\omega|^2\,\frac{D\,ln\,|\nabla\omega|}{Dt} \;=\; -\,\nabla\omega^T\mathsf{S}\,\nabla\omega \;+\; \nu\nabla\omega^{\mathsf{T}}\nabla^2\nabla\omega \tag{3.4}$$

The two terms on the right-hand side represent gradient amplification and diffusion, respectively. Here, we define two quantities associated with the production term:

$$P = -\nabla\omega^T\mathsf{S}\,\nabla\omega \tag{3.5}$$

and

$$P_s = -(\nabla\omega^T\mathsf{S}\,\nabla\omega)/|\nabla\omega|^2 \tag{3.6}$$

(P_s obtained by dividing (3.4) by $|\nabla\omega|^2$), whose sign indicates the relative orientation of $\nabla\omega$ with the principal strain axes and, in the case of P_s, the magnitude indicates the strain in the direction of $\nabla\omega$. Thus, $P, P_s > 0$ correspond to $\nabla\omega$ orienting towards the direction of the compressive strain, i.e., there is gradient amplification by compressive straining. Figure 3.10 shows the time development of the area averaged production term, $\langle P\rangle$, which indicates a global mean rate of deformation of the vorticity field. Prior to merging, the behavior of $\langle P\rangle$ is consistent with the elliptic deformation of the vortices as characterized by computed eccentricities (not shown). As discussed in Le Dizes and Verga (2002), beyond the initial flow adjustment and prior to the merging threshold, the vortices relax to a mean state in which they deform at a steady rate. This mean state corresponds to the small and nearly constant value exhibited by $\langle P\rangle$ during this time (figure 3.10). A net positive value of $\langle P\rangle$ is exhibited indicating the significance of the gradient

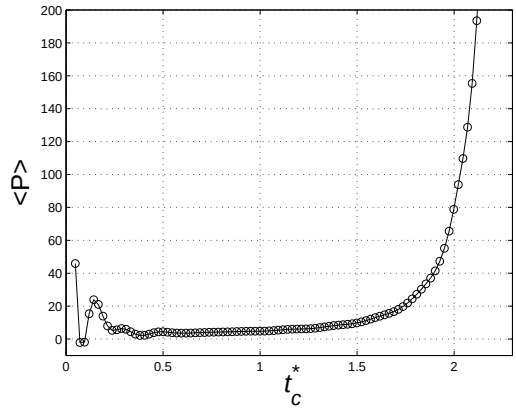

Figure 3.10: Time development of $< P >= - < \nabla\omega^T \mathsf{S} \nabla\omega >$, averaged over domain, for $Re_\Gamma = 5000$.

amplification process. Beyond the diffusive phase, there is a significant increase in $\langle P \rangle$ indicating deviation from the mean state and accelerated deformation.

In general, the local behavior of P will depend on the relative significance of rotation and strain. In rotation dominated regions ($II > 0$), P oscillates between positive and negative values. Physically, $\nabla\omega$ rotates and alternates between amplification and damping, a condition which results in the elliptic instability (Protas et al., 1999). We expect the *dynamic* effect of P on $\nabla\omega$ to be most significant in strong strain-dominated regions ($II < 0$), i.e., the exchange band region, and in particular, in the vicinity of the center of rotation where there is an enhancement of strain. In these regions, S is dynamically active and significantly alters $\nabla\omega$.

Figure 3.7 shows S (vectors) and P_s (light gray scale: $P_s > 0$, dark gray scale: $P_s < 0$) superimposed on vorticity contours at the central region of the vortex pair at three times. Each vortex exhibits the quadrapole structure of P associated with elliptic vortices (Kimura and Herring, 2001). As discussed in Kimura and Herring, in positive P_s (compressive straining) regions ω isocontours are squeezed together while at the same time, they are extended in the orthogonal direction due to flow incompressibility. The opposite is true for negative P_s regions. This is seen in figure 3.7e where, in the vicinity of the center (hyperbolic point) and above it,

ω contours in $P_s > 0$ regions extend to the left, while ω contours in $P_s < 0$ regions contract to the left. This results in the observed tilting of the upper vortex to the left and a corresponding tilting of the lower vortex to the right, which thereby tilts the vortices with respect to their connecting line. This also results in the central region to be dominated by $P_s > 0$; i.e., gradient amplification. The tilting effect also occurs in the vicinity of the outer hyperbolic points where filamentation initiates (not shown). In their study of isolated elliptic vortices, Kimura and Herring (2001) show that P plays a significant role in the filamentation process. In regions of $P > 0$, vorticity gradient amplification was found to occur prior to filament ejection. This is also observed in the present case of two co-rotating vortices.

As discussed by Le Dizes and Verga (2002), prior to merging, the vorticity and streamfunction exhibit a distinct functional relation suggesting that the flow in the rotating frame is nearly a stationary solution to the Euler equation. However, in time and near the merging threshold, the relation between ω and the streamfunction deviates at the hyperbolic points where $|\omega|$ is low (see their figure 14). At the central hyperbolic point, they find an accumulation of vorticity and a Reynolds number dependence which they suggest is due to complex advection-diffusion processes. Based on our results, we conclude that the tilt of the vortices and associated diffusion, which is enhanced by gradient amplification ($P_s > 0$ at center), results in this accumulation and the observed misalignment of ω contours with respect to the streamlines in these regions (e.g., figure 3.6a). Since the streamlines are separatrices, this causes vorticity to enter a different flow region in the co-rotating frame and be advected away.

In order to examine further the development of the tilt, we define the *central region* of the flow by a box in the co-rotating frame with a width of $0.25b_o$ (along connecting line of vortices) and a height of $0.08b_o$. The box dimensions are chosen to capture the primary misalignment in ω contours. Figure 3.11 shows $\langle P \rangle$ averaged over the central region which is predominantly positive and exhibits a

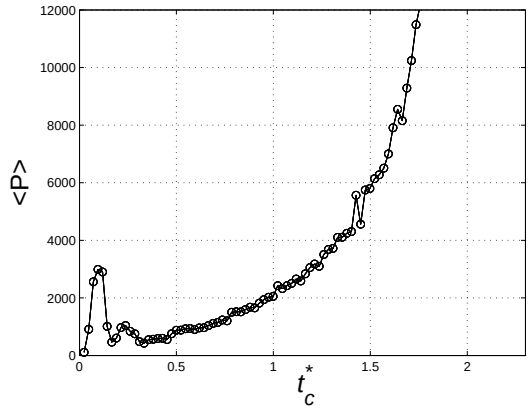

Figure 3.11: Time development of $\langle P \rangle = -\langle \nabla\omega^T \mathsf{S}\, \nabla\omega \rangle$ in the central region for $Re_\Gamma = 5000$.

significant increase beyond $t_c^* \gtrsim 0.5$. This increase corresponds directly with the extension of $P_s > 0$ regions and the positive feedback nature of gradient amplification by compressive straining. Since the production term, $\nabla\omega^T \mathsf{S}\, \nabla\omega$, depends on both the magnitudes and relative orientation of $\nabla\omega$ and S, we now isolate the directional component. Figure 3.12 shows the average angle between $\nabla\omega$ and the compressive strain eigenvector in the central region. Beyond the initial adjustment period, the average angle is $\approx 40°$ which is near the 45° associated with a *passive* strain field, i.e., controlled by the primary vortex. Beyond a time $t_c^* \approx 1$, the angle decreases towards zero indicating that the strain has become *active* in influencing the vorticity field by amplifying and reorienting $\nabla\omega$. This corresponds to the development of the tilt (figure 3.9).

3.4 Flow Phases - Redefined

In summary, we present the following description of the merging process, which we consider to consist of *four* phases. During the *diffusive/deformation phase*, $b^*(t)$ remains constant and the vortices grow by diffusion. The induced

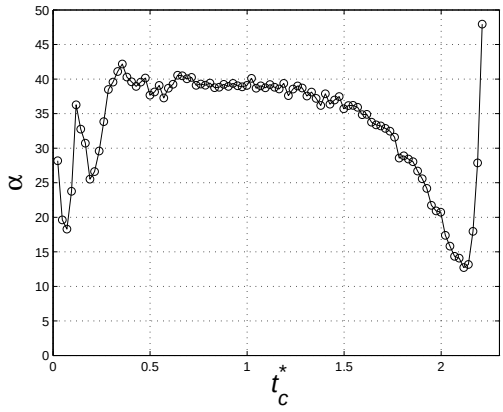

Figure 3.12: Time development of the angle between $\nabla\omega$ and compressive strain, α, in the central region for $Re_\Gamma = 5000$.

strain field of each of the vortices correspondingly spreads by diffusion and also develops through their mutual interaction. In the strain dominated regions of the flow, and in particular in the vicinity of the center hyperbolic point where the mutual interaction of strain is strongest, S becomes dynamically active and influences the vorticity field through amplification and reorientation of $\nabla\omega$. This establishes a tilt in ω contours with respect to the vortex connecting line which, together with diffusion, results in a misalignment of ω with respect to the streamlines. At the outer regions of the exchange band (near outer hyperbolic points), this causes ω to enter the outer recirculation region and filamentation to occur. The associated vorticity acts to advect the vortices towards each other but does not drive the merger to completion. We consider this as the *convective/deformation phase* since the (slow) reduction in $b^*(t)$ enhances the induced strain at the vortices and central region. In the vicinity of the center hyperbolic point, this misalignment allows inner core ω to enter the exchange band and be advected away from its source core. This is the start of the *convective/entrainment phase*, which is associated with a rapid reduction in $b^*(t)$. The inner cores are thereby stripped and eroded. The circulation of the exchange band increases at the expense of that of the inner

cores, which become increasingly weak. At some point, the cores themselves are entrained. The resulting fluid motion becomes rotation dominated and what is essentially a single vortex is established. The last phase, *diffusive/axisymmetrization phase*, is characterized by the final slow reduction in $b^*(t)$ as the two ω maxima diffuse and the flow evolves towards axisymmetry.

As will be discussed in the following chapters, this new description of merger, which resolves the convective phase into the two distinct processes, assists in accounting for the effects of asymmetry and weak stratification.

Chapter 3, in part, is a reprint of the material as it appears in *Physics of Fluids* Volume 18, pages 1-4. Brandt, L.; Nomura, K., American Institute of Physics, 2006 and *Journal of Fluid Mechanics* Volume 592, pages 413-446. Brandt, L.; Nomura, K., Cambridge University Press, 2007. The dissertation author was the primary investigator and author of these papers.

Chapter 4

Asymmetric co-rotating vortex pairs (unstratified)

In this chapter, we discuss the physics of asymmetric vortex interactions. These vortex pairs are asymmetric in that they have the same initial aspect ratio, but their circulation strengths vary with respect to one another. The stronger vortex circulation strength, for all simulations, is $Re_\Gamma = 5000$ and the weaker vortex strength varies with respect to the stronger vortex by $Re_{\Gamma,2}/Re_{\Gamma,1} = 1, 0.9, 0.8, 0.7,$ 0.6, 0.5 and 0.4.

We begin with a qualitative description of the flow behavior in §4.1 and a discussion of the frame of reference that will be used during the analysis in §4.2. The physical mechanisms are discussed in §4.3. The critical parameter is defined in §4.4 and used to define the flow regimes in §4.5. We will conclude with a brief discussion of results in §4.6.

4.1 Flow behavior and development

We begin by examining the basic development of the flows. Figure 4.1a,b shows time sequences of vorticity contour plots for different $Re_{\Gamma,2}/Re_{\Gamma,1}$. Due to

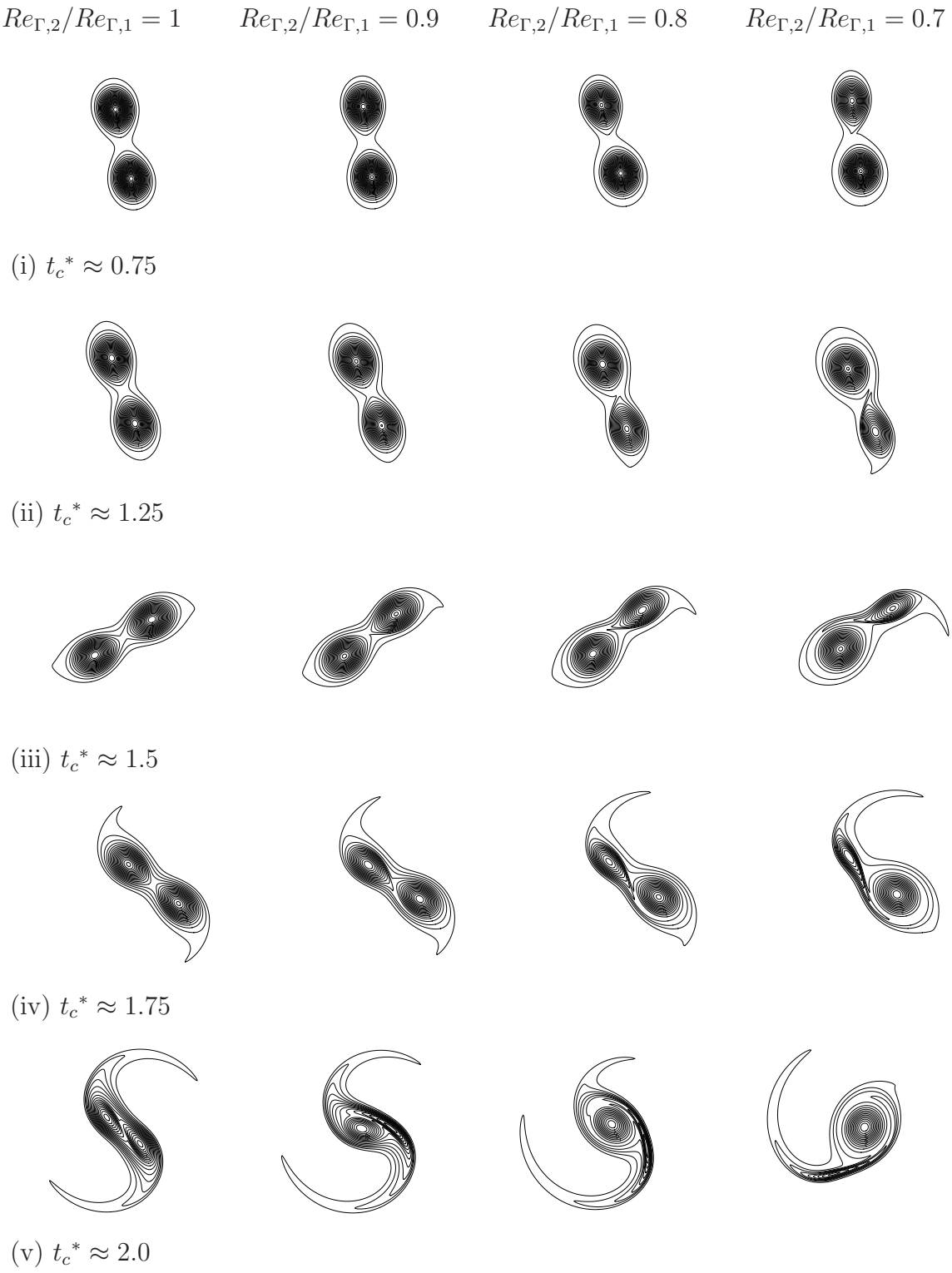

Figure 4.1a: Line plots of vorticity contours.

$Re_{\Gamma,2}/Re_{\Gamma,1} = 0.6$ $Re_{\Gamma,2}/Re_{\Gamma,1} = 0.5$ $Re_{\Gamma,2}/Re_{\Gamma,1} = 0.4$

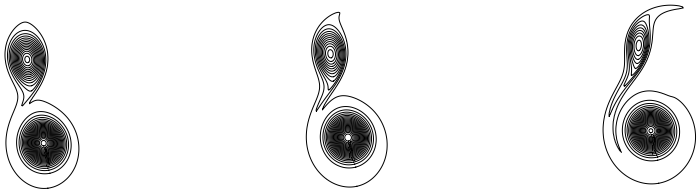

(i) $t_c^* \approx 0.75$

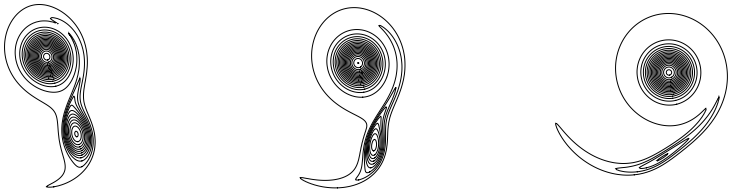

(ii) $t_c^* \approx 1.25$

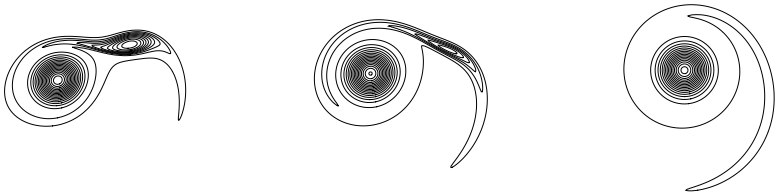

(iii) $t_c^* \approx 1.5$

(iv) $t_c^* \approx 1.75$

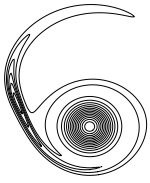

(v) $t_c^* \approx 2.0$

Figure 4.1b: Line plots of vorticity contours.

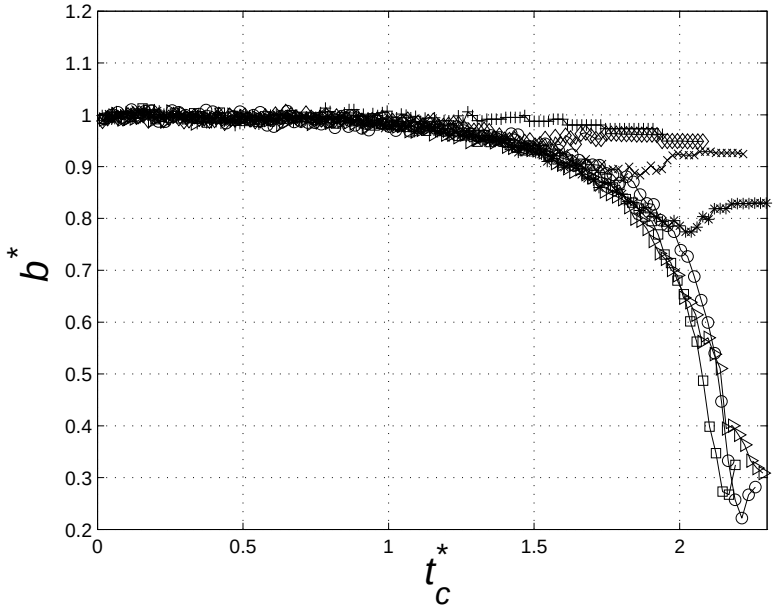

Figure 4.2: Time development of separation distance, $b^*(t) = b(t)/b_o$, Symbols: $\circ$: $Re_{\Gamma,2}/Re_{\Gamma,1} = 1$, $\square$: $Re_{\Gamma,2}/Re_{\Gamma,1} = 0.9$, $\triangleright$: $Re_{\Gamma,2}/Re_{\Gamma,1} = 0.8$, $*$: $Re_{\Gamma,2}/Re_{\Gamma,1} = 0.7$, $\times$: $Re_{\Gamma,2}/Re_{\Gamma,1} = 0.6$, $\diamond$: $Re_{\Gamma,2}/Re_{\Gamma,1} = 0.5$, $+$: $Re_{\Gamma,2}/Re_{\Gamma,1} = 0.4$

the mutually induced velocity, the vortices initially rotate about each other at a fixed distance, while diffusion causes the cores to grow.

As was discussed in chapter 3, in the case of equal vortices ($Re_{\Gamma,2}/Re_{\Gamma,1} = 1$; first column in figure 4.1a), the vortex cores deform elliptically as they diffuse. A tilt in the vorticity contours develops near the center of rotation. Filaments develop at the outer edge of each vortex. The major axes of the vortices are tilted with respect to the connecting line of the vortices; subsequently, the vortices move rapidly towards each other and intertwine. The two vorticity maxima eventually diffuse as the flow evolves towards axisymmetry (not shown).

In the case of unequal vortices ($Re_{\Gamma,2}/Re_{\Gamma,1} < 1$), the vortices do not deform at the same rate. The smaller the Re_Γ ratio, the greater the deformation of the weaker vortex in comparison with that of the stronger vortex. The tilt in the

weaker vortex develops earlier. For the cases $0.7 \leq Re_{\Gamma,2}/Re_{\Gamma,1} \leq 0.9$, the vortices approach each other, however the stronger vortex appears to endure the interaction. For lower Re_Γ ratios ($Re_{\Gamma,2}/Re_{\Gamma,1} \leq 0.6$), the vorticity maxima do not rapidly move towards each other. Instead, the weaker vortex is significantly deformed and becomes encircled about the stronger vortex, eventually diffusing into its low level outlying vorticity. The stonger vortex appears to be relatively unaffected.

Figure 4.2 shows the time development of nondimensional separation distance, $b^*(t) = b(t)/b_0$ for various $Re_{\Gamma,2}/Re_{\Gamma,1}$. In all the flows, $b^*(t)$ remains nearly constant for some time and then exhibits a gradual reduction. As shown in chapter 3, and suggested in the visualizations (figure 4.1a), the gradual reduction in $b^*(t)$ is associated with the formation of filaments. For $Re_{\Gamma,2}/Re_{\Gamma,1} \gtrsim 0.7$, a more rapid reduction in $b^*(t)$ then follows which occurs at approximately the same time in all the flows. For $Re_{\Gamma,2}/Re_{\Gamma,1} < 0.7$, $b^*(t)$ behaves differently and beyond the early gradual reduction, instead exhibits an increase.

With sufficient initial separation, the vortex cores will initially increase in time due to viscous diffusion. As stated in chapter 3, there are various ways of defining the size of vortex cores. Meunier et al. (2002) defines the core size by the second moment of vorticity, a_ω. However, in the case of asymmetric vortex pairs, this approach has difficulties since eventually, vorticity detrained from the weaker vortex is accounted for in the stronger vortex and vice versa. To circumvent this difficulty, we use the (circumferential) averaged distance between the vorticity maxima and the maximum azimuthal velocity as an indicator of the vortex core size, a_θ (chapter 3).

Figure 4.3 shows $a_\theta^{2*} = a_\theta^2/b_0^2$ for both the stronger and weaker vortices. The initial linear development in a_θ^{2*} corresponds to growth by viscous diffusion. In the symmetric case, at some point both cores deviate from its linear growth. This indicates the transition from a diffusive- to convective-dominated process which corresponds to the predominant change in $b^*(t)$. In the asymmetric vortex interactions, the weaker vortex core (figure 4.3b) deviates from its linear growth

earlier in time than the stronger vortex core. However, this does not cause b^* to rapidly decrease (figure 4.2). Rather, the rapid decrease in b^* is associated with the deviation from linear growth of the stronger vortex core. For sufficiently unequal vortices ($Re_{\Gamma,2}/Re_{\Gamma,1} \lesssim 0.6$), the latter may not be substantial or occur at all (figure 4.3a). In general, the transition from diffusive- to convective-dominated flow, which has been used to determine the critical aspect ratio for symmetric merger (Meunier et al., 2002), does not readily yield a corresponding merging criteria for the asymmetric case. In order to develop an appropriate merging criterion, we must gain a better understanding of the physics underlying the vortex interactions.

4.2 Flow structure in the co-rotating frame

As in previous studies, it is useful to consider the flow in the co-rotating reference frame. Figures 4.4a,b show the flow structure for $Re_{\Gamma,2}/Re_{\Gamma,1} = 1$ and $Re_{\Gamma,2}/Re_{\Gamma,1} = 0.6$ simulation results. Here, the shaded contours indicate vorticity and the streamlines shown are the separatrices in the co-rotating frame. In figures 4.4c,d, the separatrices are evaluated from a corresponding point vortex system. The basic flow structure is effectively represented by the point vortices as long as the separation is sufficiently large.

In §3.2, we gave a detailed explanation of the symmetric co-rotating frame (figures 4.4a,c). We showed that there are three primary flow regions. The inner core regions consist of closed streamlines encircling each individual vorticity maximum and correspond to the primary vortices. The exchange band consists of closed streamlines encompassing both inner core regions and corresponds to fluid circulating (exchanged) between the two vortices. The outer recirculation regions consist of fluid which circulates in the opposite sense (in the co-rotating frame) to that of the cores and exchange band and is where the filaments are formed. There are three hyperbolic points in the flow including the central hyperbolic (CH) point

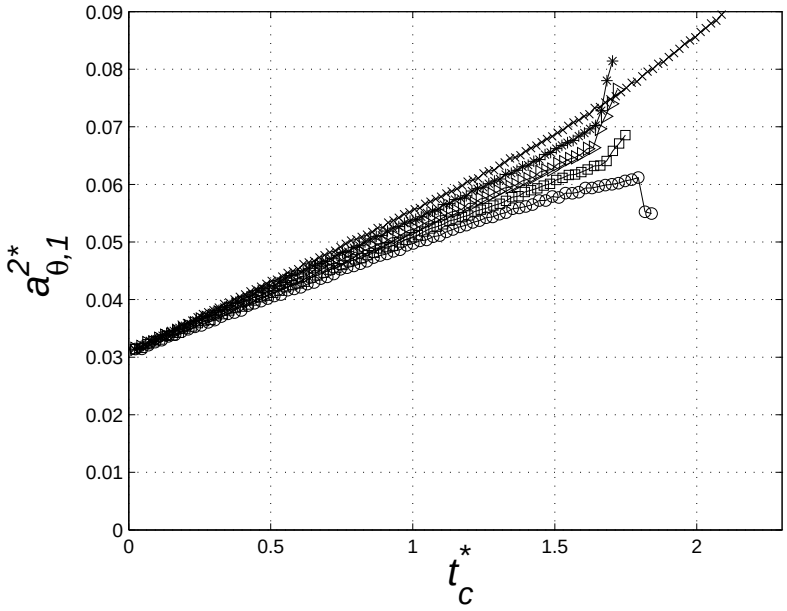

(a) Vortex 1

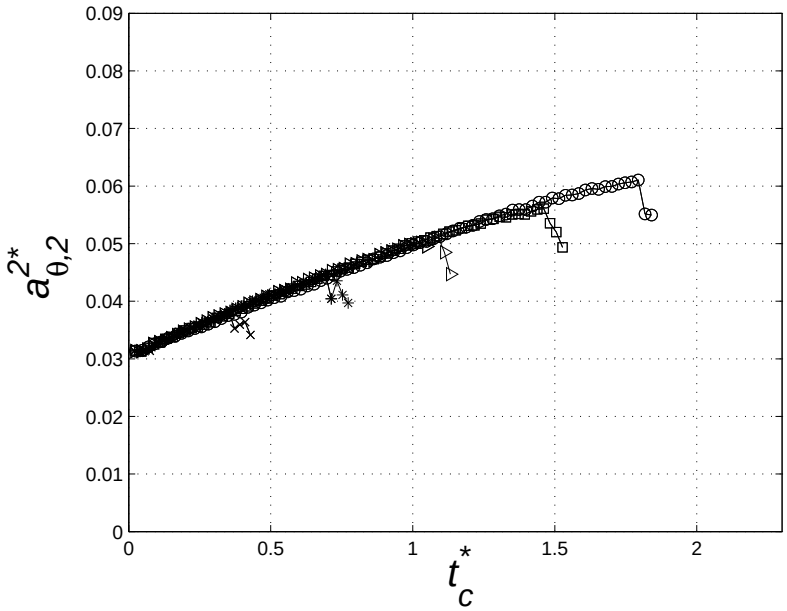

(b) Vortex 2

Figure 4.3: Time development of vortex cores based on the maximum azimuthal velocity, Symbols: ○: $Re_{\Gamma,2}/Re_{\Gamma,1} = 1$, □: $Re_{\Gamma,2}/Re_{\Gamma,1} = 0.9$, ▷: $Re_{\Gamma,2}/Re_{\Gamma,1} = 0.8$, ∗: $Re_{\Gamma,2}/Re_{\Gamma,1} = 0.7$, ×: $Re_{\Gamma,2}/Re_{\Gamma,1} = 0.6$

which coincides with the center of rotation (CR).

In the asymmetric vortex pair (figures 4.4b,d), the flow structure differs. The locations of the CR and the CH point are shifted and no longer coincide. These basic features in the flow geometry are indicated by the point vortex model (figure 4.4d). For a pair of point vortices, the normalized distance between the CR and the centers of the stronger (V1) and weaker (V2) vortices, respectively, $r^*_{|CR-V1|,o}$ and $r^*_{|CR-V2|,o}$, are given by,

$$\begin{aligned} r^*_{|CR-V1|,o} &= \frac{r_{|CR-V1|,o}}{b_o} = \frac{Re_{\Gamma,2}/Re_{\Gamma,1}}{1+Re_{\Gamma,2}/Re_{\Gamma,1}}, \\ r^*_{|CR-V2|,o} &= \frac{r_{|CR-V2|,o}}{b_o} = \frac{1}{1+Re_{\Gamma,2}/Re_{\Gamma,1}} \end{aligned} \tag{4.1}$$

which indicates that the CR shifts towards the stronger vortex as the Re_Γ ratio is reduced from unity. We note that in the simulations, the CR remains nearly fixed prior to core destruction. The point vortex system (figure 4.4d) also illustrates the modified flow structure which consists of three hyperbolic points and four primary regions.

The inner-core and exchange band regions are similar to that of the symmetric case, however, the CH point has shifted. The locations of the hyperbolic points for the point vortex system are given by,

$$\begin{aligned} \left[\frac{Re_{\Gamma,1}}{Re_{\Gamma,2}}+1\right] d^{*3}_{|H-V1|,o} - \left[\frac{Re_{\Gamma,1}}{Re_{\Gamma,2}}+2\right] d^{*2}_{|H-V1|,o} - \frac{Re_{\Gamma,1}}{Re_{\Gamma,2}} d^*_{|H-V1|,o} + \frac{Re_{\Gamma,1}}{Re_{\Gamma,2}} = 0 \\ \left[\frac{Re_{\Gamma,2}}{Re_{\Gamma,1}}+1\right] d^{*3}_{|H-V2|,o} - \left[\frac{Re_{\Gamma,2}}{Re_{\Gamma,1}}+2\right] d^{*2}_{|H-V2|,o} - \frac{Re_{\Gamma,2}}{Re_{\Gamma,1}} d^*_{|H-V2|,o} + \frac{Re_{\Gamma,2}}{Re_{\Gamma,1}} = 0 \end{aligned} \tag{4.2}$$

where $d^*_{|H-V1|,o} = d_{|H-V1|,o}/b_o$ represents the initial distance from the stronger vortex to a hyperbolic point (H) and $d^*_{|H-V2|,o} = d_{|H-V2|,o}/b_o$ represents the initial distance from the weaker vortex to a hyperbolic point. The exact solution of (4.2) is cumbersome. However, a fourth order approximation may be obtained through

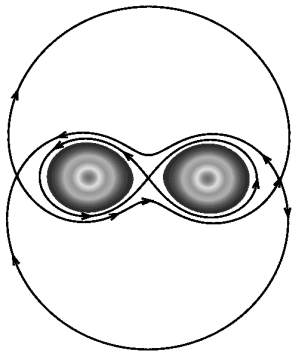

(a) $Re_{\Gamma,2}/Re_{\Gamma,1} = 1.0$, simulation

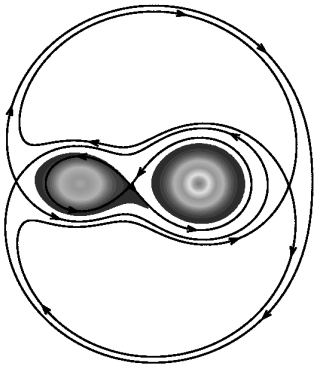

(b) $Re_{\Gamma,2}/Re_{\Gamma,1} = 0.6$, simulation

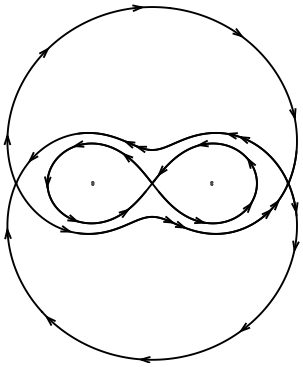

(c) $Re_{\Gamma,2}/Re_{\Gamma,1} = 1.0$, point vortices

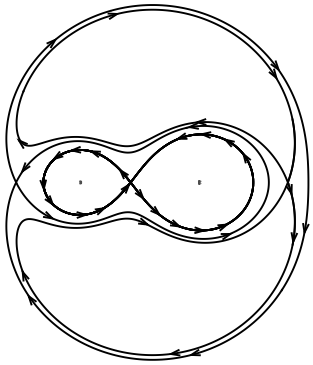

(d) $Re_{\Gamma,2}/Re_{\Gamma,1} = 0.6$, point vortices

Figure 4.4: Flow structure in the co-rotating frame (a),(b) simulation results at $t_c^* = 0.32$, and (c),(d) point vortex system. (a),(c): $Re_{\Gamma,2}/Re_{\Gamma,1} = 1.0$ and (b),(d): $Re_{\Gamma,2}/Re_{\Gamma,1} = 0.6$. Streamlines show separatrices of primary flow regions and shading corresponds to vorticity.

a perturbation expansion. This gives the location of the CH point to be,

$$\begin{aligned} d^*_{|CH-V2|,o} &= \frac{\sqrt{2}}{2}\left[\frac{Re_{\Gamma,2}}{Re_{\Gamma,1}}\right]^{1/2} - \frac{1}{8}\left[\frac{Re_{\Gamma,2}}{Re_{\Gamma,1}}\right]^{1} - \frac{19\sqrt{2}}{128}\left[\frac{Re_{\Gamma,2}}{Re_{\Gamma,1}}\right]^{3/2} + \frac{1}{8}\left[\frac{Re_{\Gamma,2}}{Re_{\Gamma,1}}\right]^{2} \\ d^*_{|CH-V1|,o} &= 1 - d^*_{|CH-V2|,o} \end{aligned} \tag{4.3}$$

where $d^*_{|CH-V1|,o} = d_{|CH-V1|,o}/b_o$ represents the initial distance from the stronger vortex to the CH point and $d^*_{|CH-V2|,o} = d_{|CH-V2|,o}/b_o$ represents the initial distance from the weaker vortex to the CH point. Equation 4.3 provides a good estimate of the initial location of the CH point and indicates that the smaller the Re_Γ ratio, the closer the CH point is to the weaker vortex. This will be used in our scaling analysis in §4.4. We note that for very small Re_Γ ratios, the point vortex result of (4.3) breaks down due to the close proximity of the CH point to the finite size core.

As will be discussed, the processes occuring in the vicinity of the CH point are key in understanding the behavior of the flow.

4.3 Asymmetric vortex interactions

As shown in figure 4.1a&b, the difference in vortex strengths in asymmetric vortex pairs alters the flow structure and interaction. Initially the two vortices will develop in a diffusive/deformation phase in which the cores grow by diffusion (figure 4.3) as in the symmetric case (chapter 3). However, the greater deformation rates at the weaker vortex will cause it to depart earlier from this phase. A measure of the rate of vortex deformation is the local eccentricity, ϵ_l, defined as the ratio of the strain rate to the rotation rate (Le Dizes and Verga, 2002). Figure 4.5 shows ϵ_l evaluated at the vorticity maximum of each vortex. The results clearly indicate the disparity in deformation rates between the vortices. We note that for low Re_Γ ratios (e.g., $Re_{\Gamma,2}/Re_{\Gamma,1} \leq 0.6$), the local eccentricity of the stronger vortex, $\epsilon_{l,1}$, remains low and in time, indicates little influence by the weaker vortex.

The implication of the differences in deformation rates is indicated in figure 4.6 where we investigate the interaction of S and $\nabla\omega$ (3.6). In §3.3, a measure of the relationship between S and $\nabla\omega$ in symmetric vortex interactions was expressed through the quantity $P_s = -(\nabla\omega^T \mathsf{S}\, \nabla\omega)/|\nabla\omega|^2$. It was found that each vortex exhibited a quadrapole structure of P_s corresponding to alternate regions of gradient amplification/attenuation by compressive/extensional straining which are associated with the elliptic deformation during this time (figure 4.6a). For the asymmetric vortex interactions it is seen in figure 4.6b that P_s is stronger at the weaker vortex due to the induced S by the stronger vortex and that conversely, P_s is weaker at the stronger vortex due to the induced S by the weaker vortex. As discussed in §4.2, the CH point is closer to the weaker vortex. The weaker vortex is thereby subject to earlier tilting in the vicinity of the CH point and resultant core detrainment.

As discussed, in the symmetric vortex pair (chapter 3), a convective/ deformation phase follows in which there is a gradual motion of the vortices towards each other due to induced flow by the filaments. As seen in figure 4.2, this occurs at approximately $t_c^* \approx 1$ (approximately one revolution of the vortex pair) for all Re_Γ ratios. After this time, filaments are observed in the flows (figure 4.1a&b). However, the more asymmetric the vortex pair, the more the filamentation occurs on the weaker vortex side. Filamentation occurs when ω from the core and exchange band enters the outer-recirculation regions due to the combined action of diffusion and tilting of ω contours in the vicinity of the two outer hyperbolic points (figure 4.4). Once ω enters the outer-recirculation region, it is advected away by the flow in this region, thereby forming filaments. As noted in §4.2, the asymmetric pair contains an additional region just outside the exchange band on the outer side of the stronger vortex (figure 4.4b,d). This acts to buffer the stronger vortex from the nearby outer hyperbolic point. Any ω diffusing out from the exchange band in this region will be advected into the filament of the weaker vortex. This change in the flow structure allows the stronger vortex to retain its shape. In contrast, the

enhanced filamentation occuring on the side of the weaker vortex further promotes the deformation and erosion of the weaker vortex.

Although the weaker vortex experiences significant erosion and detrainment, as indicated by its departure from diffusive core growth (figure 4.3b), the separation distance does not correspondingly exhibit a significant decrease (figure 4.2) as in the convective/entrainment phase of the symmetric pair. This may be understood by considering the results from Huang (2005) who uses a vortex simulation method to track Lagrangian flow structures in a symmetric vortex pair. It is shown that the primary inward motion of the computed vortex is due to a "sheet-like" structure, emitted by the opposite vortex, which wraps around the computed vortex (see figure 7 in (Huang, 2005)). In the case of the asymmetric vortex pair, the weaker vortex will emit a sheet-like structure (detrainment) earlier in time. This relatively weak vorticity may wrap around the stronger vortex, but the associated induced flow on the stronger vortex is correspondingly weak and insufficient to result in significant motion.

If, within some time period, the stronger vortex also erodes sufficiently, then there will be some extent of mutual (reciprocal), but unequal, entrainment. This is observed in the simulations with $0.7 \leq Re_{\Gamma,2}/Re_{\Gamma,1} \leq 0.9$, where it is seen that the linear growth of the stronger core, $a^2_{\theta,1}(t)$, is eventually interrupted (figure 4.3a). However in these cases, the stronger vortex ultimately dominates (figure 4.1a&b) and entrains vorticity from the weaker vortex. We therefore consider the process as vortex *merger* since the result is an enhanced (compound) vortex. If significant erosion occurs in the weaker vortex before it is established in the stronger vortex (e.g., $Re_{\Gamma,2}/Re_{\Gamma,1} = 0.6$), the weaker vortex is destroyed leaving the stronger vortex to remain in the flow relatively unaffected (since there is no longer a significant source of external strain). In this case, merger does not occur.

We therefore consider a critical state for a given vortex to be associated with the establishment of core detrainment. If both vortices reach this state, there will be some degree of mutual entrainment which results in an enhanced vortex,

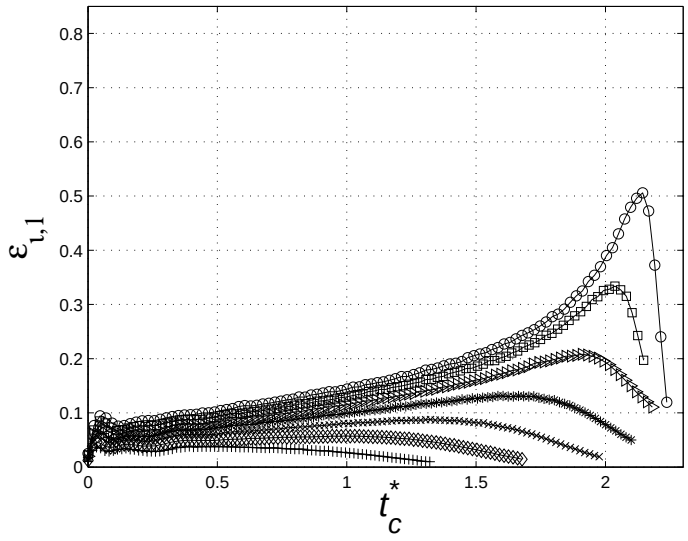

(a) Vortex 1

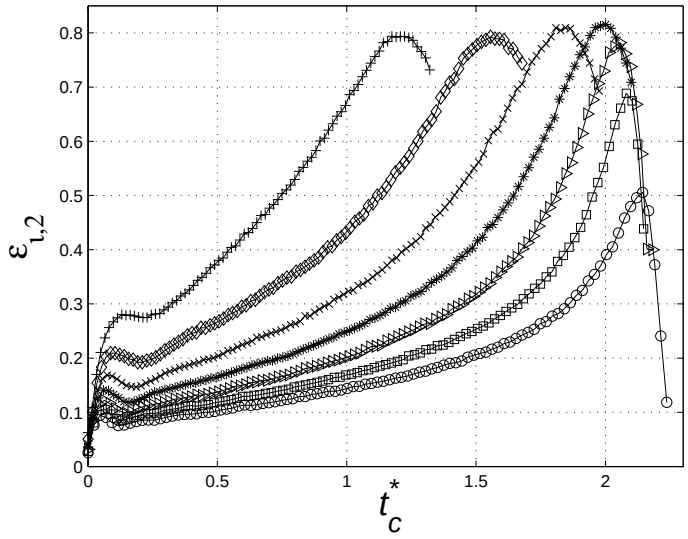

(b) Vortex 2

Figure 4.5: Time development of local eccentricity for each vortex, Symbols: $\circ$: $Re_{\Gamma,2}/Re_{\Gamma,1} = 1$, $\square$: $Re_{\Gamma,2}/Re_{\Gamma,1} = 0.9$, $\triangleright$: $Re_{\Gamma,2}/Re_{\Gamma,1} = 0.8$, $*$: $Re_{\Gamma,2}/Re_{\Gamma,1} = 0.7$, $\times$: $Re_{\Gamma,2}/Re_{\Gamma,1} = 0.6$, $\diamond$: $Re_{\Gamma,2}/Re_{\Gamma,1} = 0.5$, $+$: $Re_{\Gamma,2}/Re_{\Gamma,1} = 0.4$

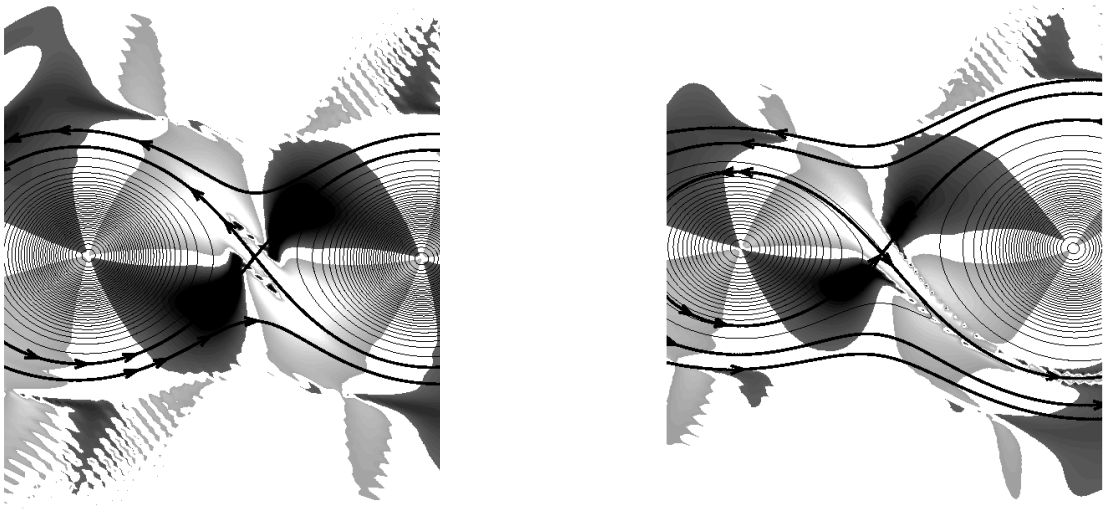

(a) $Re_{\Gamma,2}/Re_{\Gamma,1} = 1.0$ (b) $Re_{\Gamma,2}/Re_{\Gamma,1} = 0.6$

Figure 4.6: Vorticity contours with gray shading corresponding to $\bigtriangledown\omega$ production term, $P_s = -(\nabla\omega^T \mathsf{S} \nabla\omega)/|\nabla\omega|^2$ (light gray scale: $P_s > 0$, dark gray scale: $P_s < 0$) at $t_c^* = 0.32$.

i.e., convective merger will occur. Based on these ideas, we may now consider the development of a merging criterion.

4.4 Generalized merging criterion

From our analysis of results, a mean critical aspect ratio, $\frac{1}{2}(\frac{a_1+a_2}{b})$, is not expected to appropriately characterize the onset of merger in asymmetric vortex pairs and an alternative criterion is needed. As discussed above, we consider the critical state of a vortex to be associated with the establishment of core detrainment. Since the process is initiated by the interaction between S and $\bigtriangledown\omega$ in the vicinity of the CH point, we expect that it will proceed if the induced local strain rates are sufficiently high. We therefore consider one characteristic quantity to be

the strain rate at the CH point, S_{CH}. Furthermore, we expect significant core detrainment to occur if the vortex strength is relatively weak. A characteristic core vorticity is the maximum, ω_{v_i}. In order to relate the strain rate at the CH point, which has contributions from both vortices, to the maximum vorticity of the vortex, we normalize each quantity by a characteristic local strain rate,

$$S^*_{CH} = \frac{S_{CH}}{S_{CH,o}}, \quad \omega^*_{v_i} = \frac{\omega_{v_i}}{S_{v_i,o}} \tag{4.4}$$

This introduces appropriate scalings for these quantities. We may then define a strain parameter for vortex i,

$$\gamma_i(t) \equiv \left(\frac{S^*_{CH}(t)}{\frac{1}{2}\omega^*_{v_i}(t)} \right)^{1/2} \tag{4.5}$$

which is a measure of the relative strength of the induced strain rate at the CH point to the vortex strength. Figure 4.7 shows computed $\gamma_1(t)$ and $\gamma_2(t)$. We then consider the critical value of the vortex strain parameter to be the value at the critical time, $t_{cr,i}$, when core detrainment (and entrainment into exchange band) is established, i.e., $\gamma_{cr,2} = \gamma_2(t_{cr,2})$ and $\gamma_{cr,1} = \gamma_1(t_{cr,1})$. As discussed in the previous section, this also corresponds to the time at which the departure from viscous core growth occurs. From the data of figures 4.3 and 4.7, we obtain: $\gamma_{cr,1} \approx 0.249 \pm 0.003$ and $\gamma_{cr,2} \approx 0.245 \pm 0.005$. The values are within the range of error. We therefore find a *single value for the critical strain parameter*,

$$\gamma_{cr,1} \approx \gamma_{cr,2} \approx \gamma_{cr} = 0.247 \pm 0.007\,. \tag{4.6}$$

To test the generality of (4.6), additional simulations were performed for different initial aspect ratios, varying both core size and strengths. Resulting values for γ_{cr} are within the range given in (4.6). We note that data for cases in which the initial flow condition is near or beyond the critical state, e.g., $Re_{\Gamma,2}/Re_{\Gamma,1} \lesssim 0.5$, are excluded from (4.6), as will be discussed below.

We now further consider the strain parameter, and in particular γ_2, through a scaling analysis. Prior to significant vortex interaction, S_{CH} is proportional to

the local external strain rate and ω_{v_i} is proportional to the ratio of Γ_i and $a^2_{\omega,i}$,

$$S_{CH} \propto \frac{\Gamma_1}{2\pi d^2_{|CH-V1|}} + \frac{\Gamma_2}{2\pi d^2_{|CH-V2|}}, \qquad \omega_{v_i} \propto \frac{\Gamma_i}{\pi a^2_{\omega,i}}. \tag{4.7}$$

We thereby have the following scaling for the nondimensional strain rate and vorticity,

$$\begin{aligned} S^*_{CH} &= \frac{S_{CH}}{S_{CH,o}} \propto \left[\frac{\Gamma_2}{\Gamma_{2,o}}\right]\left[\frac{d^{*2}_{|CH-V2|,o}}{d^{*2}_{|CH-V2|}}\right]\left[\frac{1+\frac{Re_{\Gamma,1}}{Re_{\Gamma,2}}\frac{d^{*2}_{|CH-V2|}}{d^{*2}_{|CH-V1|}}}{1+\frac{Re_{\Gamma,1}}{Re_{\Gamma,2}}\frac{d^{*2}_{|CH-V2|,o}}{d^{*2}_{|CH-V1|,o}}},\right] \\ \omega^*_{v_i} &= \frac{\omega_{v_i}}{S_{v_i,o}} \propto \left[\frac{\Gamma_i}{\Gamma_{1,o}}\right]\left[\frac{2}{a^{*2}_{\omega,i}}\right]. \end{aligned} \tag{4.8}$$

Note that in the equation above, the approximation was made that $\frac{\Gamma_2}{\Gamma_1} = \frac{\Gamma_{2,o}}{\Gamma_{1,o}} = \frac{Re_{\Gamma,2}}{Re_{\Gamma,1}}$. This relationship, as well as the scaling in (4.7), holds reasonably well up to the critical state of the weaker vortex. The strain parameter for the weaker vortex may then be related to the Re_Γ ratio along with a_ω and $d_{|CH-V_i|}$, which is the distance from the maximum vorticity of vortex i to the CH point (§4.2),

$$\gamma_2(t) \equiv \left(\frac{S^*_{CH}}{\frac{1}{2}\omega^*_{v_2}}\right)^{1/2} = \left(\left[\frac{S_{CH}}{\frac{1}{2}\omega_{v_2}}\right]\left[\frac{d^{*2}_{|CH-V2|,o}}{\frac{Re_{\Gamma,2}}{Re_{\Gamma,1}}}\right]\left[\frac{1}{1+\frac{Re_{\Gamma,1}}{Re_{\Gamma,2}}\frac{d^{*2}_{|CH-V2|,o}}{d^{*2}_{|CH-V1|,o}}}\right]\right)^{1/2} \tag{4.9}$$

$$\propto a^*_{\omega,2}\left[\frac{Re_{\Gamma,1}}{Re_{\Gamma,2}}\right]^{1/2}\left[\frac{d^*_{|CH-V2|,o}}{d^*_{|CH-V2|}}\right]\left(\frac{1+\frac{Re_{\Gamma,1}}{Re_{\Gamma,2}}\frac{d^{*2}_{|CH-V2|}}{d^{*2}_{|CH-V1|}}}{1+\frac{Re_{\Gamma,1}}{Re_{\Gamma,2}}\frac{d^{*2}_{|CH-V2|,o}}{d^{*2}_{|CH-V1|,o}}}\right)^{1/2}. \tag{4.10}$$

This gives the following scaling for the critical strain parameter for the weaker vortex,

$$\gamma_{cr,2} = f\, a^*_{\omega,2}(t^*_{cr,2})\left[\frac{Re_{\Gamma,1}}{Re_{\Gamma,2}}\right]^{1/2}\left[\frac{d^{*2}_{|CH-V2|,o}}{d^{*2}_{|CH-V2|}(t^*_{cr,2})}\right]\left(\frac{1+\frac{Re_{\Gamma,1}}{Re_{\Gamma,2}}\frac{d^{*2}_{|CH-V2|}(t^*_{cr,2})}{d^{*2}_{|CH-V1|}(t^*_{cr,2})}}{1+\frac{Re_{\Gamma,1}}{Re_{\Gamma,2}}\frac{d^{*2}_{|CH-V2|,o}}{d^{*2}_{|CH-V1|,o}}}\right)^{1/2}. \tag{4.11}$$

where f is a proportionality constant. In the case of a *symmetric vortex pair*, this equation reduces to

$$\left(\frac{S^*_{CH}(t^*_{crit})}{\frac{1}{2}\omega^*_{v_2}(t^*_{crit})}\right)^{1/2} = \left(\frac{S_{CH}(t^*_{crit})}{4\omega_{v_i}(t^*_{crit})}\right)^{1/2} = f\frac{a^*_\omega(t^*_{crit})}{2d^*_{|CH-V|}(t^*_{crit})} = f\left(\frac{a_\omega}{b}\right)_{crit}. \tag{4.12}$$

Thus, the strain parameter for $Re_{\Gamma,1}/Re_{\Gamma,2} = 1$ is directly related to the critical aspect ratio. As stated earlier, for the weaker vortex core, $\gamma_{cr,2} \approx 0.245 \pm 0.005$, and the corresponding proportionality factor is found to be, $f \approx 1.05 \pm 0.03$. This compares well with previously determined values for the critical aspect ratio for symmetric vortex merger. In §3.1 it was found that $(a_\omega/b)_{crit} \approx 0.23$ where $\gamma_{cr,2}/f \approx 0.233 \pm 0.005$.

We note that a corresponding scaling analysis (4.11) for the stronger vortex strain parameter, $\gamma_{cr,1}$, cannot be carried out. In general, when (if) the stronger vortex reaches the critical state, significant changes may have occurred for the weaker vortex and the associated strain field and scaling for S_{CH} are no longer straightforward. We also noted earlier that data for $Re_{\Gamma,2}/Re_{\Gamma,1} \lesssim 0.5$ is not included in the determination of the critical strain parameter in (4.6). Recall that the lower the Re_Γ ratio, the closer the CH point is to the weaker vortex (4.3). From (4.9), the critical weaker vortex core size for $Re_{\Gamma,2}/Re_{\Gamma,1} = 0.5$ is $a^*_{\omega,2}(t^*_{cr,2}) \approx 0.163$, which is close to the initial value of $a^*_o = 0.157$ (initial aspect ratio). Therefore, for $a_{\omega,o}/b_o = 0.157$ and $Re_{\Gamma,2}/Re_{\Gamma,1} \lesssim 0.5$, the weaker vortex is close to or beyond the critical state and is quickly destroyed.

As discussed in §4.3, for an asymmetric vortex pair, convective merger will occur if both vortices reach the critical state. The critical state of the weaker vortex is achieved earlier, when $\gamma_2(t) = \gamma_{cr,2}$. From figure 4.7b it is observed that $\gamma_1(t)$ eventually reaches its critical value for $Re_{\Gamma,2}/Re_{\Gamma,1} \gtrsim 0.7$. However, in the case of $Re_{\Gamma,2}/Re_{\Gamma,1} = 0.6$, $\gamma_1(t)$ does not achieve the critical value and, correspondingly, $a_{\theta,1}$ does not deviate from linear viscous growth (figure 4.3a). Core detrainment is not established by the stronger vortex and convective merger does not occur in this case.

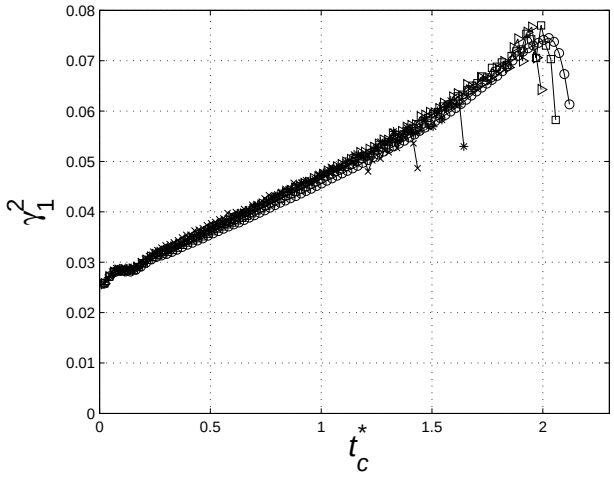

(a)

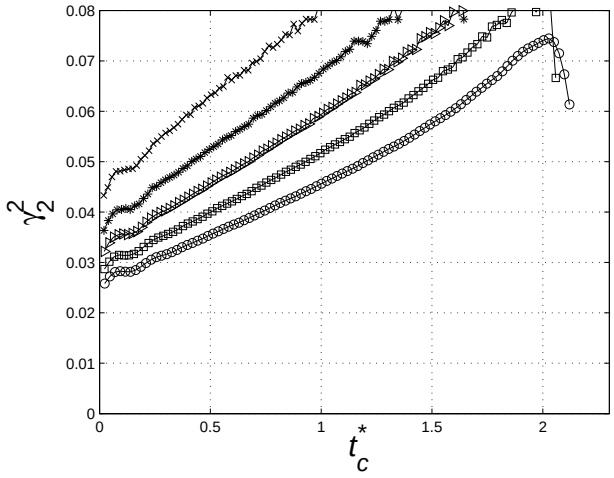

(b)

Figure 4.7: Time development of the strain parameter, γ_i, for (a) vortex 1 and (b) vortex 2. Symbols: $\circ$: $Re_{\Gamma,2}/Re_{\Gamma,1} = 1$, $\square$: $Re_{\Gamma,2}/Re_{\Gamma,1} = 0.9$, $\triangleright$: $Re_{\Gamma,2}/Re_{\Gamma,1} = 0.8$, $*$: $Re_{\Gamma,2}/Re_{\Gamma,1} = 0.7$, $\times$: $Re_{\Gamma,2}/Re_{\Gamma,1} = 0.6$

4.5 Classification of vortex interactions

From our viscous flow simulations in §4.3, several distinct vortex interactions/flow regimes are observed for the asymmetric pair. We may characterize these interactions based on the timing of key processes: weaker vortex core detrainment, stronger vortex core detrainment, and weaker vortex destruction. Figure 4.8 shows these process times (scaled by convective timescale) as a function of the Re_Γ ratio. The observed interactions may be identified in terms of the relative timing of these processes. We first consider each of the times separately.

The time required for the weaker vortex to reach the critical state ($\gamma_2(t) = \gamma_{cr}$), $t^*_{cr,2}$ ($\Box$ in figure 4.8), is seen to increase linearly with respect to the Re_Γ ratio. As stated earlier, $t^*_{cr,2}$ is evaluated in the simulations as the time of departure from viscous core growth. Based on the scaling analysis in the previous section (§4.4), $t^*_{cr,2}$ can then be estimated through the right hand side of (4.11) and using the viscous growth relation in terms of a_ω,

$$a^2_{\omega,2} \;=\; c^2_{\omega,2}\,\nu\,t + \,a^2_{\omega,o} \tag{4.13}$$

For symmetric vortex pairs, it was found that $c_\omega = 2.11$ (§3.1) for a large range of Re_Γ and that the resulting behavior was similar to that of a single vortex. However, in the asymmetric vortex pairs, the weaker vortex core growth differs (figure 4.3b) and the growth rate is found to scale with the rotation rate, $c^2_{\omega,2} = 2.11^2\sqrt{.5(1 + Re_{\Gamma,2}/Re_{\Gamma,1})}$. The resulting equation is of the form,

$$t^*_{cr,2} \;\approx\; \left(\left[\frac{\gamma^2_{cr}}{f^2}\right]\left[\frac{Re_{\Gamma,2}}{4c^2_{\omega,2}\pi^2}\right] g \;-\; \left[\frac{a^{*2}_{\omega,o}Re_{\Gamma,1}}{4c^2_{\omega,2}\pi^2}\right]\right)\left[1 + \frac{Re_{\Gamma,2}}{Re_{\Gamma,1}}\right]. \tag{4.14}$$

where the factor, g is defined as,

$$g \;=\; \left[\frac{d^{*2}_{|CH-V2|}(t^*_{cr,2})}{d^{*2}_{|CH-V2|,o}}\right]\left[\frac{1 + \frac{Re_{\Gamma,1}}{Re_{\Gamma,2}}\frac{d^{*2}_{|CH-V2|,o}}{d^{*2}_{|CH-V1|,o}}}{1 + \frac{Re_{\Gamma,1}}{Re_{\Gamma,2}}\frac{d^{*2}_{|CH-V2|}(t^*_{cr,2})}{d^{*2}_{|CH-V1|}(t^*_{cr,2})}}\right] \tag{4.15}$$

In general, the precise behaviors of $d^*_{|CH-V1|}(t)$ and $d^*_{|CH-V2|}(t)$ are complex. However we find that the changes are not substantial. Based on the simulation results,

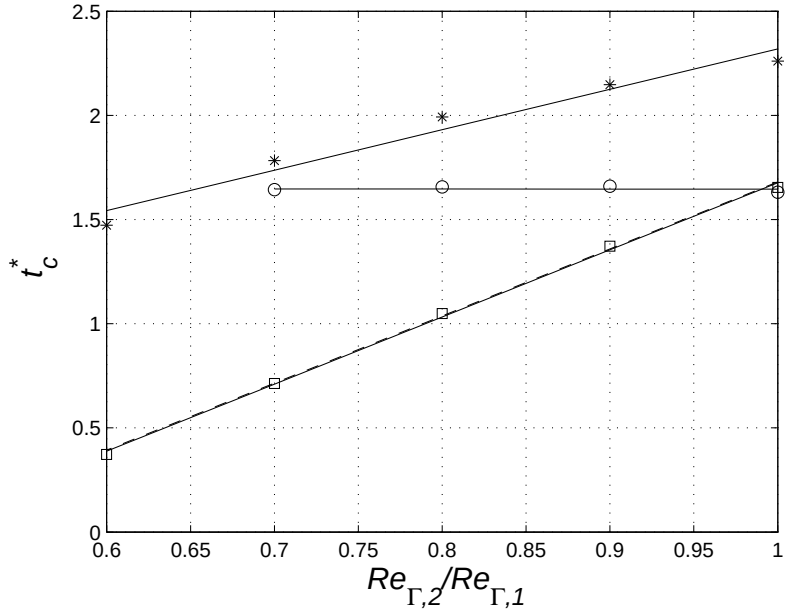

Figure 4.8: Process times (scaled by convective timescale) corresponding to □: $t^*_{cr,2}$ weaker vortex detrainment, ∘: $t^*_{cr,1}$ stronger vortex detrainment, ∗: $t^*_{de,2}$ weaker vortex destruction.

we evaluate $g \approx 0.985 \pm 0.008$. Using this approximation in (4.14) gives the resulting prediction for $t^*_{cr,2}$, which is represented by the dashed line in figure 4.8. As indicated, the relation effectively predicts the time for weaker vortex core detrainment. This also corroborates our scaling analysis in §4.4.

The time at which the stronger vortex reaches the critical state, $t^*_{cr,1}$ (∘ in figure 4.8), appears to be independent of Re_Γ ratio. Therefore, this critical time may be defined based on the case of symmetric merger. Using (4.13) and (4.12), we obtain,

$$t^*_{cr,1} = [Re_{\Gamma,1} + Re_{\Gamma,2}]\left[\frac{a^{*2}_{\omega,1} - a^{*2}_{\omega,o}}{4c^2_{\omega,1}\pi^2}\right] \approx Re_{\Gamma,1}\frac{(\gamma_{cr}/f)^2 b^{*2}_{sym} - a^{*2}_{\omega,o}}{4c^2_{sym}\pi^2} \approx 1.65 \pm 0.02. \tag{4.16}$$

We note that unlike the weaker vortex, the stronger vortex core growth is not dependent on rotation rate, $c_{\omega,1} \approx 2.11$.

The final process time considered is the time characterizing the destruction of the weaker vortex, $t^*_{de,2}$ ($*$ in figure 4.8). In the present analysis, the weaker vortex is considered to be destroyed when its core vorticity no longer dominates over the imposed strain rate field. An indicator of this is the second invariant of the velocity gradient tensor, $II = (\boldsymbol{\omega}^2/2 - \mathsf{S}^2)/2$. Thus, we estimate the destruction time, $t^*_{de,2}$, when the local value of II at the vorticity maximum, II_{V2}, is very small. The values shown in figure 4.8, correspond to $II_{V2} = 0.05II_{V1,0}$. Although this is a highly simplified characterization of vortex destruction, it serves the purposes of the present analysis.

We now formulate a classification scheme for the observed vortex interactions in §4.3, We define the interactions based on modifications of the classifications previously developed for inviscid asymmetric vortex interactions (Trieling et al., 2005; Dritschel and Waugh, 1992). Based on our analysis, we classify our simulations in terms of three interactions: complete merger, partial merger, and straining-out. These are characterized as follows,

- *Complete merger* ($Re_{\Gamma,2}/Re_{\Gamma,1} = 1.0$): detrainment from both vortices, mutual entrainment of the cores transforms the flow into a single vortex. ($t^*_{cr,2} \approx t^*_{cr,1} < t^*_{de,2}$).

- *Partial merger* ($Re_{\Gamma,2}/Re_{\Gamma,1} = 0.9, 0.8, 0.7$): detrainment from both vortices, weaker vortex is destroyed and entrained by the stronger vortex ($t^*_{cr,2} < t^*_{cr,1} < t^*_{de,2}$).

- *Strained-out* ($Re_{\Gamma,2}/Re_{\Gamma,1} \leq 0.6$): detrainment from weaker vortex only, weaker vortex is destroyed ($t^*_{cr,2} < t^*_{de,2} < t^*_{cr,1}$).

These interactions all eventually result in a single vortex for which the circulation *may* differ from that of the initial vortices. In complete merger, the circulation of

the final compound vortex increases. This increase is due to the mutual entrainment of both vortices and the transformation into a single vortex. The concept of partial merger in a viscous fluid is not as clear as in inviscid interactions. In the cases considered, vorticity is detrained from both vortices. However, the weaker vortex is destroyed before the stronger vortex is significantly eroded. Ultimately, the stronger vortex dominates and is enhanced by the entrained vorticity from the weaker vortex. The interaction thus yields a compound vortex with increased circulation. In the flows in which the weaker vortex is strained out, there is no mutual entrainment. The stronger vortex remains but its circulation may not be significantly changed. These interactions do not yield a compound vortex and thus merger does not occur.

4.6 Summary

The interaction of two unequal co-rotating vortices in a viscous fluid has been investigated using two-dimensional numerical simulations. The vortices considered have the same initial core size and different strengths. In the simulations presented, the initial aspect ratio is fixed at $a_0/b_0 = 0.157$. The initial strength of the stronger vortex is given by $Re_{\Gamma,1} = 5000$ and the initial strength of the weaker vortex is varied such that $0.4 \leq Re_{\Gamma,2}/Re_{\Gamma,1} \leq 1.0$.

The primary physical mechanisms of vortex interaction and merging are identified and described. We consider the flow in the co-rotating frame and describe the deformation of the vortices in terms of the interaction of vorticity gradient, $\nabla\omega$, and rate of strain, S. In particular, the processes occuring in the vicinity of the central hyperbolic (CH) point are key in understanding the behavior of the flow.

With unequal strengths, i.e., asymmetric pairs, the difference in vortex strengths alters the flow structure and interaction. The variation in local timescales may be such that the vortices no longer experience the flow processes simultane-

ously. As in the symmetric vortex pair, the vortices initially grow by diffusion. The deformation rates are stronger at the weaker vortex due to the difference in induced S, and the tilt of ω contours and subsequent core detrainment occurs earlier than the stronger vortex. However, the dominant attracting motion occurs only when, *and if*, core detrainment is established by the stronger vortex. If this occurs, then there will be some extent of mutual (reciprocal), but unequal, entrainment. This is observed in the present simulations for $0.7 \leq Re_{\Gamma,2}/Re_{\Gamma,1} \leq 0.9$. In these cases, the stronger vortex ultimately dominates and entrains vorticity from the weaker vortex. We therefore consider the process as vortex *merger* since the result is an enhanced compound vortex. If core detrainment is not established by the stronger vortex before significant erosion occurs in the weaker vortex ($Re_{\Gamma,2}/Re_{\Gamma,1} \leq 0.6$), the weaker vortex is destroyed leaving the stronger vortex to remain in the flow relatively unaffected. In this case, merger does not occur.

A generalized merging criterion for unequal vortices is developed. We consider the critical state for a given vortex to be associated with the establishment of core detrainment. A vortex strain parameter, γ_i, is defined in terms of the ratio of the strain rate at the CH point, S_{CH}, to the maximum vorticity of vortex i, ω_{v_i}, thereby providing a measure of the relative strength of the induced strain rate at the CH point to the vortex strength. We then consider the critical value of γ_i to be the value at the critical time, $t_{cr,i}$, when core detrainment (and entrainment into exchange band) is established, i.e., $\gamma_{cr,2} = \gamma_2(t_{cr,2})$ and $\gamma_{cr,1} = \gamma_1(t_{cr,1})$. The onset of merging is associated with the joint achievement of the critical strain by both vortices. For all our simulations, we find a single critical value for both vortices, i.e., $\gamma_{cr,1} = \gamma_{cr,2} = \gamma_{cr} \approx 0.247 \pm 0.007$. In the case of equal vortices, the critical strain rate is shown to be related to the critical aspect ratio. From the present results, $\gamma_{cr,2}/f \approx 0.233 \pm 0.005$, which compares well with previously determined values for the critical aspect ratio for symmetric vortex merger.

From our viscous flow simulations, three distinct vortex interactions are observed for the asymmetric pair. We define the interactions based on modifi-

cations of the classifications previously developed for inviscid asymmetric vortex interactions (Trieling et al., 2005; Dritschel and Waugh, 1992). However, here we characterize the interactions based on the timing of key processes: weaker vortex core detrainment ($t_{cr,2}$), stronger vortex core detrainment ($t_{cr,1}$), and weaker vortex destruction ($t_{de,2}$). We consider *complete merger* to occur if both vortices reach γ_{cr} and are mutually entrained prior to vortex destruction ($t^*_{cr,2} \approx t^*_{cr,1} < t^*_{de,2}$). The flow is transformed into a single compound vortex in which the final circulation is increased due to the contribution of both vortices. We consider *partial merger* to occur when both vortices reach γ_{cr}, however, the weaker vortex is destroyed before the stronger vortex is significantly eroded ($t^*_{cr,2} < t^*_{cr,1} < t^*_{de,2}$). Ultimately, the stronger vortex dominates and is enhanced by the entrained vorticity from the weaker vortex. The interaction thus yields a compound vortex with increased circulation. We consider flows in which the weaker vortex is *strained out* when only the weaker vortex core is detrained ($t^*_{cr,2} < t^*_{de,2} < t^*_{cr,1}$). There is no mutual entrainment. The stronger vortex remains but its circulation may not be significantly altered. These interactions do not yield a compound vortex and thus merger does not occur.

Chapter 4, in part, is a reprint of the material as it appears in *Journal of Fluid Mechanics* submitted. Brandt, L.; Nomura, K., Cambridge University Press, 2008. The dissertation author was the primary investigator and author of this paper.

Chapter 5

Symmetric co-rotating vortex pairs and the generation of vorticity (weakly stratified)

This chapter expands upon the study conducted in chapter 3, where the merging process of a co-rotating vortex pair was studied in an unstratified environment. In this chapter, the effect of weak stratification on the merging process is taken under consideration. The range of Reynolds number considered, $2000 \leq Re_{\Gamma} \leq 5000$, which is comparable to laboratory experiments (Meunier and Leweke, 2001). The Froude numbers considered are $Fr = 2,\ 3,$ and 5, which cover a range of conditions corresponding to relatively strong ($Fr = 2$), moderate ($Fr = 3$) and weak ($Fr = 5$) stratification. In general however, stratification is not a dominating effect in the flows considered ($Fr > 1$), and vortex merger will result. In flows with lower Fr, stratification will hinder fluid motion and/or result in significant internal waves. Such flows are taken into consideration in chapters 6 & 7. The case of $Fr = \infty$ corresponding to an unstratified flow is also considered for comparison.

The discussion of results is organized as follows. First, the general flow

development is examined in §5.1. This is followed by a discussion of baroclinic torque, which is prevalent in stratified fluids (§5.2). Then, utilizing the same framework in which the unstratified study was conducted (chapter 3), the effects of stratification on the mechanism of merger (§5.3) and the relationship between strain and vorticity (§5.4) is investigated. A generalized description of the merging process is then developed (§5.5) and the effects of Reynolds number are considered (§5.6). We conclude with a brief summary of results in §5.7.

5.1 Flow behavior and development

Figures 3.1 and 5.1 show time sequences of vorticity contours illustrating the basic development of unstratified ($Fr = \infty$) and stratified ($Fr = 3$) flows, respectively, for $Re_\Gamma = 5000$. In both flows, due to the mutually induced velocity, the two vortices rotate about each other in the counter-clockwise direction. Before merging is initiated, the rate of rotation is nearly equal to that of a two point vortex system, $\Gamma/\pi b^2$.

As discussed in chapter 3, the unstratified flow (figure 3.1) develops as observed in previous studies. Early in time, the vortices grow due to viscous diffusion and adjust to the induced strain field. As time increases, deformation becomes more significant in the areas of low level vorticity, where filaments are formed and the vorticity contours tilt (center of rotation). The major axes of the vortices tilt with respect to the connecting line of the vortices. This leads to the vortex centers rapidly moving towards and around each other resulting in merger. In time, the two maxima eventually disappear by viscous diffusion. A single vortex is established.

In the stratified flow (figure 5.1), as the vortex pair rotates, it stirs the stably stratified ambient fluid. After approximately half a revolution, opposite signed vorticity appears at the periphery of the outer recirculation regions (figure 5.1c, $t_c^* = 0.78$). This is due to baroclinic torque generation as will be discussed

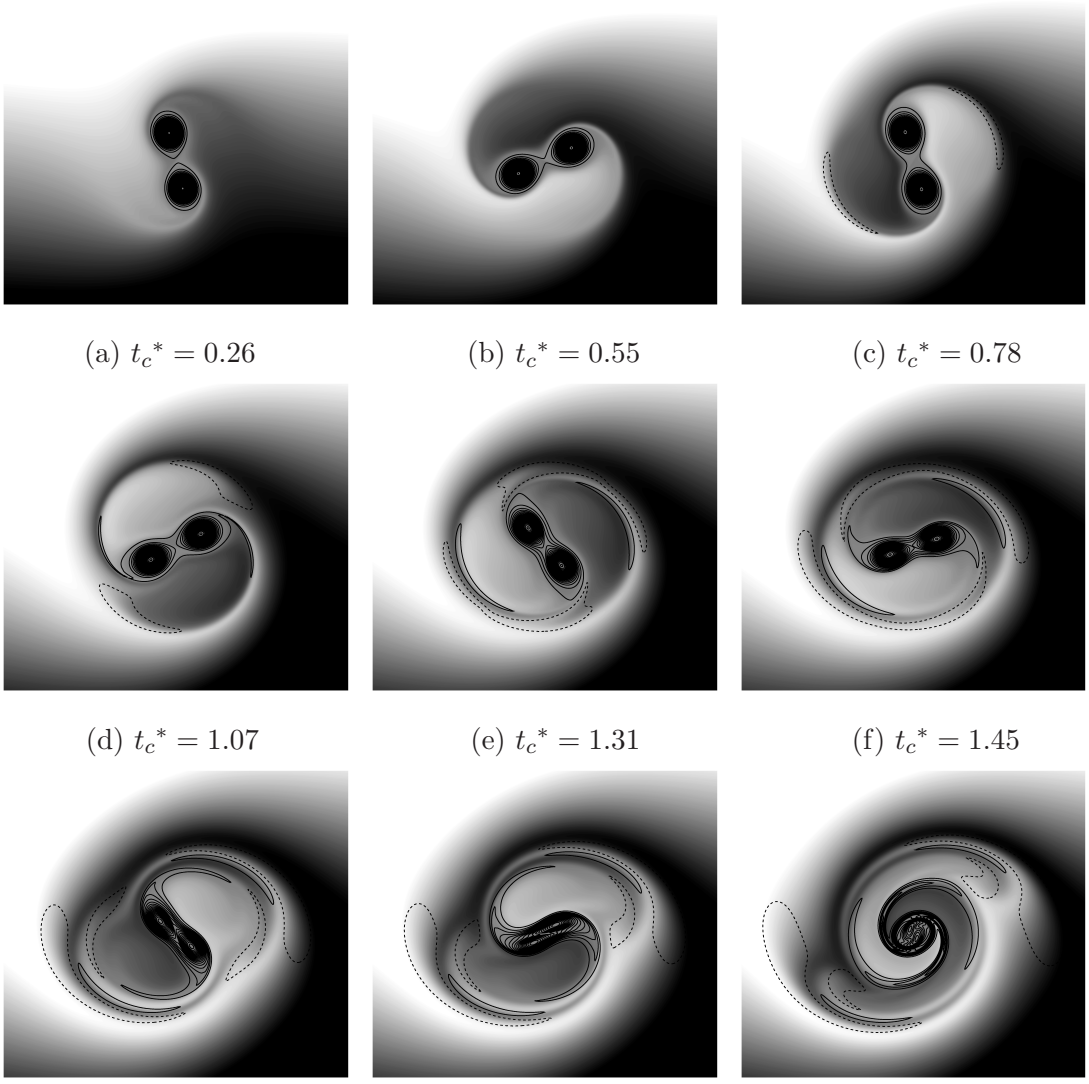

(a) $t_c{}^* = 0.26$ (b) $t_c{}^* = 0.55$ (c) $t_c{}^* = 0.78$

(d) $t_c{}^* = 1.07$ (e) $t_c{}^* = 1.31$ (f) $t_c{}^* = 1.45$

(g) $t_c{}^* = 1.69$ (h) $t_c{}^* = 1.78$ (i) $t_c{}^* = 1.97$

Figure 5.1: Vorticity contours (solid line: $\omega > 0$, dash line: $\omega < 0$) superimposed on density field (shading) for $Re_\Gamma = 5000$, $Fr = 3$.

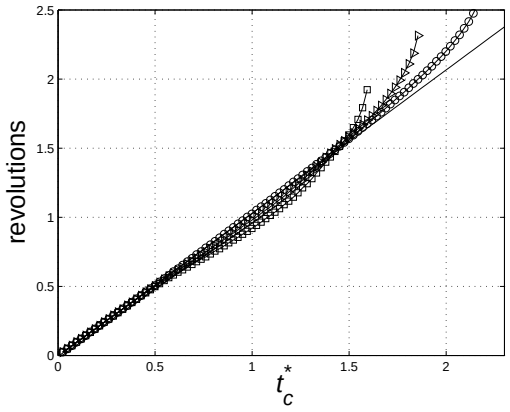

Figure 5.2: Revolutions versus time for $Re = 5000$. Symbols: $\circ$: $Fr = \infty$, $\triangleright$: $Fr = 3$, $\square$: $Fr = 2$.

in §5.2. There is a slight decrease in the rate of rotation of the vortex pair (figure 5.2). Later in time (figure 5.1d, ${t_c}^* = 1.07$), both opposite-signed vorticity and same-signed vorticity occur just outside and within the outer-recirculation regions. Filamentation and tilting of the primary vortices, and the motion of the vortices towards each other all occur earlier in time (figure 5.1e, ${t_c}^* = 1.31$) than in unstratified flow. At late times (figure 5.1g-i, ${t_c}^* \geq 1.69$), the structure of the vorticity field is more complex and consists of alternating signed vorticity patches and filaments. Some reduction in the vertical scale of the flow is also observed.

When looking at the flow separation distance (figure 5.3a; $Fr = 2, 3$), a slight increase in b^* is initiated at approximately $t^* = 0.5$ for stratified flow, followed by an earlier decrease as compared with the $Fr = \infty$ flow. The rate of increase and initial decrease in $b^*(t)$ is greater with increased stratification ($Fr = 2$). In both stratified flows, the rapid linear decrease in $b^*(t)$ exhibits nearly the same slope as that of the unstratified flow. Overall, convective effects and merger, as indicated by $b^*(t)$, occur earlier in the stratified flows. From figure 5.3b, we see that the initial development of $a_\omega^2(t)$ is linear. However, since a_ω^2 is evaluated by integration of ω which includes generated vorticity (figure 5.1), it does not solely describe the growth by viscous diffusion during this time. In contrast, the quantity

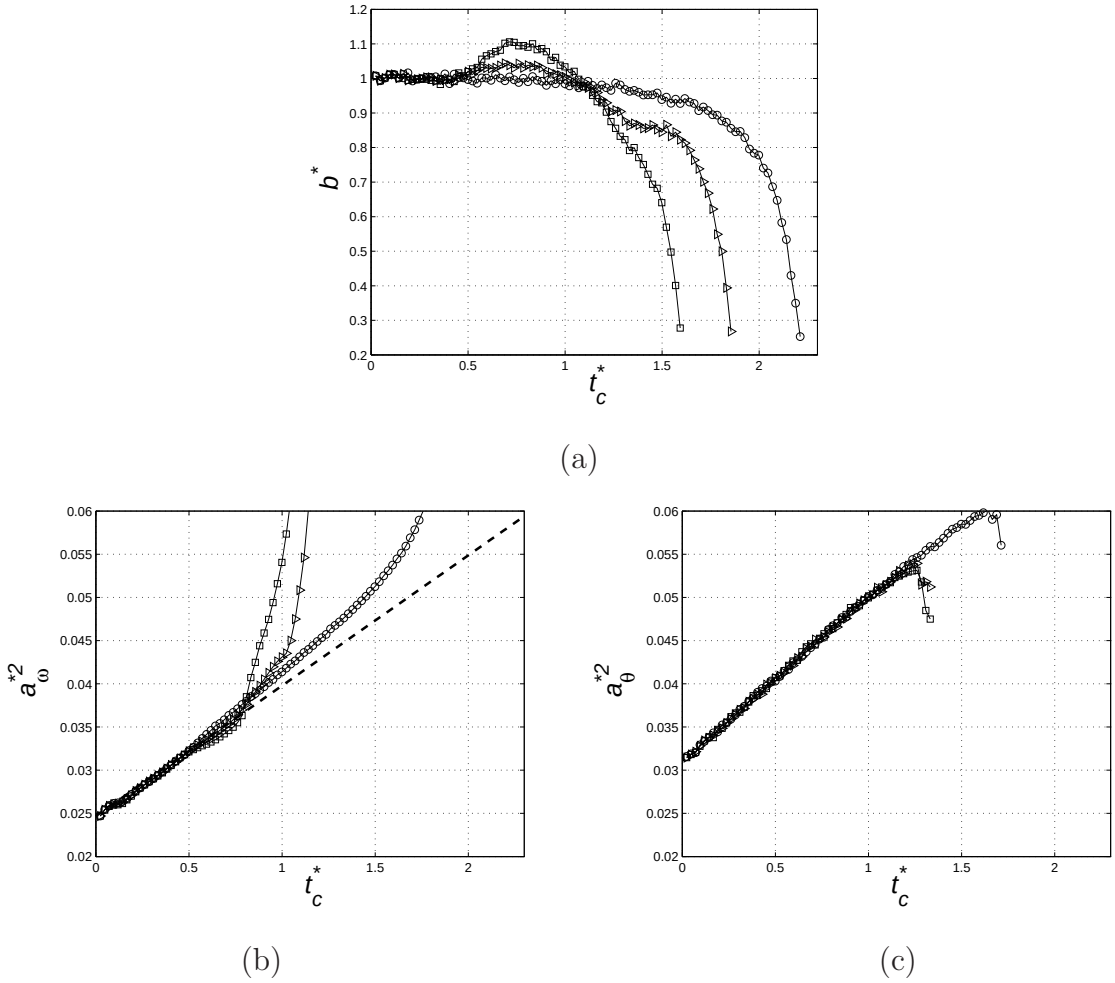

Figure 5.3: Time development of (a) separation distance, $b^*(t) = b(t)/b_o$, (b) core size evaluated by second moment, $a_\omega^2(t)/b_o^2$, (c) core size evaluated by maximum azimuthal velocity, $a_\theta^2(t)/b_o^2$. The dashed line in (b) corresponds to (5.1) where $c' = c_\theta/1.12 = 1.94$. Symbols: $\circ$: $Fr = \infty$, $\triangleright$: $Fr = 3$, $\square$: $Fr = 2$.

$a_\theta^2(t)$ in figure 5.3c does not have this ambiguity and is used here to indicate the core growth in stratified flow. From figure 5.3c, we observe that $a_\theta^2(t)$ grows linearly and with the same growth rate as that in unstratified flow, as expected since they have the same Re_Γ. Note that the dashed line in figure 5.3b corresponds to:

$$a^2 \;=\; \left(\frac{c_\theta}{1.12}\right)^2 \nu t \,+\, {a_o}^2 \;\;=\; {c'}^2 \nu t \,+\, {a_o}^2 \tag{5.1}$$

where $c' = 1.94$ based on the above results and $(a_o/b_o) = 0.157$ (a_o based on a_ω). This allows us to evaluate an *effective* a^2 for stratified flows that is consistent with the defined a_o (to be used in §5.6). As also observed in figure 5.3c, $a_\theta^2(t)$ indicates deviation from linear behavior earlier in the stratified flows, and it occurs at approximately the same time, $t_c{}^* \approx 1.25$, for both $Fr = 3$ and $Fr = 2$. From the results in figure 5.3, we find that $b^*(t)$ and $a^*(t)$ show convective effects initiating at different times. Thus, the evaluation of a critical aspect ratio and the demarcation of the first diffusive phase and convective phase are unclear. These issues will be considered in the following sections and resolved in §5.6. As in the unstratified flow, the convective phase terminates when b reaches approximately $0.2b_o$ and the second diffusive phase allows for the final reduction in $b^*(t)$ (see figure 5.11).

5.2 Baroclinic torque generation

We first consider the basic physics of the stratified flow. As observed in figure 5.1, additional vorticity develops in the flow. As the vortex pair rotates, it stirs the stably stratified ambient fluid and establishes horizontal density gradients, $\partial\rho'/\partial x$, which generates vorticity through baroclinic torque, as described by the last term in the vorticity equation for two-dimensional flow,

$$\frac{\partial\omega}{\partial t} \,+\, (\boldsymbol{v}\cdot\nabla)\omega \;=\; \nu\nabla^2\omega \,+\, \frac{1}{\rho_o}\nabla\rho' \times \mathbf{g}\,, \tag{5.2}$$

where $\mathbf{g} = (0, -g)$ is the gravitational acceleration. Plots are presented showing vorticity contours superimposed on the associated baroclinic torque (figure 5.4) for $Fr = 3$ at the same times in figure 5.1.

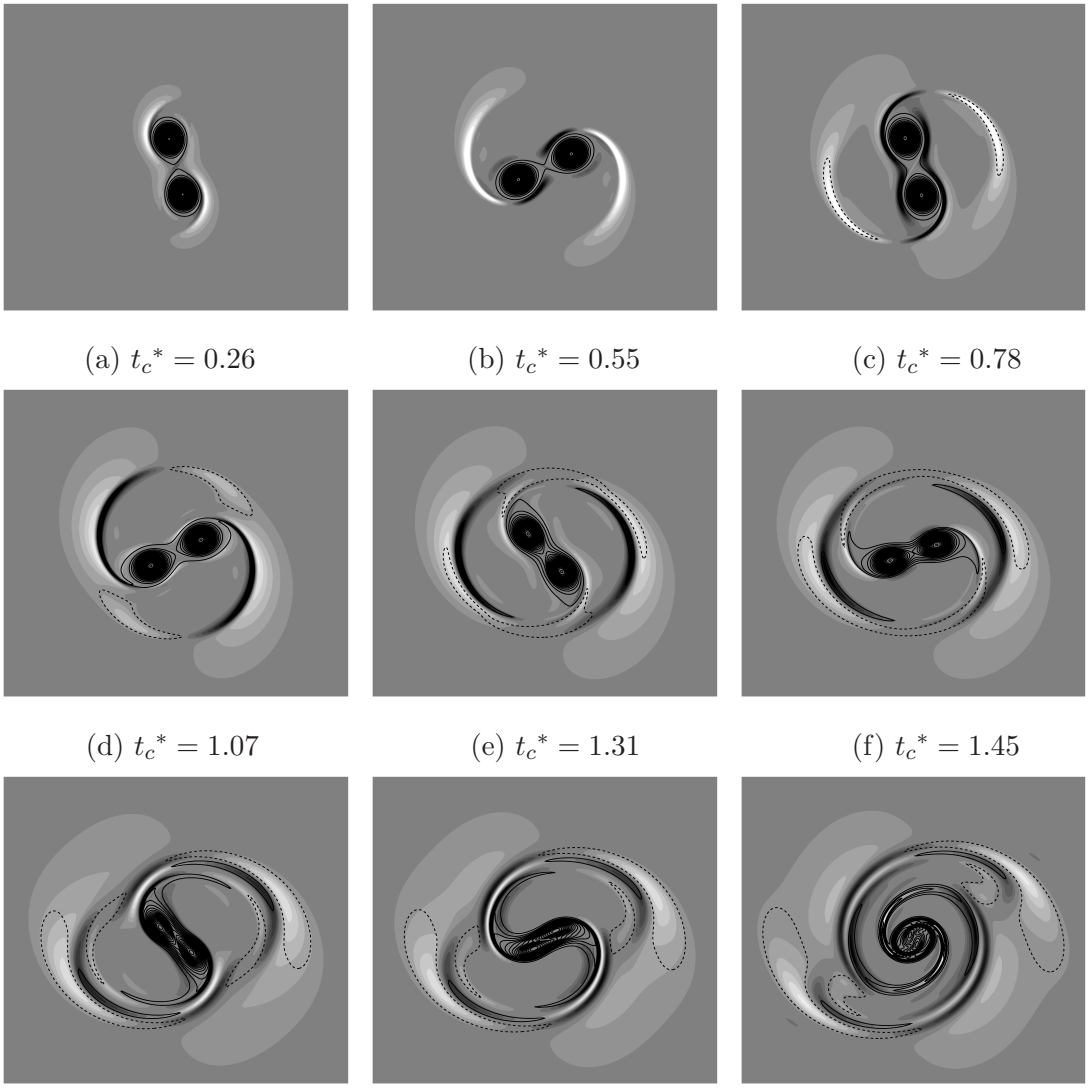

(a) $t_c{}^* = 0.26$ (b) $t_c{}^* = 0.55$ (c) $t_c{}^* = 0.78$

(d) $t_c{}^* = 1.07$ (e) $t_c{}^* = 1.31$ (f) $t_c{}^* = 1.45$

(g) $t_c{}^* = 1.69$ (h) $t_c{}^* = 1.78$ (i) $t_c{}^* = 1.97$

Figure 5.4: Vorticity contours (lines) superimposed on baroclinic torque, $\nabla\rho' \times \mathbf{g}/\rho_o$ (dark shading: positive, light shading: negative), for $Re_\Gamma = 5000$, $Fr = 3$.

As indicated in figure 5.1, after approximately a quarter rotation and then another half a rotation beyond (figure 5.1a-c, $t_c{}^* = 0.26 - 0.78$), the vortex pair establishes significant $\partial\rho'/\partial x$ at its periphery, thereby resulting in negative baroclinic torque on the left and right sides of the pair (figure 5.4a-c). As indicated at the later time (figures 5.1c, 5.4c; $t_c{}^* = 0.78$), this results in *opposite-signed baroclinically generated vorticity*, OSBV, which forms at the boundary of the outer recirculation regions. After three-quarters rotation ($t_c{}^* = 0.78$), we also observe significant $\partial\rho'/\partial x$ at the periphery of the primary cores due to fluid that is entrained into the outer recirculation regions (figures 5.1). The presence of this entrained fluid leads to a layer of *same-signed baroclinically generated vorticity*, SSBV, just inside the previous OSBV after the completion of one full revolution (figures 5.1d, 5.4d; $t_c{}^* = 1.07$). The SSBV is extended as the vortex pair continues its rotation, thereby establishing same-signed ω, filament-like structures (figures 5.1e, 5.4e; $t_c{}^* = 1.31$). Note that filamentation of primary ω is also occuring. This is observed in the vorticity contours in figures 5.1f,g and 5.4f,g in which ω from the primary cores is entering into the outer recirculation region. At later times, continued stirring of ρ results in successive generation of $\partial\rho'/\partial x$ resulting in layers of alternate-signed baroclinic torque (figure 5.4i, $t_c{}^* = 1.97$).

5.3 Physical Mechanisms

As indicated in figure 5.3a, merging is completed earlier in stratified flows, although $b^*(t)$ exhibits a more complex development. The contributions to the change in b^* of each of the flow regions are shown in figure 5.5. Here, the outer recirculation region is subdivided into two regions: (a) OSBV and (b) filaments and SSBV (i.e., same-signed $\boldsymbol{\omega}$ is considered together).

The OSBV (figure 5.5a) causes the vortices to initially move apart after half a rotation ($t_c^* \approx 0.5$). After $t_c{}^* \approx 0.78$, the vortices then move together until $t_c^* \approx 1.45$, approximately half a revolution later, at which time they begin

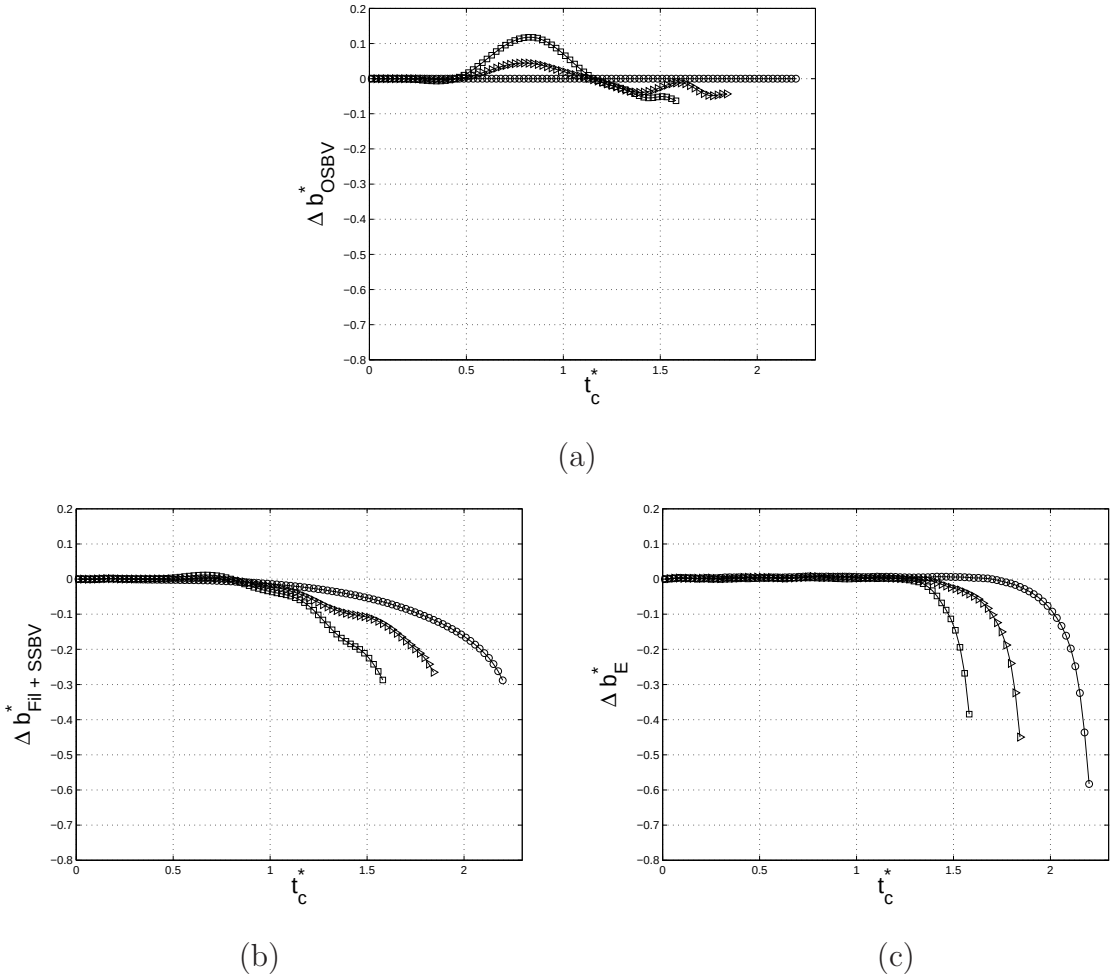

Figure 5.5: Contribution of flow regions to separation distance development, $\Delta b^*_{region}(t)$, for $Re_\Gamma = 5000$, $Fr = \infty, 3, 2$: (a) opposite-signed baroclinically generated vorticity (OSBV), (b) same-signed baroclinically generated vorticity (SSBV) and filaments, (c) exchange band (Symbols: $\circ$: $Fr = \infty$. $\triangleright$: $Fr = 3$. $\square$: $Fr = 2$).

to move apart again. As observed in figures 5.1 and 5.4, OSBV forms arches at the lower left and upper right peripheral regions that are nearly stationary as the vortex pair rotates. The resulting spatial distribution causes the induced motion to vary with the rotation as described. Beyond the first complete revolution, the behavior is more complex as additional layers of OSBV are formed (figures 5.4, 5.5; $t_c^* > 1.45$). With increased stratification ($Fr = 2$), the magnitudes of OSBV are greater thereby increasing the amplitude of the corresponding induced velocity and contribution to $b^*(t)$. However, the frequency of the contribution is unchanged since baroclinic torque depends on the rotation of the vortex pair.

The SSBV, together with the filaments (figure 5.5b), contributes to a decrease in b^*. The induced motion of same-signed ω in the outer-recirculation region is initiated at nearly the same time ($t_c{}^* \approx 1$) in both the stratified and unstratified flows. However, the presence of the additional vorticity, i.e. the SSBV, enhances the motion and thereby the *rate of decrease* in $b^*(t)$, the effect being stronger with increased stratification ($Fr = 2$).

The exchange band contribution (figure 5.5c) occurs earlier in time in the stratified flows. From the vorticity contour plots for $Fr = \infty$ and $Fr = 3$ flows (figures 3.1d, 5.1d; $t_c^* = 1.07$), we see that a slight tilt in the lowest level ω contour near the origin appears at an early time in both flows. At the subsequent time (figures 3.1e, 5.1e; $t_c^* = 1.31$), the tilt is diminished in the unstratified flow while it is maintained in the stratified flow. This causes the exchange band process to proceed earlier in time.

From figure 5.5c, we see that while the exchange band process in stratified flows initiates earlier than in unstratified flow, the slope of the rapid decrease is not significantly altered by stratification indicating that the same physics is associated with this process, i.e., core entrainment is not significantly influenced by stratification in the considered flows.

Figure 5.6 shows the induced flow fields of the OSBV and the filaments and SSBV for the $Fr = 3$ flow. The OSBV induced flow (figure 5.6a-c) resembles

that of the filaments, but exhibits a cyclic behavior with respect to its direction, consistent with the results in figure 5.5a. As the plotted streamlines indicate, this influences both the magnitude and the relative orientation of the strain rate in the vicinity of the center of rotation. The flow induced by the filaments and SSBV combined (figure 5.6d-f) is similar to that of solely filaments in unstratified flow (figure 3.6b,e). The induced flow by the exchange band (not shown) is similar to that of unstratified flow (figure 3.6c,f). Note that although the tilt in ω contours is established earlier in time ($t_c^* = 1.31$), a reduction in the tilt is observed at a later time ($t_c^* = 1.45$) in this flow. This is also indicated by the strain orientation in figure 5.10.

5.4 Influence of strain and vorticity on vortex merger

The development of the tilt in the ω contours is now considered. Recall the unstratified discussion in §3.3 where the equation for $|\nabla\omega|^2$ is give by (3.4), $P = -\nabla\omega^T \mathsf{S}\, \nabla\omega$ and $P_s = P/|\nabla\omega|^2$. The equation for $|\nabla\omega|^2$ in stratified flow is,

$$\frac{D\frac{1}{2}|\nabla\omega|^2}{Dt} \;=\; -\nabla\omega^T \mathsf{S}\, \nabla\omega \;+\; \nu\nabla\omega^{\mathsf{T}}\nabla^2\nabla\omega \;+\; \frac{1}{\rho_o}\nabla\omega^{\mathsf{T}}\nabla\left(\nabla\rho' \times \mathbf{g}\right) \qquad (5.3)$$

in which there is an additional term associated with the gradient of baroclinic torque. However, in the central region of the flow, it is not expected to be significant in comparison with P, and evaluation of this term confirms this. Figure 5.7 shows the P_s field for the $Fr = 3$ flow. At $t_c^* = 1.31$ (figure 5.7a), we observe the same basic features as in the unstratified flow (figure 3.7). However, higher values of $P_s > 0$ are observed consistent with the establishment of the tilt at this earlier time. At $t_c^* = 1.45$ (figure 5.7b), there is an enhancement of regions of $P_s < 0$ in the central region associated with the reduction in the tilt. The time development of $\langle P \rangle$ for the central region is given in figure 5.8. In the stratified flows, a slight decrease to negative values is observed at $t_c^* \approx 0.5$ followed by an increase to

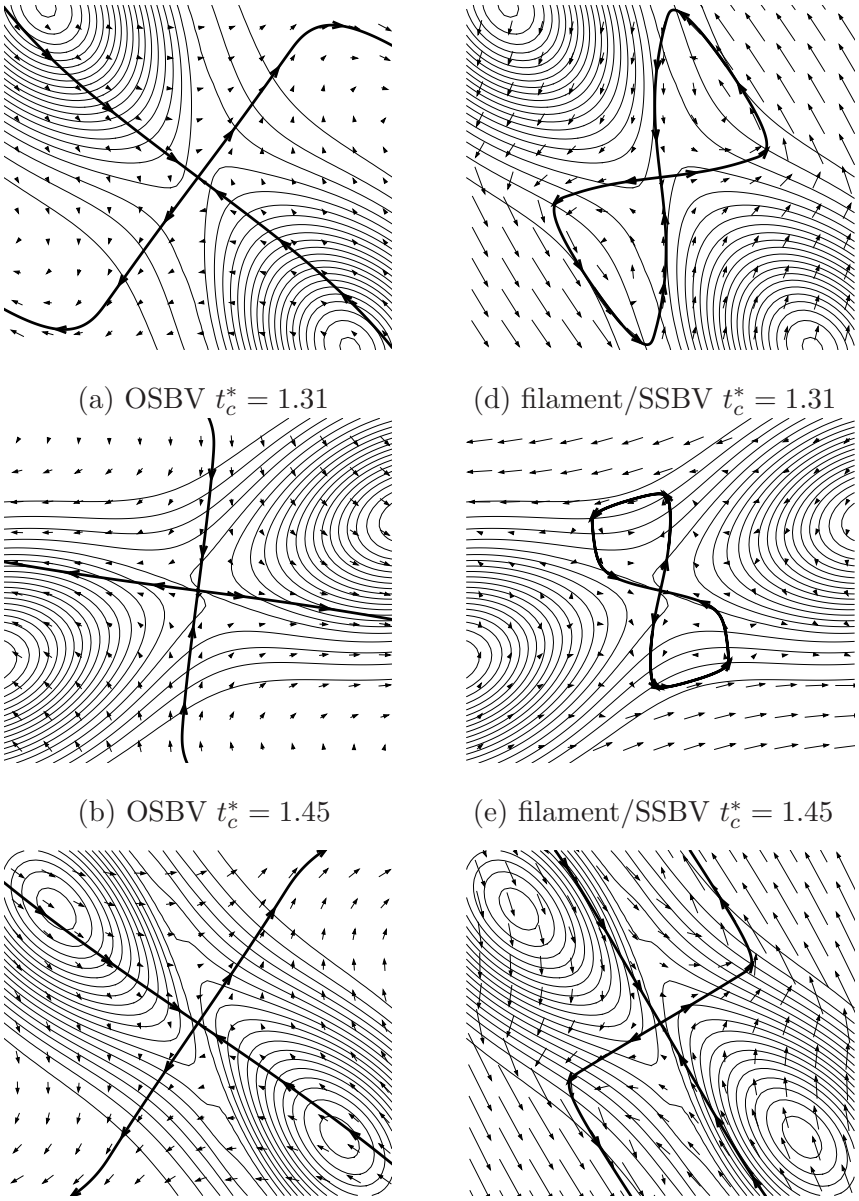

(a) OSBV $t_c^* = 1.31$ (d) filament/SSBV $t_c^* = 1.31$

(b) OSBV $t_c^* = 1.45$ (e) filament/SSBV $t_c^* = 1.45$

(c) OSBV $t_c^* = 1.69$ (f) filament/SSBV $t_c^* = 1.69$

Figure 5.6: Vorticity contours (thin solid lines) superimposed with vectors of the induced velocity field of the indicated flow regions for $Re_\Gamma = 5000$, $Fr = 3$ at (a),(d) ${t_c}^* = 1.31$, (b),(e) ${t_c}^* = 1.45$, (c),(f) ${t_c}^* = 1.69$. The dark solid line represents the induced flow streamline which passes through the center hyperbolic point.

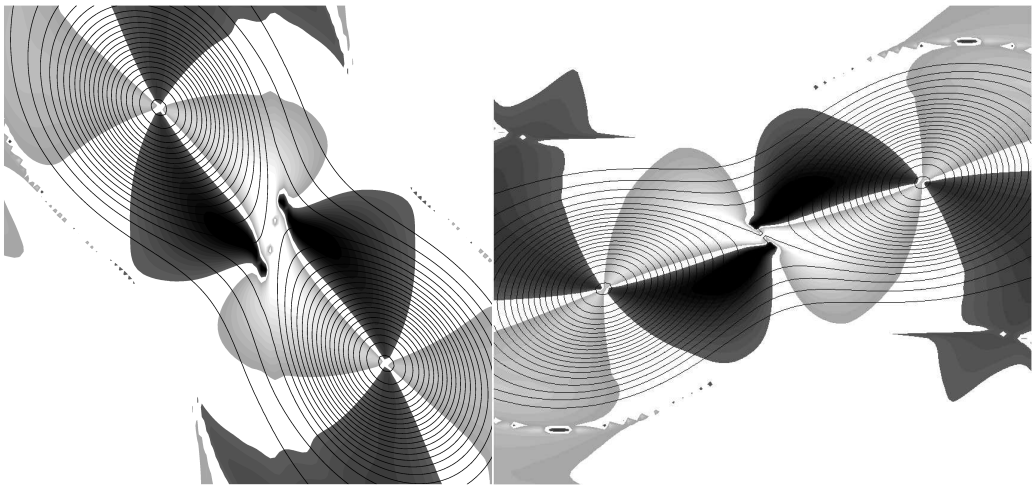

(a) $t_c{}^* = 1.31$ (b) $t_c{}^* = 1.45$

Figure 5.7: Vorticity contours with gray shading corresponding to $|\nabla\omega|^2$ production term, $P_s = -(\nabla\omega^T \mathsf{S} \nabla\omega)/|\nabla\omega|^2$ (light gray scale: $P_s > 0$, dark gray scale: $P_s < 0$), for $Re_\Gamma = 5000$, $Fr = 3$, (a) $t_c{}^* = 1.31$, (b) $t_c{}^* = 1.45$.

predominantly positive values for $t_c{}^* > 0.75$. For $t_c{}^* > 1$, the rate of increase in $\langle P \rangle$ is greater than that of the unstratified flow. This results in the earlier development of the tilt and subsequent exchange band process. Note that there is a marked difference between the two stratified cases. In the $Fr = 3$ flow, $\langle P \rangle$ exhibits a sharp dip, while in the $Fr = 2$ flow, $\langle P \rangle$ continues to increase. The reduction in $\langle P \rangle$ for $Fr = 3$ corresponds with the observed reduction in tilt (figure 5.7b; $t_c{}^* = 1.45$). Beyond $t_c{}^* \approx 1.5$, $\langle P \rangle$ resumes its rapid increase.

The behavior of $\langle P \rangle$ is explained by considering both the magnitude and orientation of S. Time development of the local strain rate at the center of rotation is shown in figure 5.9a and indicates a reduction in magnitude during $0.5 < t_c{}^* < 0.78$, followed by an increase until $t_c{}^* \approx 1.5$. Prior to core entrainment, the induced strain is directly related to changes in the separation distance and generally follows

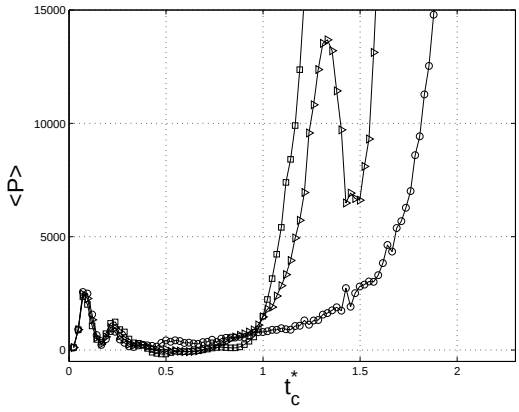

Figure 5.8: Time development of $\langle P \rangle = -\langle \nabla\omega^T \mathsf{S}\, \nabla\omega \rangle$ in the central region for $Re_\Gamma = 5000$ (Symbols: $\circ$: $Fr = \infty$. $\triangleright$: $Fr = 3$. $\square$: $Fr = 2$).

(3.3) as indicated by figure 5.9b. As the vortices move away from each other due to the OSBV ($0.5 < {t_c}^* < 0.78$), the strain at the center of rotation is reduced, and as they move towards each other ($0.78 \lesssim {t_c}^* \lesssim 1.35$), the strain is increased; the effect of OSBV on $\langle P \rangle$ is cyclic. Beyond $t_c^* \approx 1.35$ the OSBV has less of an effect, particularly in the $Fr = 2$ flow. This may be attributed to the greater extent of OSBV surrounding the vortex pair which results in some effective cancelation of the associated flow. Since the SSBV acts only to reduce $b^*(t)$, SSBV enhances the strain thereby resulting in higher strain in the stratified flows than that of the unstratified flow for ${t_c}^* > 1.1$ (figure 5.9a). Thus, the effect of SSBV is to promote $\langle P \rangle$. In the $Fr = 2$ flow, the strain magnitude continues to increase due to the OSBV, SSBV and exchange band induced flows until it exhibits a sharp drop due to core entrainment, which occurs earlier in time. In the $Fr = 3$ flow, while the SSBV enhances the strain, its induced radial velocity is much smaller than in the $Fr = 2$ flow and the OSBV counteracts this effect. The reduction in $b^*(t)$ is thereby delayed during $1.35 \lesssim {t_c}^* \lesssim 1.55$. Beyond this, the strain magnitude levels off before it drops as core entrainment occurs (figure 5.9a). This does not, however, fully explain the observed reduction in tilt at ${t_c}^* \approx 1.45$ in the $Fr = 3$

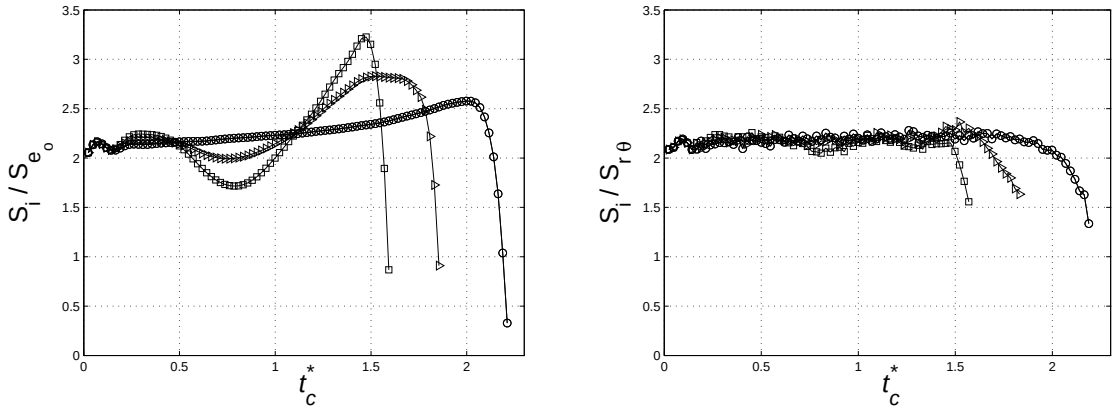

(a) (b)

Figure 5.9: Time development of the local strain rate, S_i, at the center of rotation normalized by the external strain rates (3.3) (a) $S_{eo} = S_{r\theta}(b/2, 0)$, (b) $S_{r\theta}(b/2, t)$. for $Fr = \infty$, 3, 2, $Re_\Gamma = 5000$ (Symbols: $\circ$: $Fr = \infty$. $\triangleright$: $Fr = 3$. $\square$: $Fr = 2$).

flow.

As indicated earlier, the induced flows (figure 5.6) also influence the orientation of S. As shown in figure 5.10, the orientation angle of the extensional strain at the center of rotation begins to decrease from 45° at approximately $t_c{}^* \approx 1$ and does so at a greater rate in the stratified flows than in the unstratified flow. Examination of figures 5.6a-c indicates that the induced flow of the OSBV rotates with respect to the vortex connecting line and thus has a cyclic influence on the strain rate orientation. In the $Fr = 3$ flow, for $1.0 \lesssim t_c{}^* \lesssim 1.35$, the induced flow enhances the reduction in the strain orientation angle while for $1.35 \lesssim t_c{}^* \lesssim 1.55$, it opposes the reduction. This explains the observed increase in the angle at $t_c{}^* \approx 1.45$ (figure 5.6b,e). The reduction in $\langle P \rangle$ during this time (figure 5.8b,e) and corresponding reduction in the tilt is associated with a reduced alignment between $\nabla\omega$ and the compressive strain (figure 5.10). However, beyond this time, the angle resumes its decrease until core entrainment occurs, at which point the strain angle sharply diverges as the flow becomes vorticity dominated. In both stratified

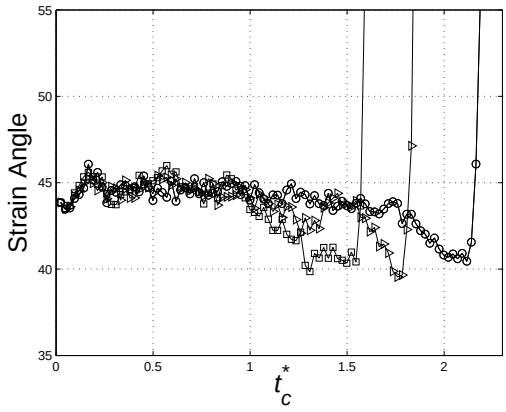

Figure 5.10: Time development of the angle between extensional strain eigenvector and vortex connecting line at the center of rotation for $Re_\Gamma = 5000, Fr = \infty, 3, 2$ (Symbols: $\circ$: $Fr = \infty$. $\triangleright$: $Fr = 3$. $\square$: $Fr = 2$).

flows, the rotation of the strain axes is such to generally promote the alignment of the compressive strain and $\nabla\omega$ thereby increasing P and enhancing the gradient amplification process. As illustrated by this process, the interaction of $\nabla\omega$ and S is complex. While local S interacts directly with $\nabla\omega$, through both its magnitude and relative orientation, both local and nonlocal ω will feedback on S.

5.5 Flow Phases

In summary, we describe vortex merging in the stratified flows in terms of the four phases of development presented in §3.4. This is illustrated in figure 5.11. The diffusive/deformation phase begins as in unstratified flow; however, it is interrupted by an earlier convective/deformation phase due to baroclinically generated vorticity. Essentially, the OSBV and SSBV play a similar role to that of the filaments, i.e., the induced flow advects the vortices thereby modifying S, which in general may hinder or enhance the gradient amplification process. In the flows considered, the combined effects of the enhanced magnitude and change

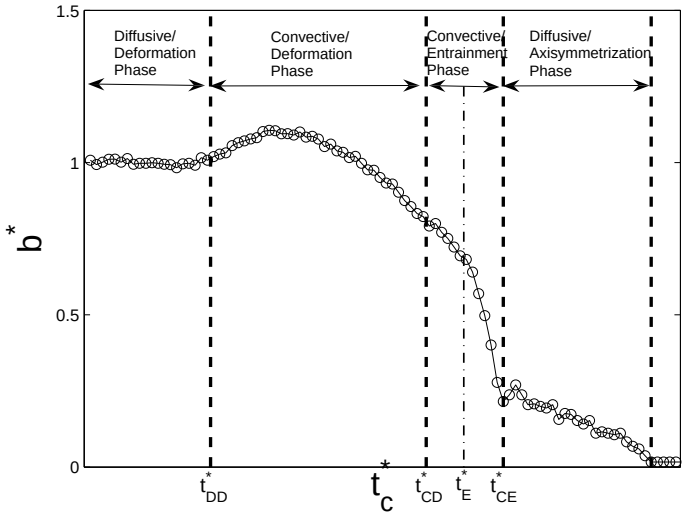

Figure 5.11: Diagram illustrating four phases of merging process with respect to the development of $b^*(t)$ for $Re_\Gamma = 5000$, $Fr = 2$ ($t^*_{DD} = 0.49$, $t^*_{CD} = 1.32$, $t^*_E = 1.46$, $t^*_{CE} = 1.62$).

in orientation of S by OSBV and SSBV leads to a more rapid development of the tilt in ω contours and subsequent exchange band process. In general, the effects of both OSBV and SSBV depend on the rotation of the vortex pair and are cyclic. Thus, their implication on the merging process will depend on the relative time and stage of flow development that they appear. This issue will be considered in the following section. Once the core entrainment process is initiated, the convective/entrainment phase proceeds as in the unstratified flow.

5.6 Flow development and the effect of Re_Γ

We have developed a description of the vortex merging process in both unstratified and stratified flows in terms of four phases of development (figure 5.11) based on results for $Re_\Gamma = 5000$. We now further develop this description by more explicitly defining and delimiting the phases. In particular, we consider the

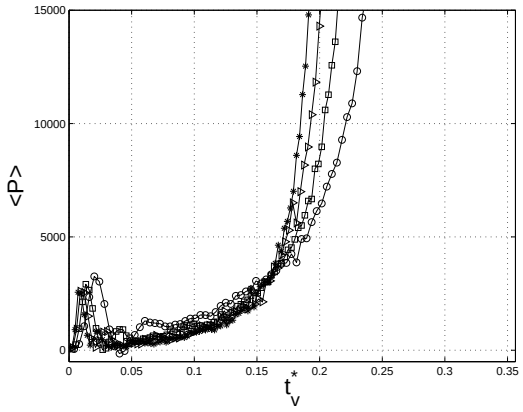

Figure 5.12: Time development of $< P >= - < \nabla\omega^T \mathsf{S} \nabla\omega >$ over central region for $Fr = \infty$ flows (Symbols: $\circ$: $Re_\Gamma = 2000$ $\Box$: $Re_\Gamma = 3000$, $\triangleright$: $Re_\Gamma = 4000$, $*$: $Re_\Gamma = 5000$).

determination of the critical aspect ratio. We also generalize the description for stratified flows by considering the effect of Re_Γ.

During the diffusive/deformation phase ($t_c{}^* < t^*_{\rm DD}$), $a^2_\theta(t)$ grows linearly by diffusion while $b(t)$ remains constant. As indicated in figure 5.3b, the growth of $a^2(t)$ is well described by (5.1) and the average growth rate for all our simulations, $2000 \leq Re_\Gamma \leq 5000$ and $Fr = \infty, 5, 3, 2$, is $c' = 1.94 \pm 0.05$. Physically, as the vorticity distribution spreads by diffusion, the induced strain field of each of the vortices correspondingly spreads and develops through their mutual interaction. The vortices adjust to the induced strain which results in deformation of the vorticity field. Thus, the interaction of $\nabla\omega$ and S is established by diffusion. This is indicated in figure 5.12 which shows the development of $\langle P \rangle$ plotted against time scaled by the diffusive time scale, t^*_v,

$$t^*_v \;=\; \frac{t}{t_v} \;=\; \frac{t_c}{t_v}\frac{t}{t_c} \;=\; \frac{8\pi^2}{(a_o/b_o)^2 Re_\Gamma}\; t_c{}^*\,, \tag{5.4}$$

for the unstratified flows at different Re_Γ. The diffusion rate of ω and S is higher for lower Re_Γ and the initial interaction is established earlier. Beyond the initial rapid adjustment from initial conditions, the behavior of $\langle P \rangle$ generally scales well

with t_v^* until $t_v^* \approx 1.1$ (figure 5.12). Beyond this time, convective effects become important and the higher Re_Γ flows exhibit a greater rate of increase in $\langle P \rangle$.

During the convective/deformation phase ($t_{\mathrm{DD}}^* \leq {t_c}^* < t_{\mathrm{CD}}^*$), $a_\theta^2(t)$ continues to grow linearly and $b(t)$ changes by advection. In unstratified flow, the change in $b^*(t)$ is due to filamentation. The induced flow by the filaments causes a relatively slow reduction in $b^*(t)$ and thus $(a/b_o)_{cr}$ will vary only slightly with Re_Γ. At the end of the convective/deformation phase, $t_c^* = t_{\mathrm{CD}}^*$, and $a_\theta^2(t)$ deviates from linear growth at $(a/b_o)_{cr} \approx 0.23$ (e.g., figure 5.3c) which we find to be nearly independent of Re_Γ. In stratified flow, OSBV and SSBV, together with the filaments, cause $b^*(t)$ to vary more significantly during the convective/deformation phase. The induced flow from OSBV and SSBV may advect the vortices, either away from or towards each other, thereby modifying S and hindering or enhancing, respectively, the development of the tilt in ω contours. In the stratified flows presented in §5.3, a greater rate of decrease in $b^*(t)$ leads to an earlier start of the exchange band process. However, in general, the effects of OSBV and SSBV may also separate the vortices, i.e., the merger process may, to some extent, be reversed. We therefore distinguish this convective process explicitly by this phase.

During the convective/entrainment phase ($t_{\mathrm{CD}}^* \leq {t_c}^* < t_{\mathrm{CE}}^*$), $a_\theta^2(t)$ no longer grows linearly (the ω field is significantly altered) and $b(t)$ significantly decreases as the vortex cores are eroded and entrained into the exchange band. In contrast to the convective/deformation processes, we consider erosion and entrainment to be irreversible. We now define the critical state of the flow to be the start of the exchange band process, beyond which there is no reversal and merging will occur. The corresponding time, t_{CD}^*, is marked by the initiation of the contribution to $b^*(t)$ from the exchange band, Δb_{E}^* (figure 5.5c). This is also comparable to the time $a_\theta^2(t)$ deviates from linear growth. The critical state is therefore characterized by the aspect ratio (a/b) at ${t_c}^* = t_{\mathrm{CD}}^*$ for which the corresponding values of $a(t)$ and $b(t)$ are thereby determined. In the stratified flows, an effective a is determined from (5.1) at ${t_c}^* = t_{\mathrm{CD}}^*$. For all flows considered, $2000 \leq Re_\Gamma \leq 5000$ and $Fr =$

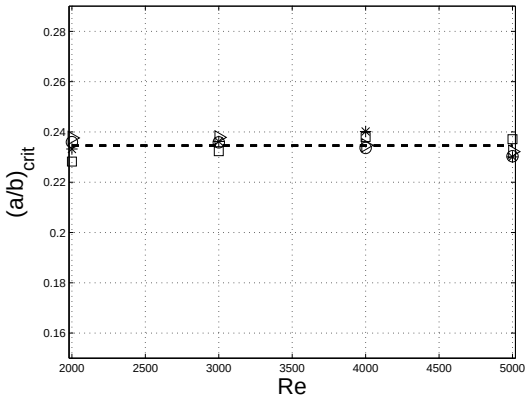

Figure 5.13: Critical aspect ratio, $(a/b)_{crit}$ according to (5.1), versus Re_Γ for different Fr. Dashed line represents the mean value, $(a/b)_{crit} \approx 0.235$ (Symbols: $\circ$: $Fr = \infty$, $*$: $Fr = 5$, $\triangleright$: $Fr = 3$, $\square$: $Fr = 2$).

$\infty, 5, 3, 2$, $(a/b)_{cr} = 0.235 \pm 0.006$ (figure 5.13). This is in agreement with the values $(a/b)_{cr} = 0.24 \pm 0.01$ reported by Meunier et al. (2002) for unstratified flow. As discussed earlier, the latter portion of the convective/entrainment phase is clearly marked by the rapid, nearly linear decrease in $b^*(t)$ due to the exchange band contribution, $\Delta b^*_{\rm E}$ (e.g., figure 5.5c). We consider a time, $t^*_{\rm E}$, as the effective start of core entrainment and defined by extending the linear portion of $\Delta b^*_{\rm E}$ to where it intersects with $\Delta b^*_{\rm E} = 0$. A plot of $\Delta b^*_{\rm E}$ versus $t_c{}^* - t^*_{\rm E}$ (figure 5.14) thereby overlays the exchange band process for the different Re_Γ and Fr flows. For all flows, the process proceeds at nearly the same rate. We therefore consider the core entrainment process, $t^*_{\rm E} < t_c{}^* < t^*_{\rm CE}$ (figure 5.11), to be independent of Re_Γ and Fr.

The merging time is therefore controlled by the processes prior to $t^*_{\rm E}$, which depend on Re_Γ, Fr, and the initial aspect ratio. Thus, for the a_o/b_o considered, $t^*_{\rm E} = t^*_{\rm E}(Re_\Gamma, Fr)$. Figure 5.15 shows $t^*_{\rm E}$ versus Re_Γ for various Fr. In unstratified flow, a linear dependence is exhibited, consistent with results of Meunier et al. (2002), and is due to the predominance of diffusion prior to the exchange band

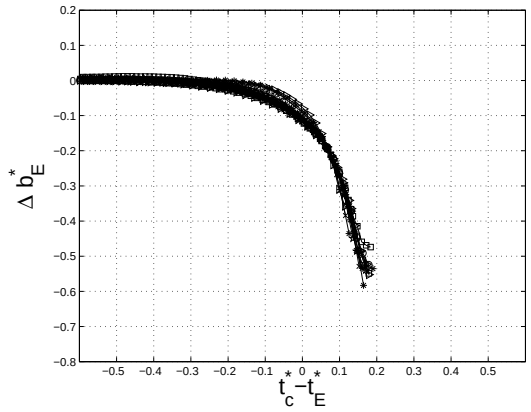

Figure 5.14: Exchange band contribution to separation distance development, $\Delta b_E^*(t)$, versus $t_c{}^* - t_{\mathrm{E}}^*$ for $Re_\Gamma = 2000, 3000, 4000, 5000$, $Fr = \infty, 5, 3, 2$.

process which is the dominant convective process. For the stratified flows, we see that there is a crossover Reynolds number ($Re_\Gamma \approx 2500$), above which convective merging is accelerated with respect to the unstratified flow at that Re_Γ, and below which merging is delayed. In stratified flow, convective effects (in the convective/deformation phase) become more significant due to the OSBV and SSBV. Since they arise due to the stirring of the density field by the co-rotating vortices, they have a timescale corresponding to the rotation, $t_c = 2\pi^2 {b_o}^2/\Gamma_o$, i.e., the turnover time. The effects of OSBV and SSBV will therefore depend on to what extent diffusion has developed the ω and S fields by the time OSBV/SSBV are generated. That is, for a given initial aspect ratio, the merging time in stratified flow will depend on the ratio of the diffusive time scale to the turnover time and hence, Re_Γ (5.4). From results of the unstratified flows, for $Re_\Gamma = 5000$, $t_{\mathrm{E}}^* = 2.02$ and for $Re_\Gamma = 2000$, $t_{\mathrm{E}}^* = 1.05$. Thus, the $Re_\Gamma = 5000$ flow rotates more than one revolution while the $Re_\Gamma = 2000$ flow just reaches one revolution prior to core entrainment. We may therefore expect their behaviors to differ with stratification. Results in figure 5.15 indicate that stratification accelerates merg-

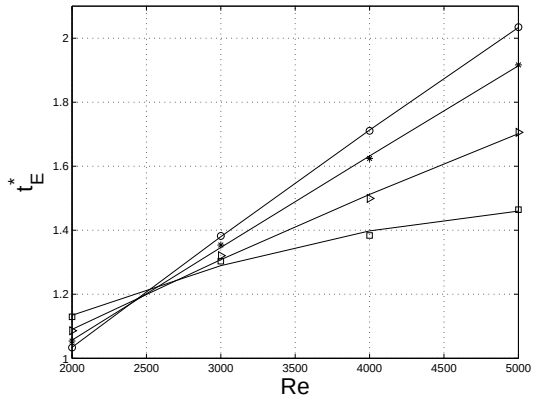

Figure 5.15: Effect of Re_Γ and stratification on merging time, t^*_E (Symbols:$\circ$: $Fr = \infty$, $\triangleright$: $Fr = 3$, $\square$: $Fr = 2$).

ing for $Re_\Gamma = 5000$ and delays merging for $Re_\Gamma = 2000$. In general, the Re_Γ dependency will be cyclic. The effects of OSBV and SSBV will also, of course, depend on their strength, and hence, Fr. Additionally, in the present study, we have considered only $a_o/b_o = 0.157$. In general, the crossover Reynolds number will vary with aspect ratio. As indicated by (5.4), the diffusion time will increase with smaller a_o/b_o. Additional simulation results (not shown) indicate a lower crossover Reynolds number for smaller a_o/b_o.

We now examine the $Re_\Gamma = 2000$ flow in which stratification delays merging. Figure 5.16a shows $b^*(t)$ for $Fr = \infty$, 3 and 2 and clearly indicates greater delay with increased stratification. Figure 5.16b-d shows the contribution of each flow region to $b^*(t)$. We observe that the OSBV (figure 5.16b) again acts to move the vortices apart during $0.5 \lesssim t_c{}^* \lesssim 0.8$, as in the $Re_\Gamma = 5000$ flow (figure 5.5). However, since this occurs near the end of the convective/deformation phase in this flow, the OSBV counteracts the initiation of convective/entrainment. Note that the amplitude of the OSBV contribution is reduced in comparison with that of $Re_\Gamma = 5000$ due to the increased diffusion of $\nabla\rho'$ (recall $Pr = 1$). In addition, since the core entrainment phase begins at approximately one full revolution, there

is little SSBV generated (figure 5.16c) to assist in the merging process. Figure 5.17 indicates that $\langle P \rangle$ is generally reduced with increasing stratification. As the OSBV moves the vortices apart during $0.5 < t_c{}^* < 0.8$, the magnitude of the strain decreases as it does in the $Re_\Gamma = 5000$. This affects and controls the behavior of $\langle P \rangle$ (figure 5.17). Since $\langle P \rangle$ is reduced in the stratified flows, the tilting of ω contours is delayed. The core entrainment process therefore initiates later in time (figure 5.16d).

The final phase of the merging process is the diffusive/axisymmetrization phase ($t_c{}^* > t^*_{\mathrm{CE}}$), during which $b(t)$ is reduced to zero and $a^2(t)$ eventually returns to linear growth for the single vortex. As stated earlier, this phase begins when b reaches approximately $0.20b_o - 0.25b_o$, at the end of the convective/entrainment phase at which point the inward velocities at the centroids are nearly zero. Although two ω maxima are still detected, inspection of the general flow structure shows that it is rotation dominated and essentially consists of a single vortex. Thus, we consider this final phase, which extends beyond the time at which $b^*(t)$ reaches zero, as a diffusion process in which the flow evolves towards axisymmetry. Details of this process are beyond the scope of this work.

5.7 Summary

The merging of a pair of symmetric, horizontally oriented vortices in a viscous fluid with and without stable stratification has been investigated using two-dimensional numerical simulations. The flow conditions considered consist of a fixed initial aspect ratio $a_o/b_o = 0.157$, a range of circulation Reynolds numbers $2000 \leq Re_\Gamma \leq 5000$, and a range of stratification levels given by Froude numbers, $Fr = \infty, 5, 3, 2$. All of these flows are dominated by convection and diffusion, not by stratification ($Fr > 1$), and merging always occurs. The stratification essentially introduces a disturbance to the merging process. By determining its effects, we have obtained further insight and understanding of the fundamental physics

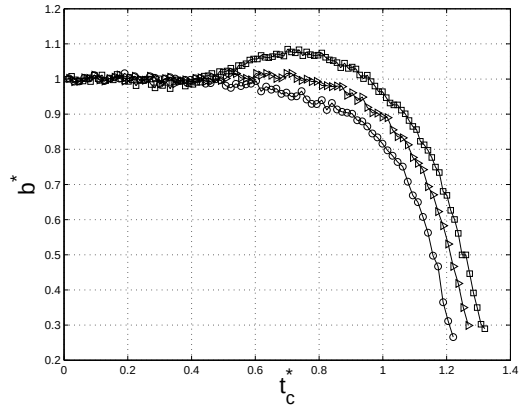

(a) Separation Distance

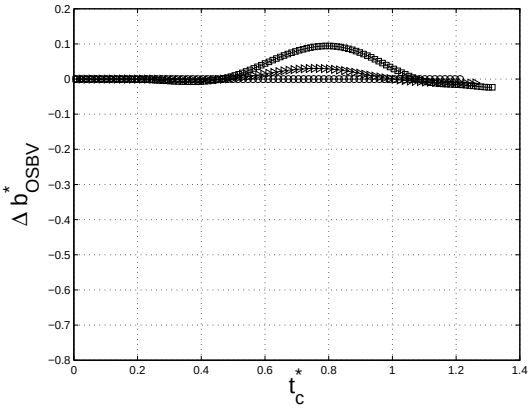

(b) OSBV

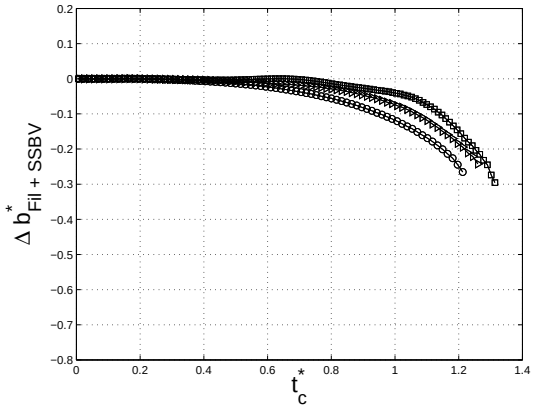

(c) SSBV and filaments

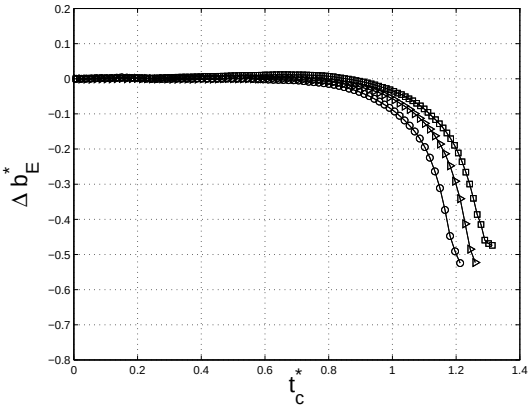

(d) exchange band

Figure 5.16: Contribution of flow regions to separation distance development, $\Delta b^*(t)$, for $Re_\Gamma = 2000$ (Symbols: $\circ$: $Fr = \infty$. $\triangleright$: $Fr = 3$. $\square$: $Fr = 2$).

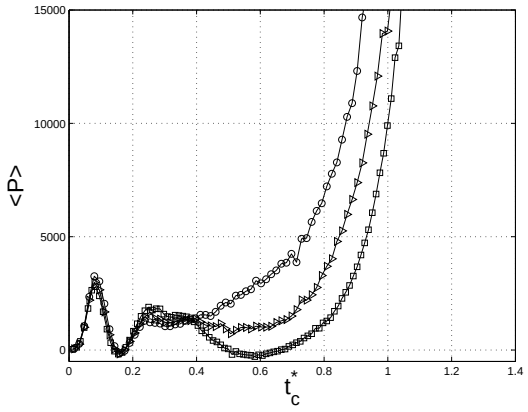

Figure 5.17: Time development of $< P >= - < \nabla\omega^T \mathsf{S} \nabla\omega >$, averaged over central region, for $Re_\Gamma = 2000$, $Fr = \infty$ (Symbols: $\circ$: $Fr = \infty$. $\triangleright$: $Fr = 3$. $\square$: $Fr = 2$).

of merging. We have also developed a generalized description of the merging process which consists of four phases: diffusive/deformation, convective/deformation, convective/entrainment, and diffusive/axisymmetrization. The phases are clearly defined and summarized in §5.6. This new description of merger, which resolves the convective effects into two distinct processes, assists in accounting for the effects of stratification and allows for a more explicit determination of the critical aspect ratio.

With stably stratified ambient fluid, as the vortex pair rotates, it stirs the density field and generates both opposite-signed and same-signed vorticity through baroclinic torque. As in the unstratified flow, the interaction of $\nabla\omega$ and S is established by diffusion. The merging process in stratified flow therefore depends on the ratio of the diffusive time scale (growth of cores, establishment of $\nabla\omega$ and S interaction) to the turnover time (establishment of baroclinically generated vorticity, BV), i.e., the Reynolds number. A crossover Reynolds number ($Re_\Gamma \approx 2500$ for this initial aspect ratio) is found, above which convective merging is accelerated with respect to unstratified flow and below which merging is delayed. In general, the effect of the BV is similar to that of the filaments. The induced

flow field will advect the vortices, either towards or away from each other, and this will modify the strain rate field, both in magnitude and direction. We distinguish this convective process by defining the convective/deformation phase, which may initiate while diffusion remains significant. Depending on the relative timescales, and stage of evolution (also initial aspect ratio), it may either enhance or hinder the $\nabla\omega$ amplification process. The strength of the BV depends on the level of stratification, as characterized by the Froude number. Therefore, initiation of the exchange band process and the convective/entrainment phase depends on both Re_Γ and Fr. Once initiated, the core entrainment process is relatively unaffected by either viscosity or level of stratification.

For both unstratified and stratified flows, we define the critical state of the flow to be the start of the convective/entrainment phase, beyond which there is no reversal and merging will occur. This is also approximately the time $a^2(t)$ deviates from linear growth. However, since $b(t)$ may change significantly, the critical aspect ratio must be determined by $a(t)/b(t)$ at the time the exchange band process initiates. For all flows considered, $2000 \leq Re_\Gamma \leq 5000$ and $Fr = \infty, 5, 3, 2$, $(a/b)_{cr} = 0.235 \pm 0.006$, where the core size is effectively based on the second moment of vorticity. This is in agreement with values previously determined for unstratified viscous flows (Meunier et al., 2002).

Chapter 5, in part, is a reprint of the material as it appears in *Journal of Fluid Mechanics* Volume 592, pages 413-446. Brandt, L.; Nomura, K., Cambridge University Press, 2007. The dissertation author was the primary investigator and author of this paper.

Chapter 6

Symmetric vortex pairs and the generation of linear internal waves

As a first step toward improving our understanding of the behavior of a turbulent patch in a stratified fluid, we investigate the effects of stable stratification on two-dimensional, symmetric, horizontally oriented *co-rotating* vortex pairs and *counter-rotating* vortex pairs. In this chapter, analytical methods are used to compute the evolution of the vorticity field and the internal wave field that is produces.

In strongly stratified fluids, the flow evolves according to the inviscid linearized Navier-Stokes equations. We define the flow to be strongly stratified when, $N >> \Gamma_o/(2\pi b_o^2)$, so that $Fr = \frac{\Gamma_o}{2\pi b_o^2 N} << 1$. This chapter is a preliminary study in which we review the effects of strong stratification on vortex configurations. In the next chapter, the insight gained from these results is used in a numerical study concerning the effects of moderate stratification, where nonlinear interactions are important.

The discussion will commence with a derivation of the linearized equations and initial conditions for vortex pairs (§6.1). Solutions of these equations are obtained in the form of inverse Fourier transforms. In §6.2, these solutions are

approximated by use of the *stationary phase approximation* (Lighthill, 1996). Once these general results are established, the energy field is investigated (§6.3). In §6.4, multiple vortex pairs are examined, which gives insight into the effect that strong stratification will have on a turbulent patch. In §6.5, we conclude with a brief discussion of results.

6.1 Linearized Equations

In this section the linearized inviscid set of equations is derived for the perturbed density and velocity fields. The first step is to calculate the exact linear density perturbations for the *horizontally* oriented vortex systems in a stably stratified fluid. From these equations it is straightforward to calculate the corresponding velocity fields.

6.1.1 Density Perturbation

The linearized inviscid primitive governing equations (Fernando and Hunt, 1997) are:

$$\frac{\partial u}{\partial t} = -\frac{1}{\rho_o}\frac{\partial p'}{\partial x} \tag{6.1}$$

$$\frac{\partial w}{\partial t} = -\frac{\rho'}{\rho_o}g - \frac{1}{\rho_o}\frac{\partial p'}{\partial z} \tag{6.2}$$

$$\frac{\partial \rho'}{\partial t} = -w\frac{d\overline{\rho}}{dz} \tag{6.3}$$

$$\frac{\partial u}{\partial x} + \frac{\partial w}{\partial z} = 0, \tag{6.4}$$

which can be reduced to a single equation for ρ' (details may be found in Appendix B.1):

$$\frac{\partial^2}{\partial t^2} \bigtriangledown^2 \rho' + N^2 \frac{\partial^2 \rho'}{\partial x^2} = 0. \tag{6.5}$$

The initial conditions for the density perturbation are:

$$\rho'(x,z) = f_1(x,z), \tag{6.6}$$

$$\frac{\partial \rho'}{\partial t}(x,z) = f_2(x,z). \tag{6.7}$$

Using Fourier transform methods, the solution for the Fourier transform of the density perturbation is, with Fourier Transform indicated by a " ˆ ":

$$\hat{\rho}'(k,m,t) = \hat{f}_1 \cos(\omega t) + \frac{\hat{f}_2 \sin(\omega t)}{i\omega} \tag{6.8}$$

in which the frequency, ω, is given by the dispersion relation,

$$\omega^2 = \frac{k^2 N^2}{k^2 + m^2} \tag{6.9}$$

and k and m are the horizontal and vertical components of the wave-number. Details of this derivation are found in Appendix B.2.

The initial conditions corresponding to no initial density perturbation and a nonzero velocity field:

$$\hat{f}_1(k,m) = 0 \tag{6.10}$$

$$\hat{f}_2(k,m) = -\hat{w}_o \frac{d\bar{\rho}}{dz}, \tag{6.11}$$

where $\hat{w}_o$ is the Fourier transform of the vertical velocity field associated with the vortices. Substituting in $\hat{f}_1$ and $\hat{f}_2$ into (6.8), $\hat{\rho}'$ becomes:

$$\hat{\rho}'(k,m,t) = -\frac{\hat{w}_o}{i\omega} \frac{d\overline{\rho}(z)}{dz} \sin(\omega t). \tag{6.12}$$

For a single Lamb-Oseen vortex with a Gaussian shape vorticity distribution, the vertical velocity is given by

$$w_o = \frac{\Gamma_o}{2\pi r}(1 - e^{-r^2/a_o^2}) \cos\theta. \tag{6.13}$$

Here r represents the radial distance from the vortex center and θ represents the angle from the positive horizontal axis. In Fourier space w_o becomes (details found in Appendix B.3):

$$\hat{w}_o = -\frac{i\Gamma_o \cos\phi}{K} e^{-K^2 a_o^2/4}, \tag{6.14}$$

where $K^2 = k^2 + m^2$ and $\phi = \tan^{-1}(m/k)$. The *shifting theorem*,

$$f(x - \Delta) \leftrightarrow exp(-ik\Delta)\hat{f}(k),$$

may be used to calculate the initial vertical velocities for the vortex pairs (details found in Appendix B.4). By substituting in the equations for the initial vertical velocities into (6.12), the exact linear solutions for the perturbed density fields in Fourier space are found for the co-rotating vortex pair

$$\frac{\hat{\rho}'(k,m,t)}{b_o^3 N^2 \frac{\rho_o}{g}} = -\frac{4\pi i Fr}{K b_o} e^{-K^2 a_o^2/4} \sin(\omega t) sgn(\cos\phi)[\cos(\frac{1}{2}kb_o)] \tag{6.15}$$

and for the counter-rotating vortex pair

$$\frac{\hat{\rho}'(k,m,t)}{b_o^3 N^2 \frac{\rho_o}{g}} = -\frac{4\pi Fr}{K b_o} e^{-K^2 a_o^2/4} \sin(\omega t) sgn(\cos\phi)[\sin(\frac{1}{2}kb_o)]. \tag{6.16}$$

6.1.2 Vorticity Field

Equation 6.3 provides a relationship between the vertical velocity and density field:

$$w = -\frac{\partial\rho'/\partial t}{d\overline{\rho}/dz}. \tag{6.17}$$

With the substitution of N (2.4) into this equation and taking the Fourier transform:

$$\frac{\hat{w}}{N b_o^3} = \frac{1}{b_o^3 N^2 \frac{\rho_o}{g}} \left[\frac{1}{N}\frac{\partial\hat{\rho}'}{\partial t}\right]. \tag{6.18}$$

By taking the time derivative of $\hat{\rho}'$ (6.15 & 6.16) and substituting it into (6.18), the vertical velocity in terms of $\hat{\rho}'$ is:

$$\frac{\hat{w}}{N b_o^3} = \cot(\omega t)|\cos\phi| \left[\frac{\hat{\rho}'}{b_o^3 N^2 \frac{\rho_o}{g}}\right]. \tag{6.19}$$

The horizontal velocity may be found through the Fourier transform of the continuity equation (6.4) and solving for $\hat{u}$:

$$\frac{\hat{u}}{N b_o^3} = -\frac{m}{k}\frac{\hat{w}}{N b_o^3} = -\frac{m}{k}\cot(\omega t)|\cos\phi| \left[\frac{\hat{\rho}'}{b_o^3 N^2 \frac{\rho_o}{g}}\right]. \tag{6.20}$$

Utilizing these equations, the vorticity field ($\zeta(x,z) = \partial w(x,z)/\partial x - \partial u(x,z)/\partial z$) in Fourier space is,

$$\hat{\zeta} = i[k\hat{w} - m\hat{u}] = i\frac{K^2}{k}\hat{w},$$

which leads to:

$$\frac{\hat{\zeta}}{b_o^2 N} = iKb_o \cot(\omega t) sgn(\cos\phi)\left[\frac{\hat{\rho}'}{b_o^3 N^2 \frac{\rho_o}{g}}\right]. \tag{6.21}$$

6.1.3 Validation of Analytical Solution

In order to validate the derived equations, linearized inviscid simulations were conducted using a pseudospectral DNS code. In order to directly compare with simulations, approximate solutions for $\rho'(x,z,t)$ and $\zeta(x,z,t)$ in physical space were made by taking the discrete Fourier transforms of $\hat{\rho}'(k,m,t)$ and $\hat{\zeta}(k,m,t)$, respectively. Results from the linear analytical equations and numerical simulations for ρ' and ζ are consistent. The maximum error is 0.4% at $Nt = \pi$, which is within truncation error.

6.2 Large-Time Approximation

After a long time, *dispersion* causes all waves to separate in space, such that at every location (x,z) there will be one wave-number (k,m). In this section, the *stationary phase approximation* (Lighthill, 1996) will be employed to approximate the linearized perturbation density solution in physical space at large time. This approximation becomes more accurate as time increases, $t \to \infty$. We note that this solution is accurate only for the *far field*.

The inverse Fourier transform of $\hat{\rho}'$ is:

$$\rho'(x,z,t) = \int_{-\infty}^{\infty}\int_{-\infty}^{\infty}\left[\frac{1}{2}F_+(k,m)e^{i\omega t} + \frac{1}{2}F_-(k,m)e^{-i\omega t}\right]e^{i(kx+mz)}dkdm. \tag{6.22}$$

Since $\int_{-\infty}^{0} f dk$ equals the complex conjugate of $\int_{0}^{\infty} f dk$, an alternative expression, using $\omega(-k) = \omega(k)$, is:

$$\rho'(x,z,t) = Real\left\{ \int_{-\infty}^{\infty}\int_{0}^{\infty} \left[F_+(k,m)e^{it\Phi_+(k,m)} + F_-(k,m)e^{it\Phi_-(k,m)} \right] dkdm \right\}, \tag{6.23}$$

where $\Phi_\pm(k,m)(k,m) = k\frac{x}{t} + m\frac{z}{t} \pm \omega$, $F_-(k,m) = \hat{f}_1(k,m) - \hat{f}_2(k,m)/i\omega$ and $F_+(k,m) = \hat{f}_1(k,m) + \hat{f}_2(k,m)/i\omega$. In this formulation, the first term in the integral represents the waves propagating in the negative horizontal direction ($x < 0$) and the second term represents the waves propagating in the positive horizontal direction ($x > 0$).

We seek an approximate evaluation of this integral as $t \to \infty$ with x/t and z/t held constant. According to the method of *stationary phase* set forth by Lighthill (1996), the major contributors to the integral at a particular time are where $\frac{\partial\Phi_\pm}{\partial k} = \frac{\partial\Phi_\pm}{\partial m} = 0$. The spacial locations at which this occurs is known as the *points of stationary phase* and are found to be:

$$\begin{aligned} [x,z] &= \left[-\frac{\partial\omega}{\partial k}t, -\frac{\partial\omega}{\partial m}t \right] && x < 0 \\ [x,z] &= \left[\frac{\partial\omega}{\partial k}t, \frac{\partial\omega}{\partial m}t \right] && x > 0. \end{aligned} \tag{6.24}$$

The group velocities, $(c_{g,x}, c_{g,z})$, in the horizontal and vertical directions are:

$$\begin{aligned} c_{g,x} &= \frac{\partial\omega}{\partial k} = N\frac{m^2}{K^3}sgn(k) \\ c_{g,z} &= \frac{\partial\omega}{\partial m} = -N\frac{m|k|}{K^3}sgn(k), \end{aligned} \tag{6.25}$$

respectfully, where $\omega = \frac{|k|N}{K} = N|\cos\phi|$ and $k = K|\cos\phi|$. Since only positive k are being considered $c_{g,x}$ is always positive and $c_{g,z}$ is the opposite sign of m. Therefore, (6.24) may be rewritten as:

$$[x,z] = \left[-Nt\frac{m^2}{K^3}, \quad Nt\frac{m|k|}{K^3} \right] \qquad x < 0 \tag{6.26}$$

$$[x,z] = \left[Nt\frac{m^2}{K^3}, -Nt\frac{m|k|}{K^3} \right] \qquad x > 0. \tag{6.27}$$

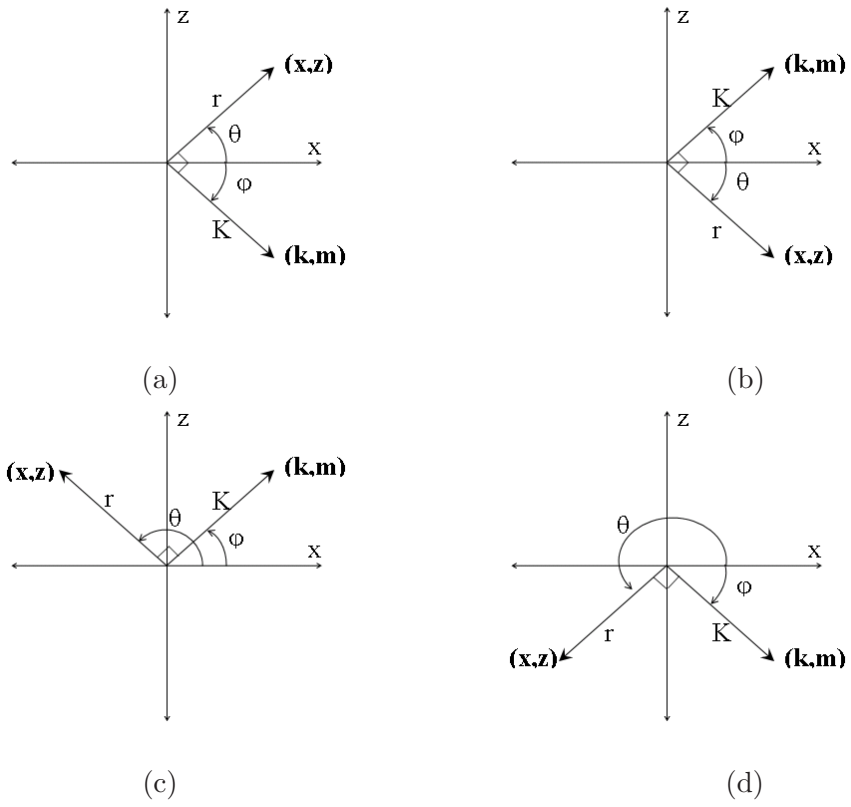

Figure 6.1: Shows relationship between θ and ϕ based on direction of wave propagation.

Since $\underline{c_g} \cdot \underline{k} = 0$, the group speed is perpendicular to the wave vector, $\phi = \theta \pm \pi/2$. Therefore, the direction of the propagation of the waves must be taken into consideration when solving.

Figures 6.1a&b show the relation between θ and ϕ for waves propagating in the $x > 0$ direction, while figures 6.1c&d show the relation between θ and ϕ for waves propagating in the $x < 0$ direction. With the knowledge that $k = K|\cos\phi|$ and $m = K\sin\phi$, it is seen that:

$$k_s = K_s|\sin\theta| \tag{6.28}$$

$$m_s = -K_s\cos\theta sgn(\sin\theta). \tag{6.29}$$

Substituting in (6.28) & (6.29) into (6.26) & 6.27, the spacial coordinates in terms of (K_s, θ) are found:

$$[x, z] = \frac{Nt\cos\theta}{K_s}\Big[\cos\theta, \sin\theta\Big], \qquad x < 0 \tag{6.30}$$

$$[x, z] = -\frac{Nt\cos\theta}{K_s}\Big[\cos\theta, \sin\theta\Big], \qquad x > 0. \tag{6.31}$$

This corresponds to

$$K_s = \frac{Nt}{r}|\cos\theta|, \tag{6.32}$$

where r is the radius outward from the vortex center, $r^2 = x^2 + z^2$.

According to Lighthill (1996), the stationary phase approximation of (6.23) is

$$\rho'(x, z, t) \approx Real\left\{\frac{2\pi}{t}|detA_-|^{-1/2}F_-(k_s, m_s)e^{-it\omega(k_s,m_s)}\right\} \tag{6.33}$$

$$+Real\left\{\frac{2\pi}{t}|detA_+|^{-1/2}F_+(k_s, m_s)e^{it\omega(k_s,m_s)}\right\}, \tag{6.34}$$

where $detA$ is dependent on the partial derivatives of $\underline{c_g}$ with respect to (k_s, m_s). Details of the calculation of $|detA|^{-1/2}$ are worked out in Appendix B.5. The solution is

$$|detA_-|^{-1/2} = |detA_+|^{-1/2} = \frac{K_s^2}{N|\cos\theta|}. \tag{6.35}$$

The final equation for the stationary phase approximation is:

$$\rho'(x,z,t) \approx \left(2\pi \frac{K_s^2}{Nt|\cos\theta|}\right) \times \\ Real\left\{F_+(k_s,m_s)e^{it\omega(k_s,m_s)} + F_-(k_s,m_s)e^{-it\omega(k_s,m_s)}\right\}. \tag{6.36}$$

The equations for $F_-(k_s,m_s)$ and $F_+(k_s,m_s)$ are dependent on the initial conditions of the flow and may be found similarly to that of the exact solution, where $F_-(k,m) = \hat{f}_1(k,m) - \hat{f}_2(k,m)/i\omega$ and $F_+(k,m) = \hat{f}_1(k,m) + \hat{f}_2(k,m)/i\omega$. These quantities are worked out in detail in Appendix B.6. Substituting in the values for $F_-(k_s,m_s)$ and $F_+(k_s,m_s)$ into (6.36), it is found that the linearized density perturbation may be approximated at large times for the co-rotating vortex pair as

$$\frac{\rho'(x,z,t)}{b_o N^2 \rho_o/g} \sim 4Fr \frac{K_s b_o}{Nt|\cos\theta|} e^{-K_s^2 a_o^2/4} \cos(\frac{1}{2}k_s b_o)\cos(\omega_s t) sgn(x) \tag{6.37}$$

and for the counter-rotating vortex pair as

$$\frac{\rho'(x,z,t)}{b_o N^2 \rho_o/g} \sim -4Fr \frac{K_s b_o}{Nt|\cos\theta|} e^{-K_s^2 a_o^2/4} \sin(\frac{1}{2}k_s b_o)\sin(\omega_s t), \tag{6.38}$$

where k_s, m_s and K_s are defined by (6.28), (6.29) and (6.32), respectively, and $\omega_s = N|\sin\theta|$.

Therefore, we now have a set of equations that approximate the far field density perturbation at large times for vortex pairs.

6.2.1 Validation of Large-Time Approximation

Figures 6.2 shows the discrete Fourier transform of the exact analytical solution for ρ' and the stationary phase approximation of ρ' for $Fr = 0.01$ at $Nt = 30$. In figure 6.2a&c, it is observed that the approximation captures the general wave behavior. In both the analytical and stationary phase solutions, the waves are seen to propagate as rays away from the disturbance region and their phases appear to propagate from the vertical to the horizontal axis in time

(not shown). As time progresses, the far field solution for the stationary phase approximation more accurately reproduces the exact analytical solution.

However, there are a few discrepancies in the approximation. In the case of a co-rotating vortex pair, it is observed that near the vertical axis of figure 6.2b, the stationary phase approximation begins to break down. This discrepancy is to be expected since (6.37) is dependent on the sign of x. As time increases, this dependence becomes less pronounced at the axis, but it will inherently have to be included in the approximation. The stationary phase approximation also cannot resolve the interactions taking place at the disturbance region.

6.3 Energy Exchange

The equations for the kinetic (KE), potential (PE), and total (E) energies per unit area of the flow are:

$$PE = \frac{1}{2}\frac{g^2}{\rho_o N^2}\rho'^2, \tag{6.39}$$

$$KE = \frac{1}{2}\rho_o(u^2 + w^2), \tag{6.40}$$

$$E = PE + KE. \tag{6.41}$$

By taking the Fourier transform of these equations, the kinetic (KE), potential (PE), and total (E) energies per unit area may be written as:

$$\frac{\widehat{KE}(k,m,t)}{b_o^6 N^2 \rho_o} = \frac{1}{2}\left[\left(\frac{\hat{u}}{N b_o^3}\right)\left(\frac{\hat{u}^*}{N b_o^3}\right) + \left(\frac{\hat{w}}{N b_o^3}\right)\left(\frac{\hat{w}^*}{N b_o^3}\right)\right], \tag{6.42}$$

$$\frac{\widehat{PE}(k,m,t)}{b_o^6 N^2 \rho_o} = \frac{1}{2}\left(\frac{\hat{\rho}'}{N^2 b_o^3 \frac{\rho_o}{g}}\right)\left(\frac{\hat{\rho}'^*}{N^2 b_o^3 \frac{\rho_o}{g}}\right), \tag{6.43}$$

$$\frac{\widehat{E}(k,m,t)}{b_o^6 N^2 \rho_o} = \frac{\widehat{PE}}{b_o^6 N^2 \rho_o} + \frac{\widehat{KE}}{b_o^6 N^2 \rho_o}, \tag{6.44}$$

respectfully, where * represents the complex conjugate. Substituting in (6.42) (where $\hat{w}$ and $\hat{u}$ are described by (6.19) & (6.20), respectively) and (6.43) into

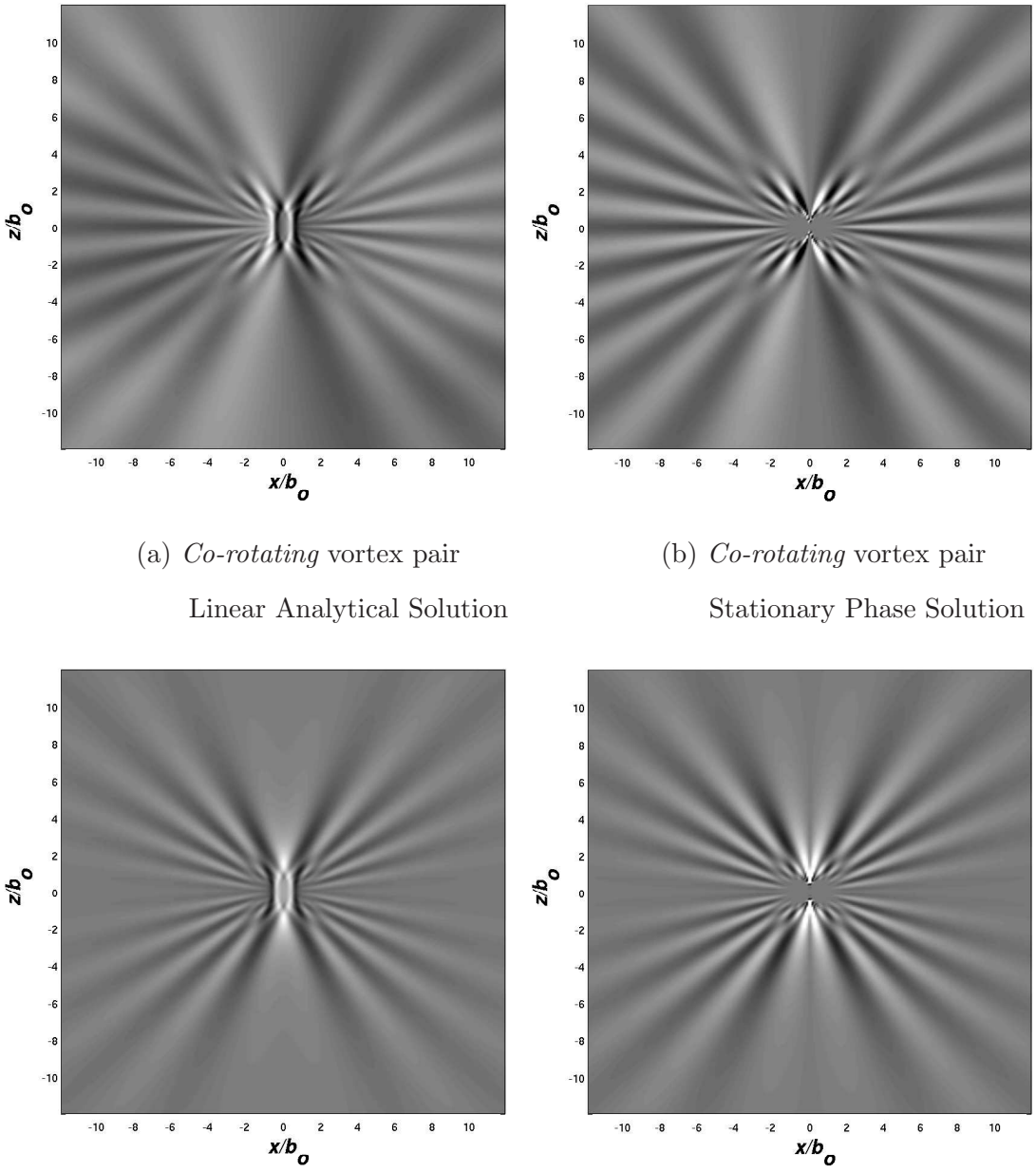

(a) *Co-rotating* vortex pair Linear Analytical Solution

(b) *Co-rotating* vortex pair Stationary Phase Solution

(c) *Counter-rotating* vortex pair Linear Analytical Solution

(d) *Counter-rotating* vortex pair Stationary Phase Solution

Figure 6.2: Contours of perturbed density for $Fr = 0.01$ at $Nt = 30$ produced by (a)&(c) equations 6.15 & 6.16 and (b)&(d) equations 6.37 & 6.38.

(6.44), a generalized equation for $\hat{E}$ may be found in terms of $\hat{\rho}$:

$$\frac{\widehat{E}(k,m,t)}{b_o^6 N^2 \rho_o} = \frac{1}{2\sin^2(\omega t)} \left(\frac{\hat{\rho}'}{N^2 b_o^3 \frac{\rho_o}{g}} \right) \left(\frac{\hat{\rho}'^*}{N^2 b_o^3 \frac{\rho_o}{g}} \right). \tag{6.45}$$

Substituting in (6.15) & (6.16) into (6.45), the total energy for the co-rotating vortex pair is:

$$\frac{\widehat{E}(k,m)}{b_o^6 N^2 \rho_o} = Fr^2 \frac{8\pi^2}{K^2 b_o^2} e^{-K^2 a_o^2/2} \cos^2(\frac{1}{2} k b_o). \tag{6.46}$$

and for the counter-rotating vortex pair is:

$$\frac{\widehat{E}(k,m)}{b_o^6 N^2 \rho_o} = Fr^2 \frac{8\pi^2}{K^2 b_o^2} e^{-K^2 a_o^2/2} \sin^2(\frac{1}{2} k b_o). \tag{6.47}$$

Recall that the initial flow field consists of the superposition of the vortex pairs in a stably stratified fluid with the initial conditions of $\hat{\rho}'(k,m,t_o) = 0$ and $\partial\hat{\rho}'(k,m,t_o)/\partial t \neq 0$. Therefore, since the initial density field is not perturbed, there is no initial $\widehat{PE}$ and $\widehat{E} = \widehat{KE}$. As the density field is perturbed, the energy is transferred between $\widehat{KE}$ and $\widehat{PE}$, where $\widehat{E} = \widehat{KE} + \widehat{PE} = constant$ since we do not have any viscous dissipation. Thus, there is no time dependence in the total energy (6.46) & (6.47).

Equations (6.46) & (6.47) are the two-dimensional power spectral density (2DPSD) equations that describe how the energy of the flow is distributed in every wave-number. Figures 6.3a,c show the 2DPSD for the linearized analytical equations of the co-rotating and counter-rotating vortex pairs. There is a distinctive pattern of energy in wave-space. From (6.46) & (6.47), the energy of the flow is based on a harmonic function in the k direction. In the case of the co-rotating vortex pair it is dependent on $\cos^2(.5kb_o)$ and in the case of the counter-rotating vortex pair it is dependent on $\sin^2(.5kb_o)$. These terms enter the analysis when configuring the initial vertical velocity field with the *shifting theorem*. Therefore, different orientations of the initial velocity field will greatly affect the wave-numbers in which the energy is concentrated. For our given flow conditions, what we see is a

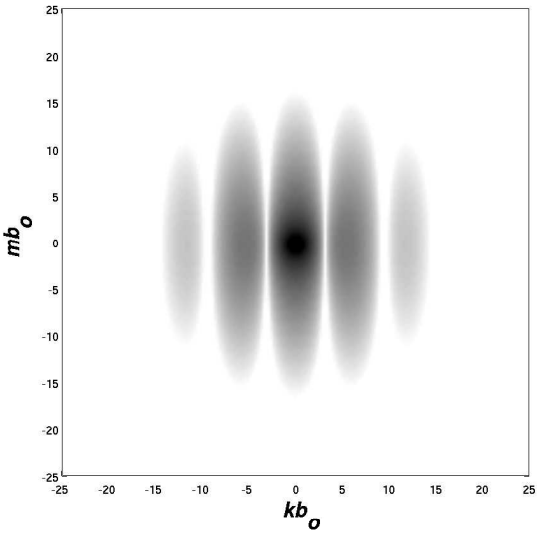

(a) *Co-rotating* vortex pair
Linear Analytical Solution

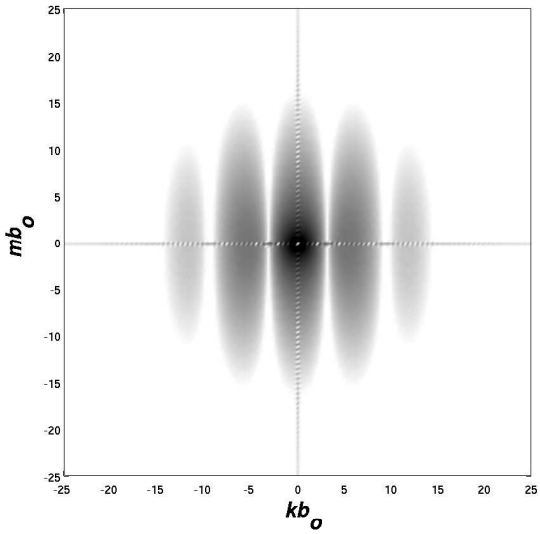

(b) *Co-rotating* vortex pair
Linear Numerical Solution

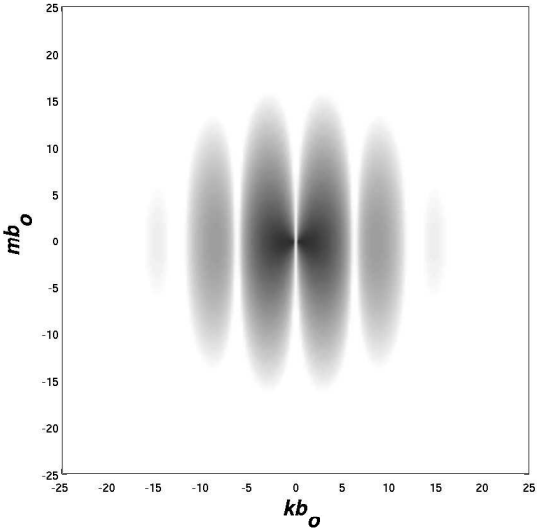

(c) *Counter-rotating* vortex pair
Linear Analytical Solution

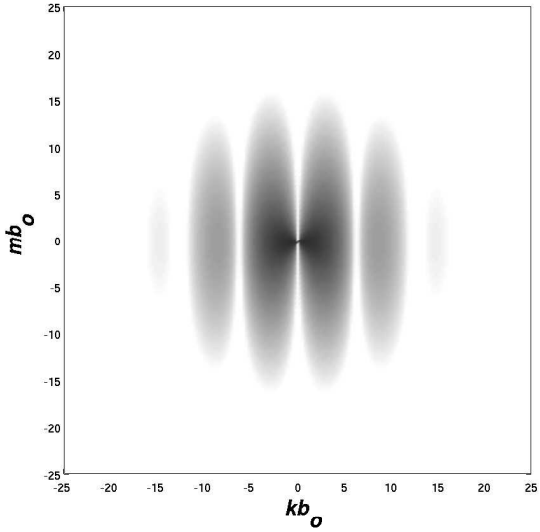

(d) *Counter-rotating* vortex pair
Linear Numerical Solution

Figure 6.3: 2DPSD for vortex pairs at $Nt = 3\pi$.

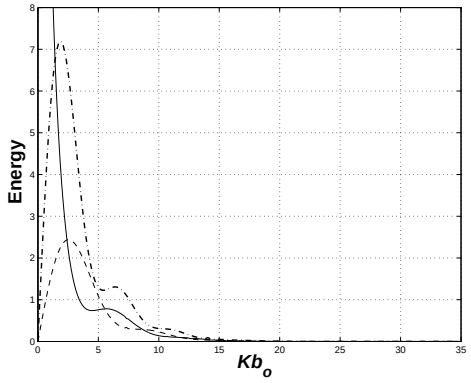

Figure 6.4: 1DPSD calculated by use of the linearized analytical equations for a co-rotating vortex pair (-), a counter-rotating vortex pair (- -) and VQ (-·-).

series of constructive and destructive wave interactions in the horizontal direction, which occur every $kb_o = 2\pi$.

As was done for the analytic solutions of ρ' and ζ, the analytical solution for the energy field was validated by numerical simulations. Figure 6.3b,d presents results from the linearized numerical simulations at $Nt = 3\pi$. It is found that the 2DPSD for the analytical and linear numerical solutions are within numerical error.

As seen in figure 6.3a, the co-rotating vortex pair energy peaks at $k = m = 0$. The reason for this energy at the zero-wave-number may be seen from (6.46), where it is observed that there is a $1/K^2$ multiplied by $\cos^2(.5kb_o)$. Therefore, at $k = 0$, the function goes to infinity and, hence, there is energy at infinity. This indicates that the motion of the flow in space does not decay sufficiently rapidly as it approaches infinity. While attempts were made to remove this infinite energy by superimposing a uniform background vorticity field, the energy of the field was still predominantly in the large wavelengths indicating that the motion of the flow in space was still not decaying sufficiently rapidly in the spatial domain as it approached large distances. In order to remove this energy at the large

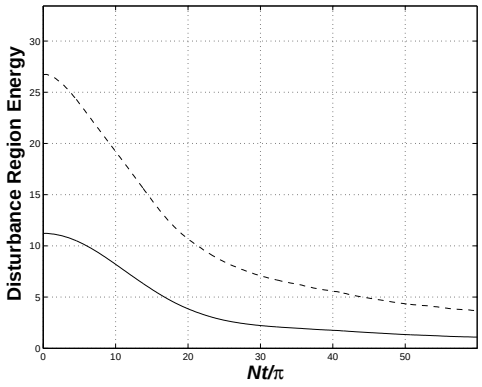

Figure 6.5: Disturbance Region Energy for counter-rotating vortex pair (-) and VQ (- -).

wavelengths, a point vortex of opposite sign was superimposed on the flow field. However, the resulting energy field was dominated by the point vortex which was not the intent of the study. Therefore, the study proceeds with the same vortex configurations, but emphasis is placed on the counter-rotating vortex pair study.

The energy distribution as a function of wavelength may more clearly be seen by looking at the one dimensional power spectral density (1DPSD) in figure 6.4. The peak energy in the counter-rotating vortex pair is at $Kb_o \approx 2.5$. This distribution of energy in wave space does not change in time even though the energy is being transferred between KE and PE. However, it does change in the physical domain.

We may evaluate the rate at which the energy is removed from the disturbance region in physical space by evaluating the energy in that vicinity. Figure 6.5 shows E integrated over a square domain, with sides of length $L_{source} = 12b_o$, surrounding the counter-rotating vortex pair. Here the energy is calculated from (6.39) through (6.41), with w, u and ρ' were calculated through the discrete Fourier transforms of (6.19), (6.20) and (6.16), respectively.

In figure 6.5, it is observed that the energy associated with the disturbance region behaves according to three phases. The first phase roughly occurs during

the first buoyancy period where the energy rate of change is gradual. The next phase consists of a rapid and constant change in the energy rate, where the waves with higher group velocities are removed early in time. There appears to be a transition after about 9 buoyancy periods where the rate of decrease significantly reduces. During the remaining time, the energy is slowly propagated away. The fluid at the disturbance region will eventually return to rest and a state of stable stratification.

6.4 Multiple Vortex Pairs

Now that we have developed and verified our analytical set of equations for the simple cases of vortex pairs, we are now ready to address more complex flows. In this section, we will make the flow more complex by looking at a set of co-rotating vortex pairs in a quadrupole configuration (VQ), where the pairs are of opposite sign. Figure 2.1 presents the geometry of this flow field. Note, the flow is set up such that the direction of the initial outward advection velocity is aligned perpendicular to the horizontal axis.

6.4.1 Analytical Solution

The analytical set of equations for this more complex flow remains unaltered with the exception of the initial vertical velocities, which are worked out in detail in Appendix B.4. By substituting in the equations for the initial vertical velocities into (6.12), the exact linear solution for the perturbed density field in Fourier space of VQ is found

$$\frac{\hat{\rho}'(k,m,t)}{b_o^3 N^2 \frac{\rho_o}{g}} = -\frac{8\pi Fr}{Kb_o} e^{-K^2 a_o^2/4} \sin(\omega t) sgn(\cos\phi)[\sin(\frac{1}{2}kb_o)\cos(\frac{1}{2}mb_o)]. \qquad (6.48)$$

The corresponding velocity fields may be calculated with (6.19) & (6.20). Results show that the analytical set of equations and inviscid linear simulations are in agreement (not shown).

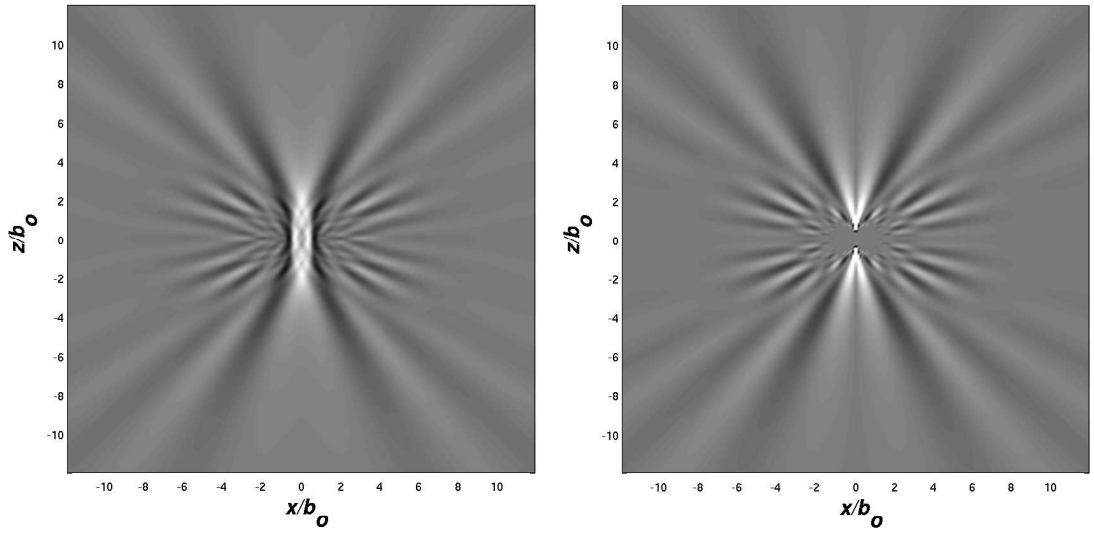

(a) Analytical Solution (b) Stationary Phase Solution

Figure 6.6: Contours of VQ perturbed density for $Fr = 0.01$ at $Nt = 30$ produced by (a) equation 6.48 and (b) equations 6.49.

6.4.2 Large Time Approximation

We also may calculate the long time and far field density perturbation approximation to the flow through the *stationary phase approximation* with the knowledge of the initial velocity field (Details may be found in Appendix B.6):

$$\frac{\rho'(x,z,t)}{b_o N^2 \rho_o/g} \approx -8Fr \frac{K_s b_o}{Nt|\cos\theta|} e^{-K_s^2 a_o^2/4} \sin(\frac{1}{2}k_s b_o)\cos(\frac{1}{2}m_s b_o)\sin(\omega_s t), \qquad (6.49)$$

where k_s, m_s and K_s are defined by (6.28), (6.29) and (6.32), respectfully. Figure 6.6 shows a comparison between the analytic and linearized numerical solutions, which besides the differences found at the disturbance region and vertical axis, are in agreement.

6.4.3 Energy Exchange

As was discussed in the cases of the single vortex pairs, the energy is transferred between $\widehat{KE}$ and $\widehat{PE}$, where $\widehat{E} = \widehat{KE} + \widehat{PE} = constant$. Substituting in

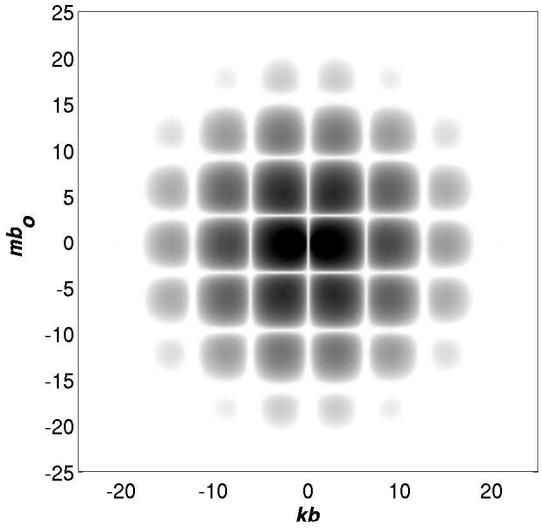

Figure 6.7: 2DPSD for VQ

(6.48) into (6.45), the 2DPSD equation for the total energy per unit area is:

$$\frac{\widehat{E}(k,m)}{b_o^6 N^2 \rho_o} = Fr^2 \frac{16\pi^2}{K^2 b_o^2} e^{-K^2 a_o^2/2} \sin^2(\frac{1}{2}kb_o)\cos^2(\frac{1}{2}mb_o). \tag{6.50}$$

Figure 6.7 shows a figure of the 2DPSD equations, where it is observed that there is a series of constructive and destructive wave interactions in the horizontal and vertical directions, which occur every 2π. This is due to the energy of the flow being based on harmonic functions in the k and m directions as seen in (6.50). It is also noted that as in the counter-rotating vortex pair, there is a sine operator present in the equation that acts on the horizontal wave-number. Therefore, the peak energy in the flow is not located at $k = m = 0$ as it was in the co-rotating vortex pair flow, thereby indicating that the energy goes to zero at infinity.

Figure 6.4 shows the energy distribution as a function of wavelength (1DPSD). The peak energy in the VQ is at $Kb_o \approx 1.9$, which is significantly lower than the wave-number found in the counter-rotating vortex pair. It is also observed that the peak energy's magnitude of the more complex system is significantly higher than the counter-rotating vortex pair. Therefore, it is interesting to see how the disturbance region's energy field change in time given these circumstances.

As was done for the counter-rotating vortex pair, we may evaluate the rate at which the energy is removed from the disturbance region by evaluating E in that vicinity. Figure 6.5 shows the E integrated over a square, with sides of length $L_{source} = 12b_o$, region surrounding the disturbance region. The change in the energy rate for the VQ behaves according to the same 3 phases as found for the counter-rotating vortex pair. The initial gradual change in the energy rate occurs during the first buoyancy period. This is followed by a rapid, constant change in the disturbance region's energy. When comparing the disturbance region's energy of this more complex flow with the counter-rotating vortex pair, it is observed that the rate at which energy is transferred is increased. However in both configurations, the rate at which energy is removed from the disturbance region decreases in time and becomes more steady after approximately 9 buoyancy periods.

6.5 Summary

Through analytical techniques, we have investigated the linear interactions of co-rotating and counter-rotating vortex pairs. The formulated equations for the density, vorticity and energy fields accurately describe the interactions taking place in a strongly stratified environment, where nonlinear effects may be neglected (validated through numerical simulations).

The 2DPSD gives information about the distribution of energy in wave-number space. There is a distinctive harmonic pattern of constructive and destructive wave interactions in the horizontal direction, which occur every $kb_o = 2\pi$.

From the evaluation of the rate at which energy is removed from the region near the initial disturbance, it is observed that during the first buoyancy period the initial rate of change is quite gradual. This period is followed by a rapid, constant rate of change of the energy where the waves with higher group velocities are removed. After approximately 9 buoyancy periods, the rate decreases, where the rate of change comparatively becomes very small and the remaining waves

slowly propagate away leaving the initial disturbance region as a stably stratified fluid.

We also investigated, two sets of co-rotating vortex pairs in a quadrupole configuration, VQ. From our analysis of the energy field we found that modifying the flow's initial velocity distribution greatly affects the distribution of energy and the rate at which energy is transported away from the disturbance region. Since the initial velocity field contains harmonic functions in the k and m wave-numbers, the energy field in wave space is seen to have constructive and destructive wave interactions in the horizontal direction and vertical directions, which occur every 2π. Looking at the energy in terms of the 1DPSD, it was seen that the peak energy associated with the VQ is maintained in a lower wave-number than in the counter-rotating vortex pair. However, the peak energy magnitude of the VQ was significantly higher than the counter-rotating vortex pair. Through the evaluation of the rate at which energy is removed from the disturbance region, it was found that the time duration of the change in the energy rate was comparable with that of the counter-roasting vortex pair. During the first buoyancy period both the VQ and counter-rotating vortex pair energy gradually decreased. This trend was followed by a rapid, nearly constant decrease in the energy. After approximately 9 buoyancy periods, the energy rate relaxed to a gradual steady rate. However, over the time duration between $Nt = 2\pi$ and $Nt = 18\pi$, the rate at which energy was removed from the disturbance region surrounding the VQ was much more substantial than for the counter-rotating vortex pair.

In the future it would be interesting to use these equations to calculate the linear flow behavior of a statistical distribution of vortex pairs that would be representative of turbulence and compare the results with a real turbulent patch in order to see if our linearized equations accurately captures the energetics of the flow. In the next chapter, we will investigate numerically the effects of moderate stratification and the influences of nonlinear and viscous effects on the flow. We will also identify the validity of this linear set of equations in describing flows which

contain nonlinear interactions.

Chapter 7

Symmetric vortex pairs and the generation of nonlinear internal waves

In this chapter we expand upon the study of chapter 6 by investigating the effects of moderately stable stratification on the counter-rotating vortex pair and the co-rotating vortex quadrupole configuration, VQ. We note that we are not considering the isolated case of the co-rotating vortex pair, since it was found in chapter 6 that the energetics of that flow are unrealistic.

We define moderate stratification as $Fr \approx 1$, so that $N \approx \Gamma_o/(2\pi b_o^2)$. In the previous chapter we investigated $Fr \ll 1$ analytically using the linearized inviscid Navier Stokes equations. However, as stratification levels decrease, i.e. Fr increases, inertial effects become more important, which brings in nonlinearity. Studying the nonlinear effects of the flow analytically would be very tedious. For each configuration considered, a detailed mathematical model would need to be developed, such as that done for a single Rankine vortex in Griffiths (1999). This means that the generality in studying these flows analytically would be lost. Therefore, we will analyze the flow numerically in order to study the nonlinear

effects.

In the previous chapter, viscosity was neglected. The lower Fr, the less of an effect viscosity will have on the flow. From §2.2.1 it may be shown that the ratio of viscous to inertial time scales is:

$$\frac{t_v}{t_s} = \frac{(a_o/b_o)^2}{8\pi}\frac{Re_\Gamma}{Fr}.$$

For viscous effects to be negligible $t_v >> t_s$ and therefore $Re_\Gamma >> \frac{8\pi}{(a_o/b_o)^2}Fr$. In strongly stratified flow, where $Fr \ll 1$, Re_Γ may be neglected. However, in moderately stratified flow where $Fr \approx 1$, Re_Γ must be taken into consideration. In the current simulations $Re_\Gamma = 5000$ and $a_o/b_o = 0.157$.

We will begin by addressing the effect of Fr on the density and vorticity fields of a counter-rotating vortex pair in §7.1 and §7.2, respectively. These results will then be used to explain the behavior of the energy field for different Fr in §7.3. We then investigate the effect of moderate stratification on VQ in §7.4. With the knowledge gained from studying these flow configurations, we classify the strongly stratified and moderately stratified regimes in §7.5 and conclude in §7.6 with a brief discussion.

7.1 Density Field - Counter-rotating vortex pair

From our analysis of the previous chapter, it is seen from (6.16) that in an inviscid linearized flow the perturbed density field magnitude is affected by the level of stratification. However, when analyzing the flow on the buoyancy time scale, the flow behavior develops in a similar fashion. As was previously discussed, regardless of Fr, the waves are seen to propagate as rays away from the disturbance region and their phases appear to propagate from the vertical to the horizontal axis.

The effect of viscosity on the linear interactions of the flow may be seen by comparing the analytical model with viscous linearized numerical simulations. In figure 7.1a, the analytical model (i & iii) and numerical simulations (ii & iv) are

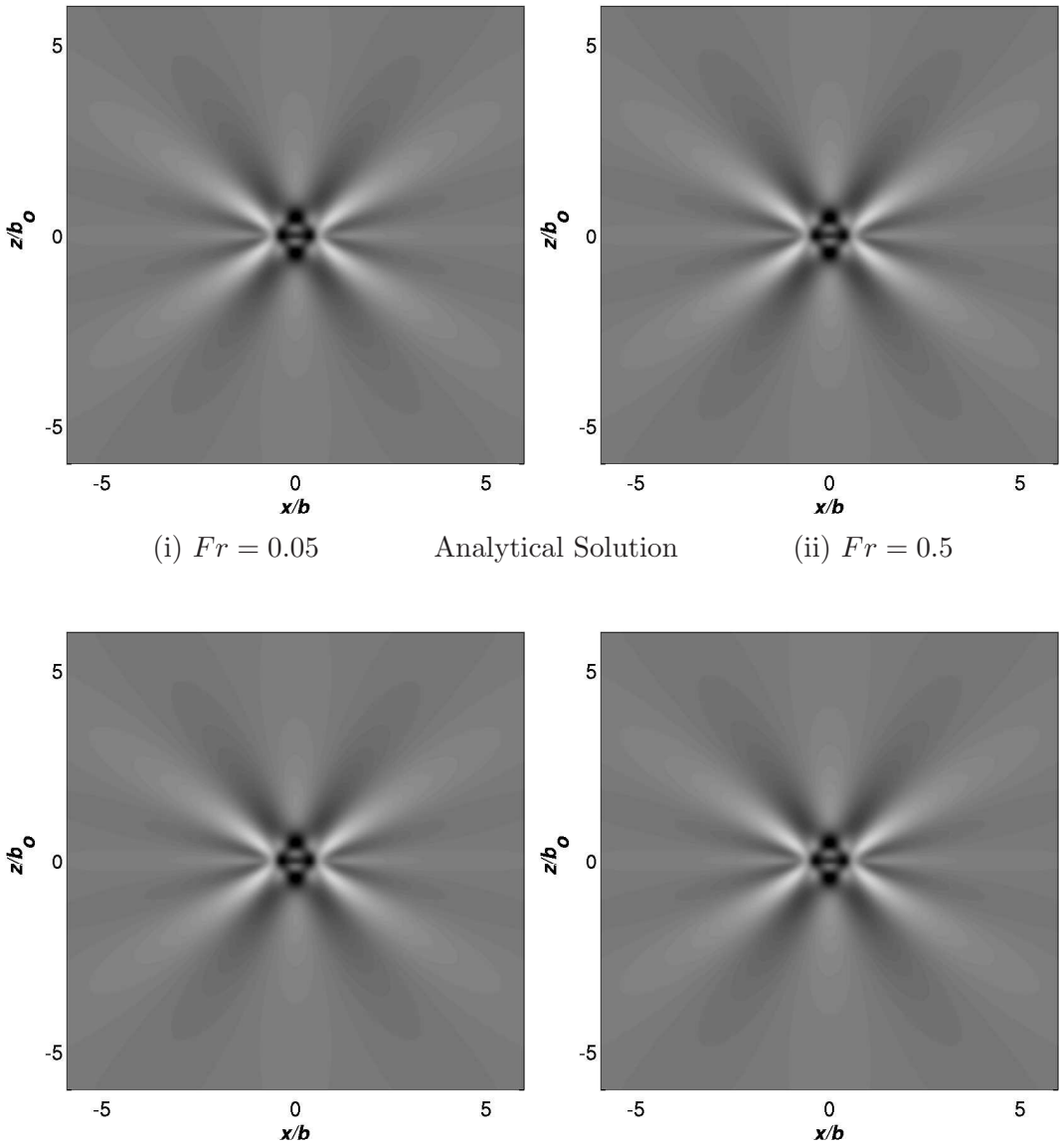

(i) $Fr = 0.05$ Analytical Solution (ii) $Fr = 0.5$

(iii) $Fr = 0.05$ Linear Viscous Numerical Solution (iv) $Fr = 0.5$

Figure 7.1a: Density contours of a counter-rotating vortex pair at $Nt = 3\pi$ (Domain $L = 24b_o$).

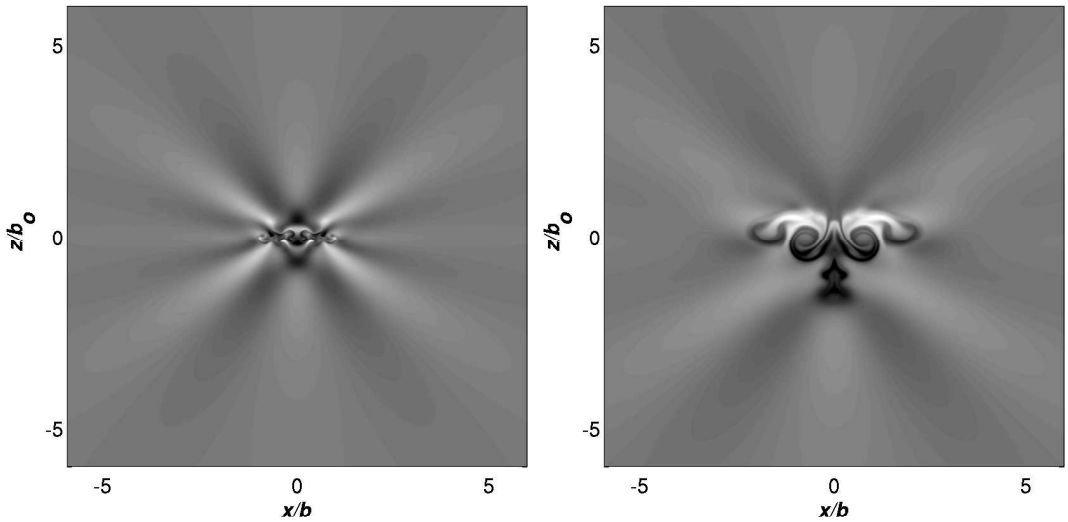

(i) $Fr = 0.05$ Nonlinear Viscous Numerical Solution (ii) $Fr = 0.5$

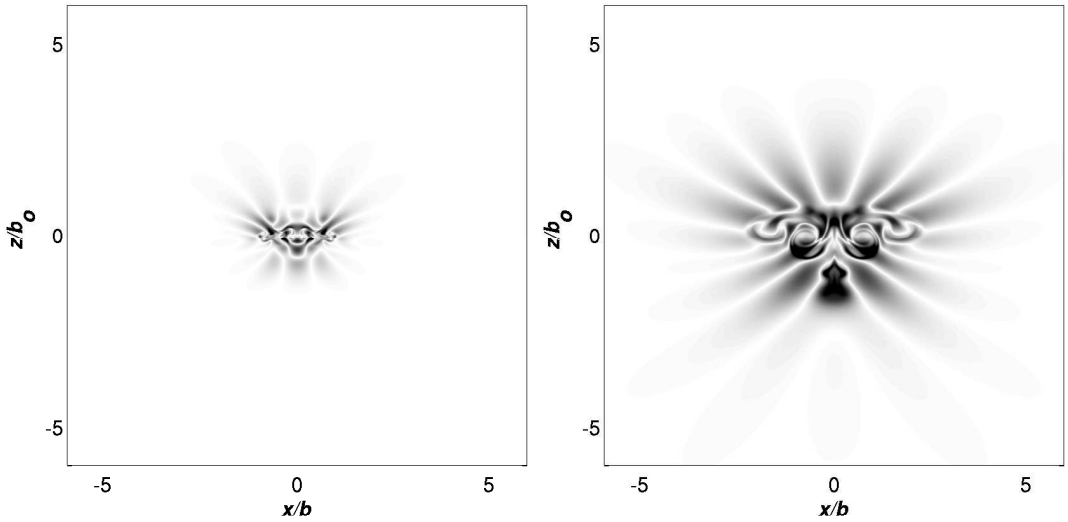

(iii) $Fr = 0.05$ Difference in Viscous Numerical Solutions (iv) $Fr = 0.5$

Figure 7.1b: Density contours of a counter-rotating vortex pair at $Nt = 3\pi$ (Domain $L = 24b_o$).

shown for $Nt = 3\pi$. It is seen that there is a minimal effect due to viscosity in the flows presented. The general behavior of the flow is well represented by the analytical solution of the inviscid linearized equations.

For the nonlinear viscous simulations presented in figure 7.1b (i & ii) for $Nt = 3\pi$, we observe that the general behavior of the wave field is similar to the linearized model. The waves are still seen to propagate as rays away from the disturbance region and their phases still propagate from the vertical to the horizontal axis. However, the flow has been significantly altered in the vicinity of the disturbance region.

This may be seen more clearly in figure 7.1b (iii & iv), where the density perturbation fields of the linear viscous simulations have been subtracted from the density perturbation fields of the nonlinear viscous simulations. There are several key differences observed in the vicinity of the disturbance region. It is seen that the nonlinearities in the flow enhance mixing and are more pronounced the larger the value of Fr. The nonlinear interactions also appear to generate waves and alter the existing wave field surrounding the disturbance region. The region in which the nonlinear effects modify the flow field increases in size for increasing Fr.

7.2 Vorticity Field - Counter-rotating vortex pair

The effects of stratification and viscosity can clearly be seen when looking at contours of vorticity. In figure 7.2a the vorticity field at $Nt = 3\pi$ for the analytic linearized solution (i & ii) and the linearized viscous numerical simulations (iii & iv) are shown. It is seen that for increasing Fr, the more viscosity acts to diffuse the vorticity of the flow, which is seen when comparing ii & iv. However, the general distribution of vorticity is unaltered.

Figure 7.2b shows contours of vorticity for the nonlinear viscous simulations for $Nt = 3\pi$. Here the effects of viscosity and Fr are clearly evident. As was found for the perturbed density field, there is significant mixing found in the region

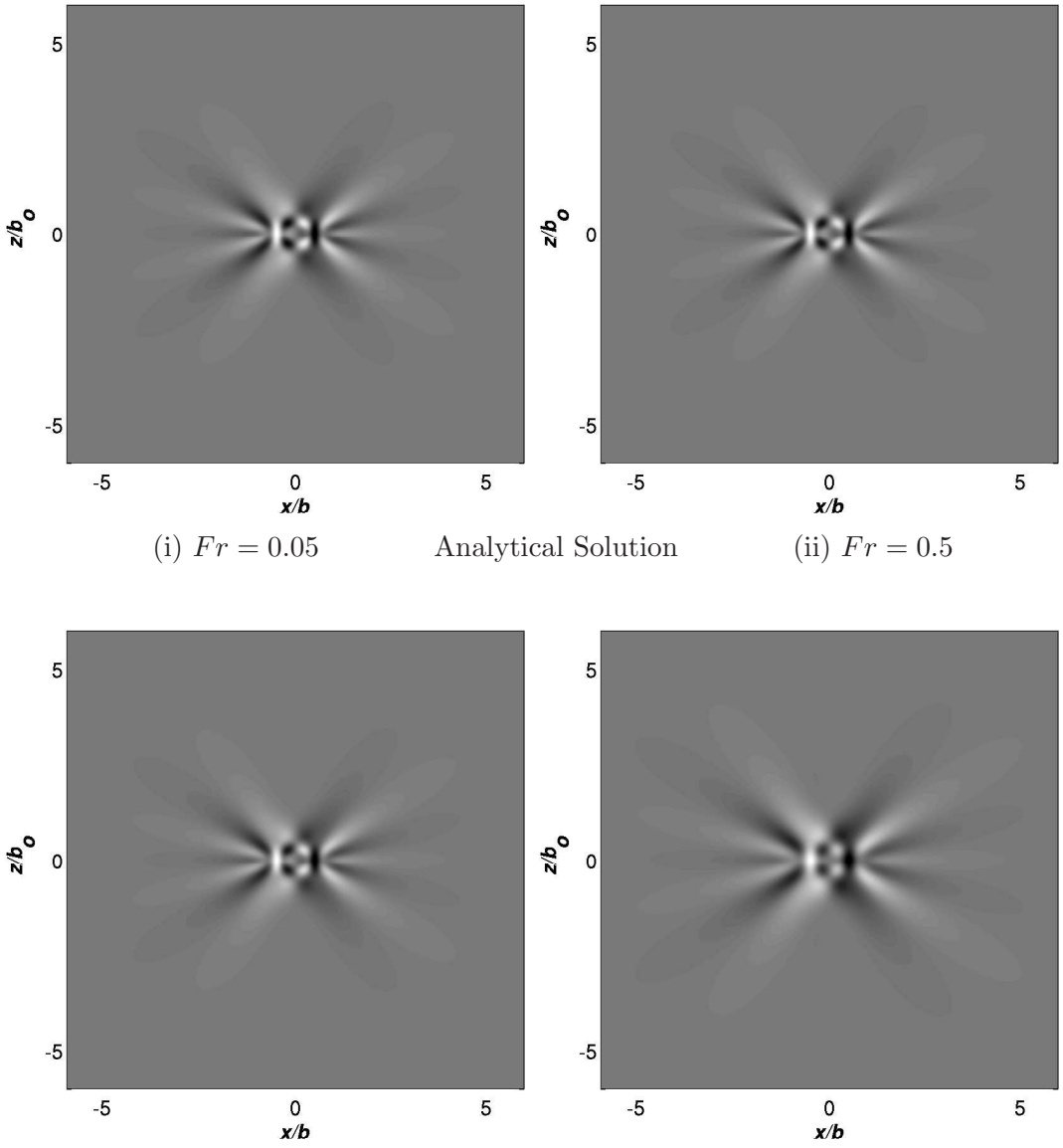

(i) $Fr = 0.05$ Analytical Solution (ii) $Fr = 0.5$

(iii) $Fr = 0.05$ Linear Viscous Numerical Solution (iv) $Fr = 0.5$

Figure 7.2a: Vorticity contours of a counter-rotating vortex pair at $Nt = 3\pi$.

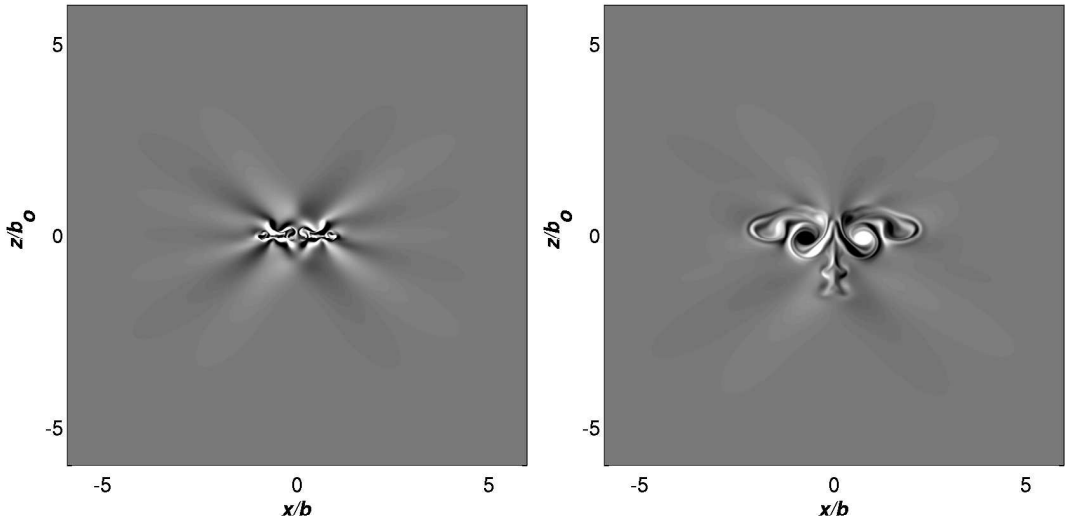

(i) $Fr = 0.05$ Nonlinear Viscous Numerical Solution (ii) $Fr = 0.5$

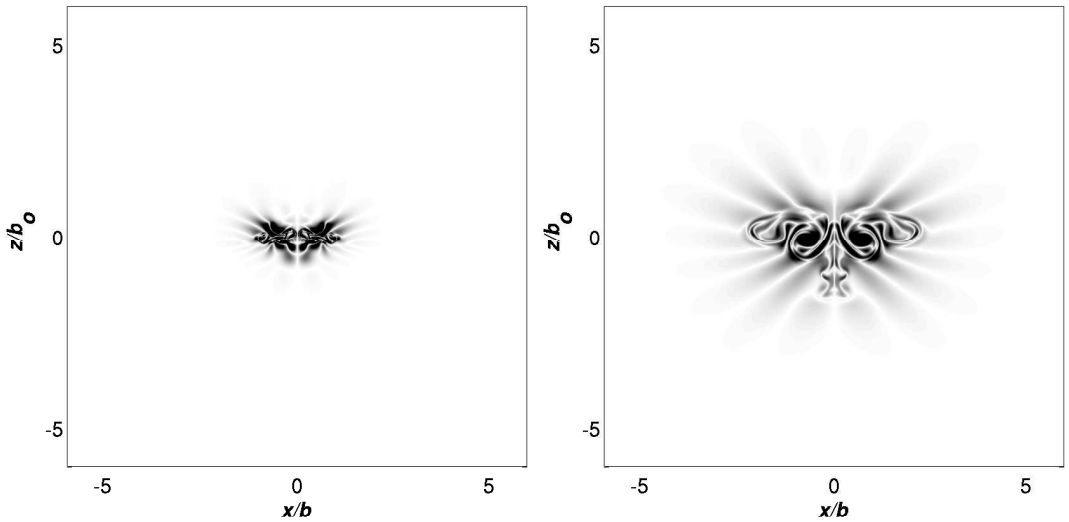

(iii) $Fr = 0.05$ Difference in Viscous Numerical Solutions (iv) $Fr = 0.5$

Figure 7.2b: Vorticity contours of a counter-rotating vortex pair at $Nt = 3\pi$.

surrounding the initial disturbance and that the size of this region is enlarged for increasing Fr. This may be seen more clearly in figure 7.2b (iii & iv), where the vorticity fields from the linear viscous simulations were subtracted from the nonlinear viscous simulations. For increasing Fr, the disturbance region's vorticity field breaks down into smaller structures through nonlinear interactions, which are more susceptible to dissipation.

7.3 Energy Exchange - Counter-rotating vortex pair

As seen in the density and vorticity fields, nonlinear interactions enhance mixing and viscous effects. These interactions can significantly influence the energetics of the flow field.

Figure 7.3 shows the 2DPSD for the linear viscous simulations and nonlinear viscous simulations for $Fr = 0.05$ and $Fr = 0.5$ at $Nt = 3\pi$. As observed in the linear viscous simulations, the energy magnitude is reduced for increasing Fr due to viscous dissipation. However, since it is the nonlinear interactions that cause energy to transfer to different wave-numbers, the energy field retains the same general profile. In the nonlinear simulations it is seen that the energy is transferred among wave-numbers. This trait is enhanced the weaker the stratification, where it is seen in figure 7.3d that there is spreading of energy to higher wave-numbers, leading to a transfer of energy to smaller scales which are more susceptible to viscous dissipation. Therefore, we observe that the larger the Fr, the more the energy's magnitude decreases.

Recall that in the analytical study there is no transfer of energy between wave-numbers, resulting in a time independent 1DPSD (figure 6.4). Figure 7.4 shows the 1DPSD for the linear viscous simulations and nonlinear viscous simulations for $Fr = 0.05$ and $Fr = 0.5$ at $Nt = 0, \pi, 2\pi, 3\pi, 4\pi$. As observed in the

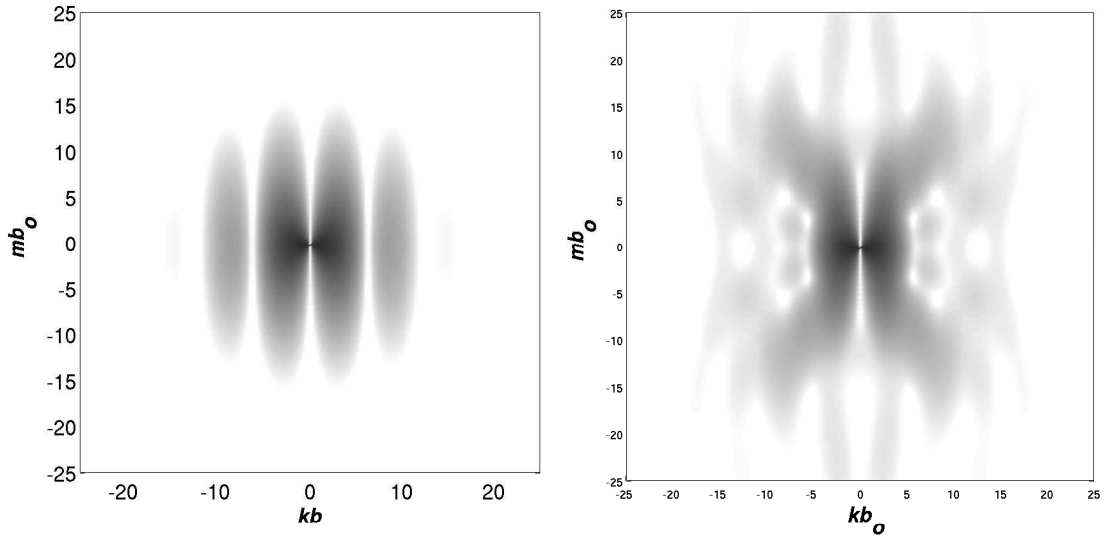

(a) Linear Viscous Solution $Fr = 0.05$ (b) Nonlinear Viscous Solution

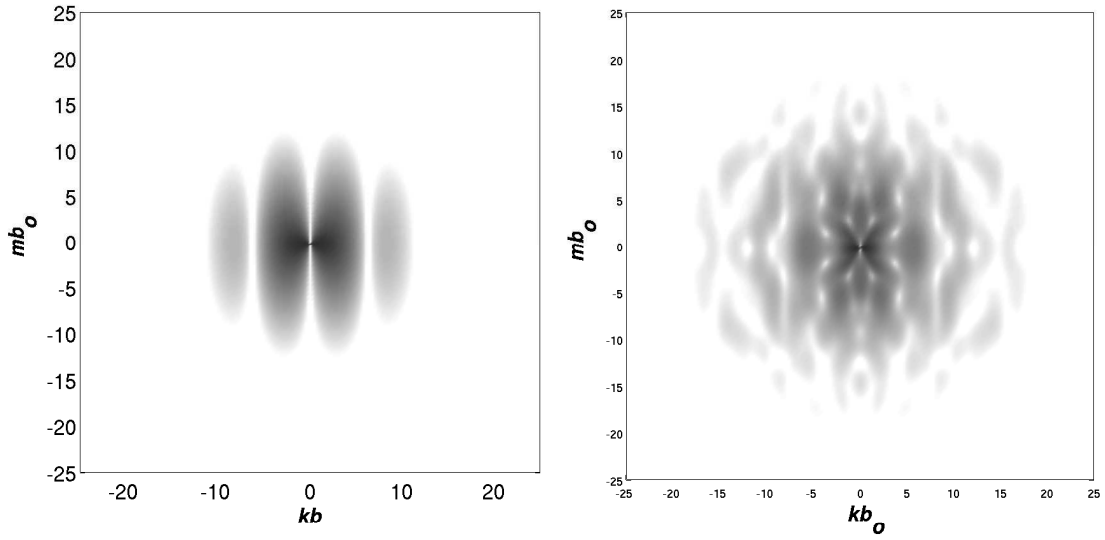

(c) Linear Viscous Solution $Fr = 0.5$ (d) Nonlinear Viscous Solution

Figure 7.3: 2DPSD plots for counter-rotating vortex pair in a viscous fluid at $Nt = 3\pi$

2DPSD (figure 7.3), the energy magnitude in the linearized viscous simulations is reduced for increasing Fr due to viscous dissipation (figure 7.4a,c). However, the peak energy is found to retain its corresponding K value in time. In the nonlinear simulations (figure 7.4b,d), the peak energy and corresponding K value change in time. For the $Fr = 0.05$, the nonlinearities in the flow cause the peak energy to decrease slightly and for the energy to spread to other wave-numbers. For $Fr = 0.5$ (figure 7.4d), there are two distinct peaks during the time evolution. These peaks are due to the wave-wave interactions. In time the peak at larger wave-numbers decreases at an enhanced rate compared with the peak at lower wave-numbers. The energy is removed by viscous dissipation which is enhanced by nonlinear interactions. The peak energy found at the lower wave-numbers converges to a relatively constant value indicating that the flow field reaches a relatively linear state. The time that it takes for the flow to reach this state is Fr dependent.

In order to estimate when this conversion time occurs, the behavior of the peak energy associated with the lower wave-number for the nonlinear simulations is investigated for various Fr (figure 7.5a). We observed that the peak energy for each Fr converges in time to a relatively constant value, indicating a relatively linear state. We will note that in the case of $Fr = 1$ that the peak energy magnitude varies due to difficulties in distinguishing between the numerous peaks in the 1DPSD.

We are able to estimate subjectively the times, Nt_{steady}, at which the distribution of energy in wave space is relatively steady. For $Fr \lesssim 0.1$, specific times at which this relatively linear state was reached were estimated by observing the transition in the peak energy rate of change to a nearly stable decay. In figure 7.6a, we see that the time at which this state is reached is relatively linear for these lower Fr, where we may estimate the time at which the nonlinear effects become relatively insignificant by $Nt_{steady} = 21.5\pi Fr$. For $Fr > 0.1$, the time to reach the relatively linear state is difficult to decipher due to oscillations in the peak energy in time. However, it is observed that the main changes in the peak

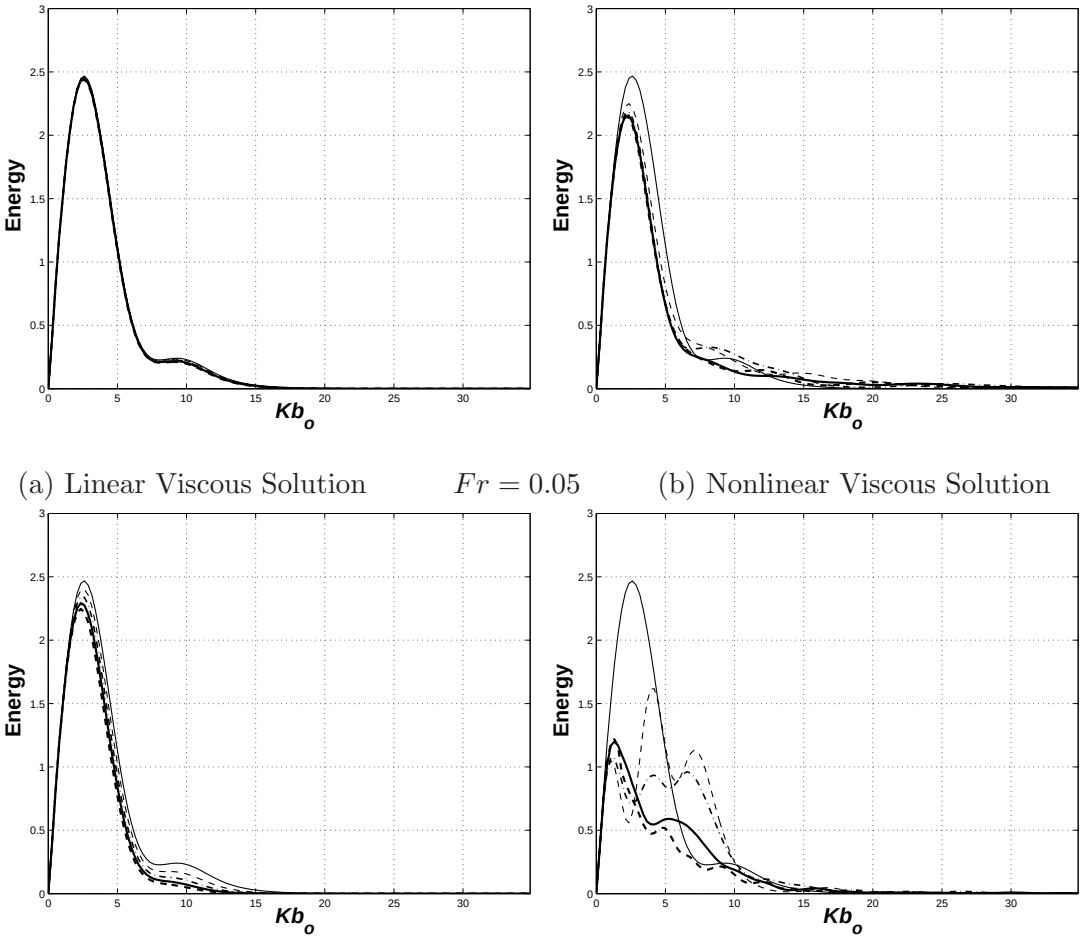

(a) Linear Viscous Solution $Fr = 0.05$ (b) Nonlinear Viscous Solution

(c) Linear Viscous Solution $Fr = 0.5$ (d) Nonlinear Viscous Solution

Figure 7.4: 1DPSD for *Counter-rotating* vortex pair, where $Nt = 0$ (-), $Nt = \pi$ (- -), $Nt = 2\pi$ (-·-), $Nt = 3\pi$ (**-**), $Nt = 4\pi$ (**- -**)

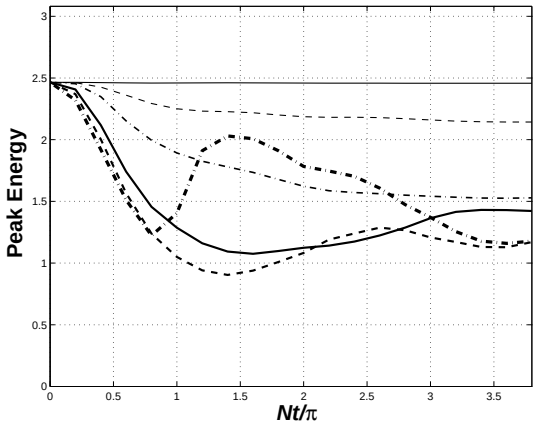

Figure 7.5: 1DPSD peak energy for counter-rotating vortex pair versus time for nonlinear viscous simulations, where $Fr = 0.01$ (-), $Fr = 0.05$ (- -), $Fr = 0.1$ (-··-), $Fr = 0.3$ (-), $Fr = 0.5$ (- -), $Fr = 1$ (-··-) .

energy occurs over the duration of the first buoyancy period.

During the time duration $Nt \lesssim Nt_{steady}$, the wave-number associated with the peak energy converges to a relatively constant value. Figure 7.6b shows the wave-number associated with this nearly linear state, K_{steady}. We observe that K_{steady} rapidly decreases for increasing Fr, for $Fr \lesssim 0.1$. However for Fr ranging between 0.1 and 1, K_{steady} decreases minimally in comparison with the lower Fr indicating that buoyancy has less of an effect on the wave-number in which the peak energy resides. We would then expect to see a change in the rate that energy is being removed from the disturbance region around $Fr = 0.1$.

Figure 7.7 provides a comparison of the rate at which the energy is removed from the disturbance region for the analytical model, linear viscous simulations and nonlinear viscous simulations. In this figure, E is integrated over a square region surrounding the counter-rotating vortex pair, where $L_{source} = 12b_o$. It is observed that in the case of $Fr = 0.05$, the effect of viscosity on the linearized simulation is nearly negligible. However, there is a notable decrease in energy for the nonlinear simulations. For $Fr = 0.5$, the effect of viscosity on the linear simulations is more substantial and the effect of the nonlinear interactions cause the energy to rapidly

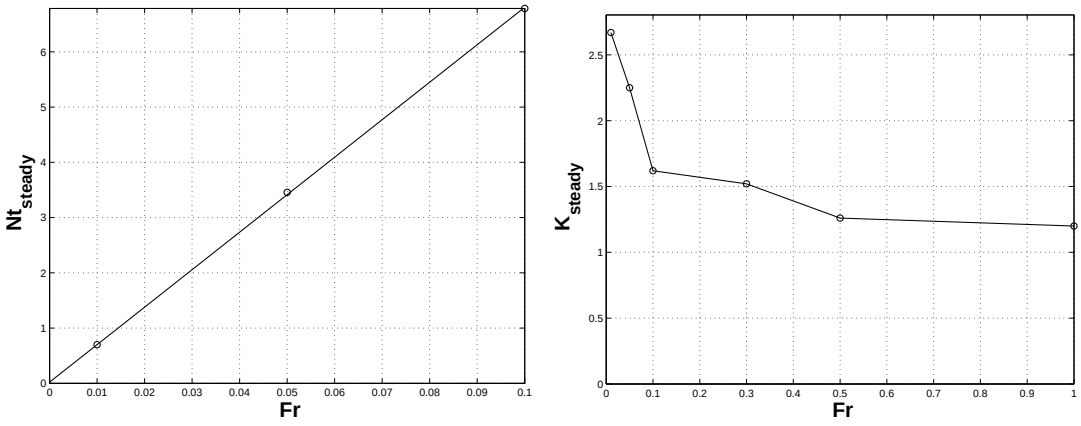

(a) Nt of linear state (b) K of linear state

Figure 7.6: Relatively linear state conditions for counter-rotating vortex pair nonlinear viscous simulations.

dissipate and propagate away from the disturbance region.

Figure 7.8a shows the disturbance region's energy from the nonlinear simulations for $0.01 \leq Fr \leq 1.0$. It is evident that for increasing Fr there is an increase in energy being removed from the disturbance region due to viscosity and internal waves. Recall that in chapter 6 the analytical solution's rate of decay of energy in the initial disturbance region changed from a gradual decay to a rapid decay around $Nt = 2\pi$. Observing the behavior of the nonlinear simulations for $Fr \lesssim 0.1$ during the first buoyancy period, we see that for increasing Fr that this gradual change in energy rate becomes more substantial. After $Nt = 2\pi$, it is seen that the energy rate of change is linear with Fr (figure 7.8b). For $Fr > 0.1$, we find that Fr significantly influences the disturbance regions energy rate of change during the first buoyancy period. However after the first buoyancy period, Fr does not significantly effect the rate of change. This indicates that the nonlinear interactions are becoming less influential after $Nt = 2\pi$.

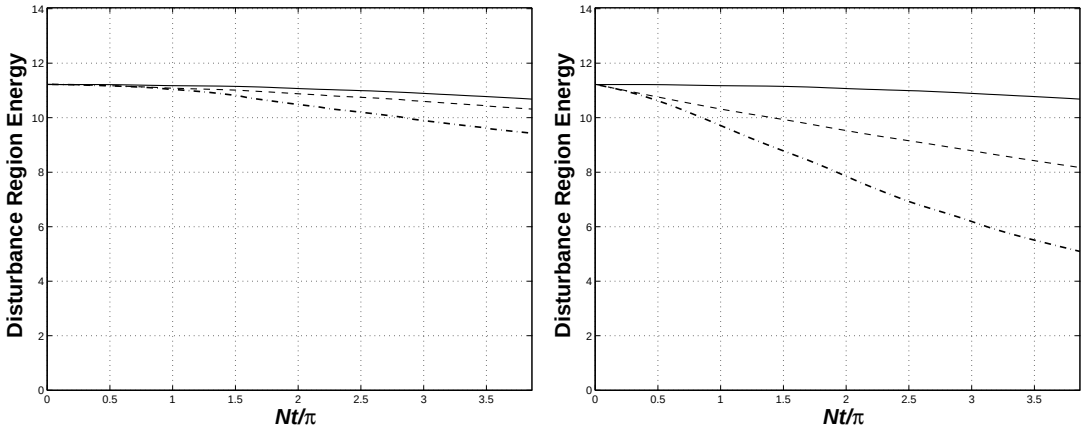

(a) $Fr = 0.05$ (b) $Fr = 0.5$

Figure 7.7: Disturbance region energy for the counter-rotating vortex pair. (Lines: Analytical (-), Linear Viscous Simulations (- -), Nonlinear Viscous Simulations (-·-))

7.4 Multiple Vortex Pairs

With a better understanding of the nonlinear interactions taking place in a viscous fluid with the initial condition of a counter-rotating vortex pair, we are now ready to address the more complicated co-rotating vortex quadrupole configuration (VQ) that was previously studied in chapter 6.

Figure 7.9a,b shows the VQ perturbed density fields from the analytical solution, linear viscous simulations and nonlinear viscous simulations for $Fr = 0.05$ and $Fr = 0.5$ at $Nt = 3\pi$. In figure 7.9a, if we compare the results from the linear viscous simulations (iii & iv) with the analytical solution (i & ii), we observe that as Fr increases that the effects of viscosity are greater, while it is seen that the density field appears more diffused. However, viscosity has done little to change the general flow behavior as was found in the counter-rotating vortex pair. In figure 7.9b (i & ii) the nonlinear simulation results are presented. It is apparent that the flow is experiencing mixing and viscous dissipation at the disturbance region. When comparing it to the linear viscous simulations (figure 7.9b (iii &

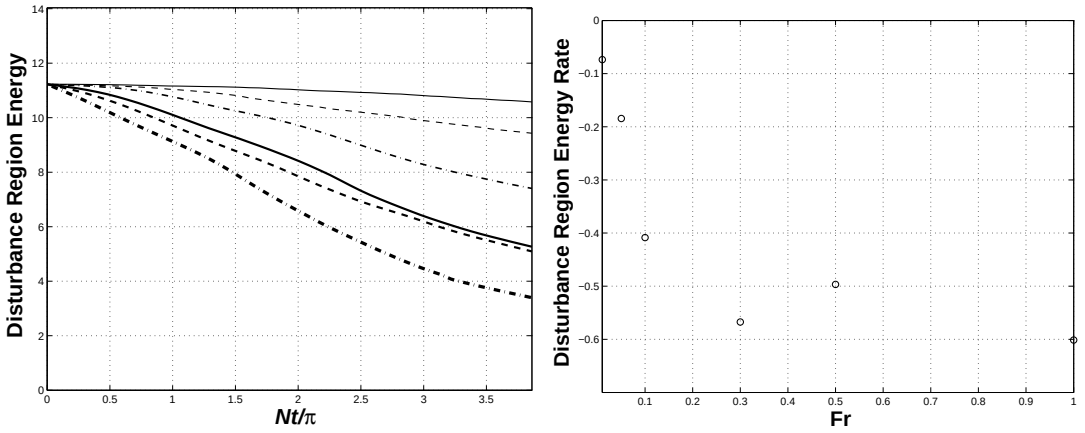

(a) Energy (b) Energy Rate

Figure 7.8: Disturbance region (a) energy and (b) energy rate after $Nt = 2\pi$ for counter-rotating vortex pair nonlinear viscous simulations, where $Fr = 0.01$ (-), $Fr = 0.05$ (- -), $Fr = 0.1$ (-·-), $Fr = 0.3$ (-), $Fr = 0.5$ (- -), $Fr = 1$ (-··-).

iv)), it is seen that as Fr is increased the region in which nonlinear interactions affect the flow's behavior is increased, as was also observed in the counter-rotating vortex pair.

The mixing occurring in the disturbance region may more clearly be observed when looking at contours of vorticity. Figure 7.10a,b shows the VQ vorticity fields from the analytical linearized equations, linear viscous simulations and nonlinear viscous simulations for $Fr = 0.05$ and $Fr = 0.5$ at $Nt = 3\pi$. As shown in the density perturbation contours, when we compare the results from the linear viscous simulations with the analytical solution, we observe that as Fr increases, viscous dissipation is enhanced, but that the general flow behavior is the same. However, when comparing the nonlinear and linear viscous results, it becomes apparent that increasing Fr causes the disturbance region to be greatly modified. In figure 7.10b (i & ii) the nonlinear simulation results are presented. When observing the disturbance region, it is seen that there is an enhanced amount of mixing

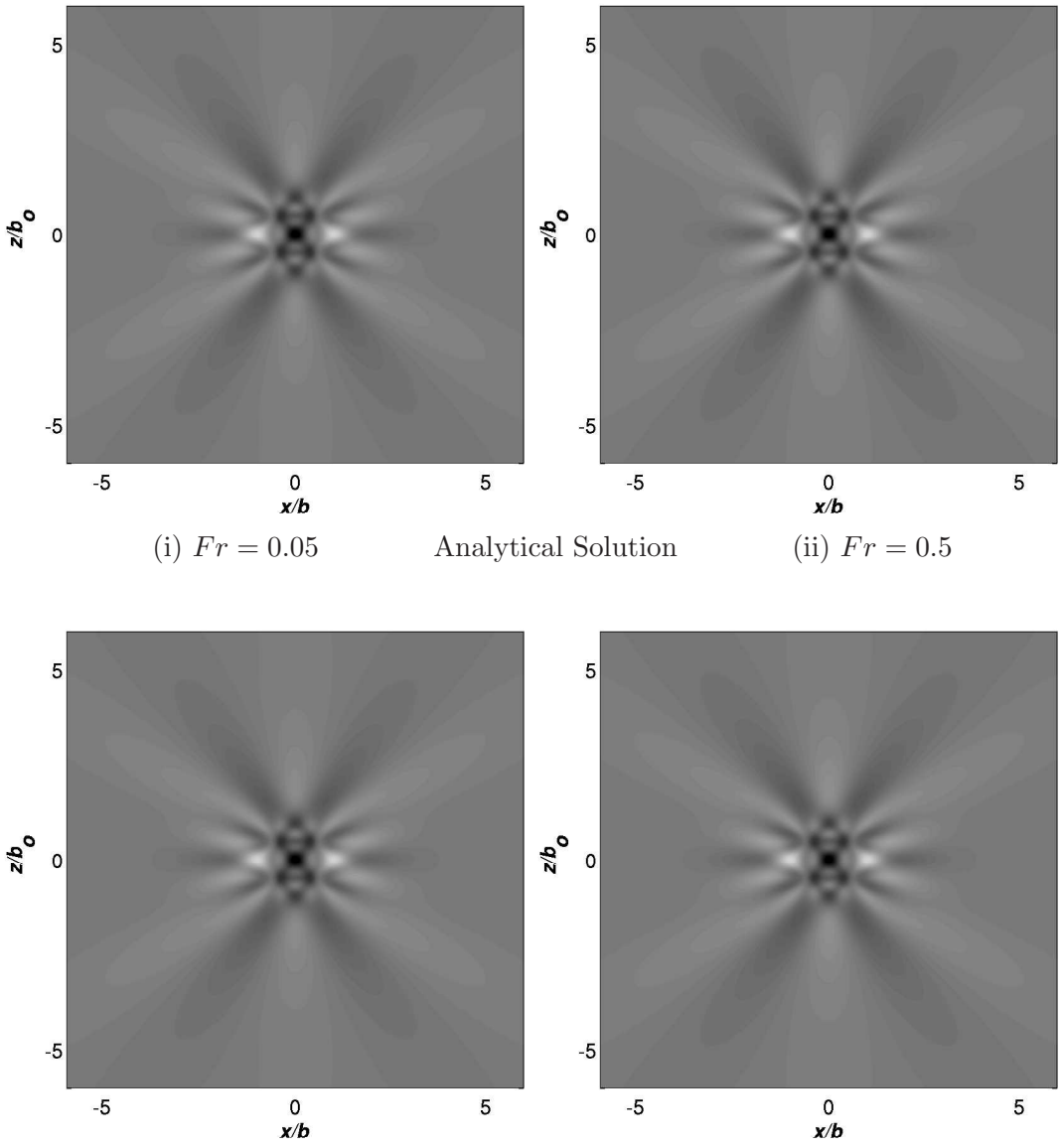

(i) $Fr = 0.05$ Analytical Solution (ii) $Fr = 0.5$

(iii) $Fr = 0.05$ Linear Viscous Numerical Solution (iv) $Fr = 0.5$

Figure 7.9a: Perturbed density contours of VQ at $Nt = 3\pi$ (Domain $L = 24b_o$).

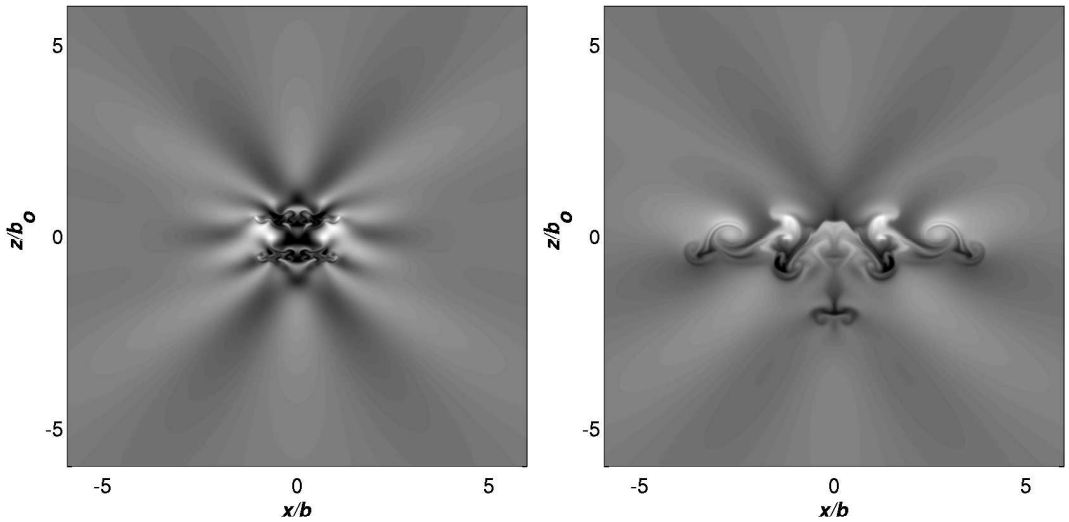

(i) $Fr = 0.05$ Nonlinear Viscous Numerical Solution (ii) $Fr = 0.5$

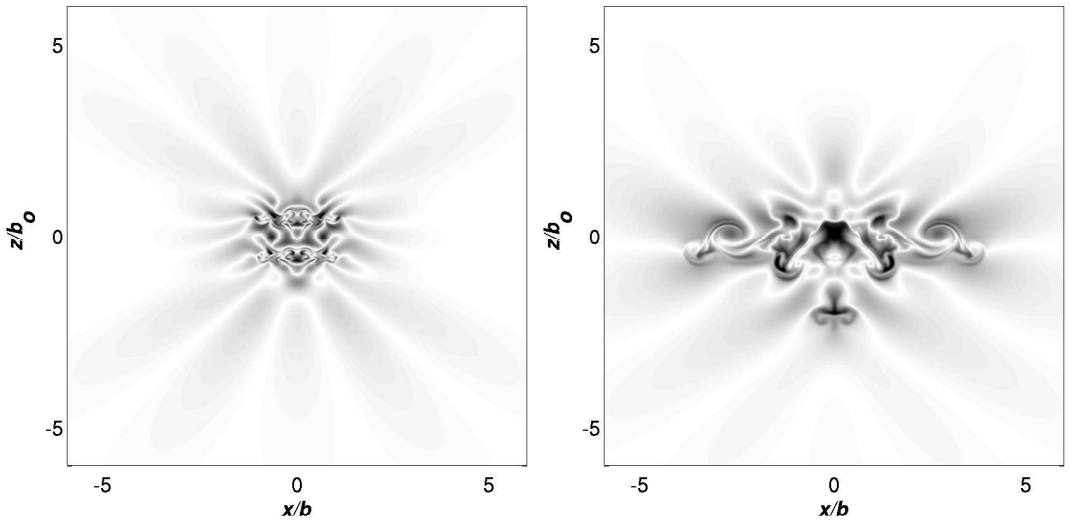

(iii) $Fr = 0.05$ Difference in Viscous Numerical Solutions (iv) $Fr = 0.5$

Figure 7.9b: Perturbated density contours of VQ at $Nt = 3\pi$ (Domain $L = 24b_o$).

for increasing Fr, which occurs on smaller scales. We can see the extent of the affects that nonlinear interactions have on the disturbance region if we subtract out the linear viscous vorticity from the nonlinear viscous vorticity (figure 7.10b (iii & iv)). The region in which nonlinear interactions affect the flow increases as Fr increases.

Figure 7.11 shows the 2DPSD for the linear viscous simulations and nonlinear viscous simulations for $Fr = 0.05$ and $Fr = 0.5$ at $Nt = 3\pi$. As we observed in the single vortex pair study, the energy magnitude is reduced in the linear viscous simulations for increasing Fr due to viscous dissipation. For the nonlinear flow, the energy is seen to transfer between wave-numbers more significantly for increasing Fr. While the energy was spread among wave-numbers in the vortex pair study, it is evident that for this more complex flow that there is much more energy being transferred to higher wave-numbers. We note that our wave-number space is carried out to $k = m = \pm 268$ in order to properly resolve the flow and avoid aliasing.

Figure 7.12 shows the 1DPSD for the linear viscous simulations and nonlinear viscous simulations for $Fr = 0.05$ and $Fr = 0.5$ at various Nt, results of which emulate the counter-rotating vortex pair. As observed in 2DPSD (figure 7.11), the energy magnitude in the linearized viscous simulations is reduced for increasing Fr due to viscous dissipation. However, the peak power is found to retain its corresponding wave-number in time since there is no mechanism for transferring energy among wave-numbers in linear flow. For the nonlinear viscous simulations, we find that there is substantial spreading of energy to higher wave-numbers for increasing Fr. Note that as in the counter-rotating vortex pair that during the duration of the time evolution there is more than one peak. This trait is enhanced for increasing Fr. However, the peak energy associated with the linear terms converge to a relatively constant value at lower wave-numbers, indicating a convergence to a nearly linear state. The duration time of this convergence is dependent on the level of stratification as will be discussed below.

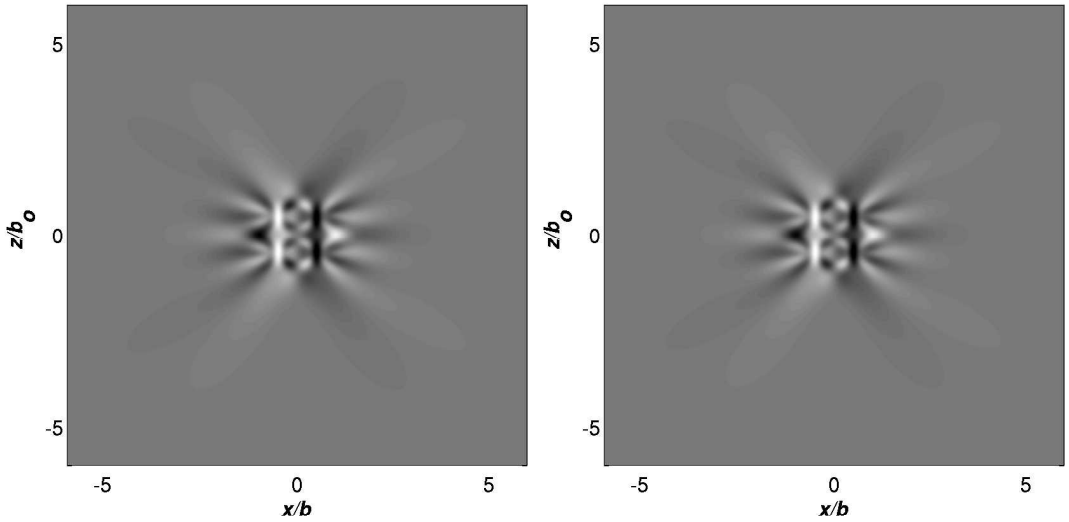

(i) $Fr = 0.05$ Analytical Solution (ii) $Fr = 0.5$

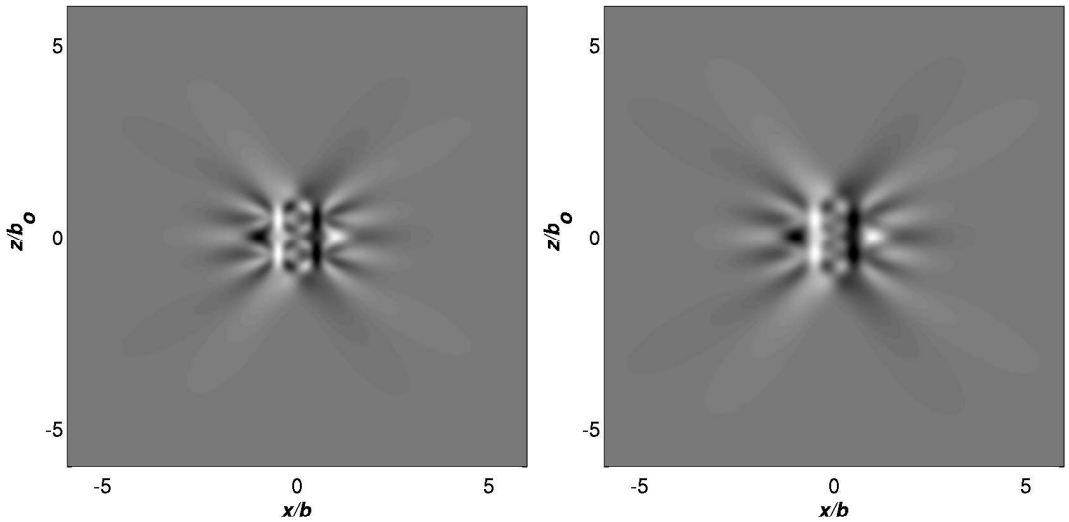

(iii) $Fr = 0.05$ Linear Viscous Numerical Solution (iv) $Fr = 0.5$

Figure 7.10a: Vorticity contours of VQ at $Nt = 3\pi$.

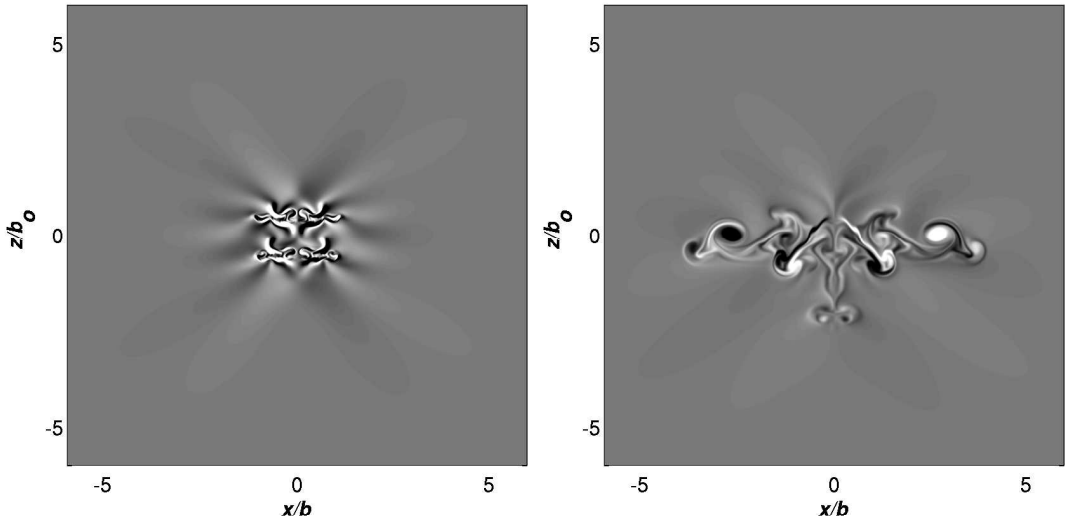

(i) $Fr = 0.05$ Nonlinear Viscous Numerical Solution (ii) $Fr = 0.5$

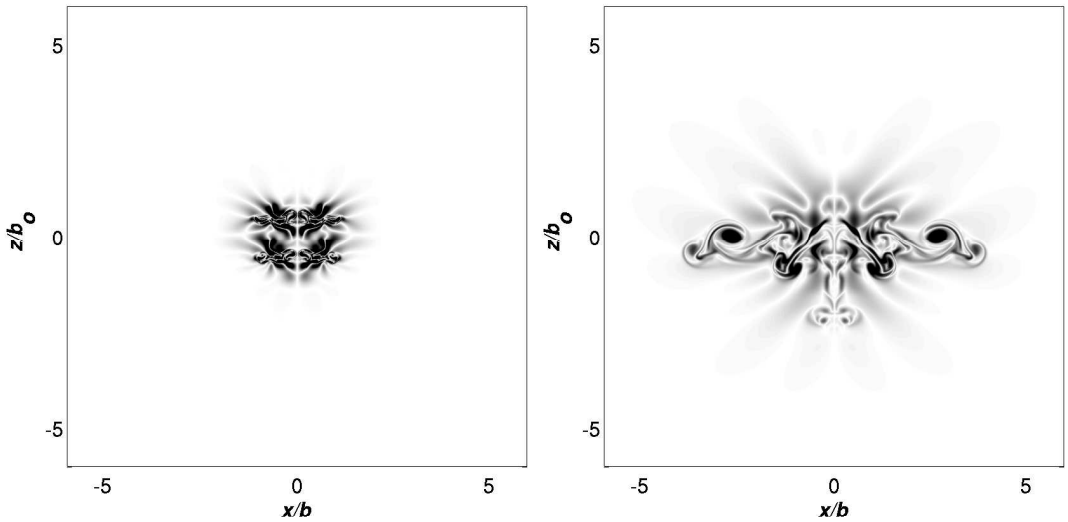

(iii) $Fr = 0.05$ Difference in Viscous Numerical Solutions (iv) $Fr = 0.5$

Figure 7.10b: Vorticity contours of VQ at $Nt = 3\pi$.

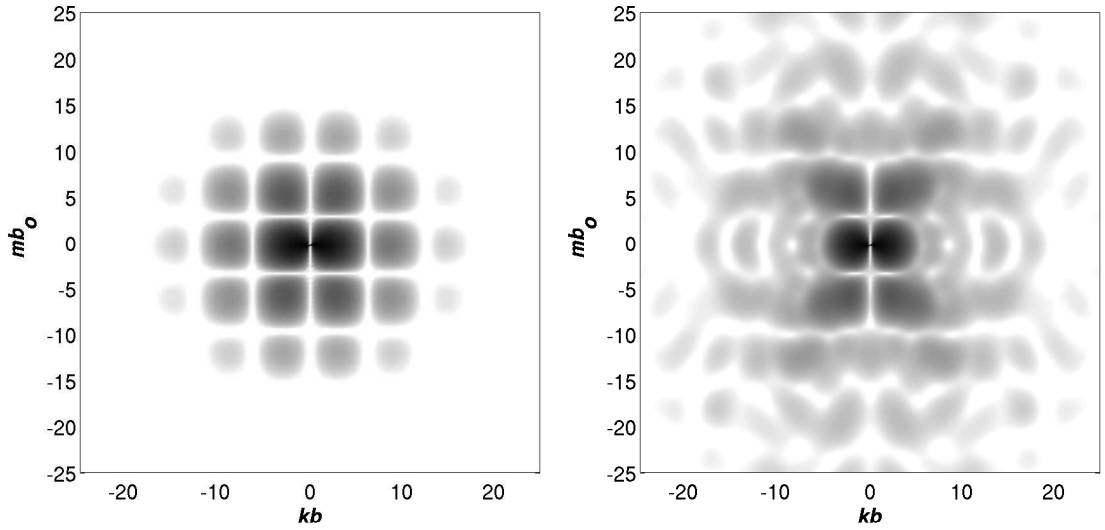

(a) Linear Viscous Solution $Fr = 0.05$ (b) Nonlinear Viscous Solution

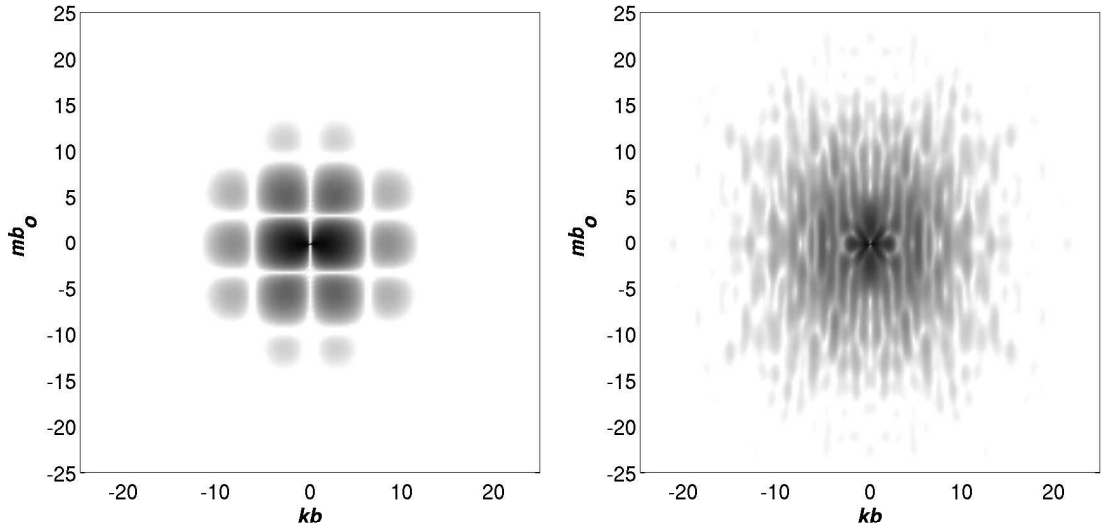

(c) Linear Viscous Solution $Fr = 0.5$ (d) Nonlinear Viscous Solution

Figure 7.11: 2DPSD for VQ in a viscous fluid at $Nt = 3\pi$.

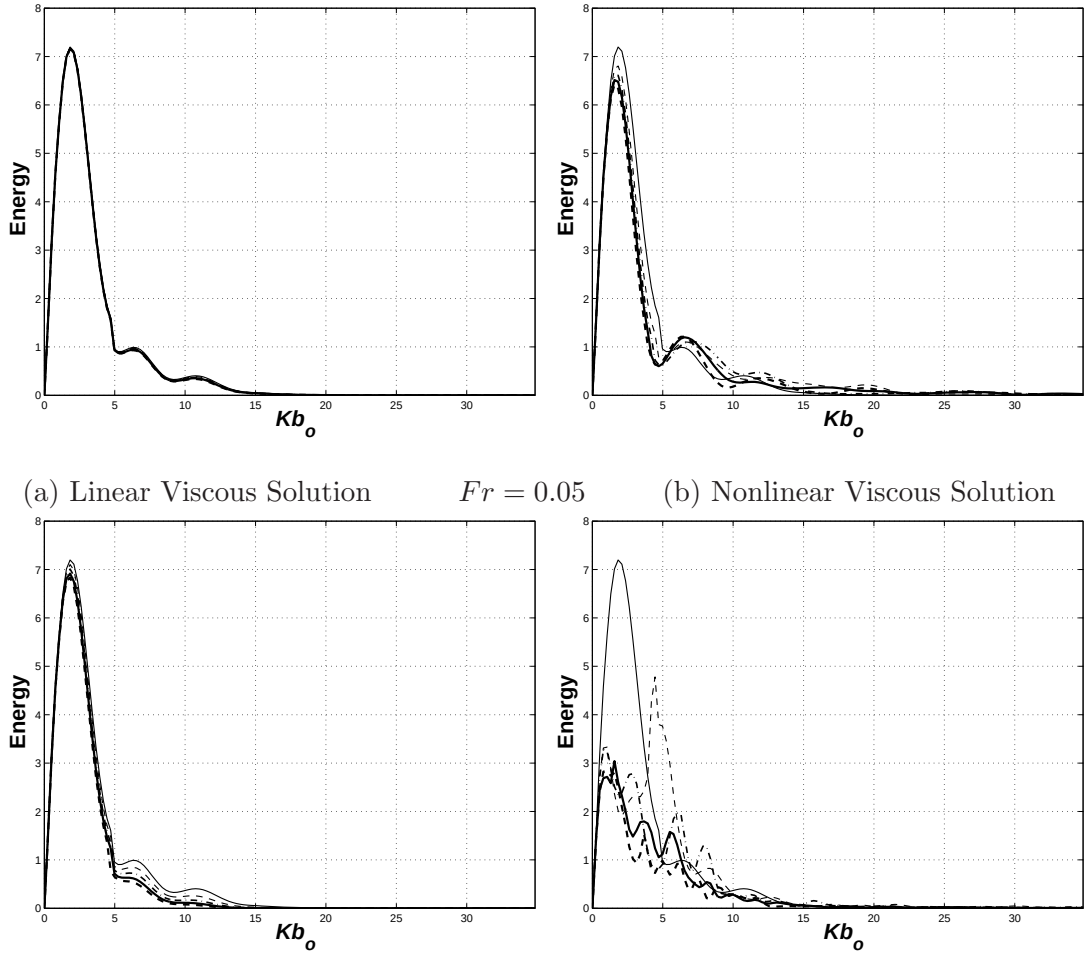

(a) Linear Viscous Solution $Fr = 0.05$ (b) Nonlinear Viscous Solution

(c) Linear Viscous Solution $Fr = 0.5$ (d) Nonlinear Viscous Solution

Figure 7.12: 1DPSD for VQ, where $Nt = 0$ (-), $Nt = \pi$ (- -), $Nt = 2\pi$ (-·-), $Nt = 3\pi$ (-), $Nt = 4\pi$ (- -).

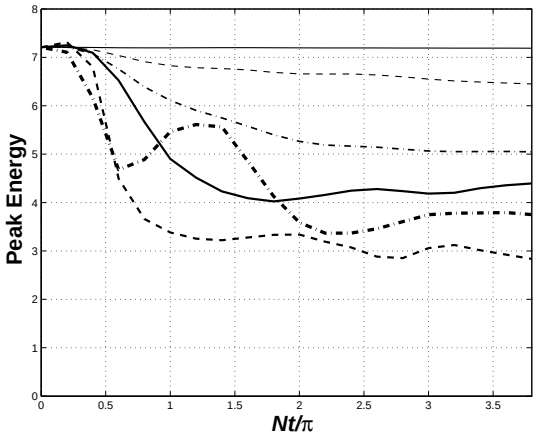

Figure 7.13: 1DPSD peak energy for VQ versus time for nonlinear viscous simulations, where $Fr = 0.01$ (-), $Fr = 0.05$ (- -), $Fr = 0.1$ (-·-), $Fr = 0.3$ (-), $Fr = 0.5$ (- -), $Fr = 1$ (-·-) .

Figure 7.13, shows the peak power for the nonlinear simulations versus Nt for various Fr, where it is observed that the peak power for each Fr converges in time to a relatively constant value. In the same manner as done in the counter-rotating vortex pair, we estimate the time, Nt_{steady}, at which the flow reaches a relatively linear state. For $Fr \leq 0.1$, we see that the time at which this state is reached is linear with Fr (figure 7.14a), where the line may be described by the slope $Nt_{steady} = 22.3\pi Fr$. In the previous section, it was found that Nt_{steady} for the counter-rotating vortex pair may be described by $Nt_{steady} = 21.5\pi Fr$. These time estimates are within a fraction of half a buoyancy period. For $Fr > 0.1$, we observe that the main changes in the peak energy occur prior to $Nt = 2\pi$ as was also found for the counter-rotating vortex pair.

We have estimated the wave-number associated with the peak energy, K_{steady} (figure 7.14b). We note the similarity of this figure to the counter-rotating vortex pair (figure 7.6b), where it is seen that for all flows that K_{steady} rapidly decreases for increasing Fr, for $Fr \lesssim 0.1$. However for Fr ranging between 0.1 and 1, the change in K_{steady} is minimal.

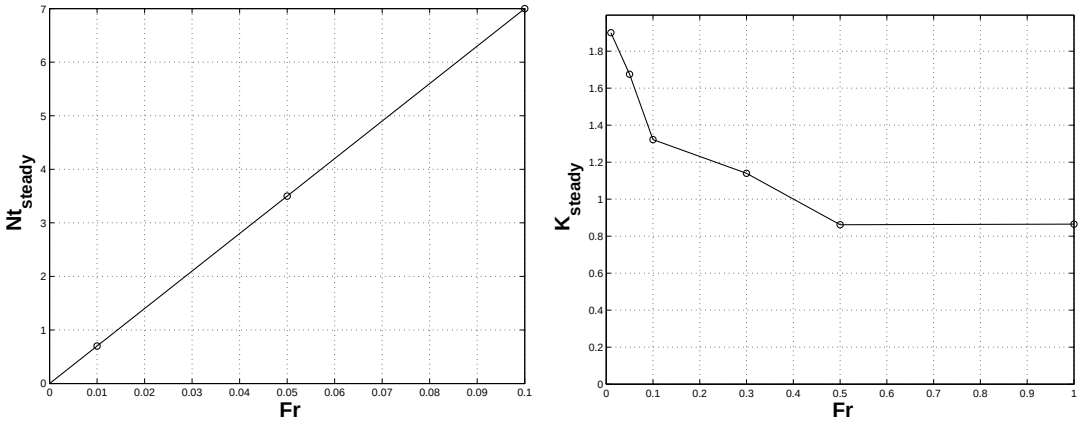

(a) Nt of linear state (b) K of linear state

Figure 7.14: Relatively linear state conditions for VQ nonlinear viscous simulations.

As was done for the counter-rotating vortex pair, we provide a comparison of the rate at which the energy is removed (dissipated or propagated away) from the disturbance region for the analytical solution, linear viscous simulations and nonlinear viscous simulations. In figure 7.15, the E is integrated over a square region surrounding the vortices, where $L_{source} = 12b_o$. As in the counter-rotating vortex pair for $Fr = 0.05$, the effect of viscosity on the linear interactions is nearly negligible for these more complex flows. However, there is a notable decrease in energy when nonlinear interactions are taken into account. For $Fr = 0.5$, there is a substantial affect due to the nonlinear interactions in the flow. When compared to the counter-rotating vortex pair it is seen that the rate at which the disturbance region loses energy is significantly enhanced for this more complex flow.

Figure 7.16a compares the disturbance region's energy from the nonlinear simulations for $0.01 \leq Fr \leq 1.0$. When comparing the disturbance region's energy of the VQ (figure 7.16a) with the counter-rotating vortex pair (figure 7.8a), it is apparent that there is a distinctive relationship between Fr and the rate at which energy leaves the vicinity. The same observations that were made for the counter-rotating vortex pair may be made for the VQ. For $Fr \lesssim 0.1$, the energy rate is linear

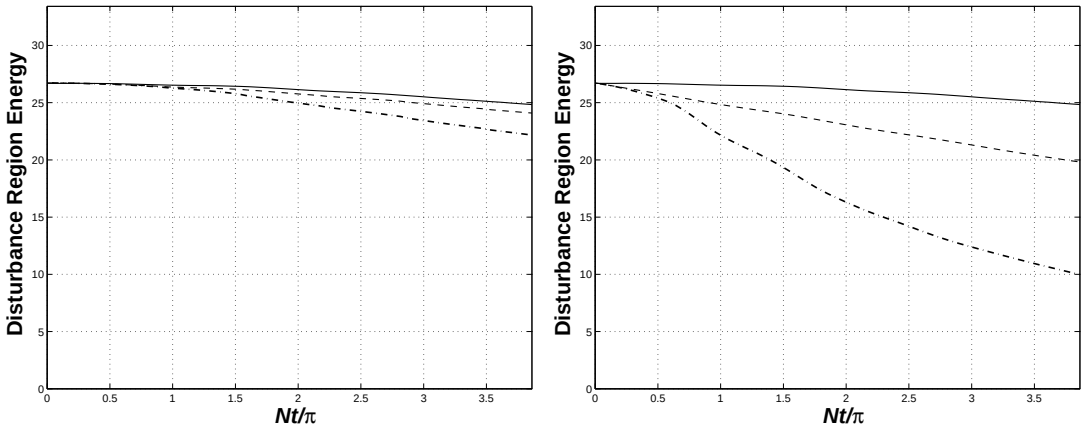

(a) $Fr = 0.05$ (b) $Fr = 0.5$

Figure 7.15: Disturbance region energy for the :w VQ, (Lines: Analytical (-), Linear Viscous Simulations (- -), Nonlinear Viscous Simulations (-·-).

with Fr after $Nt = 2\pi$. For $Fr > 0.1$, the energy rate is not significantly altered by Fr after $Nt = 2\pi$, indicating a transition in the flow where the disturbance region's energy rate is not dependent on Fr. However, the rate at which energy leaves the disturbance region for VQ is significantly enhanced when compared with the counter-rotating vortex pair. The rate is more than a factor of two greater.

7.5 Stratification Levels

From the above analysis, we are now better able to characterize the flow based on the level of stratification.

From observations of the density and vorticity fields, we have seen that the effects of stratification on the nonlinear interactions in the flow increase with increasing Fr. We also have seen that the region over which nonlinearities effect the flow surrounding the vortex pairs increases with increasing Fr. Therefore, the solutions to the linearized analytical equations developed in the previous chapter begin to break down as Fr increases.

In our energy analysis, we discussed the influence of Fr on the nonlinear in-

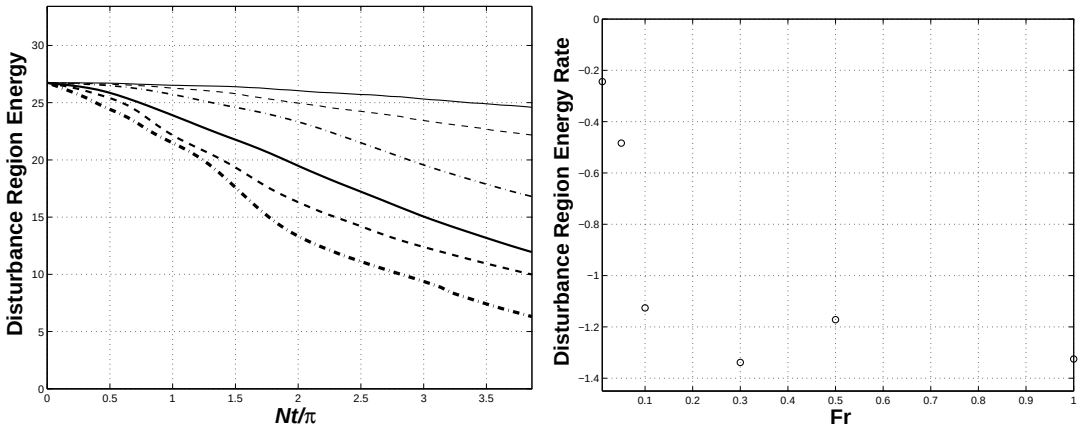

(a) Energy (b) Energy Rate

Figure 7.16: Disturbance region (a) energy and (b) energy rate after $Nt = 2\pi$ for VQ nonlinear viscous simulations, where $Fr = 0.01$ (-), $Fr = 0.05$ (- -), $Fr = 0.1$ (-·-), $Fr = 0.3$ (-), $Fr = 0.5$ (- -), $Fr = 1$ (-·-).

teractions of the flow. It was found that for increasing Fr, the greater the nonlinear interactions which caused energy to be transferred to higher wave-numbers. The energy at these higher wave-numbers are more susceptible to viscosity. Therefore, in time the flow's energy field became relatively linear. We were able to estimate specific times at which this linear state is reached for $Fr \lesssim 0.1$. We also found that the corresponding K value associated with the relatively linear state decreased linearly. For $Fr > 0.1$, we found that the primary changes in the peak energy in relation to wave-space occurred during the first buoyancy period and that the corresponding K value of this relatively linear state are comparable among Fr. Through qualitative estimates of the disturbance region's energy, we found that for $Fr > 0.1$ that Fr has less of an influence on the rate at which energy is removed (dissipated and propagated away) from the region. Therefore, we conclude that a transition occurs for Fr between 0.1 and 0.3. Based on this conclusion, we define a strongly stratified flow as $Fr \lesssim 0.1$ and a moderately stratified flow having $Fr > 0.1$. Note we have not discussed the upper limit of the moderately stratified flow regime marking the distinction between moderately and weakly stratified. In

chapter 5, we found that for $Fr \gtrsim 2$ that the flow was convectively dominated, falling within the weakly stratified regime. While a better distinction should be made, for now we leave the stratification levels falling between $1 \lesssim Fr \lesssim 2$ as undefined.

In the previous chapter, we derived the linearized, inviscid, analytical equations that describe vortex pairs, which we found is valid for $Fr << 1$, where nonlinear and viscous effects are not important for adequately large Re_{Γ}. Through this analysis, we are now better able to distinguish for what range of Fr the solution is valid. We conclude that the analytical solutions are quantitatively correct for $Fr \lesssim 0.01$ and qualitatively correct for $Fr \lesssim 0.1$. Although there is some influence of weak nonlinearities and viscous effects, the general flow behavior remains unaltered and we are able to predict when the flow reaches a relatively linear state, indicating that the flow is governed by linear interactions.

7.6 Summary

In this chapter, we numerically studied the effect of stratification on different vortex pair configurations. The levels of stratification considered are within the range of strongly to moderately stratified environments, $0.01 \leq Fr \leq 1.0$. In all simulations $Re_{\Gamma} = 5000$. Results from this study show the effect that Fr has on the generated internal wave field, vorticity field and energy field of vortex pairs.

We have qualitatively shown through analysis of the density and vorticity fields that nonlinear interactions cause significant mixing and dissipation of the disturbance region and that the region containing these nonlinear interactions grows with increasing Fr. Nonlinear interactions cause energy to be transferred from large scales to small scales. Therefore, viscosity has more of an influence in these flows.

We have observed that the orientation of the vortex pairs within the stratified environment plays a significant role in energy transport. However, in all flow

configurations, the peak power associated with the energy field of the nearly linear state decreases for increasing Fr. It was shown that the time it takes for the energy field to reach this relatively linear state is approximately proportional to Fr when $Fr \lesssim 0.1$ and that the primary changes in the peak energy occur during the first buoyancy period for $Fr > 0.1$. By evaluating the evolution of the energy in the vicinity of the disturbance region, the rate at which energy leaves the region after the first buoyancy period is shown to increase for increasing $Fr \lesssim 0.1$. However, it is seen that for $Fr > 0.1$ that the rate is relatively independent of Fr.

Therefore, we clarify the definition of strong stratification when considering vortex pair configurations. We have found that there is a transition point at which the flow becomes less susceptible to buoyancy effects. We classify $Fr \lesssim 0.1$ as being strongly stratified where the behavior may be qualitatively modeled by the linear equations developed in chapter 6. The moderate regime is classified as $2.0 > Fr > 0.1$ where there appears to be a convergence to a relatively linear state after $Nt = 2\pi$.

Chapter 8

Conclusions

This work considers the fundamental dynamics of two-dimensional vortex pairs in unstratified and stratified environments and in particular:

- co-rotating vortex interactions and merging; and
- internal wave generation by co-rotating and counter-rotating vortex pairs.

These studies identify and describe key physical mechanisms and characterize flow behavior based on convective, diffusive and stratification effects. The investigation was conducted by means of analytical techniques and numerical simulations.

8.1 Symmetric co-rotating vortex pairs (unstratified)

In chapter 3, we identify the physical mechanism leading to merger through two-dimensional numerical simulations of a symmetric co-rotating vortex pair consisting of vortices of equal size and strength ($Re_\Gamma = 5000$). The evolution of the flow and merging process are described in terms of *four* phases. During the first phase (*diffusive/deformation phase*) the vortices grow by viscous diffusion and the

separation distance, b, remains constant. The diffusive growth of the vortices establishes the interaction of the gradient of vorticity, $\nabla\omega$, and mutually induced strain, S, which causes the vortices to deform elliptically. During this time, a distinct functional relation between vorticity and streamfunction exists, suggesting quasi-equilibrium conditions. However, in the vicinity of the hyperbolic points, and in particular of the central hyperbolic point (CH) where mutual interaction strengthens, the interaction of $\nabla\omega$ and S eventually produces a tilt in vorticity contours. At the outer hyperbolic points, this initiates filamentation. During the second phase (*convective/deformation* phase), the induced flow by the filaments acts to advect the vortices towards each other and enhances the mutually induced S but does not drive the merger to completion. The enhanced tilting and diffusion of vorticity near the CH causes vorticity from the core region to enter the exchange band where it is advected away. In the third phase (*convective/entrainment* phase), the vortex cores erode and the integrity of the vortices is significantly diminished. The cores are mutually entrained into the exchange band, whose induced flow becomes dominant and transforms the flow into a single compound vortex. The beginning of the last phase (*diffusive/axisymmetrization* phase) is marked by the end of the rapid reduction in b. During this phase there is a slow reduction in b as flow evolves towards axisymmetry.

Results from this study clarify the timing of the flow processes and the merging criterion. Past studies have stated that merger begins when the vortex cores growth rate deviates from that of a single vortex, but there was a lack of physical significance. We have identified the key physical mechanism of merger and showed that the rapid decrease in b is due to fluid from the cores being entrained into the exchange band. The time at which this process starts corresponds with the vortex cores growth rate deviation.

The present study provides fundamental insight on vortex interaction and the merging process. Most importantly, it provides a framework with which more complex flows may be analyzed. Further studies should consider other vorticity

distributions and higher Reynolds numbers. It is expected that vortex pairs in these flows will behave quite differently.

8.2 Asymmetric co-rotating vortex pairs (unstratified)

In chapter 4, we further consider vortex interactions and merging by considering an asymmetric (vortices of unequal strengths) case in which there is unequal influence of each of the vortices on each other. This enables the development of a more generalized merging criterion and a classification scheme for co-rotating vortex interactions in a viscous fluid. In the simulations presented, the same initial aspect ratio that was used in our previous study was utilized, $a_o/b_o = 0.157$. The initial strength of the stronger vortex is fixed at $Re_\Gamma = 5000$ and the initial strength of the weaker vortex is varied such that $0.4 \leq Re_{\Gamma,2}/Re_{\Gamma,1} \leq 1.0$.

The same physical mechanisms that govern symmetric vortex merger were found to govern asymmetric vortex interactions. We consider the flow in the co-rotating frame, which rotates at the same rate as the vortices rotate about one another, and describe the deformation of the vortices in terms of the interaction of vorticity gradient, $\nabla\omega$, and rate of strain, S, with emphasis placed on the interactions taking place in the vicinity of the CH point.

In asymmetric pairs, the flow structure and interactions are altered by the difference in vortex strengths. As in the symmetric vortex pair, the vortices initially grow by diffusion. However, the rate at which the vortices deform differs from each other. The stronger vortex deforms less than the weaker vortex due to the difference in induced S, and the tilt of $\nabla\omega$ contours. Therefore, the subsequent core detrainment of the weaker vortex occurs earlier than for the stronger vortex. However, the dominant attracting motion occurs only when, and if, core detrainment is established by the stronger vortex. When this occurs, if it occurs at all,

the vortex cores will be entrained into the exchange band. We found that this occurs for $0.7 \leq Re_{\Gamma,2}/Re_{\Gamma,1} \leq 0.9$. However in these cases, the stronger vortex ultimately dominates and entrains vorticity from the weaker vortex. We consider, therefore, the process as vortex merger since the result is an enhanced compound vortex. If the stronger vortex core is not detrained prior to significant erosion of the weaker vortex ($Re_{\Gamma,2}/Re_{\Gamma,1} \leq 0.6$), the weaker vortex is destroyed leaving the stronger vortex to remain in the flow relatively unaffected. In this case, merger does not occur.

From this understanding of the physics behind asymmetric vortex interactions, we develop a generalized merging criterion for unequal vortices. We consider the critical state for a given vortex to be associated with the establishment of core detrainment. A vortex strain parameter, γ_i, is defined in terms of the ratio of the strain rate at the CH point, S_{CH}, to the maximum vorticity of vortex i, ω_{vi}, thereby providing a measure of the relative strength of the induced strain rate at the CH point to the vortex strength. For all our simulations (including those conducted in the weakly stratified study), we find a single critical value for both vortices, $\gamma_{cr,1} = \gamma_{cr,2} = \gamma_{cr} \approx 0.247 \pm 0.007$, marking the point at which each vortex core is detrained. Through a scaling analysis, the critical strain rate is shown to be related to the critical aspect ratio in the case of symmetric vortex pairs. Similarly, through a scaling analysis, the time at which this critical strain rate is reached is found for both vortices.

We have developed a description for asymmetric vortex pair interactions for viscous flow. The key result is a generalized merging criterion formulated in terms of strain and vorticity. Through scaling analysis, this criterion is related to the critical aspect ratio found for symmetric vortex merger. This criterion is then used to predict when the flow processes occur and when/if the vortices merge.

This criterion was developed using moderate Re_Γ and Lamb-Oseen vortices with a Gaussian vorticity distribution. It would be of interest to test the criterion with further numerical simulations and laboratory experiments for higher Reynolds

numbers to see its generality. It is expected that the criterion would have to be modified to account for different vorticity profiles, which may only entail an additional scaling factor.

8.3 Symmetric co-rotating vortex pairs (weakly stratified)

In chapter 5, we used two-dimensional numerical simulations and considered a range of Reynolds numbers, $2000 \leq Re_\Gamma \leq 5000$, and Froude numbers, $Fr = 2$, 3, and 5. Stratification is considered weak, i.e. the flow is dominated by convection and diffusion, not by stratification ($Fr > 1$), and merging always occurs.

In a weakly stratified fluid, the flows state is dependent on the ratio of the diffusive time scale (growth of cores, establishment of $\nabla\omega$ and S interaction) to the turnover time (establishment of baroclinically generated vorticity, BV), i.e., the Reynolds number. It was found that a crossover Reynolds number, which is dependent on the initial aspect ratio, exists above which convective merging is accelerated with respect to unstratified flow and below which merging is delayed. The induced flow field caused by BV advects the vortices towards or away from each other, the amount of which is governed by the level of stratification which is characterized by Fr. This advection modify the strain rate field, resulting in an enhancement or hindrance of the $\nabla\omega$ amplification process. Therefore, initiation of the exchange band process and the convective/entrainment phase depends on both Re_Γ and Fr. However, once initiated the process is Re_Γ and Fr independent.

This description of merger allows for a more explicit determination of $(a/b)_{cr}$. We define the critical state of the flow to be the start of the convective/entrainment phase, beyond which there is no reversal and merging will occur. This time corresponds to when $a^2(t)$ deviates from linear growth and the exchange band process begins. At this point, we have found that for all flows considered that

$(a/b)_{cr} = 0.235 \pm 0.006$, where a is defined based on the second-moment of vorticity.

The results presented in this study apply to pairs of symmetric (equal) co-rotating Gaussian vortices at moderate Re_Γ and weak stratification. For more strongly stratified flows, buoyancy effects will alter the flows behavior causing the vortices to no longer merge. Future work should consider for what Fr this transition takes place. Furthermore, future studies should test to see if this criterion is valid for larger Re_Γ and different vorticity distributions.

8.4 Symmetric vortex pairs and the generation of linear internal waves

In chapter 6, through analytical techniques, we investigated the linear interactions of co-rotating vortex pairs, counter-rotating vortex pairs and two sets of co-rotating vortex pairs in a quadrupole configuration (VQ). Our linearized equations accurately approximate the flow in a strongly stratified environment ($Fr \lesssim 0.01$), where nonlinear effects may be neglected. In these equations, we assume moderate to large Re so that viscous effects are negligible.

Information concerning the flow's energy and distribution in wave space was computed analytically. It was found that there is a distinctive harmonic pattern of constructive and destructive wave interactions which are dependent on the flow geometry. For flows consisting of two vortices at the same vertical location, there is a harmonic pattern in the horizontal direction, which occur every $kb_o = 2\pi$. For more complex flows consisting of multiple vortex pairs, this harmonic pattern will become more complicated. In the VQ flow, which consists of four vortices, there is a harmonic pattern in the horizontal and vertical direction, which occur every $kb_o = 2\pi$ and $mb_o = 2\pi$. If more vortices were included there would be a more complicated pattern of constructive and destructive wave interactions.

Looking at the energy in terms of the one dimensional power spectral density (1DPSD), it was seen that the peak energy associated with the VQ is maintained in a lower wave-number than in the counter-rotating vortex pair. However, the peak energy magnitude of the VQ was significantly higher than the counter-rotating vortex pair. Through evaluation of the rate at which energy is removed from the disturbance region due to viscous dissipation and internal waves, it was found that early in time energy was removed faster from the VQ than the counter-rotating vortex pair, but that after approximately 9 buoyancy periods the rate at which energy is transferred from the disturbance region becomes relatively steady in both the VQ and counter-rotating vortex pair.

Solutions to these linearized equations provide accurate results for strongly stratified flows. It was shown that these equations may be manipulated to allow for varying initial conditions, which in the future could be used to calculate the linear flow behavior of a statistical distribution of vortex pairs that represents turbulence.

8.5 Symmetric vortex pairs and the generation of nonlinear internal waves

In chapter 7, we used numerical simulations to study the effect of moderately to strongly stratified fluid on a counter-rotating vortex pair and VQ. The levels of stratification considered are within the range of strongly to moderately stratified environments, $0.01 \leq Fr \leq 1.0$. In all simulations $Re_{\Gamma} = 5000$.

Through analysis of the density and vorticity fields, it was seen that nonlinear interactions cause significant mixing of vorticity. These interactions cause large-scale structures to evolve to small scale structures, which enhance dissipation. Therefore, viscosity has more of an influence in these flows. The time duration that it takes for the influences of these small structures to decay and reach a relatively linear state is Fr dependent. For $Fr \lesssim 0.1$, it was found that this time is approx-

imately linear with Fr and occurred prior to the completion of the first buoyancy period. For $Fr > 0.1$, it was found that the primary influences of these small structures occurred during the first buoyancy period. By evaluating the evolution of the energy in the vicinity of the disturbance region, it is shown that after the first buoyancy period the rate at which energy leaves the region increase for increasing $Fr \lesssim 0.1$ and is relatively constant for $Fr > 0.1$.

With this knowledge, we clarified the definition of strong stratification when considering vortex pair configurations. We have found that there is a transition point at which the flow becomes less susceptible to buoyancy effects after the first buoyancy period. We classify $Fr \lesssim 0.1$ as being strongly stratified and the behavior may be qualitatively modeled utilizing the analytical equations developed in chapter 6. The moderate regime is classified as $Fr > 0.1$ where convective effects are required to be taken into consideration during the first buoyancy period, but that there is a convergence of the flow to a relatively linear state occurring around the first buoyancy period. Note we have not discussed the upper limit of the moderately stratified flow regime marking the distinction between moderate and weak stratification. In chapter 5, we found that for $Fr \gtrsim 2$ that the flow was convectively dominated falling within the weakly stratified regime. While a better distinction should be made, for now we leave the stratification levels falling between $1 \lesssim Fr \lesssim 2$ as undefined. This is considered future work.

This study is a preliminary investigation into the effects of moderate stratification on vortex pairs and more complex flows. The study needs to distinguish between energy lost to internal waves and energy removed due to dissipation. The next step in this study, is to calculate the buoyancy flux across the boundary of the disturbance region in order to estimate the rate at which energy is being lost to internal waves. This would allow us to predict the strength of the wave and give us insight into the effect that dissipation has on the disturbance region.

8.6 Further Work

In unstratified two-dimensional flow there are a number of aspects of vortex pair interactions that are of interest. Further studies should consider larger Re_Γ that are more representative of flows found in the oceans and atmosphere. As observed in the weakly stratified and asymmetric co-rotating vortex pair studies, there is a strong Re_Γ dependence; at larger Re_Γ the flow may be greatly modified and not behave according to our low-Re_Γ criterion. Another aspect of these flows that should be researched further is the impact of vortex vorticity distributions. The addition of a turbulent core, which is realistic of aircraft wake and geophysical flows, is also of interest. Such strong cores will cause the dissipation and destruction of the vortices to be inhibited and may inevitably result in different regimes than that found at lower Re_Γ and more stable flows.

Future studies in stratified flows should consider the influence of strong and moderate stratification on multiple vortices and the internal wave field development. It would be interesting to investigate the internal wave field generated by a flow containing a turbulent patch both analytically for strongly stratified flows and numerically for moderately stratified flows.

Future research should consider the extension of these studies into three dimensions. It is known that pairs of co-rotating and counter-rotating vortex pairs undergo an elliptic instability in there axial direction when perturbed. In a stratified environment, this instability may be hindered or enhanced depending on the level of stratification and Re_Γ. Such studies have not been performed in regards to *horizontally* co-rotating vortex pairs in a stratified environment.

Appendix A

Elementary Vortex Systems

A.1 Initial Vorticity Distributions

The initial base flow consists of the superposition of Lamb-Oseen (Gaussian) vortices. The corresponding vorticity distribution for a single vortex (rotating in a clockwise direction) is given by,

$$\omega(x,z,t_o) = \Omega_o\, e^{\frac{-((x-x_c)^2+(z-z_c)^2)}{a_o^2}},$$

where $\Omega_o = \Gamma_o/\pi a_o^2$ is the peak magnitude of vorticity and $x_c = z_c = 0$. In the cases of multiple vortices, the distributions may be added together. The vorticity distribution for a co-rotating vortex pair (rotating in a counter-clockwise direction) is given by,

$$\omega(x,z,t_o) = \Omega_{o,1}\, e^{\frac{-((x-x_1)^2+(z-z_1)^2)}{a_o^2}} + \Omega_{o,2}\, e^{\frac{-((x-x_2)^2+(z-z_2)^2)}{a_o^2}},$$

where $\Omega_{o,i} = \Gamma_{o,i}/\pi a_o^2$ is the peak magnitude of vorticity for a particular vortex ($i = 1, 2$) and $x_1 = -x_2 = b_o/2$ and $z_1 = z_2 = 0$. For a counter rotating vortex pair with an advection velocity in the negative vertical direction,

$$\omega(x,z,t_o) = \Omega_{o,1}\, e^{\frac{-((x-x_1)^2+(z-z_1)^2)}{a_o^2}} - \Omega_{o,2}\, e^{\frac{-((x-x_2)^2+(z-z_2)^2)}{a_o^2}},$$

where $x_1 = -x_2 = b_o/2$ and $z_1 = z_2 = 0$. For a co-rotating quadrapole configuration with an outward advection velocity in the vertical direction,

$$\begin{aligned}\omega(x,z,t_o) = \Omega_{o,1}\, e^{\frac{-((x-x_1)^2+(z-z_1)^2)}{a_o^2}} - \Omega_{o,2}\, e^{\frac{-((x-x_2)^2+(z-z_2)^2)}{a_o^2}} \\ -\Omega_{o,3}\, e^{\frac{-((x-x_3)^2+(z-z_3)^2)}{a_o^2}} + \Omega_{o,4}\, e^{\frac{-((x-x_4)^2+(z-z_4)^2)}{a_o^2}},\end{aligned} \tag{A.1}$$

where $x_1 = -x_2 = -x_3 = x_4 = b_o/2$ and $z_1 = z_2 = -z_3 = -z_4 = b_o/2$.

A.2 Initial Velocity Distributions

The velocity field of the vortex systems may be described by $u = \frac{\partial \Psi}{\partial z}$ and $w = -\frac{\partial \Psi}{\partial x}$, where $\omega_y = -\nabla^2 \Psi$. This leads to the the velocity field of a single vortex (rotating in a counter-clockwise direction) to be described by

$$u(x,z,t_o) = \frac{1}{2}\frac{a_o^2 \Omega_o (z - z_c)}{(x-x_c)^2 + (z-z_c)^2}(1 - e^{-((x-x_c)^2-(z-z_c)^2)/a_o^2}) \tag{A.2}$$

and

$$w(x,z,t_o) = -\frac{1}{2}\frac{a_o^2 \Omega_o (x - x_c)}{(x-x_c)^2 + (z-z_c)^2}(1 - e^{-((x-x_c)^2-(z-z_c)^2)/a_o^2}), \tag{A.3}$$

where $x_c = z_c = 0$. In the case of the co-rotating vortex pair, the velocity components u and w are

$$\begin{aligned}u(x,z,t_o) = \frac{1}{2}\frac{a_o^2 \Omega_{o,1} (z - z_1)}{(x-x_1)^2 + (z-z_1)^2}(1 - e^{-((x-x_1)^2-(z-z_1)^2)/a_o^2}) \\ +\frac{1}{2}\frac{a_o^2 \Omega_{o,2} (z - z_2)}{(x-x_2)^2 + (z-z_2)^2}(1 - e^{-((x-x_2)^2-(z-z_2)^2)/a_o^2})\end{aligned} \tag{A.4}$$

and

$$\begin{aligned}w(x,z,t_o) = -\frac{1}{2}\frac{a_o^2 \Omega_{o,1} (x - x_1)}{(x-x_1)^2 + (z-z_1)^2}(1 - e^{-((x-x_1)^2-(z-z_1)^2)/a_o^2}) \\ -\frac{1}{2}\frac{a_o^2 \Omega_{o,2} (x - x_2)}{(x-x_2)^2 + (z-z_2)^2}(1 - e^{-((x-x_2)^2-(z-z_2)^2)/a_o^2}),\end{aligned} \tag{A.5}$$

where $x_1 = -x_2 = b_o/2$ and $z_1 = z_2 = 0$. In the case of the counter-rotating vortex pair, the velocity components u and w are

$$\begin{aligned} u(x,z,t_o) = &\frac{1}{2}\frac{a_o^2\Omega_{o,1}(z-z_1)}{(x-x_1)^2+(z-z_1)^2}(1-e^{-((x-x_1)^2-(z-z_1)^2)/a_o^2}) \\ &-\frac{1}{2}\frac{a_o^2\Omega_{o,2}(z-z_2)}{(x-x_2)^2+(z-z_2)^2}(1-e^{-((x-x_2)^2-(z-z_2)^2)/a_o^2}) \end{aligned} \tag{A.6}$$

and

$$\begin{aligned} w(x,z,t_o) = &-\frac{1}{2}\frac{a_o^2\Omega_{o,1}(x-x_1)}{(x-x_1)^2+(z-z_1)^2}(1-e^{-((x-x_1)^2-(z-z_1)^2)/a_o^2}) \\ &+\frac{1}{2}\frac{a_o^2\Omega_{o,2}(x-x_2)}{(x-x_2)^2+(z-z_2)^2}(1-e^{-((x-x_2)^2-(z-z_2)^2)/a_o^2}), \end{aligned} \tag{A.7}$$

where $x_1 = -x_2 = b_o/2$ and $z_1 = z_2 = 0$. For a co-rotating quadrapole configuration with an outward advection velocity in the vertical direction,

$$\begin{aligned} u(x,z,t_o) = &\frac{1}{2}\frac{a_o^2\Omega_{o,1}(z-z_1)}{(x-x_1)^2+(z-z_1)^2}(1-e^{-((x-x_1)^2-(z-z_1)^2)/a_o^2)} \\ &-\frac{1}{2}\frac{a_o^2\Omega_{o,2}(z-z_2)}{(x-x_2)^2+(z-z_2)^2}(1-e^{-((x-x_2)^2-(z-z_2)^2)/a_o^2)} \\ &-\frac{1}{2}\frac{a_o^2\Omega_{o,3}(z-z_3)}{(x-x_3)^2+(z-z_3)^2}(1-e^{-((x-x_3)^2-(z-z_3)^2)/a_o^2)} \\ &+\frac{1}{2}\frac{a_o^2\Omega_{o,4}(z-z_4)}{(x-x_4)^2+(z-z_4)^2}(1-e^{-((x-x_4)^2-(z-z_4)^2)/a_o^2)} \end{aligned} \tag{A.8}$$

and

$$\begin{aligned} w(x,z,t_o) = &-\frac{1}{2}\frac{a_o^2\Omega_{o,1}(x-x_1)}{(x-x_1)^2+(z-z_1)^2}(1-e^{-((x-x_1)^2-(z-z_1)^2)/a_o^2)} \\ &+\frac{1}{2}\frac{a_o^2\Omega_{o,2}(x-x_2)}{(x-x_2)^2+(z-z_2)^2}(1-e^{-((x-x_2)^2-(z-z_2)^2)/a_o^2)} \\ &+\frac{1}{2}\frac{a_o^2\Omega_{o,3}(x-x_3)}{(x-x_3)^2+(z-z_3)^2}(1-e^{-((x-x_3)^2-(z-z_3)^2)/a_o^2)} \\ &-\frac{1}{2}\frac{a_o^2\Omega_{o,4}(x-x_4)}{(x-x_4)^2+(z-z_4)^2}(1-e^{-((x-x_4)^2-(z-z_4)^2)/a_o^2)} \end{aligned} \tag{A.9}$$

where $x_1 = -x_2 = -x_3 = x_4 = b_o/2$ and $z_1 = z_2 = -z_3 = -z_4 = b_o/2$.

A.3 Initial Normalized Velocity Distributions

The normalized velocity field of the vortex systems may be described u/W_o and w/W_o, where for a single vortex

$$W_o = \frac{1}{2} a_o \Omega_o (1 - e^{-1}) \tag{A.10}$$

and for all other systems

$$W_o = \frac{1}{2} \frac{a_o^2 \Omega_{o,1}}{b_o} (1 - \exp(-b_o^2/a_o^2)). \tag{A.11}$$

This leads to the the velocity field of a single vortex (rotating in a counter-clockwise direction) to be described by

$$u^*(x, z, t_o) = \frac{a_o(z - z_c)}{(x - x_c)^2 + (z - z_c)^2} \left(\frac{1 - e^{-((x-x_c)^2 - (z-z_c)^2)/a_o^2}}{1 - e^{-1}} \right) \tag{A.12}$$

$$w^*(x, z, t_o) = -\frac{a_o(x - x_c)}{(x - x_c)^2 + (z - z_c)^2} \left(\frac{1 - e^{-((x-x_c)^2 - (z-z_c)^2)/a_o^2}}{1 - e^{-1}} \right). \tag{A.13}$$

where $x_c = z_c = 0$. In the case of the co-rotating vortex pair, the velocity components u and w are

$$\begin{aligned} u^*(x, z, t_o) = & \frac{b_o(z - z_1)}{(x - x_1)^2 + (z - z_1)^2} \left(\frac{1 - e^{-((x-x_1)^2 - (z-z_1)^2)/a_o^2}}{1 - e^{-b_o^2/a_o^2}} \right) \\ & + \frac{\Omega_{o,2}}{\Omega_{o,1}} \frac{b_o(z - z_2)}{(x - x_2)^2 + (z - z_2)^2} \left(\frac{1 - e^{-((x-x_2)^2 - (z-z_2)^2)/a_o^2}}{1 - e^{-b_o^2/a_o^2}} \right) \end{aligned} \tag{A.14}$$

and

$$\begin{aligned} w^*(x, z, t_o) = & -\frac{b_o(x - x_1)}{(x - x_1)^2 + (z - z_1)^2} \left(\frac{1 - e^{-((x-x_1)^2 - (z-z_1)^2)/a_o^2}}{1 - e^{-b_o^2/a_o^2}} \right) \\ & - \frac{\Omega_{o,2}}{\Omega_{o,1}} \frac{b_o(x - x_2)}{(x - x_2)^2 + (z - z_2)^2} \left(\frac{1 - e^{-((x-x_2)^2 - (z-z_2)^2)/a_o^2}}{1 - e^{-b_o^2/a_o^2}} \right), \end{aligned} \tag{A.15}$$

where $x_1 = -x_2 = b_o/2$ and $z_1 = z_2 = 0$. In the case of the counter-rotating vortex pair, the velocity components u and w are

$$\begin{aligned} u^*(x, z, t_o) = & \frac{b_o(z - z_1)}{(x - x_1)^2 + (z - z_1)^2} \left(\frac{1 - e^{-((x-x_1)^2 - (z-z_1)^2)/a_o^2}}{1 - e^{-b_o^2/a_o^2}} \right) \\ & - \frac{\Omega_{o,2}}{\Omega_{o,1}} \frac{b_o(z - z_2)}{(x - x_2)^2 + (z - z_2)^2} \left(\frac{1 - e^{-((x-x_2)^2 - (z-z_2)^2)/a_o^2}}{1 - e^{-b_o^2/a_o^2}} \right) \end{aligned} \tag{A.16}$$

and

$$w^*(x,z,t_o) = -\frac{b_o(x-x_1)}{(x-x_1)^2+(z-z_1)^2}\left(\frac{1-e^{-((x-x_1)^2-(z-z_1)^2)/a_o^2}}{1-e^{-b_o^2/a_o^2}}\right) + \frac{\Omega_{o,2}}{\Omega_{o,1}}\frac{b_o(x-x_2)}{(x-x_2)^2+(z-z_2)^2}\left(\frac{1-e^{-((x-x_2)^2-(z-z_2)^2)/a_o^2}}{1-e^{-b_o^2/a_o^2}}\right), \tag{A.17}$$

where $x_1 = -x_2 = b_o/2$ and $z_1 = z_2 = 0$. For a co-rotating quadrapole configuration with an outward advection velocity in the vertical direction,

$$\begin{aligned} u^*(x,z,t_o) = {} & \frac{b_o(z-z_1)}{(x-x_1)^2+(z-z_1)^2}\left(\frac{1-e^{-((x-x_1)^2-(z-z_1)^2)/a_o^2}}{1-e^{-b_o^2/a_o^2}}\right) \\ & -\frac{\Omega_{o,2}}{\Omega_{o,1}}\frac{b_o(z-z_2)}{(x-x_2)^2+(z-z_2)^2}\left(\frac{1-e^{-((x-x_2)^2-(z-z_2)^2)/a_o^2}}{1-e^{-b_o^2/a_o^2}}\right) \\ & -\frac{\Omega_{o,3}}{\Omega_{o,1}}\frac{b_o(z-z_3)}{(x-x_3)^2+(z-z_3)^2}\left(\frac{1-e^{-((x-x_3)^2-(z-z_3)^2)/a_o^2}}{1-e^{-b_o^2/a_o^2}}\right) \\ & +\frac{\Omega_{o,4}}{\Omega_{o,1}}\frac{b_o(z-z_4)}{(x-x_4)^2+(z-z_4)^2}\left(\frac{1-e^{-((x-x_4)^2-(z-z_4)^2)/a_o^2}}{1-e^{-b_o^2/a_o^2}}\right) \end{aligned} \tag{A.18}$$

and

$$\begin{aligned} w^*(x,z,t_o) = {} & -\frac{b_o(x-x_1)}{(x-x_1)^2+(z-z_1)^2}\left(\frac{1-e^{-((x-x_1)^2-(z-z_1)^2)/a_o^2}}{1-e^{-b_o^2/a_o^2}}\right) \\ & +\frac{\Omega_{o,2}}{\Omega_{o,1}}\frac{b_o(x-x_2)}{(x-x_2)^2+(z-z_2)^2}\left(\frac{1-e^{-((x-x_2)^2-(z-z_2)^2)/a_o^2}}{1-e^{-b_o^2/a_o^2}}\right) \\ & +\frac{\Omega_{o,3}}{\Omega_{o,1}}\frac{b_o(x-x_3)}{(x-x_3)^2+(z-z_3)^2}\left(\frac{1-e^{-((x-x_3)^2-(z-z_3)^2)/a_o^2}}{1-e^{-b_o^2/a_o^2}}\right) \\ & -\frac{\Omega_{o,4}}{\Omega_{o,1}}\frac{b_o(x-x_4)}{(x-x_4)^2+(z-z_4)^2}\left(\frac{1-e^{-((x-x_4)^2-(z-z_4)^2)/a_o^2}}{1-e^{-b_o^2/a_o^2}}\right) \end{aligned} \tag{A.19}$$

where $x_1 = -x_2 = -x_3 = x_4 = b_o/2$ and $z_1 = z_2 = -z_3 = -z_4 = b_o/2$.

Appendix B

Analytical Model

B.1 General Wave Equation

The derivation of the general wave equation begins with the two dimensional inviscid primitive governing equations with the Boussinesq approximation (6.1-6.4).

We begin, by taking the time derivative of (6.2) and substituting it into (6.3) to get:

$$\frac{\partial^2 w}{\partial t^2} + N^2 w = \frac{-1}{\rho_o}\frac{\partial^2 p'}{\partial z \partial t}. \tag{B.1}$$

Then by taking the derivative of (6.1) and substituting it into (6.4), we obtain:

$$\frac{-1}{\rho_o}\frac{\partial^2 p'}{\partial x^2} + \frac{\partial^2 w}{\partial z \partial t} = 0. \tag{B.2}$$

Through observation, it seen that these two equations may be related if (B.1) is differentiated by $\partial^2/\partial x^2$ and (B.2) is differentiated by $\partial^2/\partial z \partial t$. The resulting governing wave equation in terms of w and N is, therefore,

$$\frac{\partial^2}{\partial t^2} \bigtriangledown^2 w + N^2 \frac{\partial^2 w}{\partial x^2} = 0. \tag{B.3}$$

In order to re-write this equation in terms of ρ' and N, the plane wave assumption is utilized,

$$w(x,z,t) = \hat{w}(k,m,t)e^{i(kx+mz-\omega t)} \tag{B.4}$$

$$\rho'(x,z,t) = \hat{\rho}'(k,m,t)e^{i(kx+mz-\omega t)} \tag{B.5}$$

where k and m are the wave numbers in the horizontal and vertical directions, respectively, and ω is the dispersion relation.

By substituting these equations into equation 6.3, it is found that

$$w = -i\frac{g\omega}{\rho_o N^2}\rho' \tag{B.6}$$

By substituting this equation into (B.3), the governing wave equation in terms of ρ' and N becomes

$$\frac{\partial^2}{\partial t^2} \bigtriangledown^2 \rho' + N^2 \frac{\partial^2 \rho'}{\partial x^2} = 0. \tag{B.7}$$

B.2 General solution for $\hat{\rho}'$

We define the equations for the Fourier transform and reverse Fourier transform as:

$$\hat{f}(k,m) = \int_{-\infty}^{\infty}\int_{-\infty}^{\infty} f(x,z)e^{-i(kx+mz)}dxdz \tag{B.8}$$

$$f(x,z) = (1/4\pi)\int_{-\infty}^{\infty}\int_{-\infty}^{\infty} \hat{f}(k,m)e^{i(kx+mz)}dkdm. \tag{B.9}$$

By taking the Fourier transform of ρ' (B.5) and substituting it into (B.7), the governing wave equation in Fourier space is found

$$\frac{\partial^2 \widehat{\rho'}}{\partial t^2} + \omega^2 \widehat{\rho'} = 0, \tag{B.10}$$

where $\omega^2 = \frac{k^2 N^2}{k^2+m^2}$ is the dispersion relation.

The general solution to this equation is of the form:

$$\hat{\rho}'(k,m,t) = c_1(k,m)e^{i\omega t} + c_2(k,m)e^{-i\omega t}, \tag{B.11}$$

where c_1 and c_2 are based on the flows initial conditions. The initial conditions are defined as:

$$\hat{f}_1(k,m) = \hat{\rho}'(k,m,t_o) \tag{B.12}$$

$$\hat{f}_2(k,m) = \frac{d\hat{\rho}'(k,m,t_o)}{dt}. \tag{B.13}$$

By substituting (B.12) into (B.11) and substituting (B.13) into the time derivative of (B.11), equations for c_1 and c_2 are found:

$$c_1(k,m) = \frac{1}{2}(\hat{f}_1(k,m) + \hat{f}_2(k,m)/i\omega) \tag{B.14}$$

$$c_2(k,m) = \frac{1}{2}(\hat{f}_1(k,m) - \hat{f}_2(k,m)/i\omega). \tag{B.15}$$

Substituting these equations into (B.11) produces the generic equation for $\hat{\rho}'$:

$$\hat{\rho}'(k,m,t) = \frac{1}{2}\left[\hat{f}_1(k,m) + \frac{\hat{f}_2(k,m)}{i\omega}\right]e^{i\omega t} + \frac{1}{2}\left[\hat{f}_1(k,m) - \frac{\hat{f}_2(k,m)}{i\omega}\right]e^{-i\omega t}, \tag{B.16}$$

which may be re-written as

$$\hat{\rho}'(k,m,t) = \hat{f}_1\cos(\omega t) + \frac{\hat{f}_2\sin(\omega t)}{i\omega} \tag{B.17}$$

In the flows presented here, the initial velocity field is superimposed on a linearly stable density field. Therefore, the initial density field is undisturbed and

$$\hat{f}_1(k,m) = \hat{\rho}'(k,m,t_o) = 0 \tag{B.18}$$

Utilizing (6.3), the initial time derivative of the density perturbation is found,

$$\frac{\partial\rho'}{\partial t}(x,z,t_o) = -w_o\frac{d\overline{\rho}(z)}{dz}, \tag{B.19}$$

which leads to

$$\hat{f}_2(k,m) = \frac{\partial\hat{\rho}'(k,m,t_o)}{\partial t} = -\hat{w}_o\frac{d\overline{\rho}(z)}{dz} \tag{B.20}$$

in Fourier space where $d\overline{P}/dz = const.$

Substituting $\hat{f}_1$ and $\hat{f}_2$ into equation B.17, $\hat{\rho}'$ becomes:

$$\hat{\rho}'(k,m,t) = -\frac{\hat{w}_o}{i\omega}\frac{d\overline{\rho}(z)}{dz}\sin(\omega t), \tag{B.21}$$

B.3 Single vortex, $\hat{w}_o$

In all configurations considered, the initial flow field is made up of Lamb-Oseen vortices with Gaussian profiles. The velocity field of a single vortex is

$$w_o = \left[\frac{\Gamma_o}{2\pi r}(1 - e^{-r^2/a_o^2})\right]\cos\theta \tag{B.22}$$

$$u_o = \left[\frac{\Gamma_o}{2\pi r}(1 - e^{-r^2/a_o^2})\right]\sin\theta. \tag{B.23}$$

Here r represents the radial distance from the vortex center and θ represents the angle from the positive horizontal axis.

In Fourier space w becomes:

$$\hat{w}_o(k,m) = \int_{-\infty}^{\infty}\int_{-\infty}^{\infty} w(x,z)e^{-i(kx+mz)}dxdz \tag{B.24}$$

$$= \int_0^{\infty}\int_0^{2\pi} w(x,z)e^{-iKr\cos(\theta-\phi)}rd\theta dr \tag{B.25}$$

$$= \frac{\Gamma_o}{2\pi}\int_0^{\infty}(1 - e^{-r^2/a_o^2})\int_0^{2\pi}\cos\theta e^{-iKr\cos(\theta-\phi)}d\theta dr, \tag{B.26}$$

where ϕ represents the angle made by k and m, $\phi = tan^{-1}(m/k)$, and where $K = \sqrt{k^2+m^2}$.

This equation reduces to:

$$\hat{w}_o = -i\cos\phi\Gamma_o\left[\frac{1}{K}\int_0^{\infty} J_1(Kr)d(Kr) - \int_0^{\infty} e^{-r^2/a_o^2}J_1(Kr)dr\right] \tag{B.27}$$

where $J_1(Kr)$ is a Bessel function of the first order and first kind.

The first integral term of (B.27) is $1/K$. However, the second integral term of (B.27) is complicated:

$$\int_0^{\infty} e^{-r^2/a_o^2}J_1(Kr)dr = \frac{\Gamma(1)(Ka_o^2)}{\Gamma(2)}M\left(1,2,-\frac{-K^2a_o^2}{4}\right), \tag{B.28}$$

where M is the confluent hypergeometric function (Abramowitz and Stegun, 1972) and Γ is the Gamma function.

Utilizing the Handbook of Mathematical Functions (Abramowitz and Stegun, 1972), it is found that:

$$M\left(1, 2, -\frac{-K^2 a_o^2}{4}\right) = -\frac{e^{-K^2 a_o^2/2}}{K^2 a_o^2/2} \sinh(-K^2 a_o^2/2). \tag{B.29}$$

Therefore bringing everything together, it is found that:

$$\hat{w}_o = -\frac{i\Gamma_o \cos\phi}{K} e^{-K^2 a_o^2/4}. \tag{B.30}$$

B.4 Vortex systems, $\hat{w}_o$

As stated earlier, since the initial condition is based on the superposition of vortices, the initial flow field may be added together using the shifting theorem:

$$f(x - \Delta, z) \leftrightarrow exp(-ik\Delta)\hat{f}(k, m). \tag{B.31}$$

Equation B.30 gives us $\hat{w}_o$ for a single vortex. In the cases of co-rotating or counter-rotating vortex pairs separated by a distance, b_o, the shifting theorem becomes,

$$f(x - \frac{b_o}{2}) \leftrightarrow e^{-i\frac{1}{2}kb_o}\hat{f}(k), \tag{B.32}$$

where $\Delta = b_o/2$ and the vertical axis corresponds to the midpoint between the vortices. This leads to $\hat{w}_o$, found in equation B.30, to be multiplied by $e^{\pm i\frac{1}{2}kb_o}$. In the co-rotating vortex pair, the vortices are of the same sign circulation. Therefore, the quantities may be summed together to get:

$$\hat{w}_o = -2i\frac{\Gamma_o \cos\phi}{K} e^{-K^2 a_o^2/4} \cos(\frac{1}{2}kb_o).$$

In the case of a counter-rotating vortex pair, the vortices are of opposite sign. Therefore, one term is subtracted from the other term. This provides the equation of:

$$\hat{w}_o = 2\frac{\Gamma_o \cos\phi}{K} e^{-K^2 a_o^2/4} \sin(\frac{1}{2}kb_o).$$

In the quadrapole configurations we are positioning each vortex in its own quadrant. Therefore, the shifting theorem becomes,

$$f(x-\frac{b_o}{2},z-\frac{b_o}{2}) \leftrightarrow e^{-i\frac{1}{2}(k+m)b_o}\hat{f}(k,m). \tag{B.33}$$

By applying this theorem to the VQ and taking into consideration the signs of the vortex circulation, the $\hat{w}_o$ equation becomes:

$$\hat{w}_o = 4\frac{\Gamma_o \cos\phi}{K} e^{-K^2 a_o^2/4} \sin(\frac{1}{2}k_s b_o)\cos(\frac{1}{2}m_s b_o).$$

B.5 Determinant of A

In this section, the calculation for the determinant of A found in (6.34) is calculated, where

$$A = \begin{bmatrix} \frac{\partial c_{g,x}}{\partial k_s} & \frac{\partial c_{g,x}}{\partial m_s} \\ \frac{\partial c_{g,z}}{\partial k_s} & \frac{\partial c_{g,z}}{\partial m_s} \end{bmatrix} \tag{B.34}$$

and

$$detA = \frac{\partial c_{g,x}}{\partial k_s}\frac{\partial c_{g,z}}{\partial m_s} - \frac{\partial c_{g,x}}{\partial m_s}\frac{\partial c_{g,z}}{\partial k_s}. \tag{B.35}$$

Note that $detA = t^{-2}det(At)$. With the knowledge that $\underline{x} = \underline{c_g}t$, At may be written as:

$$At = \begin{bmatrix} \frac{\partial x}{\partial k_s} & \frac{\partial x}{\partial m_s} \\ \frac{\partial z}{\partial k_s} & \frac{\partial z}{\partial m_s} \end{bmatrix} = \begin{bmatrix} \frac{\partial x}{\partial K_s} & \frac{\partial x}{\partial \theta} \\ \frac{\partial z}{\partial K_s} & \frac{\partial z}{\partial \theta} \end{bmatrix} \begin{bmatrix} \frac{\partial K_s}{\partial k_s} & \frac{\partial K_s}{\partial m_s} \\ \frac{\partial \theta}{\partial k_s} & \frac{\partial \theta}{\partial m_s} \end{bmatrix}. \tag{B.36}$$

We are defining the matrices on the right hand side of the equation as B and C, respectively. In section 6.2, the stationary wave numbers and their corresponding spacial locations for $x > 0$, were calculated to be:

$$[k_s, m_s] = K_s sgn(\sin\theta)\Big[\sin\theta, -\cos\theta\Big]$$
$$[x, z] = \frac{Nt\cos\theta}{K_s}\Big[\cos\theta, \sin\theta\Big].$$

Therefore, the partial derivatives required to solve for B are:

$$\frac{\partial x}{\partial K_s} = -Nt\frac{\cos^2\theta}{K_s^2} \qquad \frac{\partial x}{\partial \theta} = Nt\frac{-2\cos\theta\sin\theta}{K_s}$$
$$\frac{\partial z}{\partial K_s} = -Nt\frac{\cos\theta\sin\theta}{K_s^2} \qquad \frac{\partial z}{\partial \theta} = Nt\frac{\cos^2\theta - \sin^2\theta}{K_s}$$

and the partial derivatives required to solve for C are:

$$\frac{\partial \theta}{\partial k_s} = \frac{sgn(\sin\theta)}{K_s\cos\theta} \qquad \frac{\partial K_s}{\partial k_s} = \frac{sgn(\sin\theta)}{\sin\theta}$$
$$\frac{\partial \theta}{\partial m_s} = \frac{sgn(\sin\theta)}{K_s\sin\theta} \qquad \frac{\partial K_s}{\partial m_s} = -\frac{sgn(\sin\theta)}{\cos\theta}.$$

Therefore,

$$det(B) = det\begin{bmatrix} \frac{\partial x}{\partial K_s} & \frac{\partial x}{\partial \theta} \\ \frac{\partial z}{\partial K_s} & \frac{\partial z}{\partial \theta} \end{bmatrix} = \frac{\partial x}{\partial K_s}\frac{\partial z}{\partial \theta} - \frac{\partial x}{\partial \theta}\frac{\partial z}{\partial K_s} = -\frac{Nt\cos^2\theta}{K^3} \tag{B.37}$$

$$det(C) = det\begin{bmatrix} \frac{\partial K_s}{\partial k_s} & \frac{\partial K_s}{\partial m_s} \\ \frac{\partial \theta}{\partial k_s} & \frac{\partial \theta}{\partial m_s} \end{bmatrix} = \frac{\partial K_s}{\partial k_s}\frac{\partial \theta}{\partial m_s} - \frac{\partial K_s}{\partial m_s}\frac{\partial \theta}{\partial k_s} = -\frac{Nt}{K}, \tag{B.38}$$

which leads to

$$det(At) = det(BC) = det(B)det(C) = \left[\frac{Nt\cos\theta}{K^2}\right]^2. \tag{B.39}$$

Rewriting this equation, it may be shown that:

$$|detA|^{-1/2} = |t^{-2}det(At)|^{-1/2} = \frac{K_s^2}{N|\cos\theta|}. \tag{B.40}$$

B.6 Vortex Configuration - Stationary Phase Approximation

In section 6.2, the equation for the stationary phase approximation was found to be:

$$\rho'(x,z,t) \approx Real\left\{\frac{2\pi}{Nt}\frac{K_s^2}{|\cos\theta|}\left[F_+(k_s,m_s)e^{it\omega(k_s,m_s)} + F_-(k_s,m_s)e^{-it\omega(k_s,m_s)}\right]\right\}, \tag{B.41}$$

where

$$F_-(k_s,m_s)=\hat{f}_1(k_s,m_s)-\hat{f}_2(k_s,m_s)/i\omega,//F_+(k_s,m_s)=\hat{f}_1(k_s,m_s)+\hat{f}_2(k_s,m_s)/i\omega$$

and k_s, m_s and K_s are defined by equations 6.28, 6.29 and 6.32, respectfully. Recall that:

$$\hat{f}_1(k,m)=\hat{\rho}'(k,m,t_o)=0$$
$$\hat{f}_2(k,m)=\frac{\partial\hat{\rho}'(k,m,t_o)}{\partial t}=-\hat{w}_o\frac{d\bar{\rho}}{dz}.$$

Therefore, equations $F_-(k_s,m_s)$ and $F_+(k_s,m_s)$ will very between the vortex systems due to different w_o. Therefore, by substituting in the values for $\hat{w}_o$ (found in Appendix B.4) into (B.42), and solving for $F_-(k_s,m_s)$ and $F_+(k_s,m_s)$, it is found that:

for a single vortex

$$F_-(k_s,m_s)=\left[\frac{\rho_o}{g}N^2L_o\right]\frac{1}{2\pi}\frac{FrL_o^2}{K_sL_o}e^{-K_s^2a_o^2/4}$$
$$F_+(k_s,m_s)=-\left[\frac{\rho_o}{g}N^2L_o\right]\frac{1}{2\pi}\frac{FrL_o^2}{K_sL_o}e^{-K_s^2a_o^2/4},$$

for a co-rotating vortex pair

$$F_-(k_s,m_s)=\left[\frac{\rho_o}{g}N^2L_o\right]\frac{2}{2\pi}\frac{FrL_o^2}{K_sL_o}e^{-K_s^2a_o^2/4}\cos(\frac{1}{2}kb_o)$$
$$F_+(k_s,m_s)=-\left[\frac{\rho_o}{g}N^2L_o\right]\frac{2}{2\pi}\frac{FrL_o^2}{K_sL_o}e^{-K_s^2a_o^2/4}\cos(\frac{1}{2}kb_o),$$

for a counter-rotating vortex pair

$$F_-(k_s,m_s)=-i\left[\frac{\rho_o}{g}N^2L_o\right]\frac{2}{2\pi}\frac{FrL_o^2}{K_sL_o}e^{-K_s^2a_o^2/4}\sin(\frac{1}{2}kb_o)$$
$$F_+(k_s,m_s)=i\left[\frac{\rho_o}{g}N^2L_o\right]\frac{2}{2\pi}\frac{FrL_o^2}{K_sL_o}e^{-K_s^2a_o^2/4}\sin(\frac{1}{2}kb_o),$$

for a VQ

$$F_-(k_s,m_s)=-i\left[\frac{\rho_o}{g}N^2L_o\right]\frac{4}{2\pi}\frac{FrL_o^2}{K_sL_o}e^{-K_s^2a_o^2/4}\cos(\frac{1}{2}kb_o)$$
$$F_+(k_s,m_s)=i\left[\frac{\rho_o}{g}N^2L_o\right]\frac{4}{2\pi}\frac{FrL_o^2}{K_sL_o}e^{-K_s^2a_o^2/4}\cos(\frac{1}{2}kb_o).$$

Substituting these equations into equation B.41, it is found that:

for a single vortex

$$\frac{\rho'(x,z,t)}{L_o N^2 \rho_o/g} \approx \left(Fr \frac{K_s L_o}{Nt|\cos\theta|} e^{-K_s^2 a_o^2/4} \right) Real\left\{ -e^{it\omega(k_s,m_s)} + e^{-it\omega(k_s,m_s)} \right\}$$
$$\approx \left(2Fr \frac{K_s L_o}{Nt|\cos\theta|} e^{-K_s^2 a_o^2/4} \right) \left(sgn(x)\cos(\omega t) \right), \tag{B.42}$$

for a co-rotating vortex pair

$$\frac{\rho'(x,z,t)}{L_o N^2 \rho_o/g} \approx \left(2Fr \frac{K_s L_o}{Nt|\cos\theta|} e^{-K_s^2 a_o^2/4} \cos(\frac{1}{2} k_s b_o) \right)$$
$$\cdot Real\left\{ -e^{it\omega(k_s,m_s)} + e^{-it\omega(k_s,m_s)} \right\}$$
$$\approx \left(4Fr \frac{K_s L_o}{Nt|\cos\theta|} e^{-K_s^2 a_o^2/4} \cos(\frac{1}{2} k_s b_o) \right) \left(sgn(x)\cos(\omega t) \right), \tag{B.43}$$

for a counter-rotating vortex pair

$$\frac{\rho'(x,z,t)}{L_o N^2 \rho_o/g} \approx \left(-2Fr \frac{K_s L_o}{Nt|\cos\theta|} e^{-K_s^2 a_o^2/4} \sin(\frac{1}{2} k_s b_o) \right)$$
$$\cdot Real\left\{ ie^{it\omega(k_s,m_s)} - ie^{-it\omega(k_s,m_s)} \right\}$$
$$\approx \left(-4Fr \frac{K_s L_o}{Nt|\cos\theta|} e^{-K_s^2 a_o^2/4} \sin(\frac{1}{2} k_s b_o) \right) \left(\sin(\omega t) \right), \tag{B.44}$$

for a *VQ*

$$\frac{\rho'(x,z,t)}{L_o N^2 \rho_o/g} \approx \left(-4Fr \frac{K_s L_o}{Nt|\cos\theta|} e^{-K_s^2 a_o^2/4} \sin(\frac{1}{2} k_s b_o) \cos(\frac{1}{2} m_s b_o) \right)$$
$$\cdot Real\left\{ ie^{it\omega(k_s,m_s)} - ie^{-it\omega(k_s,m_s)} \right\}$$
$$\approx \left(-8Fr \frac{K_s L_o}{Nt|\cos\theta|} e^{-K_s^2 a_o^2/4} \sin(\frac{1}{2} k_s b_o) \cos(\frac{1}{2} m_s b_o) \right) \left(\sin(\omega t) \right). \tag{B.45}$$

Bibliography

Abramowitz, M., and Stegun, I. A., 1972: *Handbook of Mathematical Functions.* National Bureau of Standards, Washington.

Briggs, D. A., Ferziger, J. H., Koseff, J. R., and Monismith, S. G., 1996: Entrainment in a shear-free turbulent mixing layer. *J. Fluid Mech.*, **310**, 215241.

Buhler, O., and McIntyre, M. E., 1999: On shear-generated gravity waves that reach the mesophere. part 1: Wave generation. *American Meteorological Society.*, **56**, 3749–3763.

Cadot, O., Douady, S., and Couder, Y., 1995: Characterization of the low-pressure filaments in a three-dimensional turbulent shear flow. *Phys. Fluids A*, **7**, 630–646.

Carnevale, G. F., McWilliams, J. C., Pomeau, Y., Weiss, J. B., and Young, W. R., 1991: Evolution of vortex statistics in two-dimensional turbulence. *Phys. Rev. Lett.*, **66**, 2735.

Cerretelli, C., and Williamson, C. H. K., 2003: The physical mechanism for vortex merging. *J. Fluid Mech.*, **475**, 41–77.

Crow, S. C., 1974: Motion of a vortex pair in a stably stratified fluid. *Poseidon Research Report 1, Santa Monica, CA*, 1–48.

Delisi, D. P., Robins, R. E., and D., L. R., 1991: Initial laboratory observations of the evolution of a vortex pair in a stratified shear flow. *Phys. Fluids A*, **3**, 2489–2791.

Diamessis, P. J., and Nomura, K. K., 2004: The structure and dynamics of overturns in stably stratified homogeneous turbulence. *J. Fluid Mech.*, **499**, 197–229.

Dohan, K., and Sutherland, B. R., 2005: Numerical and laboratory generation of internal waves from turbulence. *Dyn. Atmos. Oceans*, **40**, 43–56.

Dritschel, D. G., 1985: The stability and energetics of corotating uniform vortices. *J. Fluid Mech.*, **157**, 95–134.

Dritschel, D. G., 1998: On the persistence of non-axisymmetric vortices in inviscid two-dimensional flows. *J. Fluid Mech.*, **371**, 141–155.

Dritschel, D. G., and Waugh, D. W., 1992: The nonlinear evolution of rotating configurations of uniform vorticity. *Phys. Fluids*, **4**, 1737.

Ehrenstein, U., and Rossi, M., 1999: Equilibria of corotating nonuniform vortices. *Phys. Fluids*, **11**, 3416.

Fernando, H. J. S., and Hunt, J. C. R., 1997: Turbulence, waves and mixing at shear-free density interfaces. part 1. a theoretical model. *J. Fluid Mech.*, **347**, 197234.

Garten, J. F., Arendt, S., Fritts, D. C., and Werne, J., 1998: Dynamics of counter-rotating vortex pairs in stratified and sheared environments. *J. Fluid Mech.*, **361**, 189–236.

Garten, J. F., Werne, J., Fritts, D. C., and Arendt, S., 2001: Direct numerical simulations of the crow instability and subsequent vortex reconnection in a stratified fluid. *J. Fluid Mech.*, **426**, 1–45.

Gerz, T., Schumann, U., and Elghobashi, S., 1989: Direct simulation of stably stratified homogeneous turbulent shear flows. *J. Fluid Mech.*, **200**, 563–594.

Griffiths, R. M., 1999: Interaction of vorticity and internal gravity waves. Ph.D Thesis, University of Cambridge, England.

Griffiths, R. W., and Hopfinger, E. J., 1987: Coalescing of geostrophic vortices. *J. Fluid Mech.*, **178**, 73–97.

Hill, F. M., 1975: A numerical study of the descent of a vortex pair in a stably stratified atmosphere. *J. Fluid Mech.*, **71**, 1–13.

Holzapfel, F., and Gerz, T., 1999: Two-dimensional wake vortex physics in the stably stratified atmosphere. *Aerosp. Sci. Technol.*, **5**, 261–270.

Huang, M. J., 2005: The physical mechanism of symmetric vortex merger: A new viewpoint. *Phys. Fluids*, **17**, 1–7.

Jeong, J., and Hussain, F., 1995: On the identification of a vortex. *J. Fluid Mech.*, **285**, 69–94.

Kida, S., 1981: Motion of an elliptic vortex in a uniform shear flow. *J. Phys. Soc. Jpn.*, **50**, 3517.

Kimura, Y., and Herring, J. R., 2001: Gradient enhancement and filament ejection for a non-uniform elliptic vortex in two-dimensional turbulence. *J. Fluid Mech.*, **439**, 43–56.

Le Dizes, S., and Verga, A., 2002: Viscous interactions of two co-rotating vortices before merging. *J. Fluid Mech.*, **467**, 389–410.

Legras, B., and Dritschel, D. G., 1993: Vortex stripping and the generation of high vorticity gradients in two-dimensional flows. *Appl. Sci. Res.*, **51**, 445.

Lighthill, J., 1996: General lectures: Internal waves and related initial-value problems. *Dyn. Atmos. Oceans*, **23**, 3–17.

Lin, J. T., and Pao, Y. H., 1979: Wakes in stratified fluids. *Ann. Rev. Fluid Mech.*, **11**, 317–338.

Lin, J. T., and Veenhuizen, S. D., 1974: Measurements of the decay of grid generated turbulence in a stably stratified fluid. *Bull. Am. Phys. Soc.*, **19**, 1142–1143.

Mariotti, A., Legras, B., and Dritschel, D. G., 1994: Vortex stripping and the erosion of coherent structures in two-dimension flows. Phys. Fluids.

McGrath, J. L., Fernando, H. J. S., and Hunt, J. C. R., 1997: Turbulence, waves and mixing at shear-free density interfaces. part 2. laboratory experiments. *J. Fluid Mech.*, **347**, 235261.

Melander, M. V., McWilliams, J. C., and Zabusky, N. J., 1987a: Asymmetric vortex merger in two dimensions: Which vortex is "victorious"? *Phys. Fluids*, **30**, 2610–2612.

Melander, M. V., McWilliams, J. C., and Zabusky, N. J., 1987b: Axisymmetrization and vorticity-gradient intensification of an isolated two-dimensional vortex through filamentation. *J. Fluid Mech.*, **178**, 137–159.

Melander, M. V., Zabusky, N. J., and McWilliams, J. C., 1988: Symmetric vortex merger in two dimensions: causes and conditions. *J. Fluid Mech.*, **195**, 305–340.

Meng, J. S., and Rottman, J. W., 1988: Linear internal waves generated by density and velocity perturbations in a linearly stratified fluid. *J. Fluid Mech.*, **195**, 305–340.

Metais, O., Flores, C., Yanase, S., Riley, J., and Lesieur, M., 1995: Rotating free-shear flows. part 2. numerical simulations. *J. Fluid Mech.*, **293**, 47–80.

Meunier, P., 2001: Etude experimentale de deux tourbillons co-rotatifs. *Ph.D. Dissertation, Universite d'Aix-Marseille I, France.*

Meunier, P., Ehrenstein, U., Leweke, T., and Rossi, M., 2002: A merging criterion for two-dimensional co-rotating vortices. *Phys. Fluids*, **14**, 2757–2766.

Meunier, P., Le Dizes, S., and Leweke, T., 2005: Physics of vortex merging. *C. R. Physique*, **6**, 431–450.

Meunier, P., and Leweke, T., 2001: Three-dimensional instability during vortex merging. *Phys. Fluids*, **13**, 2747–2750.

Mitchell, T. B., and Driscoll, C. F., 1996: Electron vortex orbits and merger. *Phys. Fluids*, **8**, 1828–1841.

Nomura, K. K., and Post, G. K., 1998: The structure and dynamics of vorticity and rate of strain in incompressible homogeneous turbulence. *J. Fluid Mech.*, **377**, 65–97.

Overman, E. A., and Zabusky, N. J., 1982: Evolution and merger of isolated vortex structures. *Phys. Fluids*, **25**, 1297–1305.

Pao, Y. H., Callahan, M. F., and Timm, G. K., 1968: Vortex street in stably stratified fluids. *Boeing Document*, **82-0736**.

Pao, Y. H., and Lin, J. T., 1973: Turbulent wakes of a towed slender body in stratified and nonstratified fluids: analysis and flow visualizations. *Bull. Am. Phys. Soc.*, **18**, 1484.

Protas, B., Babiano, A., and Kevlahan, N. K. R., 1999: On geometrical alignment properties of two-dimensional forced turbulence. *Physica D*, **128**, 169–179.

Rogers, M. M., and Moin, P., 1987: The structure of the vorticity field in homogeneous turbulent flows. *J. Fluid Mech.*, **176**, 33–66.

Rossow, V. J., 1977: Convective merging of vortex cores in lift-generated wakes. *J. Aircraft*, **14**, 283–290.

Saffman, P. G., 1972: The motion of a vortex pair in a stratified atmosphere. *SIAM*, **L1, 2**, 107–119.

Saffman, P. G., 1992: *Vortex dynamics*. Cambridge University Press.

Saffman, P. G., and Szeto, R., 1980: Equillibrium shapes of a pair of equal uniform vortices. *Phys. Fluids*, **23**, 2339–2342.

Sandham, N. D., and Kleiser, L., 1992: The late stages of transition to turbulence in channel flow. *J. Fluid Mech.*, **245**, 319–348.

Sarpkaya, T., 1983: Trailing vortices in homogeneous and density-stratified media. *J. Fluid Mech.*, **136**, 85–109.

Schilling, V., Siano, S., and Etling, D., 1996: Dispersion of aircraft emissions due to wake vortices in stratified shear flows: A two-dimensional numerical study. *J. Geophys. Res.*, **101**, 20965.

Scorer, R. S., and Davenport, L. J., 1970: Contrails and aircraft downwash. *J. Fluid Mech.*, **43**, 451–464.

She, Z. S., Jackson, E., and Orszag, S. A., 1990: Intermittent vortex structures in homogeneous isotropic turbulence. *Nature*, **344**, 226–228.

Spalart, P. R., 1996: On the motion of laminar wing wakes in a stratified fluid. *J. Fluid Mech.*, **327**, 139–160.

Staquet, C., and Sommeria, J., 2002: Internal gravity waves: from instabilities to turbulence. *Ann. Rev. Fluid Mech.*, **34**, 559–593.

Sutherland, B. R., Flynn, M. R., and Dohan, K., 2004: Internal wave excitation from a collapsing mixed region. *Deep-Sea Research II*, **51**, 2889–2904.

Trieling, R. R., Velasco Fuentes, O. U., and van Heijst, G. J. F., 2005: Interaction of two unequal corotating vortices. *Phys. Fluids*, **17**, 1–17.

Velasco Fuentes, O. U., 2005: Vortex filamentation: its onset and its role on axisymmetrization and merger. *Dynamics of Atmospheres and Oceans*, **40**, 23–42.

Vincent, A., and Meneguzzi, M., 1991: The spatial structure and statistical properties of homogeneous turbulence. *J. Fluid Mech.*, **225**, 1–20.

Vincent, A., and Meneguzzi, M., 1994: The dynamics of vorticity tubes in homogeneous turbulence. *J. Fluid Mech.*, **258**, 245–254.